ULB FACULTÉ DES SCIENCES

UNIVERSITÉ LIBRE DE BRUXELLES

Longwave radiative effect of ozone from IASI observations

Thesis presented by Stamatia DONIKI

with a view to obtaining the PhD Degree in Sciences ("Docteur en Sciences")

Année académique 2018-2019

Supervisor: Professor P.-F. COHEUR

Service de Chimie Quantique et Photophysique

Thesis jury :

Dr. Michel Godefroid (Université libre de Bruxelles, Chair)
Dr. Frank Pattyn (Université libre de Bruxelles, Secretary)
Dr. Steven Dewitte (Royal Meteorological Institute of Belgium)
Dr. Claude Camy-Peyret (IPSL, UPMC, Sorbonne Université)

"Though this be madness, yet there's method in it."

Polonius (Hamlet)

Abstract

Ozone is one of the most important greenhouse gases in terms of radiative forcing, as a result of increasing in its precursor emissions since pre-industrial times. Until recently, the ozone radiative forcing calculations were entirely model based, exhibiting high uncertainties and a large spread in model values, as shown in the Intergovernmental Panel on Climate Change, Assessment Report 5. Satellite sounders operating in the infrared now offer the possibility to infer directly the longwave radiative effect (LWRE) of ozone. The hyperspectral measurements allow to retrieve a vertical profile of ozone, and also the vertical distribution of the LWRE, apart from its column integrated value. The separation between troposphere and stratosphere allows to better constrain model estimates of ozone radiative forcing, but also support the predictions for its future evolution.

In this thesis, a new method for calculating the ozone LWRE is presented, by exploiting the measurements of the Infrared Atmospheric Sounding Interferometer on board the Metop satellites. The method is based on the calculation of the Instantaneous Radiative Kernel (IRK, in $\mathrm{Wm^{-2}ppb^{-1}}$), which implies the angular integration of the radiance (in the 9.6 µm band) at the top of the atmosphere using a Gaussian Quadrature. This quantity is transformed into a radiative flux density (the LWRE, in $\mathrm{Wm^{-2}}$) by multiplication with the ozone profile retrieved by FORLI, for each atmospheric scene. The LWRE calculation method is applied to IASI non-cloudy scenes, for day and night, for the period of 01/10/2007 to 31/12/2016. The results are analyzed separately for the total column of ozone, and for its tropospheric and stratospheric components; they are compared to estimations determined independently from the TES (Tropospheric Emission Spectrometer) measurements on-board Aura, and from three state-of the-art chemistry-climate models. The discussion of the results is focused then on the spatial and temporal variability of the LWRE in the troposphere and stratosphere, as well as the on the trends over 9 years of measurements.

Acknowledgements

My life in Brussels was marked by new knowledge, various events and countless new and important people from Belgium and around the world, making my every-day life a fruitful experience. First of all, I would like to thank Dimitris Balis and Mariliza Koukouli (AUTh), and Michel Van Roosendael (IASB), all of whom showed their full support when a PhD was still another idea of mine. I would like to thank the whole *Service de Chimie Quantique et Photophysique* - current and former staff - for coping with me at all times. But, special thanks will be given to: Pierre, for giving me the opportunity in the first place, for believing in me, even when I was losing faith in myself; for being always there more than just a supervisor. Lieven, for all the lunch-breaks, discussions, and help from mathematics to computers; for sharing his knowledge. Cathy, for being always there to give extra advice. Michel H. and Michel G., my supporting committee, could not ask for a better couple. Athena, my Belgian-Greek friend; Maya-Juliette-Sarah from LATMOS, always a good excuse to be in Paris for work; Catherine and Rosa, constantly by my side - literally always, work or not. Daniel, the wizard of our laboratory, for being the most important person of this work, among others, from the beginning to the end.

I would like to thank the Belgian contribution to the O3MSAF Project and BELSPO, for the financial support, and everyone else who contributed to various moments and ways, to make this work better.

Finally, I would like to thank my friends in Greece, Belgium and around the world, mostly for their patience. And, last but not least, I would like to thank my family back in Greece, who have been supporting me in this long journey, and my Greek neighbours in Brussels, who stood by my side as family from the first day we met.

Thank you all for being there.

Edit (following the private defense): I would also like to thank the Jury of this Thesis, Dr. M. Godefroid (President) and Dr. F. Pattyn (Secretary) from ULB, Dr. C. Camy-Peyret (UPMC) and Dr. S. Dewitte (RMI), for testing my knowledge, giving constructive feedback, and allowing me to reach the end of this work.

Contents

List of Figures

List of Tables

List of Acronyms

ACCMIP	Atmospheric Chemistry and Climate Model Intercomparison Project	3
AIRS	Atmospheric Infrared Sounder	68
AVK	Averaging Kernel	82
CAM-RT	Community Atmosphere Model - Radiative Transfer model	148
CCM	Chemistry - Climate Model	147
CERES	Clouds and the Earth's Radiant Energy System	91
CFC	Chlorofluorocarbon	17
CNES	Centre National d'Etudes Spatiales	69
CrIS	Cross-track Infrared Sounder	68
DOFS	Degrees of Freedom for Signal	83
DU	Dobson Unit	46
ERBE	Earth Radiation Budget Experiment	91
ERF	Effective Radiative Forcing	42
EUMETSAT	European Organisation for the Exploitation of Meteorological Satellites	78
FORLI	Fast Optimal Retrieval on Layers for IASI	77
FOV	Field of View	71
FTIR	Fourier-Transformed Infrared Radiation	66
GEO	Geostationary Earth Orbit	67
GHG	Greenhouse Gas	61
GISS-RT	Goddard Institute for Space Studies - Radiative Transfer model	148
GOME	Global Ozone Monitoring Experiment	67

GQ	Gaussian Quadrature	90
GS	Global Survey	74
HCFC	Hydro-Chlorofluorocarbon	50
HFC	Hydro-Fluorocarbon	50
HIRDLS	High Resolution Dynamics Limb Sounder	73
HITRAN	High-Resolution Transmission (molecular absorption database)	31
IAGOS	In-service Aircraft Global Observing System	66
IASI	Infrared Atmospheric Sounding Interferometer	3
IFOV	Instantaneous Field of View	71
IMG	Interferometric Monitor of Greenhouse Gases	67
IPCC	Intergovernmental Panel on Climate Change	2
IR	Infrared Radiation	20
IRF	Instantaneous Radiative Forcing	42
IRK	Instantaneous Radiative Kernel	3
ISR	Incoming Solar Radiation	40
ITCZ	Inter-Tropical Convergence Zone	13
LATMOS	Laboratoire Atmosphères, Milieux, Observations Spatiales	77
LBL-RTM	Line-by-line Radiative Transfer Model	85
LEO	Low Earth Orbit	67
LIDAR	Light Detection and Ranging	66
LTE	Local Thermodynamic Equilibrium	25
LUT	Look-Up Table	78
LW	Longwave	45
LWRE	Longwave Radiative Effect	3
MOZART	Model for Ozone And Related Chemical Tracers	86
NAO	North Atlantic Oscillation	51
NDACC	Network for the Detection of Atmospheric Composition Change	65
NH	Northern Hemisphere	51
NMHC	Non-Methane Hydrocarbon	156
NMVOC	Non-Methane Volatile Organic Compound	47

NWP	Numerical Weather Prediction	79
MLS	Microwave Limb Sounder	51
ODS	Ozone Depleting Substance	1
OEM	Optimal Estimation Method	78
OLR	Outgoing Longwave Radiation	3
OMI	Ozone Monitoring Instrument	51
PPF	Product Processing Facility	78
RF	Radiative Forcing	2
RRTMG	Rapid Radiative Transfer Model Global	148
SAOZ	Systeme d'Analyse par Observation Zenithale	84
SCIAMACHY	Scanning Imaging Absorption Spectrometer for Atmospheric Chartography	61
SH	Southern Hemisphere	51
SO	Special Observation	74
STE	Stratospheric - Tropospheric Exchange	15
SW	Shortwave	45
TES	Tropospheric Emission Spectrometer	3
TIR	Thermal Infrared Radiation	38
TOA	Top Of the Atmosphere	3
TOMS	Total Ozone Monitoring Spectrometer	67
TTL	Tropical Transition Layer	54
ULB	Université Libre de Bruxelles	72
UTLS	Upper Troposphere - Lower Stratosphere	83
UV	Ultraviolet	10
VMR	Volume Mixing Ratio	89
VOC	Volatile Organic Compound	46
WMO	World Meteorological Organization	62
WOUDC	World Ozone and Ultraviolet Data Center	65

Chapter 1

Introduction

Ozone was discovered in the middle of the 19$^{\text{th}}$ century by Schönbein. The discovery came as a result of experiments that lead to the observation of a peculiar odor. Schönbein proposed the name ozone, after the ancient Greek verb ὀζειν (to produce an unpleasant distinctive smell), and dedicated his life in researching this compound [Rubin, 2001].

Ozone is a natural constituent of the atmosphere, present mainly in the lower (troposphere) and middle (stratosphere) parts. In the troposphere, under natural conditions, ozone exists in equilibrium with other species. However, after the industrial era, which resulted to unregulated emissions of various chemical compounds, the ozone burden in the atmosphere has increased rapidly, as a consequence of anthropogenic processes. It has been identified as one of the main pollutants during photochemical smog (smoke + fog) episodes in large and populated cities, since the middle of the 20$^{\text{th}}$ century.

In the stratosphere, ozone forms the well-known ozone layer, which is crucial for the life on the planet, absorbing hazardous UV radiation from the Sun. Stratospheric ozone became known and under monitoring, after the discovery of the Antarctic Ozone Hole, which refers to a severe ozone depletion during the local spring, resulting to excessive thinness of the layer above the Antarctic. This destruction of ozone is caused by anthropogenic compounds - known as ozone depleting substances (ODSs) - that have the ability to remain for years in the atmosphere, and consequently find their way to the stratosphere and the polar regions. The past few years, there have been events of ozone loss in the Arctic as well, such as during the winter of 2010-2011 and 2015-2016, though not as extreme as in the Antarctic.

1.1 The problem

Ozone is a key substance for atmospheric chemistry and climate. It is a radiatively active gas for both solar (shortwave) and terrestrial (longwave) radiation. Even small changes in its distribution have an impact on climate [Forster et al., 2007]. To understand and accurately represent the impact of ozone on climate, a good knowledge of the distribution is required, as well as its long-term trends. In the troposphere, following an increase of around 100 Tg between 1850 and 2010 [IPCC, 2013] on its global burden, ozone is the third-most-important greenhouse gas, with respect to its impact on climate.

In order to quantify the impact of a given species or parameter on climate, the concept of the radiative forcing (RF) was introduced [IPCC, 2013]. After years of research, it is now known that the ozone RF is strongly dependent on its vertical distribution, as well as on the surface temperature and the vertical profiles of temperature, humidity and clouds [Forster and Shine, 1997; Gauss et al., 2003; Lacis et al., 1990]. Ozone RF calculations and changes over time are entirely model based, since no ozone records are available for the pre-industrial era. The assumptions and radiative transfer code of each model lead to inter-model discrepancies. According to the latest assessment report of the Intergovernmental Panel on Climate Change (IPCC) (IPCC [2013], AR5), the contribution of anthropogenic tropospheric ozone to RF is around $+0.40\,\mathrm{W\,m^{-2}}$ ($+0.20$ to $+0.60\,\mathrm{W\,m^{-2}}$), with this value representing the average of the ensemble of model calculations. Stratospheric ozone has less impact on the RF, where the IPCC reports a value of $-0.05 \pm 0.1\,\mathrm{W\,m^{-2}}$ [IPCC, 2013]. Stratospheric ozone RF is not much affected by recent changes in concentrations, following for instance a decrease in emissions of ODSs after 2000, when the stratospheric ozone RF was estimated again at $-0.05 \pm 0.10\,\mathrm{W\,m^{-2}}$ between pre-industrial times and 2005 [Forster et al., 2007]. Confidence intervals remain quite large in all studies, with questionable reliability, since until recently the present-day components of these estimates could not be tested against observations on large scales.

1.2 The motivation

Satellite measurements of vertical distribution of ozone on the global scale have started to be available in the last decade, but there are only a few previous studies that have used these satellite data for quantifying the radiative effect of ozone [Joiner et al., 2009; Worden et al., 2008]. Particularly attractive in this context are infrared nadir sounders, which have sufficient vertical sensitivity to distinguish tropospheric and stratospheric ozone distributions and allow direct measurements of the top-of-the-atmosphere (TOA) radiance

in the IR ozone band globally, with high sampling. In 2011, Worden et al. [2011] used the measurements of Aura-TES (Tropospheric Emission Spectrometer) to calculate the longwave radiative effect (LWRE) due to ozone with respect to TOA radiative flux. This radiative effect is different from the radiative forcing defined in IPCC [Ramaswamy, 2001], as it is not calculated at the tropopause and does not refer to ozone concentration changes with respect to pre-industrial levels. Worden et al. [2011] introduced the innovative concept of instantaneous radiative kernel (IRK), which represents the sensitivity of the TOA radiative flux with respect to the observed ozone profile in the 9.6 µm ozone band. With the IRK it is possible to calculate the longwave radiative effect due to ozone in each atmospheric layer. Aghedo et al. [2011] used the IRKs from TES to evaluate the ozone radiative impact of model ozone biases from chemistry-climate models included in the Atmospheric Chemistry and Climate Model Intercomparison Project (ACCMIP). Bowman et al. [2013] revealed a correlation between model outgoing longwave radiation (OLR) bias and RF in the ACCMIP models. This correlation was used to reduce the intermodel spread in RF by around 30% [IPCC, 2013]. Both studies have revealed that models show large biases locally, especially in the tropics, but that globally the agreement is better due to compensating errors. These studies show that small biases in the vertical structure of ozone can propagate to create large biases in OLR, with implications in the radiative forcing used by the IPCC.

These previous efforts served as the basis of this work, with initial goal to adapt and apply the ozone LWRE retrieval method, introduced by Worden et al. [2011], on the IASI-Metop observations. However, the existing method was proved inaccurate for off-nadir observations, as IASI measures at nadir and off-nadir angles (scanning angle ranging from -48 to 48°). Finally, we developed and published, under Doniki et al. [2015], a new retrieval methodology, called the direct integration. This work, along with the work of Worden et al. [2011], including experts from the climate-model community, led to the project of "Benchmarking climate model top-of-atmosphere radiance in the 9.6 µm ozone band compared to TES and IASI observations", under NASA ROSES 2013 Solicitation, in an effort to produce standard ozone LWRE from IASI and TES and compare them with existing - broadly used - climate models.

1.3 Thesis content

This thesis is structured as follows: Chapter 2 provides the basic knowledge regarding the atmosphere, its constituents and their transport around the globe. Chapter 3 includes all the necessary concepts of radiation in the atmosphere, radiative transfer and radiative

forcing, with a focus on infrared radiation. In Chapter 4 we provide details for ozone as a chemical compound, as well as its distribution and annual variation patterns. In Chapter 5 we introduce the IASI instrument on-board Metop satellite. Chapter 6 describes in detail the IASI-dedicated ozone retrieval algorithm and the ozone product. In Chapter 7, we provide our developed method (direct integration) for ozone LWRE retrievals, tailored for the IASI ozone retrieval algorithm. Furthermore, we compare the direct integration with the anisotropy method, introduced by Worden et al. [2011]. In Chapter 8 we present the ozone LWRE vertical and spatial distributions, as resulted from the direct integration method. We also present for the first time the LWRE time evolution over almost one decade of IASI observations, from November 2007 to January 2017. Furthermore, we investigate the relation between LWRE and ozone columns / surface temperature, as well as local processes. Finally, in Chapter 9, we present the first results of the comparison between IASI, TES and three chemistry-climate models, realized under the aforementioned project. The conclusions and perspectives of this work are presented in Chapter 10.

Chapter 2

The Earth's atmosphere

Earth's atmosphere: a thin gaseous envelope surrounding the Earth. The dry atmosphere consists almost entirely of nitrogen and oxygen, together with a number of trace gases, such as argon, helium, and radiatively active greenhouse gases such as carbon dioxide, and ozone. In addition the atmosphere contains water vapour, whose amount is highly variable. It also contains clouds and aerosols. (IPCC, Glossary)

The earth's atmosphere is mainly described by a basic chemical composition and a set of dynamical properties, all of which are fundamental to any atmospheric, climate or environmental study.

2.1 Basic composition

The composition of the Earth's atmosphere consists of three major species: nitrogen (N_2), with a contribution of nearly 78%, oxygen (O_2), around 21%, and argon (Ar), with a contribution less than 1% [Ahrens, 2008]. The other gases present in the atmosphere fall under the term "trace gases", as their concentration is negligible compared to the major gases. Moreover, they do not show the same homogeneity as the major contributors in time and/or space. Among the trace gases, those with the largest relative concentration include water vapour (H_2O), carbon dioxide (CO_2), methane (CH_4), nitrous oxide (N_2O), and ozone (O_3). The respective abundances are given in Table 2.1.

The atmosphere of Earth generally extends for hundreds of kilometers above the Earth's surface, however a typical altitude considered as the top of the atmosphere (TOA) is around 100−200 km. The majority of the atmospheric species as well as the largest part of their concentrations is within the first 30−50 km from the surface. Within this

TABLE 2.1: Major atmospheric constituents near the Earth's surface. (Adapted from Ahrens [2008])

Gas	Symbol	% by volume of dry air
Nitrogen	N_2	78.08
Oxygen	O_2	20.95
Argon	Ar	0.93
Water vapor	H_2O	0 to 4
Carbon dioxide	CO_2	0.038
Methane	CH_4	0.00017
Nitrous oxide	N_2O	0.00003
Ozone	O_3	4×10^{-6} (altitude dependent)

range, the concentration of the atmospheric constituents varies notably. Furthermore, there are exchange processes occurring between the different layers of the atmosphere, chemical interactions between the species themselves, as well as between the species and the radiation, which is mainly solar or terrestrial. Moreover, the atmosphere is strongly linked to the surface below, and there is a continuous exchange of matter between the two through emission and deposition.

The species of the atmosphere can be distinguished by the type of production, in which case there are the primary species, directly emitted into the atmosphere, and the secondary species, formed by the chemical transformation of their precursors. Other ways to categorize the species include the altitude range (neutral atmosphere, ionosphere and others) or the residence time.

2.2 Vertical structure of the atmosphere

The atmosphere of the Earth is not a single layer. It can be divided into vertical sublayers depending on different properties. Such properties, that exhibit varying behavior with the altitude, are the air temperature, the air pressure and density, and the chemical composition of each layer.

2.2.1 Vertical profiles of air pressure and air density

The air is constituted of gases and particles, and each constituent is characterized by its own unique mass. The number density of the air, n, is defined as the number of air molecules per volume of air (in molecules m^{-3}), the density of air, ρ, is defined as the mass of air per volume of air (in $\mathrm{kg\,m}^{-3}$), and the pressure of air, P, at any point in the

atmosphere, is given by the following equation:

$$P = nk_B T = \rho \frac{R}{M} T, \tag{2.1}$$

where k_B is the Boltzmann constant ($1.381 \times 10^{-23}\,\mathrm{J\,K^{-1}}$), M is the molar mass of the air in $\mathrm{kg\,mol^{-1}}$, R is the universal gas constant ($8.314\,\mathrm{J\,mol^{-1}K^{-1}}$) and T the local atmospheric temperature (in K). In fig. 2.1 it can be seen that the pressure of the air, and therefore the density as well, present an exponential decrease with increasing altitude. This is due to the fact that at any given moment and for a given layer of thickness dz in the atmosphere, the following forces apply: i. the pressure difference between the upper and bottom limits of the considered layer, with direction bottom-up, and ii. the gravity, with direction towards the ground, of the air contained in the layer considered. For situations where the pressure difference balances the gravity, the air is considered to be in hydrostatic equilibrium [Stull, 2000]; this state is described by the hydrostatic equation:

$$dP = \rho \cdot g \cdot dz \Leftrightarrow \frac{dP}{dz} = -\rho \cdot |g|, \tag{2.2}$$

where g is the gravitational acceleration (around $9.81\,\mathrm{m\,s^{-2}}$, with direction towards to and perpendicular to the surface). In a small altitude range, where T and g can be assumed to be constant, eq. 2.2 can be integrated to yield:

$$P = P_0\, e^{-\frac{z - z_0}{H}} \tag{2.3}$$

where H is the scale height, given by:

$$H = \frac{RT}{Mg} \tag{2.4}$$

For a mean atmospheric temperature of 250 K, the scale height ranges between 7 and 8 km.

Equation 2.3, also known as the *barometric law* [Atmosphere, 1976], explains the exponential dependence of pressure on altitude, as shown in fig. 2.1. Provided that the temperature changes with the altitude, eq. 2.3 is very useful to estimate the height that corresponds to different pressures in the atmosphere and vice versa, provided that P_0 is known at the lower limit.

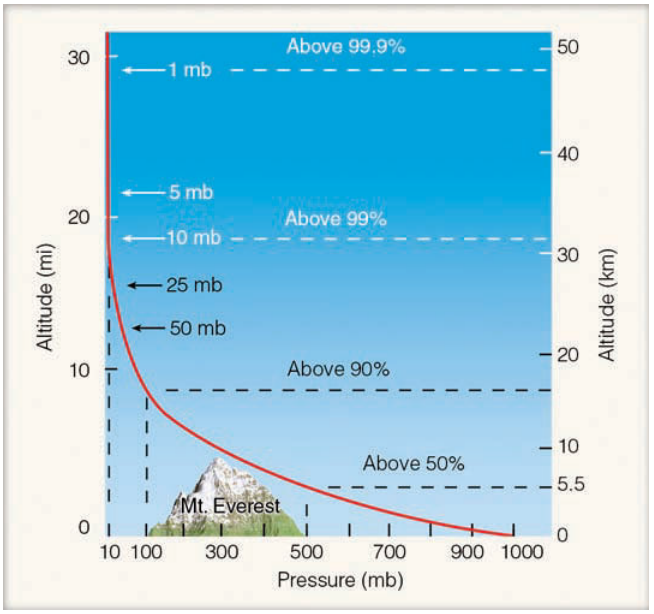

FIGURE 2.1: Air pressure vertical distribution. (Taken from Ahrens [2008])

2.2.2 Vertical profile of temperature

The vertical distribution of the atmospheric temperature is most commonly used to describe the vertical structure of the atmosphere; it divides the atmosphere in several sublayers with different properties. A typical vertical temperature profile of the atmosphere is shown in fig. 2.2. Contrary to the air pressure and density, the temperature does not necessarily decrease with the altitude. The rate at which the temperature changes with the height is called lapse rate [Ahrens, 2008]; it is negative, when the temperature decreases with the height and positive, when the temperature increases with the height.

Starting from the ground and up to the first 10−11 km, there is a near-linear decrease of the temperature with the altitude. This first layer is called troposphere, and it is where most weather phenomena take place. The upper limit of the troposphere generally varies from 9 km near the poles, to 17 km near the Equator. The decrease of the temperature is caused by the fact that, during the day, the sunlight warms the surface of the Earth, and the surface, in turn, warms the air above it. Then the layer above will warm the next one and so forth. The average lapse rate in the troposphere is around $-6.5°$ C/km. However, this value is greatly dependent on the local meteorological conditions, as well as the season, the geographical position etc. Thus, in a cold day, when the air becomes colder with the altitude, the lapse rate would steepen. On the contrary, on a sunny summer day with no wind, the temperature would decrease more slowly with height. It is also possible for the temperature to increase with the altitude in the troposphere. This phenomenon is referred to as a temperature inversion and occurs in the lower part of the

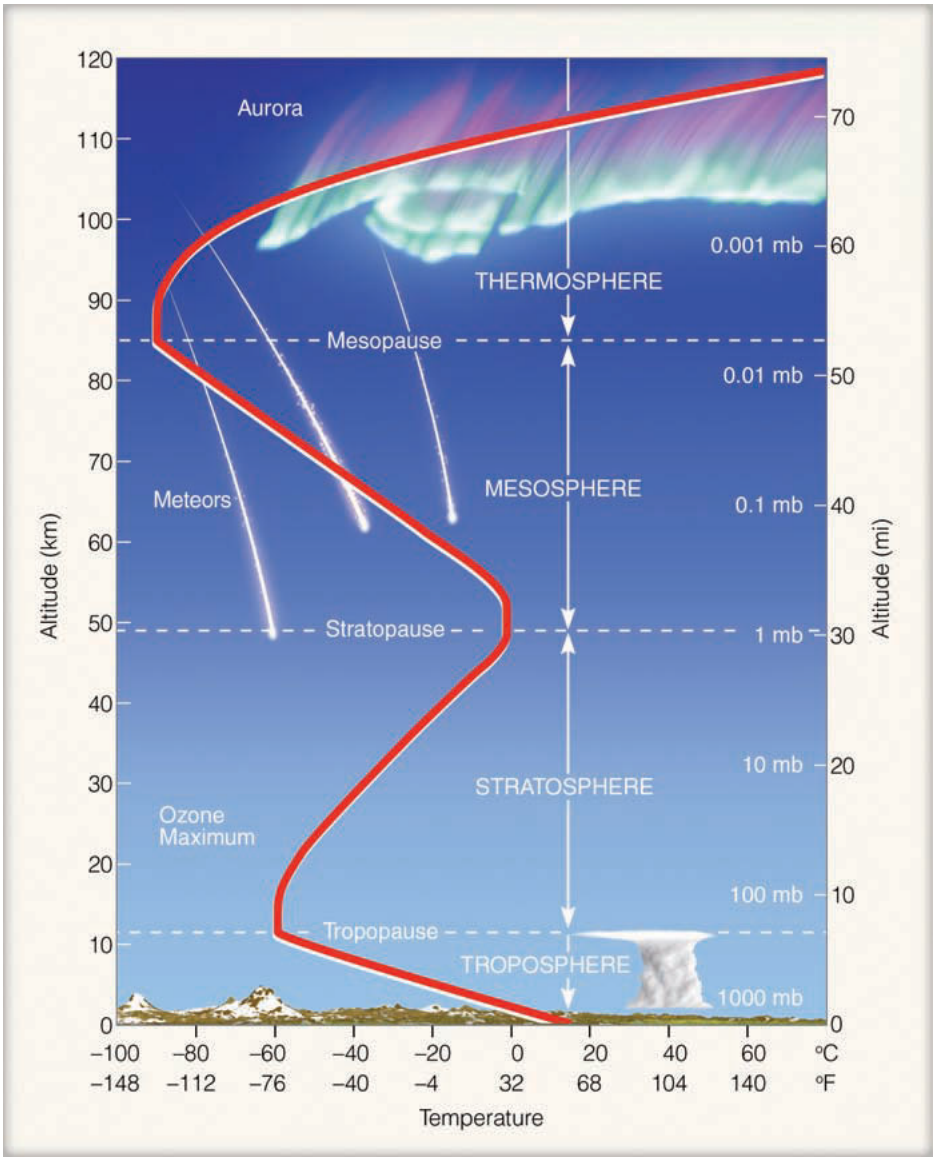

FIGURE 2.2: Vertical distribution of atmospheric temperature. (Taken from Ahrens [2008])

troposhere, called the boundary layer. Such inversions can be often observed in very cold nights.

Right above where the troposphere stops, starts the tropopause. According to the World Meteorological Organization [1957], the tropopause is defined as a layer between the troposphere and the stratosphere, characterized by an abrupt change in the lapse rate; it is the lowest level at which the lapse rate is around $-2°$ C/km or less (less negative or positive), provided that the average lapse rate between this level and the upper level within 2 km does not exceed $-2°$ C/km. The altitude of the tropopause and its vertical extent varies with the season and the location. Generally, the tropopause is higher during summer and lower during winter. There are also some cases where the tropopause breaks or folds. This is when the dry, cold stratospheric air mixes with the more humid

troposphere. Here we should also note, that there are other definitions for the tropopause in use, such as the chemical tropopause, which varies with the atmospheric species and their concentration. However, in this manuscript we will always refer to the definition provided by the World Meteorological Organization [1957].

Further above the tropopause extends the stratosphere. The upper limit of this layer is around 50 km or 1 hPa. The stratosphere is characterized by an increase of the temperature with height (positive lapse rate), of almost 50° to 60° C within 40 km. The stratosphere includes the well-known ozone layer, characterized by a maximum ozone concentration at around 25 km. The ozone molecules in the stratosphere absorb the largest part of the incoming UV radiation - a part of UV-A (315 - 400 nm) and mainly UV-B (280 - 315 nm) -, leading to the heating of the air, and consequently the heating of the stratosphere. At the top of the stratosphere there is a few kilometers thick layer of stable and relatively high temperatures, the so-called stratopause.

The mesosphere extends above the stratopause, between approximately 50 to 85 km, with atmospheric pressure ranging from 1 to 0.01 hPa. As the pressure denotes, the air in this layer is extremely sparse, leading to just a small number of molecules to absorb the solar radiation. Consequently, the molecules lose more energy than what they absorb, leading to the cooling of the atmosphere, as seen in fig. 2.2. At the top of this layer the atmospheric temperature reaches its lowest value, nearly −90° C. Following the mesosphere, and between that and the last layer of the atmosphere, the mesopause is located, which is characterized by very low temperatures, as the upper part of the mesosphere.

Finally, at the top of the atmosphere lies the thermosphere, characterized by an increase of air temperature. This layer receives almost all of the solar radiation, and while the molecular densities are very low, atomic and molecular oxygen absorb the radiation, increasing the layer's temperature. The height of the thermosphere usually extends up to 500 km.

2.3 General circulation in the atmosphere

The air of the atmosphere is a very dynamic medium. Some of the corresponding motions have impact in small scales, producing local phenomena, while others have an impact to a much larger scale of the atmosphere. The large-scale dynamical patterns result from the general circulation scheme in the atmosphere.

Whatever the scale, the circulation of the atmospheric masses is empowered, sustained and affected by the following major factors:

- Solar radiation
- Latent heat
- Thermal energy
- Coriolis force − caused by the rotation of the Earth
- Frictional drag − caused by the friction between the ground of the rotating Earth and the layer of air right above it
- Thermal conductivity of the air.

Figure 2.3 shows the annual average absorbed solar radiation flux (in red) and outgoing longwave radiation (in black) at the surface (top panel), as a function of latitude. Solar radiation is the main source of energy for Earth. However, its distribution on the surface of the Earth is uneven between the Equator and the Poles (fig. 2.3, bottom panel), due to the seasonal inclination and the revolution around the sun. Near the equator there is an excess of incoming radiation, compared to the outgoing radiation. On the contrary, near the poles there is a lack of incoming radiation, compared to the outgoing one. The net radiation flux (fig. 2.3, bottom panel) shows a varying distribution with the latitude; nonetheless, there is a striking symmetry between the two hemispheres, with only slight differences, e.g., around 10° N [Stephens et al., 2015]. The imbalance in the net flux between tropical and mid- to polar latitudes at the surface, causes the transport of heat from the warmer regions (tropical zone) to the colder ones (poles). Solar radiation, and therefore thermal energy and latent heat, are the main drivers of the vertical motions in the atmosphere, as they force the warm air masses towards the upper layers of the atmosphere, while the colder ones to descend.

The horizontal motions in the atmosphere are driven by three main forces: the Coriolis force, the pressure-gradient force and the frictional drag [Jacob, 1999]. The Coriolis force describes the air motions from the point of view of an observer in a rotating frame of reference, hence it is the force that is caused by the rotation of the Earth. It applies for both latitudinal and longitudinal motions as follows (fig. 2.4). For the latitudinal motions (fig. 2.4, left), it is the conservation of angular momentum that causes the deflection of the air masses. If an air mass is traveling from the Equator towards the North Pole, it loses angular momentum due to the decrease of the Earth's translational velocity for

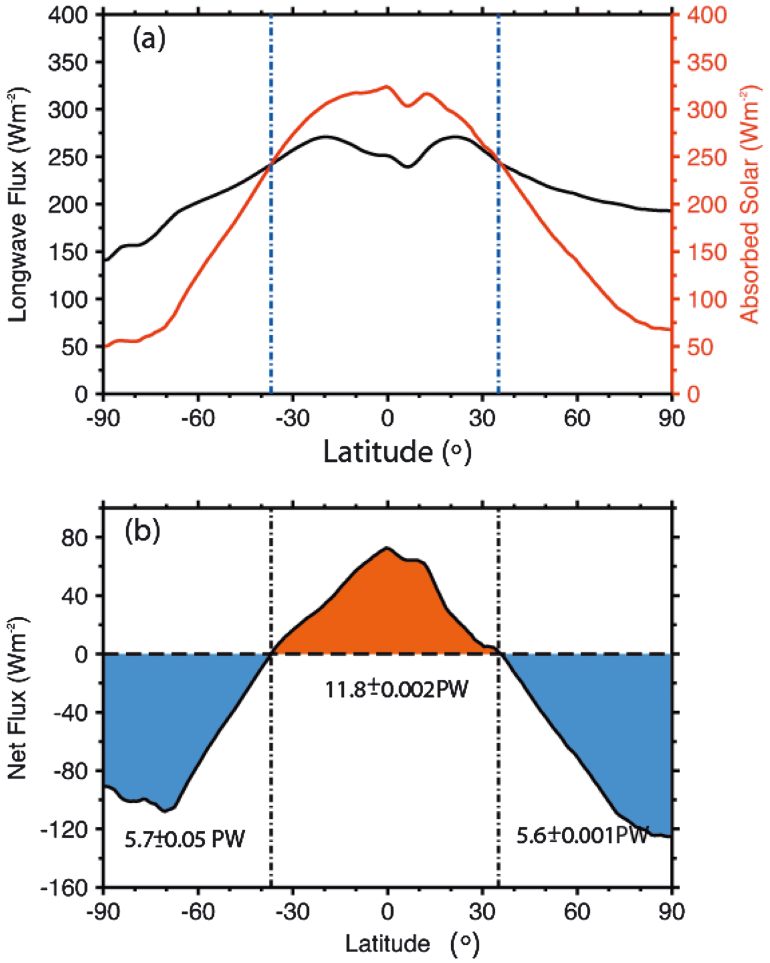

FIGURE 2.3: (a) The zonally anually averaged profile of absorbed solar radiation in red and outgoing longwave radiation (OLR) in black. The vertical dashed lines indicate the latitude at which the net TOA flux is zero (i.e., where the absorbed solar flux and OLR are equal. (b) The zonal annual averaged net flux with the integrated heat absorbed for latitudes equatorward of the dashed vertical lines and lost from those latitudes poleward of these lines. The vertical dashed lines are as in (a). The heat content values correspond to the area integrated net flux, marked by the dashed lines. (Adapted from Stephens et al. [2015])

increasing latitudes. For the conservation of the angular momentum, the air mass must acquire eastward velocity, relative to the rotating Earth. For an observer located on the Earth's surface, the air mass is deflected to the right of the direction of movement. Similarly, for the longitudinal motions (fig. 2.4, right), it is the centrifugal force that causes the deflection of the air masses. Assuming an air mass at rest and an observer on the Earth's surface, the centrifugal force, the gravity and the reaction at the surface, will all be in balance. In the case of moving from west to east in the Northern Hemisphere, the angular velocity of the air mass increases, so will the centrifugal force. The previous forces are no longer in balance, and the air mass is deflected towards the Equator. For an air mass traveling from east to west, there is a decrease in its angular velocity and the centrifugal force, which results in a deflection towards the North. The Coriolis force

equals 0 at the Equator and it increases with increasing latitude.

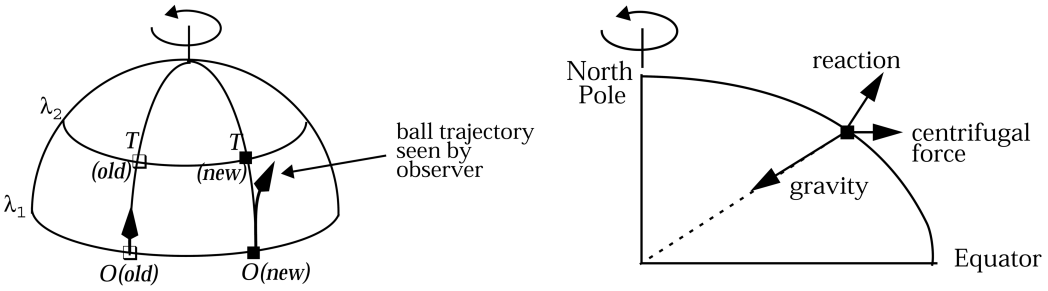

FIGURE 2.4: (Left) Coriolis effect on an air mass traveling in the latitudinal direction. (Right) Forces acting on an air mass traveling in the longitudinal direction. The observer is assumed at rest on the surface of the Earth. (Taken from Jacob [1999])

The pressure-gradient force is the force caused by the pressure difference between two areas on the same level, e.g. surface of the Earth, and forces the air masses to move from high to low pressure areas. Finally, the frictional drag is the force that accounts for the loss of momentum of the air masses due to obstacles near the surface of the Earth, e.g. orography, buildings, etc. The direction of this force is opposite to the direction of motion.

Keeping all of the above in mind, the general circulation scheme in the atmosphere can be schematized as follows: The air masses near the ground of the warm regions, such as the tropical belt, heat up and become less dense. They rise up to a certain altitude that depends on the heat they received, and move horizontally towards colder regions (northern and southern). While traveling in the cold air of the upper atmospheric layers (usually within the upper troposphere and lower stratosphere), they become cold, and gradually the air masses start to subside. As the cycle is not complete, there is one more transport, this time near the ground, where the cold descending air travels towards warmer regions. This is the basic physical explanation of a Hadley cell, as seen in fig. 2.5, which generally occurs between the equator and $30° - 40°$ N and S. The Ferrel cells, which prevail at mid-latitudes, imply motions dependent on the pressure fields near the ground. In general, the air masses move from high pressure fields to lower pressures, just as heat flows from warm to cold. Finally, the Polar cell describes the circulation from the poles toward 60° N and S. Due to the cell formation and the rotation of the Earth, the dominating winds are the Easterlies (east trade winds − within the tropical belt and the higher latitudes) and the Westerlies (west trade winds − in the mid-latitudes). The region where the Easterlies converge around the Equator is known as the Intertropical Convergence Zone (ITCZ). Moreover, where two cells meet at the tropopause, there is the appearance of jet streams: the Subtropical jet, between the Hadley and the Ferrel cells,

and the Polar jet, between the Ferrel and the Polar cells. In these regions, it is common to have tropopause foldings or breaks.

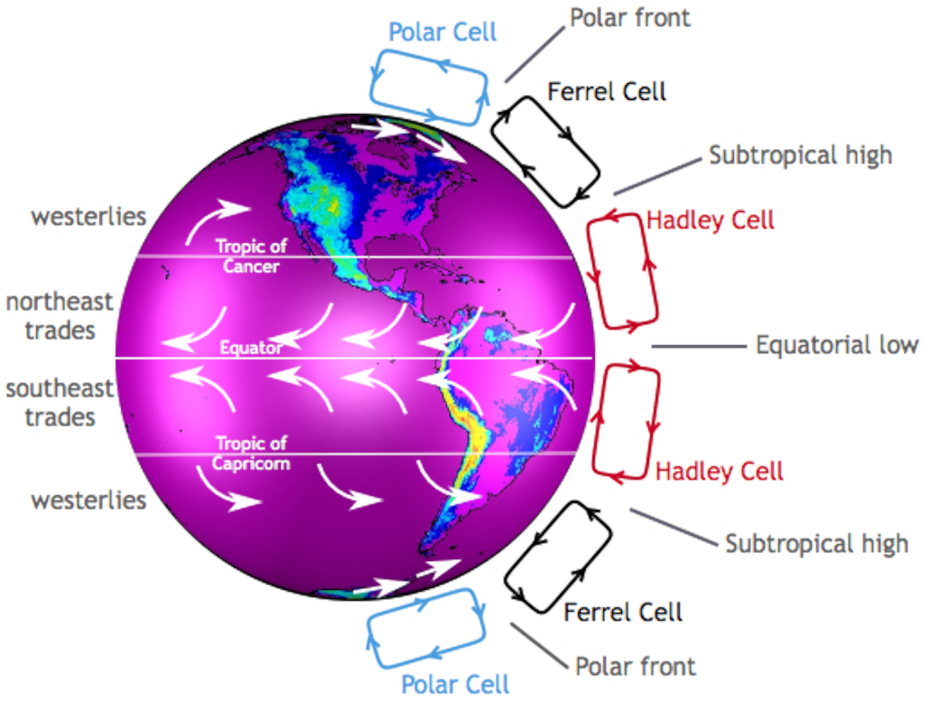

FIGURE 2.5: General atmospheric circulation patterns around the globe. (Taken from CMMAP http://www.cmmap.org/learn/climate)

The circulation of the air masses from the Equator towards the Poles is complemented by the Brewer-Dobson circulation. This pattern is strongly related to ozone transport and will be extensively covered in Chapter 4.

In general, the circulation of the air masses in the atmosphere is in reality more complex, with the occurrence of: i) small scale processes (cyclones or anticyclones), which will drive the wind patterns, ii) local winds, depending mostly on the topography of each region, iii) regional winds, which are more extended, and iv) synoptic winds or large scale dynamic structures, which cover distances of thousands of kilometers (e.g., jet streams).

The information of the radiation budget and the general circulation in the atmosphere, will be very useful to explain later in the thesis the ozone circulation and the radiative forcing and effects, which are closely linked to the surface temperature.

2.4 Transport and lifetimes of atmospheric constituents

Air masses in the atmosphere travel easier in the horizontal scale than in the vertical. That is because the horizontal motion is favored by the winds emerging from the rotation

of the Earth. Therefore, as it can be seen in fig. 2.6, a typical intercontinental transport needs about two weeks, while the meridional transport of air masses, from the mid-latitudes towards the tropics or the poles, is typically around one to two months. The timescale for the exchange of air between the two hemispheres is about a year.

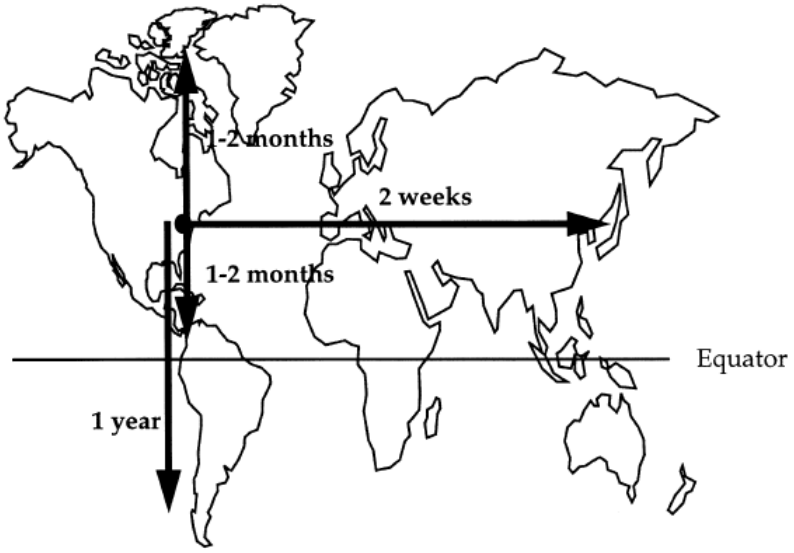

FIGURE 2.6: Typical time scales for global horizontal transport. (Taken from Jacob [1999])

On the vertical scale the air masses are mostly transported because of heat and turbulence, which are mainly powered by the solar radiation. Therefore the vertical transport is generally slow. As it can be seen in fig. 2.7, the exchange between the surface and the top of the planetary boundary layer (PBL) takes about one to two days, while the exchange with the free troposphere needs about a week, and with the tropopause about a month. The more local weather phenomena can favor or slow down these exchange/mixing processes. The exchange from the surface to the stratosphere needs about $5-10$ years, and this is because, as it was shown earlier, the stratosphere is characterized by an increase of the temperature with the altitude, which prevents vertical motions. Finally, the reverse process, the transport from the stratosphere to the troposphere, takes on average about $1-2$ years. It is known as the "stratospheric-tropospheric exchange" (STE); it takes place only under certain conditions and is closely linked to the tropopause folding. The STE is explained in detail in Chapter 4.

The species in the atmosphere are bound to the horizontal and vertical transport. Species are constantly being emitted in the atmosphere, either naturally or by anthropogenic sources (primary species), or they are chemically transformed while in the atmosphere (secondary species). Each species has a characteristic lifetime or residence time in the atmosphere. In order to define the lifetime of a species, we assume a simple one-box model [Jacob, 1999], which represents a fixed domain in the atmosphere. Following the

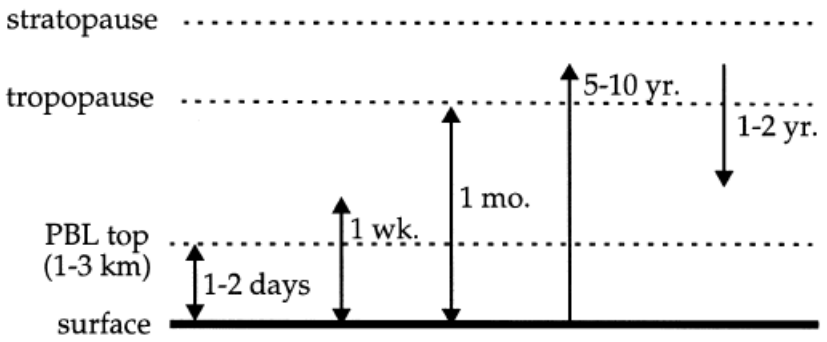

FIGURE 2.7: Typical time scales for vertical transport. (Taken from Jacob [1999])

mass balance equation, the change of mass of a species per unit of time is the result of its production in the box, which includes: a) F_{in}, inward flow from outside the box (usually transport) and b) P, production inside the box (e.g., emissions, chemical production), minus the loss in the box, which includes: a) F_{out}, outward flow from the box (transport) and b) L, loss inside the box (e.g., deposition, chemical loss). Considering the above, the lifetime of a species is defined as the ratio of the mass of the species to its sinks in $\mathrm{kg\,s^{-1}}$:

$$\tau = \frac{m}{F_{out} + L} \tag{2.5}$$

The lifetimes and transport scales of the main atmospheric species are shown in fig. 2.8. As an example, the hydroxyl radical (OH), is very reactive with other species, and therefore its lifetime is only of a few seconds. On the contrary, CH_4 has a lifetime of around a decade. Atmospheric constituents with short lifetimes can only travel a few meters distance and are usually found close to the source. Reactive species or radicals, such as OH or $O(^1D)$ are present everywhere during the day, but in very small concentrations. On the other hand, constituents with long lifetimes can travel thousands of kilometers, even circulate the globe, and their concentration is therefore globally much more homogeneous. It is obvious also that lifetime depends on the environment and local atmospheric conditions.

Ozone is a secondary species with a short lifetime of days in the troposphere, but of a few weeks in the stratosphere [IPCC, 2013]. The studies of Stevenson et al. [2006] and Young et al. [2013] for tropospheric ozone give a global mean lifetime of 22.3 $\pm$ 2 and 23.4 $\pm$ 2.2 days. However, the calculation of its lifetime is based on chemistry-climate model simulations, and as it is discussed in IPCC [2013] the ability to simulate ozone has not improved in the last decades, which accounts for strong underestimations in remote areas of the Northen Hemisphere [Lamarque et al., 2010]. Likewise, the lifetime of ozone in the stratosphere is estimated to a few weeks, based on model simulations. However, after

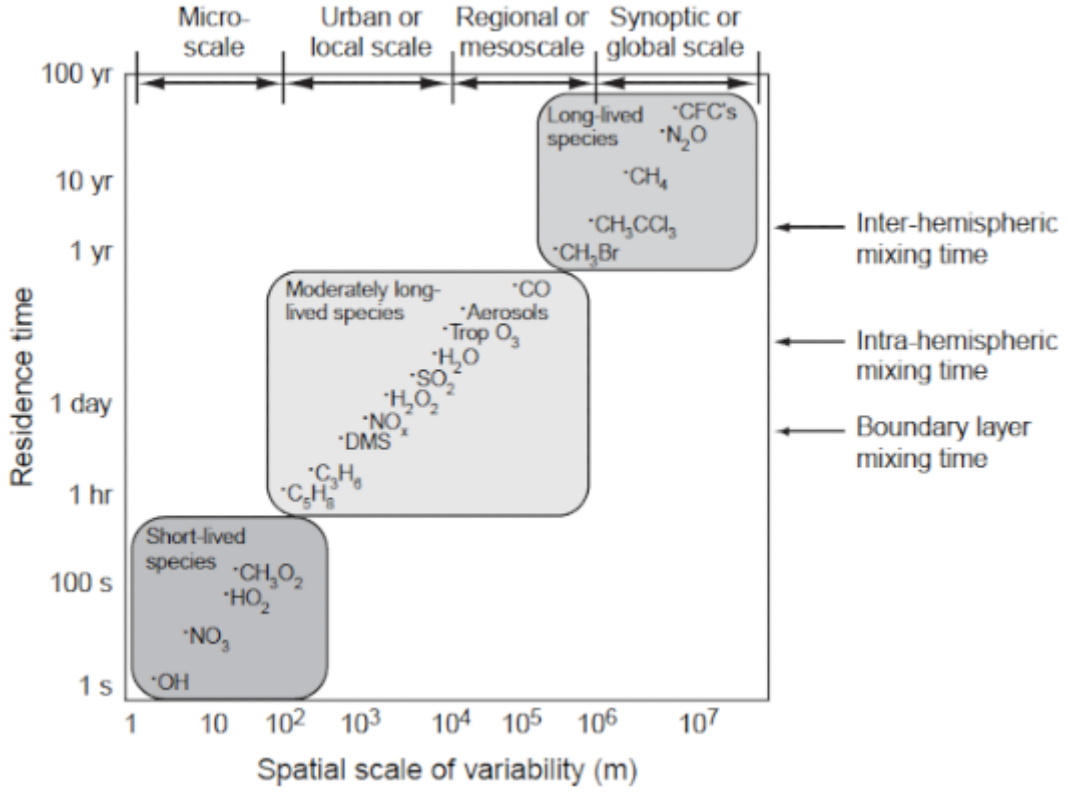

FIGURE 2.8: Characteristic lifetimes and transport scales for some atmospheric constituents. (Taken from Wallace and Hobbs [2006])

the effect of the Montreal Protocol, there are signs of stratospheric ozone stabilization, following a decline in chlorofluorocarbons (CFCs) and their replacements, which could potentially lead to an increase of its mean global lifetime. Nonetheless, observationally based estimates do not appear to be in accordance with the model simulations [IPCC, 2013].

Chapter 3

Radiative transfer in the atmosphere and radiative forcing

The concept of radiative transfer in the atmosphere is used to describe the interaction of radiation, traveling towards a direction, with matter (gases, particles). Solar radiation is emitted from the Sun and while traveling towards the Earth's surface through the atmosphere, it is absorbed, scattered and re-emitted. Only a fraction will reach the surface. On the other hand, the thermal infrared radiation emitted from the Earth's surface is modified by the atmospheric constituents through emission, absorption and scattering.

In satellite remote sensing, the concept of radiative transfer is of crucial importance, as the instruments rely on the interactions of radiation with the atmosphere and the capability of the radiative transfer models to translate the observations into meaningful information.

In this chapter, I will present the fundamentals of radiation and radiative transfer in the atmosphere, with a focus on the thermal infrared part emitted by the Earth's surface, that serve the purpose of this work. All information presented hereafter are from Liou [2002], Wallace and Hobbs [2006] and Petty [2006].

3.1 Basic concepts of radiation

3.1.1 Electromagnetic spectrum

Electromagnetic radiation is the main process of energy transfer. The electromagnetic spectrum covers the range of wavelengths or frequencies over which the electromagnetic radiation extends. The electromagnetic spectrum can be distinguished in regions, depending on the frequency or wavelength of the radiation; these are: gamma rays, X-rays, ultraviolet (UV) radiation, visible (Vis) radiation, infrared radiation (IR), microwaves and radio waves, as it can be seen in fig. 3.1. Gamma rays cover the most energetic parts of the spectrum, characterized by very high frequencies and short wavelengths. On the contrary, radio waves carry less energy and are characterized by low frequencies and long wavelengths.

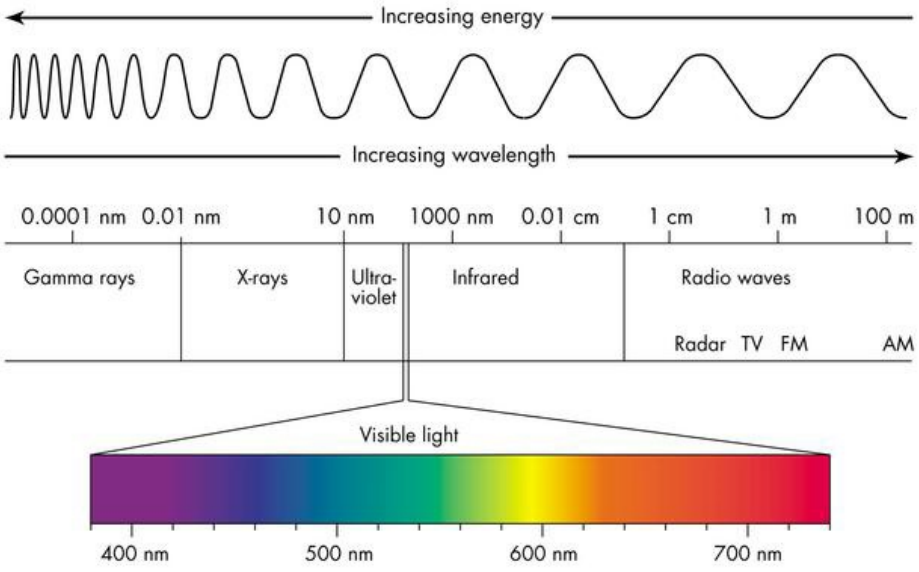

FIGURE 3.1: The electromagnetic spectrum. (Taken from http://imagine.gsfc.nasa.gov/science/toolbox/)

Frequency, ν, is the number of cycles per second characterizing the wave of electromagnetic radiation, and is expressed in Hz, where 1 Hz equals to $1\,s^{-1}$. The wavelength, which is another quantity to describe the electromagnetic radiation, is related to the frequency by the following equation:

$$\lambda = c/\nu \tag{3.1}$$

where c represents the speed of light ($2.99792458 \times 10^8\,m\,s^{-1}$ in vacuum) [Liou, 2002]. The wavelength has units of distance and is expressed in µm, nm, and others, depending

on the spectral region. For the infrared radiation, it is common to use the wavenumber $\tilde{\nu}$, expressed in cm^{-1}, which is defined as:

$$\tilde{\nu} = \nu/c = 1/\lambda. \tag{3.2}$$

The relation between frequency and wavelength can be visualized graphically in fig. 3.1.

3.1.2 Solid angle and polar coordinates

In atmospheric science, and specifically for the study of radiation propagation, it is common to express the quantities with respect to the globe; therefore the polar coordinate system is preferred over the Cartesian one. A useful parameter in the polar coordinate system, is the solid angle [Liou, 2002]. The solid angle is defined as the ratio of the area σ of a spherical surface to the square of the radius, r, of the same sphere, as seen in fig. 3.2 and is expressed as:

$$\Omega = \sigma/r^2 \tag{3.3}$$

in steradian (sr). Therefore a differential surface, in polar coordinates, is expressed as:

$$d\sigma = (rd\theta)(r\sin\theta d\phi) \tag{3.4}$$

and the differential solid angle as:

$$d\Omega = d\sigma/r^2 = \sin\theta d\theta d\phi, \tag{3.5}$$

where θ and ϕ represent the zenith and azimuthal angles, respectively.

3.1.3 Radiometric quantities

The amount of radiant energy dE_λ crossing an area dA with an angle θ, in a time interval dt and wavelength interval λ to $\lambda + d\lambda$ (fig. 3.2), is expressed as [Liou, 2002]:

$$dE_\lambda = I_\lambda \cos\theta dA d\Omega d\lambda dt \tag{3.6}$$

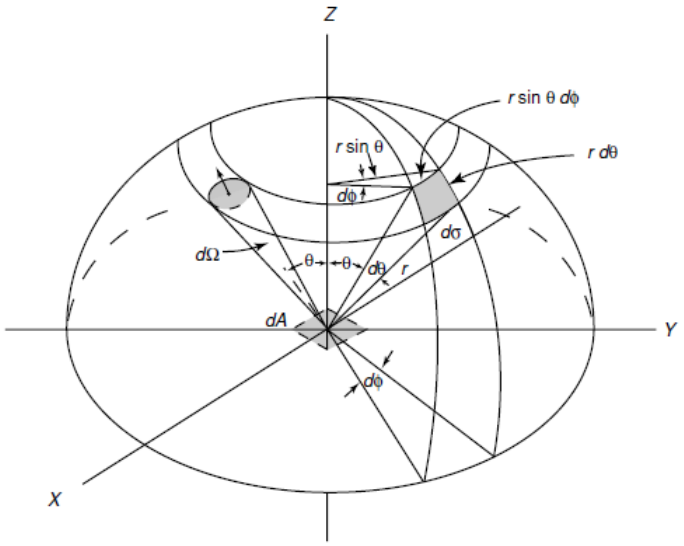

FIGURE 3.2: Polar coordinates on hemispheric projection. Notations are defined in the text. (Taken from Liou [2002])

where $\cos\theta dA$ is the effective area at which the energy is being intercepted, and I_λ is the monochromatic radiance (or intensity), in units of $\mathrm{W\,m^{-2}sr^{-1}\mu m^{-1}}$.

The monochromatic flux density (or monochromatic irradiance) is defined as the monochromatic radiance integrated over the solid angle of a whole hemisphere (in units of $\mathrm{W\,m^{-2}\mu m^{-1}}$), as follows:

$$F_\lambda = \int_0^{2\pi} \int_0^{\pi/2} I_\lambda(\theta, \phi) \cos\theta \sin\theta d\theta d\phi. \tag{3.7}$$

The flux density over a specific spectral band is the monochromatic flux density, integrated over the wavelengths of the spectral band as (in units of $\mathrm{W\,m^{-2}}$):

$$F = \int_{\lambda_1}^{\lambda_2} F_\lambda d\lambda. \tag{3.8}$$

where λ_1 and λ_2 are the lower and upper wavelengths of the spectral band [Liou, 2002].

3.2 Blackbody radiation and emissivity

3.2.1 Blackbody radiation

A black body can be depicted as a cavity (ideally a sphere) with a very small hole, which allows radiation to enter [Liou, 2002]. The largest part of the radiant flux that enters the cavity will be trapped within the cavity, and it will be internally reflected multiple times, until all the fluxes are absorbed by the walls of the cavity. The chances of any of the fluxes to escape through the only hole of the cavity are extremely small, and therefore the interior of the cavity appears dark. Ideally, the cavity will appear black and the absorption will be complete.

The inverse process of the absorption is the emission. The emission is described as the process at which the emitted flux from any little spot of the cavity, is reflected repeatedly at the walls of the cavity, and each time the flux is weakened by absorption, but at the same time reinforced by new emission. Absorption and emission occur until an equilibrium state is reached in the cavity (thermodynamic equilibrium), and with respect to the cavity walls temperature.

As the blackbody totally absorbs the flux entering the cavity, it also emits all of it, at all wavelengths. The emission of monochromatic radiance from a blackbody, expressed in units of $\mathrm{W\,m^{-2}\,sr^{-1}\,\mu m^{-1}}$, is given by Planck's law:

$$B_\lambda(T) = \frac{2hc^2}{\lambda^5(e^{\frac{hc}{\lambda k_B T}} - 1)} \tag{3.9}$$

where h is Planck's constant ($h = 6.626 \times 10^{-34}\ \mathrm{J\,s^{-1}}$), k_B is Boltzmann's constant ($1.3806 \times 10^{-23}\ \mathrm{J\,K^{-1}}$), c is the speed of light, and T is the temperature (in K). Equation 3.9 links the monochromatic intensity to the wavelength (consequently to the frequency and wavenumber too) and the temperature of the emitting medium (the source).

Figure 3.3 shows the curves of radiance emitted by blackbodies with different temperatures and as a function of the wavelength, as a result of eq. 3.9. What the Planck law implies, and what is seen in fig. 3.3, is that the blackbody radiance increases with the temperature and that the wavelength of the maximum intensity (peak of the curve) decreases with increasing temperature. As an example, the Sun, which is usually assumed to be a blackbody, at a temperature around 5700 K, has its emission curve in between the radiance curves of 5500 K and 6000 K of fig. 3.3 and a maximum around 0.5 µm.

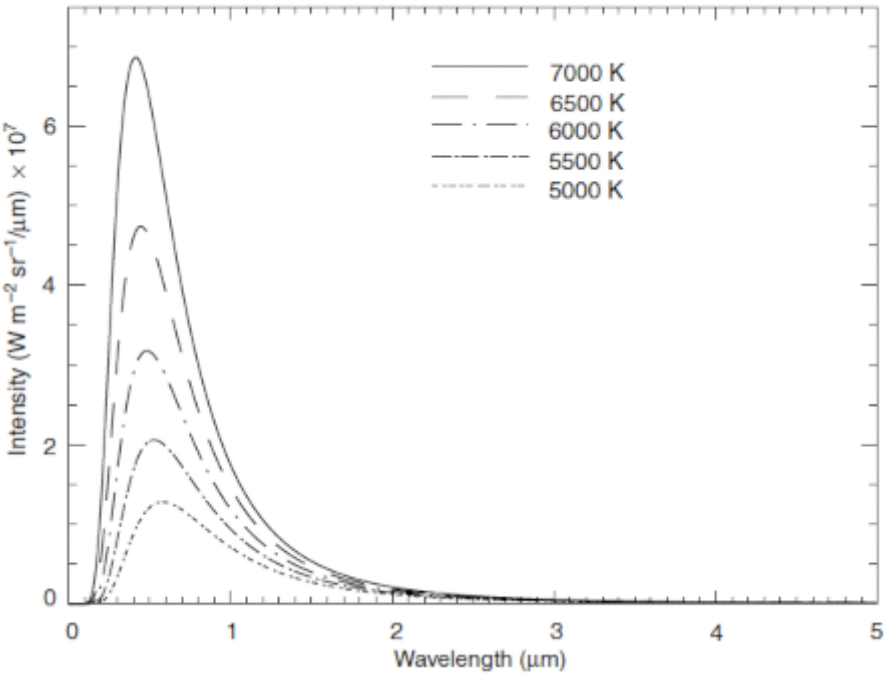

FIGURE 3.3: Blackbody radiances for different temperatures and as a function of wavelength, as resulted from the Planck function (eq. 3.9). (Taken from Liou [2002])

Planck's law defines the monochromatic radiance, that is for a certain wavelength. The total radiance emitted by a blackbody is obtained by integrating the Planck function over the entire wavelength domain, from 0 to ∞ [Liou, 2002]. Thus,

$$B(T) = \int_0^\infty B_\lambda(T)d\lambda = \int_0^\infty \frac{2hc^2\lambda^{-5}}{e^{\frac{hc}{k_B\lambda T}} - 1}d\lambda, \tag{3.10}$$

which yields to:

$$B(T) = bT^4, \tag{3.11}$$

with $b = 2\pi^4 k_B^4/(15c^2h^3)$, and since the blackbody radiation is isotropic, which means that it is not dependent on any angle and is equal in all directions, the flux is:

$$F = \pi B(T) = \sigma T^4, \tag{3.12}$$

where σ is the Stefan−Boltzmann constant, which equals to 5.67×10^{-8} $\mathrm{Wm^{-2}K^{-4}}$ [Liou, 2002].

3.2.2 Emissivity

As explained previously, a perfect blackbody absorbs all the incident radiant flux it receives, and at the same time emits at all wavelengths, following eq. 3.9. However, the surface of the Earth, land and oceans, and the atmosphere, are not perfect black bodies.

The spectral emissivity of a medium, ϵ_λ, describes the deviation, in terms of radiation, from a black body. At a given wavelength, ϵ_λ is the ratio of the emitted radiance of a medium at a given temperature, to the radiance of a true blackbody described by the Planck function (eq. 3.9) [Liou, 2002]. Following Kirchoff's law, it equals the absorptivity, A_λ (which is the ratio of the absorbed intensity to the Planck function), under thermodynamic equilibrium:

$$\epsilon_\lambda = A_\lambda = \frac{I_\lambda(abs/emit)}{B_\lambda(T)}. \tag{3.13}$$

According to eq. 3.13, a medium with an absorptivity A_λ will absorb A_λ-times the blackbody radiance $B_\lambda(T)$, and consequently it will emit ϵ_λ-times the same radiance. For a perfect blackbody, at all wavelengths, we have:

$$A_\lambda = \epsilon_\lambda = 1. \tag{3.14}$$

For a non-perfect medium [Liou, 2002], we have:

$$A_\lambda = \epsilon_\lambda < 1. \tag{3.15}$$

In order all of the above to stand true, the medium has to be in local thermodynamic equilibrium (LTE), so that it is characterized by a single temperature, which will be uniform in a given volume of the medium and its emission will be isotropic. The Earth's atmosphere is not always in thermodynamic equilibrium. However, on small scales and below about $60 - 70$ km, the condition of LTE is generally satisfied.

3.3 Spectral line formation and line shape

The absorption and emission of gases in the atmosphere produce discrete line spectra, characteristic for each species, which are driven by the electronic structure and the vibrational and rotational motions of the constituting molecules [Demtröder, 2010; Petty,

2006]. In this section we provide the physics that describe those lines formation and shaping.

3.3.1 Energy transitions

In general, the energy of a transition, either in absorption or in emission, is given by:

$$E_k - E_j = h\nu, \tag{3.16}$$

where $h\nu$ is the quantum of energy carried by the photon, and k, j are indices to distinguish two different molecular energy levels.

The total energy of the molecule is:

$$E = E_{rot} + E_{vib} + E_{el} + E_{tr} \tag{3.17}$$

with E_{rot} being the part of the energy stored in the rotation of the molecule, E_{vib} the energy stored in the vibration of the molecule from its resting position, E_{el} the electronic energy, and E_{tr} the kinetic energy of the molecule. The rotational, vibrational and electronic energies are discrete, while the kinetic energy is continuous.

The electronic transitions usually happen at the spectral region of short wavelengths (UV−VIS and below). Shortwave radiation carries indeed enough energy to change the electronic configuration of molecules. The vibrational and rotational transitions require less energy for a single transition. For the vibrational transitions, a single excitation requires energy between 500 and 10000 cm^{-1}, and usually occurs in the range from near to far IR. For the rotational transitions, the required energy is around 1 to 500 cm^{-1}, and therefore these transitions occur in the microwave and far-IR regions of the spectrum. As seen in fig. 3.4, which is a simplified example, the vibrational energy levels are present in between the discrete electronic energy levels, while the rotational energy levels are located between the vibrational energy levels.

The vibration of a molecule is defined by a set of normal modes. Each normal mode corresponds to a particular vibrational motion, independent of the others. Therefore a vibration can be described by one or a combination of normal modes. For a molecule of N atoms, the number of normal modes is $3N - 6$, and in case of a linear molecule, $3N - 5$. In polyatomic non-linear molecules, the energy of a vibrational level is defined

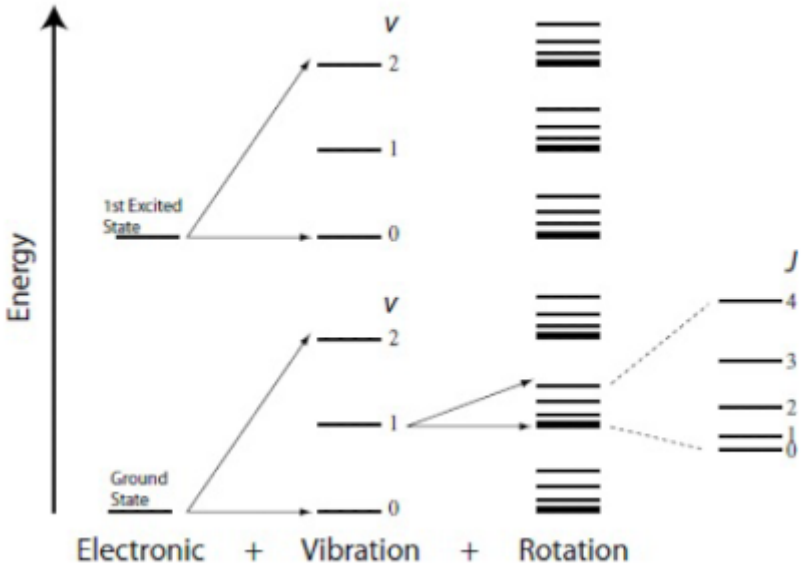

FIGURE 3.4: Schematic depiction of the superposition of electronic, vibrational and rotational energy levels. The absorption spectrum of a molecule is determined by all allowed transitions between pairs of levels in the righthand column. (Taken from Petty [2006])

by the sum of the energy of each vibrational normal mode as [Demtröder, 2010]:

$$E_{vib} = \sum_{i}^{3N-6} h\nu_i(v_i + \frac{d_i}{2}), \tag{3.18}$$

where i refers to the normal modes, v is the vibrational quantum number (or level) and d_i is the degeneracy of normal mode i. When an absorption of vibration energy occurs, the vibrational quantum number can change by +1, 2, 3, ... Vibrational transition in the IR will happen, if the vibration induces to a dipole moment. The energy between two different levels is given by:

$$\Delta E_v = E_{vib}(v'_1 v'_2 ... v'_{3N-6}) - E_{vib}(v''_1 v''_2 ... v''_{3N-6}), \tag{3.19}$$

where $'$ and $''$ refer to the upper and lower energy states.

For the rotational energy states excitation the angular momentum of the molecule has to change. The energy levels of rotation, in a linear molecule, are given by [Demtröder, 2010]:

$$E_{rot} = BJ(J+1) - DJ^2(J+1)^2 + ..., \tag{3.20}$$

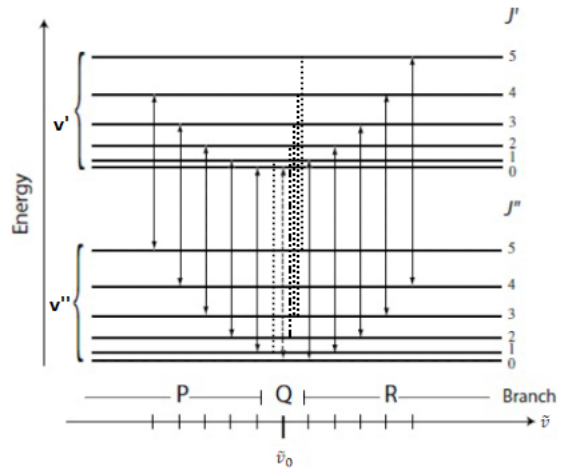

FIGURE 3.5: Relative positions of vibrational-rotational transitions. The Q-branch, if present, occurs close to wavenumber $\tilde{\nu_0}$, while its energy is associated with pure vibrational transitions. (Adapted from Petty [2006])

where J is the rotational quantum number, $B = h/8\pi^2 Ic$ is the rotational constant (in units of inverse length) corresponding to the rigid rotor approximation and D is the constant of centrifugal distortion. I is the moment of inertia with respect to the center of mass of the molecule in rotation. For non-linear polyatomic molecules, the situation is more complex and different cases can be described, depending on the symmetry of the molecule (see Section 3.3.2). Rotational transitions occur, when the following two conditions are satisfied: the molecule has a dipole moment and the difference of the rotational quantum number between the initial and final state is $\Delta J = 0, \pm 1$; $\Delta J = 0$ occurs when there is a bending mode.

For $\Delta J = -1$, the transitions are referred to as P-branch transitions, $\Delta J = +1$ are the R-branch, and $\Delta J = 0$, the Q-branch (fig. 3.5). Following eq. 3.20, the energy of an allowed pure rotational transition is:

$$\Delta E_{rot} = E_{rot}(J') - E_{rot}(J''). \tag{3.21}$$

where J' and J'' are the rotational quantum numbers, characterizing the upper and lower levels involved in the transition.

3.3.2 Transitions in polyatomic molecules: The case of O_3

In the IR, vibrational and rotational transitions occur simultaneously. As seen in fig. 3.5, the energy of a combined vibration-rotation transition is slightly greater or less than the energy a "pure" vibrational transition would have. The rotational transitions produce in

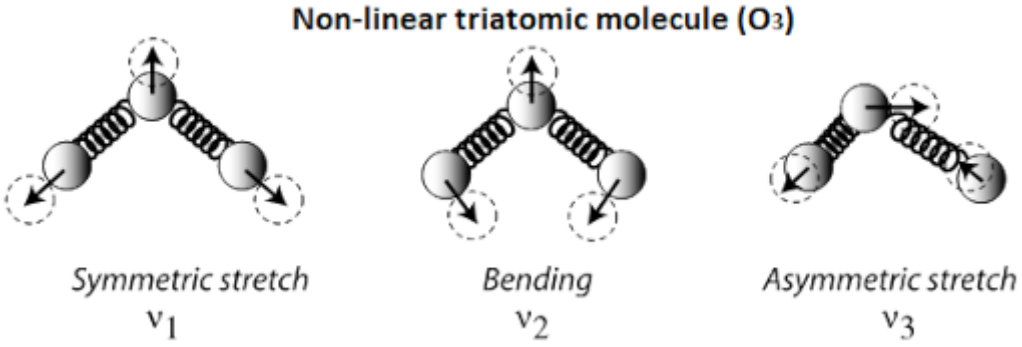

FIGURE 3.6: Vibrational normal modes of O_3. (Adapted from Petty [2006])

the vibrational band spectrum a series of separate lines, grouped around the $0_n - 0_{n+1}$ transition, called the *band origin*.

Ozone, is a triatomic non-linear molecule, of type XY_2 [Flaud et al., 1990], therefore it has 3 non-degenerate vibration modes (ν_1 around 1110 cm^{-1}, ν_2 around 701 cm^{-1} and ν_3 around 1042 cm^{-1}), as shown in fig. 3.6. All 3 modes are active in the infrared, while the strongest ν_3-mode includes P, Q and R rotational transitions.

Following eq. 3.18, the vibrational energy can be expressed as [Flaud et al., 1981]:

$$E_{vib}(v_1, v_2, v_3) = h\nu_1(v_1 + \frac{1}{2}) + h\nu_2(v_2 + \frac{1}{2}) + h\nu_3(v_3 + \frac{1}{2}). \tag{3.22}$$

Regarding the rotational energy, molecules like ozone, possessing a permanent dipole moment, can have a purely rotational spectrum in the microwave or far infrared region [Flaud et al., 1990]. Following eq. 3.20, for a non-linear triatomic molecule, the rigid rotation is characterized by three moments of inertia measured with respect to the three principal axis (a, b, c) of the molecule. Since there are three principal axes, there are three rotational constants (A, B, C), which follow the convention that $A > B > C$, and therefore for the moments of inertia it applies that $I_A < I_B < I_C$ [Demtröder, 2010]. For ozone, the three rotational constants of the ground state are: $A = 3.55366659\,\text{cm}^{-1}$, $B = 0.44528320\,\text{cm}^{-1}$ and $C = 0.39475182\,\text{cm}^{-1}$[1].

Ozone belongs in the asymmetric top family ($A \neq B \neq C$), but because of its geometry, can be approximated as a prolate symmetric top molecule ($B = C$) with a-axis symmetry. Based on these, ozone has three rotational quantum numbers, noted as (J, K_a, K_c). J is the main rotational quantum number, and K_a, K_c are the projections of J along the axes of smallest moment of inertia and of largest moment of inertia, respectively. For the rotational quantum numbers it applies that $0 \leqslant K_a, K_c \leqslant J$ and $K_a + K_c = J$ or $J + 1$

[1] http://smpo.univ-reims.fr/1280x796/en/mol/gen

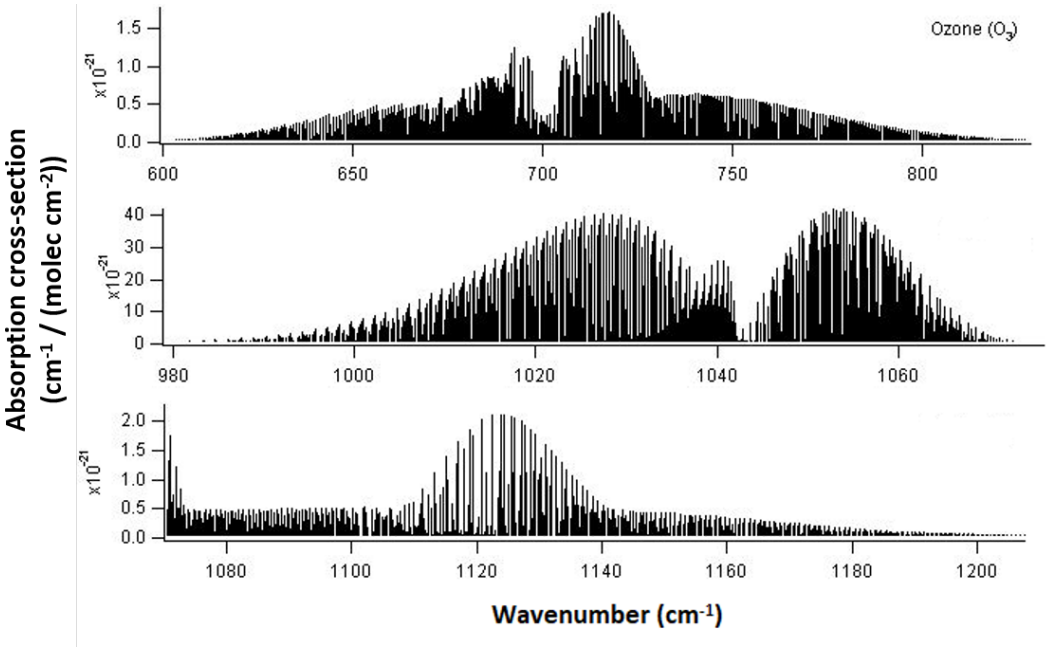

FIGURE 3.7: Ozone IR absorption cross-sections for the simple excitation of the three vibration modes: (top) ν_2, (middle) ν_3, and (bottom) ν_1, as resulting from the *HITRAN* 2012 database [Rothman et al., 2013].

[Flaud et al., 1981]. Finally, the rotational energy is given by [Demtröder, 2010]:

$$E_{rot}(J, K_a, K_c) = BJ(J+1) + (A-B)K_a^2. \tag{3.23}$$

The selection rule for J follows $\Delta J = 0 \pm 1$, while for K_a and K_c, the selection rules depend on the type of vibrational band [Flaud et al., 1990].

In fig. 3.4, we explained that the vibrational levels include several rotational levels. Therefore, a vibrational transition can occur between rotational states of two different vibrational levels (fig. 3.5). The energy of a rotational state of a vibrational level (E_{rot}^{vib}) is the sum of the respective energies:

$$E_{vib,rot} = E_{vib}(v_1, v_2, v_3) + E_{rot}(J, K_a, K_c), \tag{3.24}$$

while the difference of energy between two vibration-rotation levels is:

$$\Delta E_{vib,rot} = E_{vib}(v_1', v_2', v_3') + E_{rot}(J', K_a', K_c') - E_{vib}(v_1'', v_2'', v_3'') - E_{rot}(J'', K_a'', K_c''). \tag{3.25}$$

The computation and description of the energies ($E_{vib,rot}(v_1, v_2, v_3, J, K_a, K_c)$) for ozone is described in Flaud et al. [1990].

Figure 3.7 shows the absorption lines of ozone in the IR for the three vibration modes. In the middle panel, in the spectral region around $1042\,\mathrm{cm}^{-1}$, we can observe a "hole" corresponding to the absence of strong concentrated Q-branch in the strong ν_3 ozone band.

3.3.3 Line shapes and broadening

Previously we have seen the absorption, emission, and different energy transitions that occur, when a molecule interacts with radiation of appropriate energy. The appearing lines on the spectrum, after such processes, have finite width, following various processes that cause line broadening. These processes are: i) natural broadening, caused by the inherent uncertainty in the quantizing of energy levels, and ensures that the absorption lines have a finite width; ii) collisions between molecules and atoms and between absorbing and non-absorbing molecules, known as pressure broadening; iii) the Doppler effect, which is a result of the different thermal velocities of the atoms and molecules. The effect of natural broadening is negligible in the atmosphere. The other two are explained below.

3.3.3.1 Pressure broadening

The pressure broadening of the spectral lines is due to the collisions between the different atoms and molecules in the atmosphere. It is only logical, that the more dense the atmosphere, the more collisions will occur. Therefore, the pressure broadening is larger in the lower levels of the atmosphere, where the density is high ($< 20\,\mathrm{km}$). The shape of the spectral lines affected by pressure broadening is given by a Lorentz-type profile, as [Liou, 2002]:

$$f(\tilde{\nu} - \tilde{\nu}_0) = \frac{1}{\pi} \frac{\alpha_L}{(\tilde{\nu} - \tilde{\nu}_0)^2 + {\alpha_L}^2}, \tag{3.26}$$

where $f(\tilde{\nu} - \tilde{\nu}_0)$ is the line shape function (in cm), $\tilde{\nu}_0$ is the wavenumber of the - ideally - monochromatic line, and α_L (in cm^{-1}) is the half-width of the line at the half-maximum. A typical Lorentz line shape can be seen in fig. 3.8. The parameter α_L, also known as collision-broadening width, is a function of pressure and temperature, and is usually expressed as follows:

$$\alpha_L = \alpha_0 (\frac{p}{p_0})(\frac{T_0}{T})^n \tag{3.27}$$

where α_0 is the collision-broadening coefficient at the standard pressure ($p_0 = 1013.25\,\text{hPa}$) and temperature ($T_0 = 296$ K). The index n depends on the type of molecule, as well as on the spectral line considered. Values of n can be found in the line-by-line spectroscopic data bases, such as HITRAN [Rothman et al., 2013]. As an example, for O_3, n varies from 0.7 to 0.9.

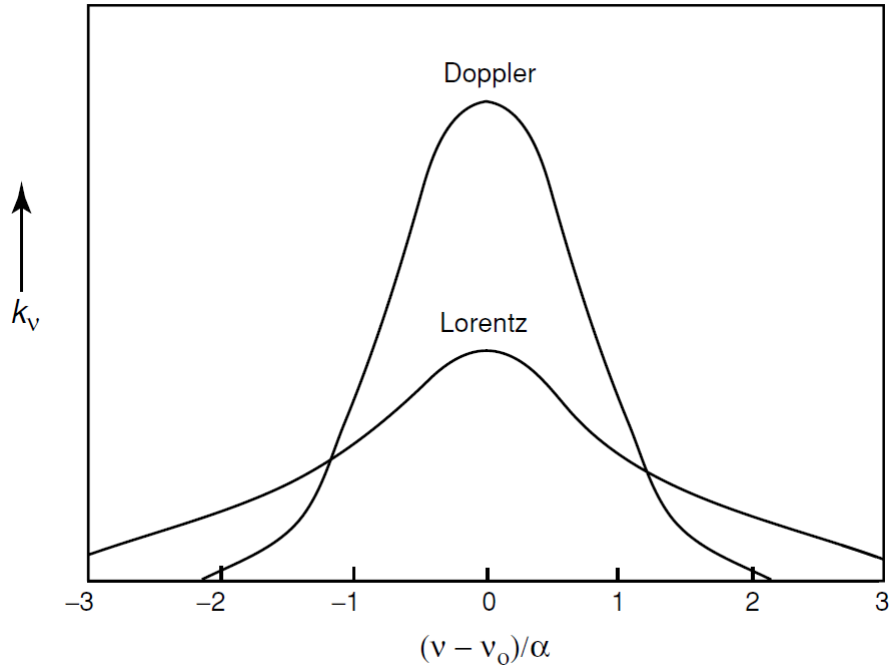

FIGURE 3.8: Lorentz and Doppler line shapes for the same intensity and width. (Taken from Liou [2002])

3.3.3.2 Doppler broadening

When collisions between the constituents of the atmosphere get rare ($> 50\,\text{km}$), the moving atoms or molecules follow individual trajectories. The line shape will be affected by the Doppler effect and the shape factor will be [Liou, 2002]:

$$f_D(\tilde{\nu} - \tilde{\nu}_0) = \frac{1}{\alpha_D\sqrt{\pi}} \exp[-(\frac{\tilde{\nu} - \tilde{\nu}_0}{\alpha_D})^2], \tag{3.28}$$

where

$$\alpha_D = \tilde{\nu}_0(2k_BT/mc^2)^{1/2}, \tag{3.29}$$

is the line width at the $1/e$ of the maximum because of the Doppler effect and m is the molecular mass ($m = M/N_A$, M the molar mass, $N_A = 6.022 \times 10^{-23}\,\text{mol}^{-1}$). The half-width at half-maximum is $\alpha_0 = \alpha_D\sqrt{ln2}$. Since the absorption coefficient (k_ν in fig. 3.8)

associated to a Doppler line-shape depends on the $\exp[-(\tilde{\nu}-\tilde{\nu}_0)^2]$, it will be larger at the line center than a corresponding line with a Lorentzian line-shape. Conversely, the absorption coefficient in the wings will be weaker, as shown in fig. 3.8.

3.3.3.3 Voigt broadening

In the altitude range between approximately 20 and 50 km, where both collisions and thermal velocity effects are quite significant, the line shape will be affected by both pressure and Doppler broadening, and (although not shown in fig. 3.8) the profile will be in-between the pressure and Doppler profiles [Liou, 2002]. A formulation of this is the Voigt line shape that is given by:

$$f_V(\tilde{\nu}-\tilde{\nu}_0) = f_L(\tilde{\nu}-\tilde{\nu}_0) \otimes f_D(\tilde{\nu}-\tilde{\nu}_0) = \int_{-\infty}^{\infty} f_L(\tilde{\nu}'-\tilde{\nu}_0) f_D(\tilde{\nu}-\tilde{\nu}')\, d\tilde{\nu}' \tag{3.30}$$

$$= \frac{\alpha_L}{\alpha_D \pi^{3/2}} \int_{-\infty}^{\infty} \frac{1}{(\tilde{\nu}'-\tilde{\nu}_0)^2+\alpha_L^2} \exp[-(\frac{\tilde{\nu}-\tilde{\nu}'}{\alpha_D})^2]\, d\tilde{\nu}'. \tag{3.31}$$

At high pressure, the combined (Voigt-type) will approach the Lorentz profile. At low pressure, it will be closer to the Doppler profile.

3.4 Radiative transfer

The fundamentals of radiative transfer in a layer of the atmosphere are common to all frequencies of the electromagnetic spectrum. However, the processes at play have relative importance that vary going from one spectral band to another, e.g. scattering is more important in the short wavelengths than in the longwave.

3.4.1 General formulation

Let us assume a beam of radiation with radiance I_λ, traveling through a medium of distance ds, as shown in fig. 3.9. The radiance of the beam will decrease, as the medium absorbs radiation. If the outgoing radiation is $I_\lambda + dI_\lambda$, then

$$dI_\lambda = -k_\lambda \rho I_\lambda ds, \tag{3.32}$$

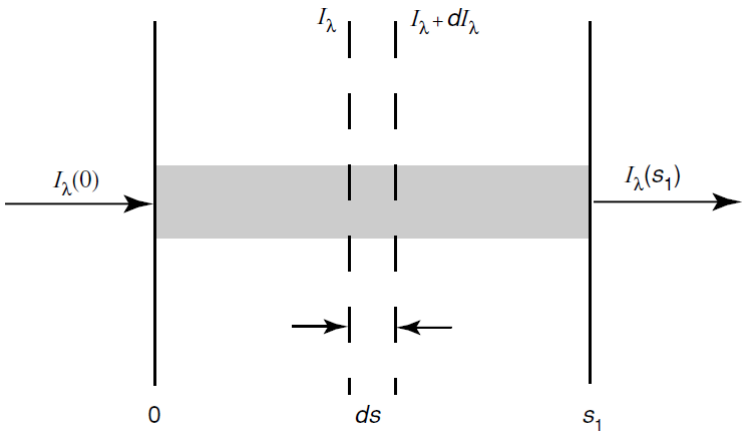

FIGURE 3.9: Propagation of light traveling through a medium.(Taken from Liou [2002])

where ρ is the density of the medium ($\mathrm{kg\,m^{-3}}$) and k_λ is the mass absorption cross-section ($\mathrm{m^2\,kg^{-1}}$) for wavelength λ [Liou, 2002]. However, as it was explained previously, a body absorbs and emits radiation, and therefore part of what is absorbed will be re-emitted, re-enforcing the outgoing radiation. The increase of the radiation due to emission is:

$$dI_\lambda = j_\lambda \rho ds, \tag{3.33}$$

where j_λ is the source function coefficient (in $\mathrm{W\,sr^{-1}\,\mu m^{-1}\,kg^{-1}}$). Combining eq. 3.32 and eq. 3.33, the total outgoing radiation will be:

$$dI_\lambda = -k_\lambda \rho I_\lambda ds + j_\lambda \rho ds. \tag{3.34}$$

For convenience, we define the source function J_λ, with units of radiant intensity, as:

$$J_\lambda = j_\lambda / k_\lambda, \tag{3.35}$$

Equation 3.34 can be rewritten as:

$$\frac{dI_\lambda}{k_\lambda \rho ds} = -I_\lambda + J_\lambda. \tag{3.36}$$

Equation 3.36 is the general radiative transfer equation, and can be applied to any coordinate system, after proper geometric transformation.

3.4.2 Beer-Bouguer-Lambert Law

Let us assume a beam of light traveling from the sun, and reaching the atmosphere of Earth. As the beam of the sunlight travels towards the ground, it will get attenuated, as it will meet different constituents of the atmosphere that will absorb part of it. Let us also assume that the source function is negligible. In that case, eq. 3.36 will become [Liou, 2002]:

$$\frac{dI_\lambda}{k_\lambda \rho ds} = -I_\lambda. \tag{3.37}$$

If at the beginning of the beam's path, $s = 0$, the intensity is $I_\lambda(0)$, the intensity at the point s_1 (see Fig. 3.9) can be obtained by integrating eq. 3.37 over the distance, as follows:

$$I_\lambda(s_1) = I_\lambda(0) \exp(-\int_0^{s_1} k_\lambda \rho ds). \tag{3.38}$$

If we define the monochromatic optical depth (or thickness) as:

$$\tau_\lambda(s_1, s) = \int_s^{s_1} k_\lambda \rho ds, \tag{3.39}$$

as shown in fig. 3.10, then combining eq. 3.38 and eq. 3.39, it results to:

$$I_\lambda(s_1) = I_\lambda(0) e^{-\tau_\lambda(0,s_1)}, \tag{3.40}$$

which is known as the Beer−Bouguer−Lambert law, and expresses that the radiance traversing through a medium decreases exponentially, with the argument of the exponential function being the optical thickness [Liou, 2002].

Finally, from eq. 3.40, it is possible to express the monochromatic transmittance for a path $(0, s_1)$:

$$t_\lambda(0, s_1) = I_\lambda(s_1)/I_\lambda(0) = e^{-\tau_\lambda(0,s_1)}, \tag{3.41}$$

which quantifies the fraction of radiation absorbed by the medium. The transmittance varies between 0 and 1. When $t_\lambda = 0$, all of the radiation is absorbed by the medium,

while when $t_\lambda = 1$, all of the radiation travels through the medium and exits without any loss.

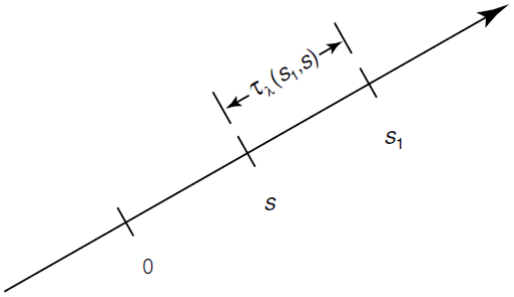

FIGURE 3.10: Representation of the monochromatic optical thickness. (Taken from Liou [2002])

3.4.3 Radiative transfer in the thermal Infrared

Thermal IR radiation is emitted from the Earth's surface, as well as the different layers in the atmosphere. In general, and according to eq. 3.36, the radiative transfer equation in the thermal IR can be written, in terms of wavenumber, $\tilde{\nu}$, as [Wallace and Hobbs, 2006]:

$$-\frac{dI_{\tilde{\nu}}}{ds} = \rho k_{\tilde{\nu}}(B_{\tilde{\nu}}(T) - I_{\tilde{\nu}}), \tag{3.42}$$

where $\tilde{\nu}$ is the wavenumber, $k_{\tilde{\nu}}$ is the absorption cross-section as previously, ρ is the density of the absorbing gas, s is the slant path, $I_{\tilde{\nu}}$ is the radiance and $B_{\tilde{\nu}}(T)$ is the source function, dependent on the temperature T, which in turn is a function of the altitude.

For the study of the thermal IR radiation transfer in the atmosphere, it is acceptable to assume that locally the atmosphere is in local thermodynamic equilibrium (LTE). Furthermore, we can assume azimuthal symmetry, and therefore the radiance will be a function of the distance, s, and zenith angle, θ, as shown in fig. 3.11.

As the IR radiation from Earth propagates upwards, we will begin from the surface, where the Earth emits [Hurtmans et al., 2012]:

$$I^{\uparrow}_{\tilde{\nu},\theta}(0) = \epsilon_{\tilde{\nu}} B_{\tilde{\nu}}(0) + (1-\epsilon_{\tilde{\nu}}) I^{\downarrow}_0(\tilde{\nu}) + r(\tilde{\nu},\theta) I^{\downarrow}_{sun}, \tag{3.43}$$

where the first term of the right hand side of eq. 3.43 is the blackbody emission of the Earth's surface corrected for the surface emissivity, $\epsilon_{\tilde{\nu}}$; the second term refers to the

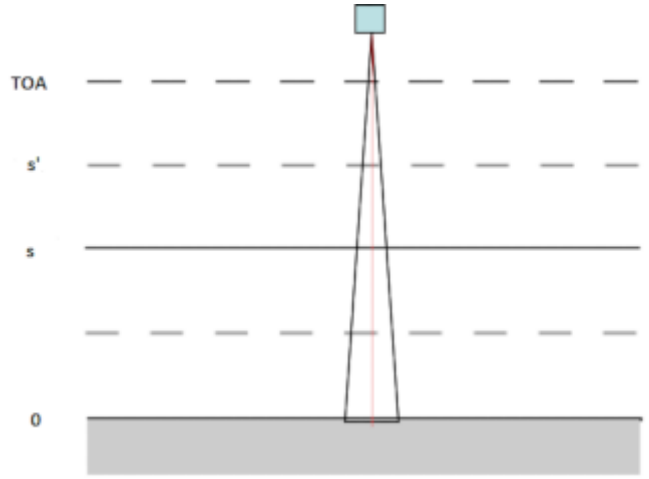

FIGURE 3.11: Atmospheric layers for IR transfer, shown as plane-parallel for simplicity. s is the altitude. TOA is the top of the atmosphere and index 0 denotes the surface. The zenith angle θ is the angle between the vertical and slant line of sight between the surface and the satellite. (Adapted from Liou [2002])

reflected downwelling thermal radiance emitted by the layers above; the third term is the reflection of the solar radiance reaching the surface (see Hurtmans et al. [2012] for further information). However, all the layers above the ground will emit both upwards and downwards, and the radiation propagating upwards will include the blackbody emission of the own layer and the transmitted part of the radiation from the layer below, such as:

for the upward emission [Liou, 2002]:

$$I^{\uparrow}_{\tilde{\nu}}(\theta, s) = I_{\tilde{\nu},\theta}(0)t_{\tilde{\nu}}(\theta, 0, s) + \int_{s}^{s'} B_{\tilde{\nu}}(T)t_{\tilde{\nu}}(\theta, s', s)ds', \tag{3.44}$$

and similarly, for the downward emission (assuming that there is no other source of radiation):

$$I^{\downarrow}_{\tilde{\nu}}(\theta, s) = \int_{0}^{s} B_{\tilde{\nu}}(s')t_{\tilde{\nu}}(\theta, s, s')ds', \tag{3.45}$$

where $t_{\tilde{\nu}}$ is the transmittance of each layer accordingly. In fig. 3.11, the atmosphere is discretized in an appropriate number of vertical layers, and consequently the equation of the radiative transfer has to be applied to each layer separately. In this discretized atmosphere, where each layer i is associated to a mean constant temperature, the upwelling radiation propagates layer by layer following:

$$I^{\uparrow}_{i} = I^{\uparrow}_{i-1}t_i + B_i(1 - t_i), \tag{3.46}$$

where the subscript $\tilde{\nu}$ has been omitted for clarity.

Equation 3.46 expresses that the upwelling radiation emitted from a layer i, is the radiance from the layer below $(i-1)$ attenuated by the layer, and the radiance of the own layer, emitting as a non-blackbody with "emissivity" $(1-t_i)$. Equation 3.46 is applied recursively layer after layer, until the last layer considered as the top of the atmosphere.

3.4.4 IR spectrum of the atmosphere

As detailed in the previous sections, the Earth absorbs solar shortwave radiation, and emits in the form of longwave (TIR-IR) radiation. If Earth was a perfect blackbody, and if we assume complete absence of the atmosphere, then its emission spectrum would be smooth curves, as in fig. 3.12, at the temperature of the surface (varying from scene to scene). The atmospheric species interact with the upward-propagating IR radiation and − as a general rule − attenuate the initial emitted radiance (see spectrum in fig 3.12) in different wavelengths, e.g. the strong absorption of O_3 at 9.6 µm.

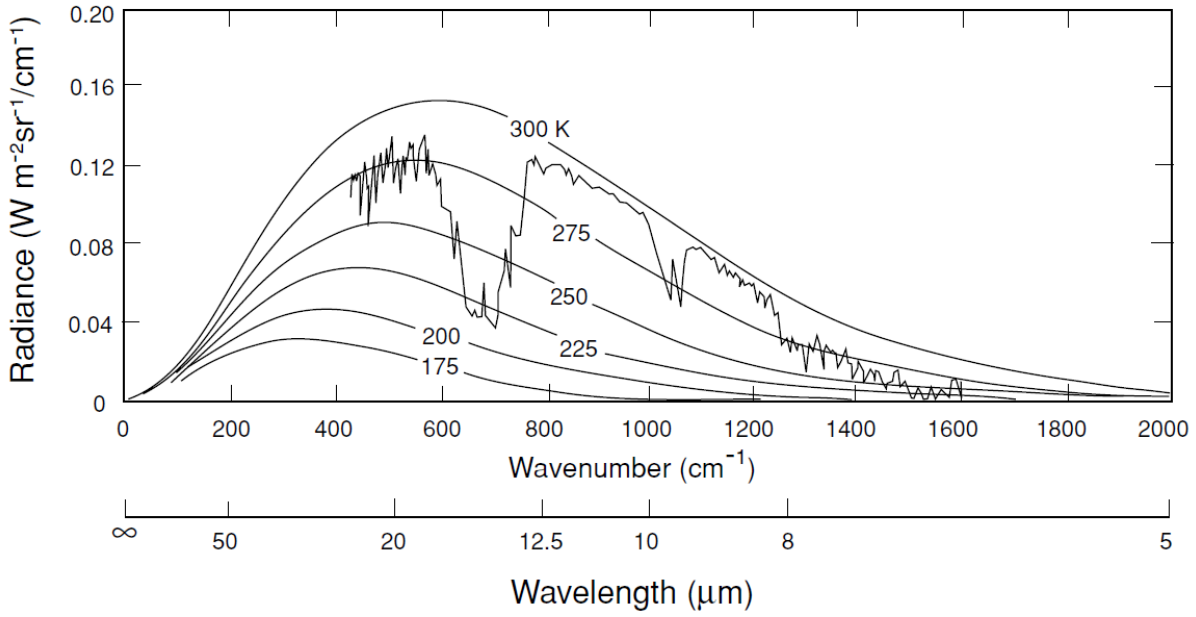

FIGURE 3.12: IR radiances emitted by Earth for different temperatures, as computed from the Planck equation. The temperatures correspond to different Planck functions at local thermodynamic equilibrium (LTE). The atmospheric spectrum was recorded from the Nimbus 4 satellite spectrometer. (Taken from Liou [2002])

In more detail, fig. 3.13 shows most of the atmospheric species that a thermal infrared sounder is detecting. As an example, water vapor absorption (H_2O) covers almost the whole spectral band, while ozone (O_3) is strong on both sides of the central hole of the ν_3 band around 1042 cm^{-1}, with maxima in the P-branch around 1025 cm^{-1} and in the

R-branch around 1055 cm^{-1} (fig. 3.13, middle panel and fig. 3.12, just above 1000 cm^{-1}). The absorption of ozone in that spectral range is due to the ν_3 vibrational mode. It dominates the spectrum in the atmospheric window, between 800 and 1200 cm^{-1} (fig. 3.13, top panel), and hence, has a key role in the radiation budget in general. Note that other ozone bands contribute to the spectrum, but they are generally much weaker.

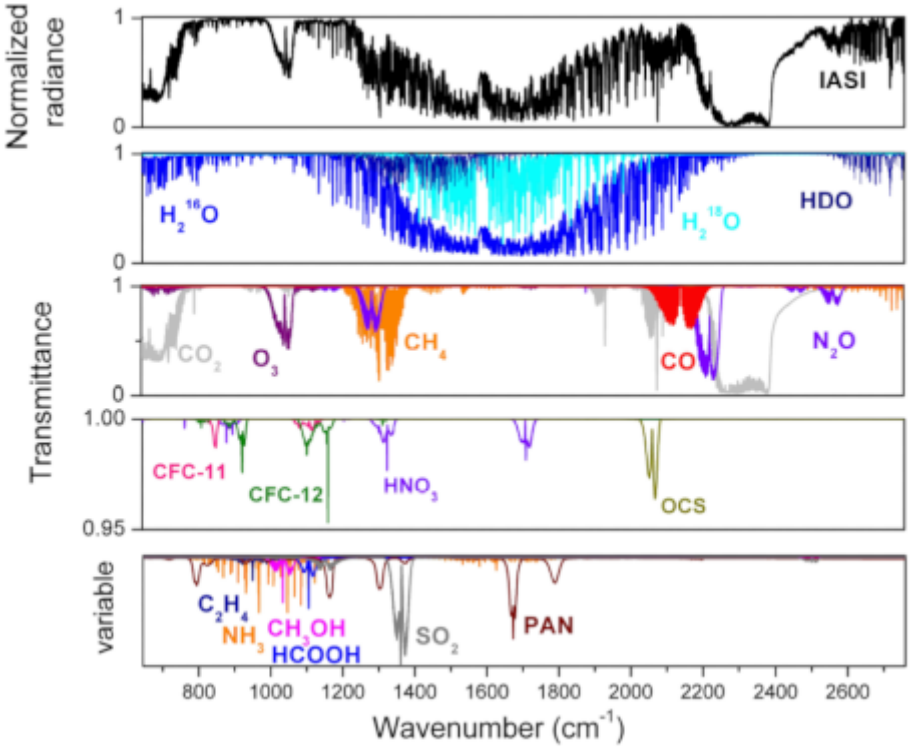

FIGURE 3.13: Absorption spectrum in the 645−2760 cm^{-1} band of the IR, as measured by IASI (see section 5.3). The four bottom panels show typical atmospheric transmittance spectra from then main atmospheric absorbers. (Taken from Clerbaux et al. [2009])

The two bottom panels of fig. 3.13 show the spectral signatures of weak or highly variable absorbers. The variable absorbers include species which are detected above the emission sources or plumes, such as SO_2 during volcanic eruptions [Clarisse et al., 2012] and volatile organic compounds such as HCOOH, C_2H_4 and PANs, from biomass burning [Coheur et al., 2009].

3.5 Radiative forcing

As seen previously in this chapter, radiation carries energy, and radiative energy is propagating through the atmosphere of Earth. The main two sources of radiation in the atmosphere are the incoming shortwave radiation (ISR) from the Sun and the outgoing longwave radiation (OLR) emitted from Earth. In principle, the total energy budget in the atmosphere is at balance. Changes in the global energy budget occur when changes happen either in the incoming solar radiation or in the outgoing longwave radiation. Changes in the solar radiation derive from changes in the energy output of the Sun, such as the 11−year sunspot solar cycle, while changes in the outgoing radiation consist of changes in the surface temperature of Earth, the albedo etc.

The above applies to the general state of the Earth system. However, as the world is currently evolving, it experiences strong modifications of its surface environment, as it can be seen by the rise of greenhouse gases, persistent air pollution, extensive land-use changes etc. All these modify the dynamic of the atmosphere and oceans, and they change the energy budget, and the Earth's climate. The main so-called global climate drivers are shown in fig. 3.14. They influence the atmosphere and the climate in many different ways.

The climate drivers, mainly related to anthropogenic activities, change the atmospheric composition and the surface of Earth, and cause an imbalance to the energy budget, which tends to be positive the past years. The alterations causing the imbalance are called forcings [IPCC, 2013]. Forcings can be positive, increasing the energy budget, or negative, decreasing the energy budget. Once a forcing is applied, the climate system responds to counterbalance the change, often through complex chains of feedback mechanisms, called climate feedback. Climate forcing drivers are distinguished in natural and anthropogenic drivers. The natural drivers refer to natural changes, such as in the incoming solar radiation, volcanic aerosols, mineral dust and others. The anthropogenic drivers include changes imposed by anthropogenic processes, such as in the greenhouse gases and aerosols emissions from anthropogenic sources, in the land surface, the contrails and others. The climate feedback on the other hand, is the response of the system (result) to the aforementioned changes. Climate feedback is also distinguished in positive and negative, as it can reinforce (positive) or dumpen (negative) the expected increase in the energy budget [2]. A very good indicator of climate feedback, that depicts the direction towards which the climate system is shifting, is the surface temperature, which is showing a rapid increase the past few decades [IPCC, 2013]. Other climate feedback indicators

[2]By convention, a positive forcing or feedback will result to an increase of the energy budget and the surface temperature, while a negative forcing/feedback will result to the opposite

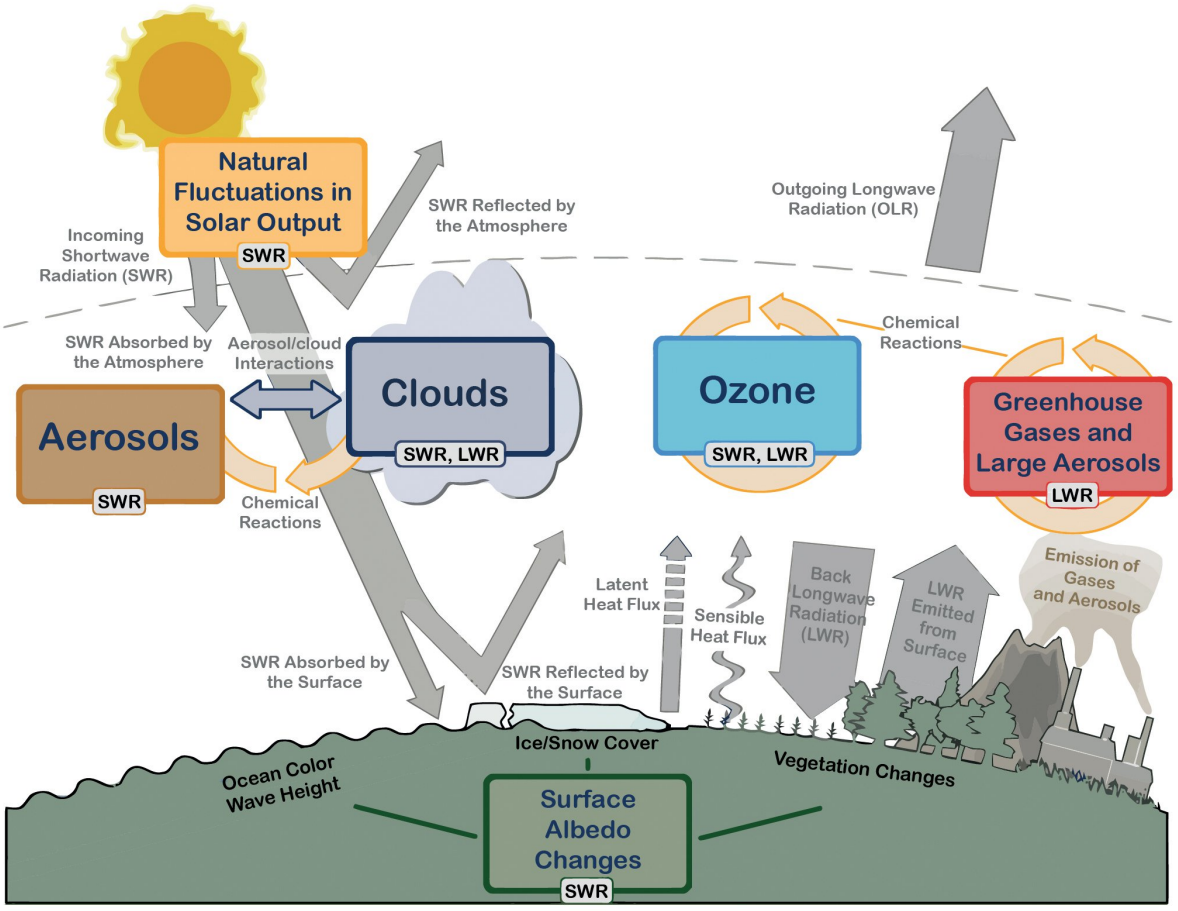

FIGURE 3.14: Main drivers of climate change. (Taken from IPCC [2013])

are the increased water vapor content in the atmosphere, the changes in the snow and cloud albedo, reduced outgoing longwave radiation and others. Characteristic climate feedbacks and their timescales are shown in fig.3.15.

The Intergovernmental Panel on Climate Change (IPCC) defines the radiative forcing (RF) as "the net change in the energy balance of the Earth system due to some imposed perturbation. It is expressed in watts per square meter (Wm^{-2}) averaged over a particular period of time and quantifies the energy imbalance that occurs when the imposed change takes place. It is presented as the value due to changes between the pre-industrial and the present−day times". From the definition above, it is logical to assume that each of the drivers discussed previously, causes its own RF, and consequently for the atmospheric composition, each species as well.

Since the first IPCC Assessment Report, other definitions for the radiative forcing have been introduced, based on the method of calculating or their application. There are three measures for the radiative forcing which are commonly used:

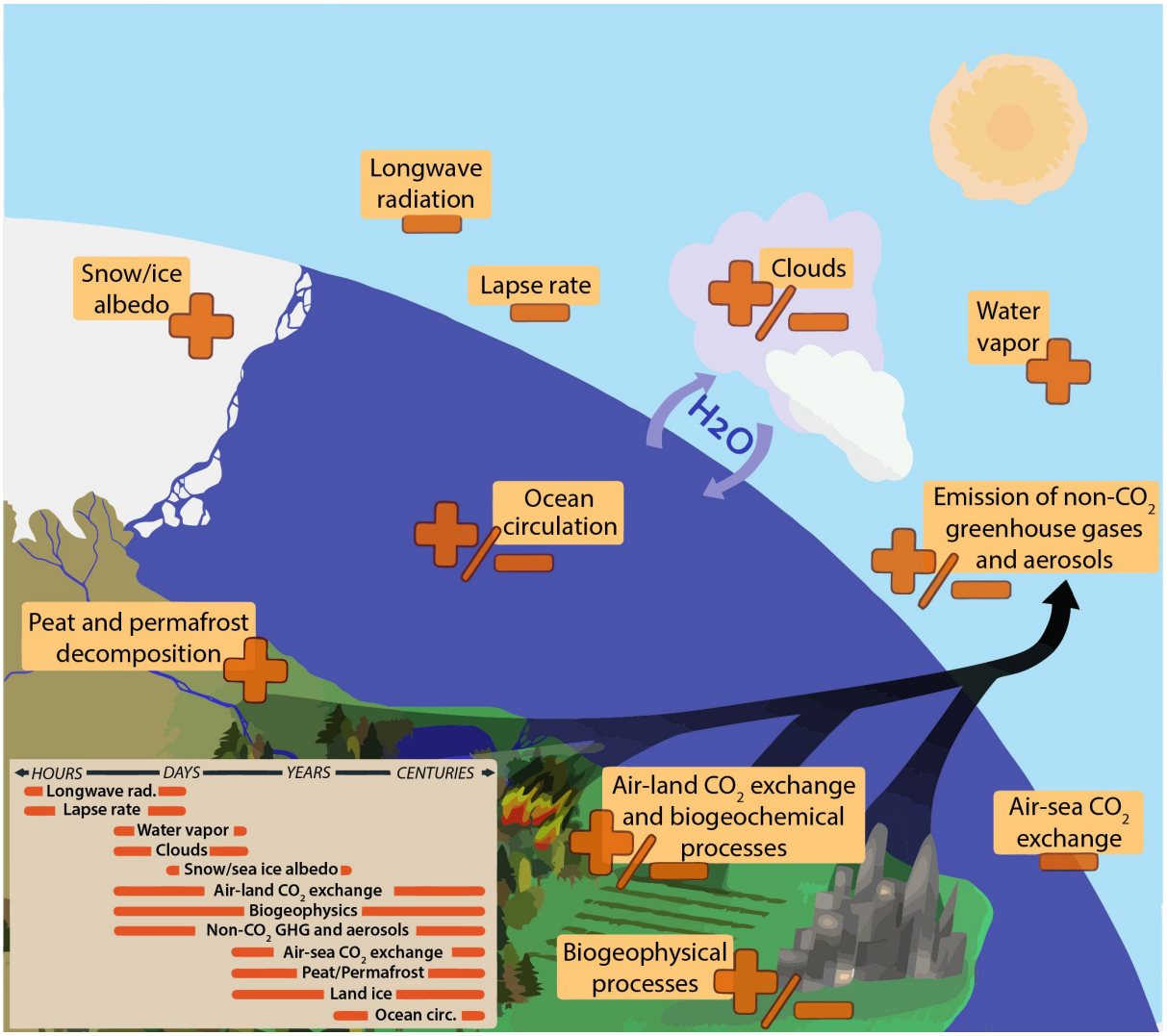

FIGURE 3.15: Climate feedbacks and timescales. The climate feedbacks related to increasing CO_2 and rising temperature include negative feedbacks (-) such as LWR, lapse rate, and air-sea carbon exchange and positive feedbacks (+) such as water vapor and snow/ice albedo feedbacks. Some feedbacks may be positive or negative (±): clouds, ocean circulation changes, air-land CO_2 exchange, and emissions of non-GHGs and aerosols from natural systems. In the smaller box, the large difference in timescales for the various feedbacks is highlighted. (Taken from IPCC [2013])

- the radiative forcing (RF), which allows the stratospheric temperature to adjust to an imposed change
- the effective radiative forcing (ERF), which allows the atmospheric and surface temperature to adjust, while sea-ice conditions are fixed
- the instantaneous radiative forcing (IRF), which refers to an instantaneous change in the net radiative flux due to an imposed change

The last two forcings (ERF and IRF) refer to a change in the net radiative flux at the top of the atmosphere, while the traditional definition (RF) refers to the tropopause.

The IPCC has been issuing reports on the evolution of the radiative forcing. In the latest report of 2013, the total anthropogenic radiative forcing (the first case of the ones listed above) was estimated to be $+2.3 \pm 1\,\mathrm{Wm}^{-2}$. Fig. 3.16 shows the global mean net (RF) and effective (ERF) radiative forcings, along with their 90% confidence intervals. It also distinguishes the contribution to this forcing from key climate drivers, such as CO_2, O_3 and aerosol interactions with radiation and clouds. The contribution of O_3 on the radiative forcing is discussed in more detail in Ch. 4.

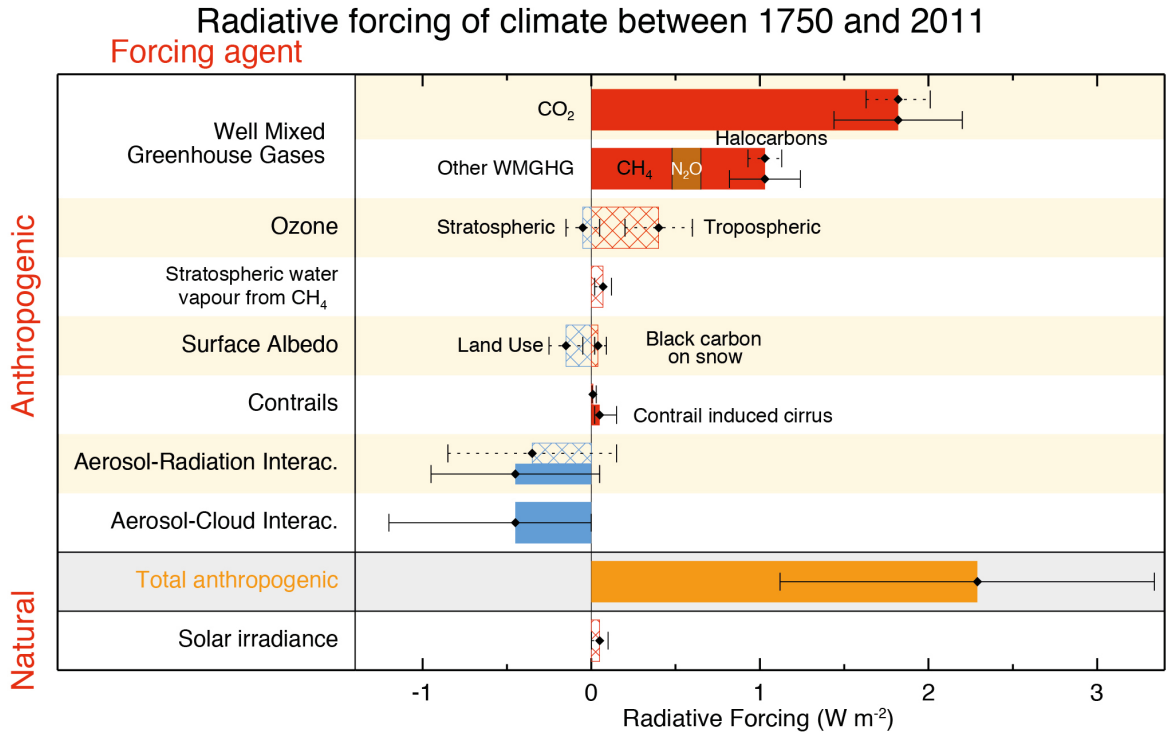

FIGURE 3.16: Bar chart for RF-hatched and ERF-solid for the period 1750−2011. Uncertainties (5 to 95% confidence range) are given for RF (dotted lines) and ERF (solid lines). (Taken from IPCC [2013])

Chapter 4

Ozone in the atmosphere

Ozone is a key substance for both atmospheric chemistry and climate. It is a secondary species, the abundance of which is controlled by the emissions of precursors, the availability of oxidizing agents and sunlight, and the availability of ozone-depleting substances (ODSs). Ozone is also a radiatively active gas in the spectral ranges of both solar (SW) and terrestrial (LW) radiation. To understand and accurately represent the impact of ozone on climate, it is essential to know its chemistry, the main patterns of its distribution, horizontally and vertically, as well as its long-term trends, in the troposphere and the stratosphere.

4.1 Chemistry of ozone

Ozone, as a secondary compound, is regulated by a variety of chemical mechanisms. Depending on the altitude it is found, it is protecting the biosphere by acting as a filter of harmful radiation in the stratosphere or can be dangerous for living species and plants as an air pollutant in the troposphere.

4.1.1 Tropospheric ozone

Ozone in the troposphere represents only about 10% of the total ozone. In that altitude range it has a relatively short lifetime, of about 22 days [IPCC, 2013]. Ozone is a natural component of the background air, as a lot of its precursors are biogenic, but can also be formed from precursor species emitted by anthropogenic activities. At low concentrations (background ozone) it is harmless. However, in the last decades, ozone

in the troposphere has been increasing, as a result of increasing emissions of precursors (from the development of technology and the industrialization) and has become an important driver of air quality. The past decade, measurements reveal that tropospheric ozone has exhibited a steady increase of around 0.2 DU y^{-1} (trends varying from 0.17 to 0.27 DU y^{-1}) (definition of DU in Appendix A) in the Northern Hemisphere, while others reveal a negative trend of 0.15 DU y^{-1} (from 0.09 to 0.2 DU y^{-1}), including IASI [Gaudel et al., 2018]. Likewise, in the Southern Hemisphere instruments show either an increase of around 0.25 DU y^{-1} (from 0.14 to 0.40 DU y^{-1}) or a decrease of around 0.23 DU y^{-1} (0.19 to 0.27 DU y^{-1}) [Gaudel et al., 2018]. High ozone concentrations are usually accompanied by the appearance of photochemical smog [Jacobson, 2002].

Due to its short lifetime, but also because of its dependence on other atmospheric substances, tropospheric ozone exhibits large spatial and temporal variability, driven by the available sources. The production of ozone in the atmosphere is photochemical and therefore takes place in the daytime. The tropospheric ozone production can be separated following two main regimes: i) the background ozone production, which happens under unpolluted conditions, and ii) the urban region ozone production, which involves more primary precursors and higher concentrations.

The main precursors of background ozone are nitrogen oxides (NO_x), carbon monoxide (CO) and volatile organic compounds (VOCs), mainly of biogenic origin; such as: methane (CH_4) and other alkanes, formaldehyde (HCHO) etc. As illustration, we show some of the chemical reactions for the two most important precursors:

i) The nitrogen oxides (NO_x):

$$NO + O_3 \rightarrow NO_2 + O_2 \tag{4.1}$$

$$NO_2 + h\nu \rightarrow NO + O \tag{4.2}$$

with $h\nu$ being the required energy to photodissociate NO_2 ($\lambda < 420$ nm), taken from the solar radiation,

and, finally:

$$O + O_2 + M \rightarrow O_3 + M \tag{4.3}$$

where M is one of the major atmospheric constituents (N_2 or O_2), that acts to stabilize the association complex.

The ozone relation to NO_x following the above equations, forms the "photo-stationary state" and the process repeats itself as long as there is available radiation.

ii) The carbon monoxide (CO); whose oxidation leads to O_3 formation in the presence of H_2O and NO_x:

$$O_3 + h\nu\,(\lambda < 320\,nm) \rightarrow O(^1D) + O_2 \tag{4.4}$$

$$O(^1D) + H_2O \rightarrow 2OH \tag{4.5}$$

and then,

$$CO + OH \rightarrow CO_2 + H \tag{4.6}$$

$$H + O_2 + M \rightarrow HO_2 + M \tag{4.7}$$

$$NO + HO_2 \rightarrow NO_2 + OH \tag{4.8}$$

$$NO_2 + h\nu \rightarrow NO + O, \tag{4.9}$$

and, finally:

$$O + O_2 + M \rightarrow O_3 + M. \tag{4.10}$$

The production of ozone from other organic compounds, and especially longer chemical chains, requires more complex chemical mechanisms, more steps and the presence-production of peroxy radicals (RO_x). Furthermore, in all of ozone production from VOCs, there is always an intermediate step that involves NO_x or CO. Readers can refer to [Jacobson, 2002] for more information. Finally, the contribution of VOCs-produced ozone is rather small compared to the production from NO_x and CO.

In the urban-regime, the main compounds and chemical reactions remain the same, however there are some additional compounds that act as precursors and some - such as NO_x - that come with much higher concentrations. The urban non-methane volatile organic compounds (NMVOCs) are mainly produced during combustion, e.g. industry or road traffic. A lot of these organic precursors, cannot be transported far from the source, as

they react quickly with free radicals. Their persistence around the source helps increasing of O_3 locally. Finally, heating and traffic in cities lead to increased concentrations of NO_x and CO, which further lead to increased O_3.

Enhanced ozone production is also observed during the lightning periods, especially in the SH Tropics and midlatitudes [Hauglustaine et al., 2001]. In a lightning stroke channel, rapid heating and cooling convert N_2 and O_2 into significant quantities of NO, which then lead to O_3 production, following eq. 4.1 to 4.3, in the presence of sunlight [Murray, 2016].

Tropospheric ozone is removed from the atmosphere by two main processes: chemical destruction and dry deposition to the ground. Of the two main processes the most favored is the chemical destruction in the troposphere. During daytime, the destruction is dominated by ozone photolysis, while at nighttime it is mainly through eq. 4.1 of the NO_x cycle, and VOCs cycles.

The complete cycle of ozone in the troposphere, along with the basic chemical reactions, is schematized in fig. 4.1. Production and destruction of ozone are parts of the same cycle and take effect depending on the available radiation in the atmosphere.

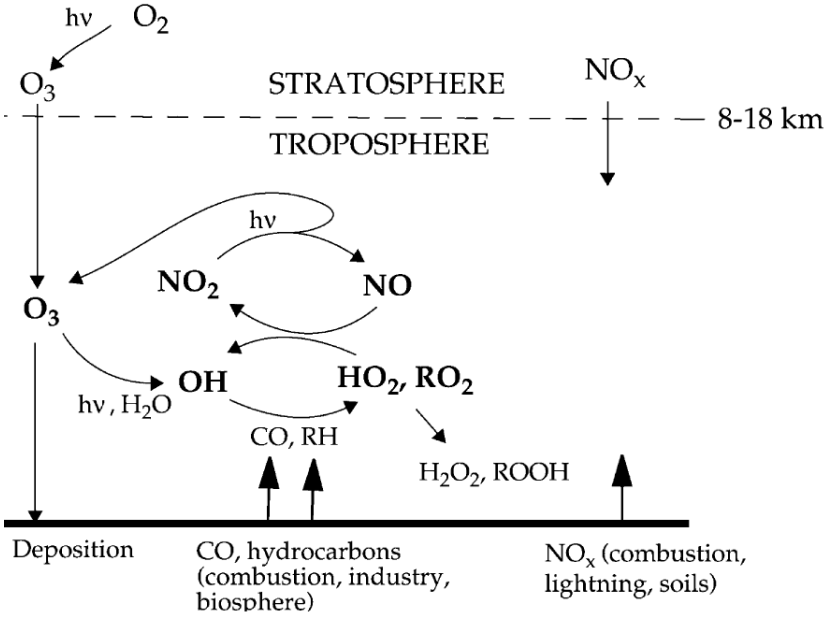

FIGURE 4.1: Schematic of tropospheric O_3 chemistry illustrating the coupling between the chemical cycles of O_3, HO_x, and NO_x. RO_2 refers to the ensemble of organic peroxy radicals. (Taken from Jacob [1999])

Finally, tropospheric ozone is enriched by intruding stratospheric ozone, which accounts for about 15% of the total tropospheric ozone burden. However, this exchange takes place only under certain atmospheric conditions and will be explained later in this section.

4.1.2 Stratospheric ozone

Stratospheric ozone refers to the layer of ozone that lies between the tropopause and around 40 km, protecting the Earth and all the living organisms on it from harmful solar UV radiation. It gained attention after discovering the "Antarctic ozone hole" [Farman et al., 1985], a phenomenon that appears around every September to December over the Antarctic since the 1980's, following a series of reactions, under cold meteorological conditions.

Stratospheric ozone represents 90% of the total ozone abundance in the atmosphere. It is produced in the atmosphere following the photolysis of molecular oxygen (O_2) from UV radiation, as shown below:

$$O_2 + h\nu \rightarrow 2O$$

$$O + O_2 + M \rightarrow O_3 + M$$

M is a collision partner that stabilizes the excited ozone transient (N_2 mostly). The UV radiation that is capable of breaking the molecular oxygen bond must have $\lambda < 242$ nm. Ozone is then also destructed through photolysis, to produce atomic and molecular oxygen, as follows:

$$O_3 + h\nu \rightarrow O + O_2,$$

with $h\nu$ as in eq. 4.4. Ultimately, O_3 reacts with molecular oxygen to generate O_2:

$$O_3 + O \rightarrow 2O_2.$$

The four above equations are known as the Chapman cycle, and are shown schematically in fig. 4.2. The first and last reactions are the rate-limiting steps of the cycle, while the two middle reactions proceed quickly and convert O_3 and O to one another.

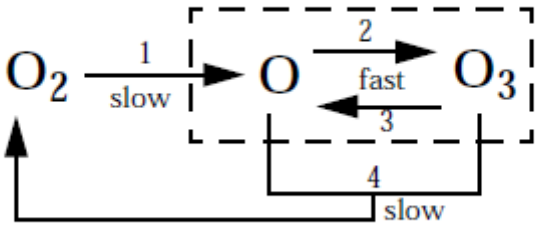

FIGURE 4.2: The Chapman cycle of ozone in the stratosphere. (Taken from Jacob [1999])

Ozone in the stratosphere would be in steady-state, if the Chapman cycle was acting alone, and it would indeed form a stratospheric layer. The observations however show, that the concentrations in the stratosphere are less than what is predicted by Chapman, and this is related to an additional sink, which proceeds through catalytic cycles and adds to the 4th reaction of the Chapman cycle. The catalytic cycles involve various source species, among which water vapor and methane, that form HO_x radicals, N_2O that generates stratospheric NO_x catalysis, and CFCs and halons (bromine compounds), among others, that form Cl_x and Br_x radicals. If on global scale the NO_x contribute most to the catalytic cycles, it is the Cl_x family of compounds that is mostly responsible for the Antarctic ozone hole.

The CFCs are industrial products, that were used around the 1970s and 1980s. CFCs are a severe threat to ozone in the stratosphere, especially as their lifetimes allow them to circulate in the atmosphere for decades. After the *Montreal Protocol* treaty, CFCs were substituted by the HCFCs and HFCs, in an effort to reduce the Antarctic ozone hole. Finally, stratospheric aerosols that reach the lower part of the stratosphere also contribute to the destruction of ozone.

4.2 Ozone distribution and seasonality

As seen in the previous section, ozone has a different behavior in the troposphere and in the stratosphere. Tropospheric ozone has a short lifetime (22 days) that causes large spatial variations around the globe, while stratospheric ozone (with a lifetime of a few weeks) exhibits more regular patterns. The ozone distribution in both layers is driven by a number of dynamical processes.

4.2.1 Tropospheric ozone distribution

Tropospheric ozone exhibits large concentrations around places where the population is concentrated, which renders it an important air pollutant. As described in the previous section, its production is associated with the presence of sunlight, and is favored under high surface temperatures. The two hemispheres of Earth have different summer periods, but also different land-ocean distribution, with the majority of anthropogenic precursors emitted in the Northern Hemisphere. All these translate to differences in the global distribution.

Figure 4.3 shows a climatology of tropospheric ozone combined from two instruments on board the Aura satellite, the Ozone Monitoring Instrument (OMI) and the Microwave Limb Sounder (MLS). As illustrated and explained in Ziemke et al. [2011] the Northern Hemisphere (NH) exhibits its peak ozone values during the boreal summer at mid-latitudes. The Southern Hemisphere (SH) peak occurs during the austral spring in the tropics and subtropics. On an annual average, the NH tropospheric O_3 column exceeds the SH one by 4 to 18%, depending on the latitudinal band. In general both hemispheres have their ozone maxima during their own spring-summer, while their minima during autumn. As seen from the seasonal maximum, the incoming solar radiation plays an important role in ozone concentration both directly and indirectly, through the increase of the atmospheric and surface temperature. Superimposed to the broad patterns, there are also more regional phenomena such as lightning and biomass burning, which cause high concentrations of ozone locally. As we show later in Ch. 8, the observations of the Infrared Atmospheric Sounding Interferometer (IASI) agree with the aforementioned patterns of tropospheric ozone, and furthermore affect the seasonal variability of the radiative content associated with ozone.

With its relatively short lifetime, ozone can be transported over long distances under certain circumstances. For example, polluted air with high concentrations of tropospheric ozone can be transported from North America into the North Atlantic through the dominating westerlies and the North Atlantic Oscillation (NAO). Large scale transport processes occur around the globe and tend to homogenize the concentrations in given latitudinal bands. Finally, a part of stratospheric ozone intrudes to the troposphere, enhancing the tropospheric ozone locally.

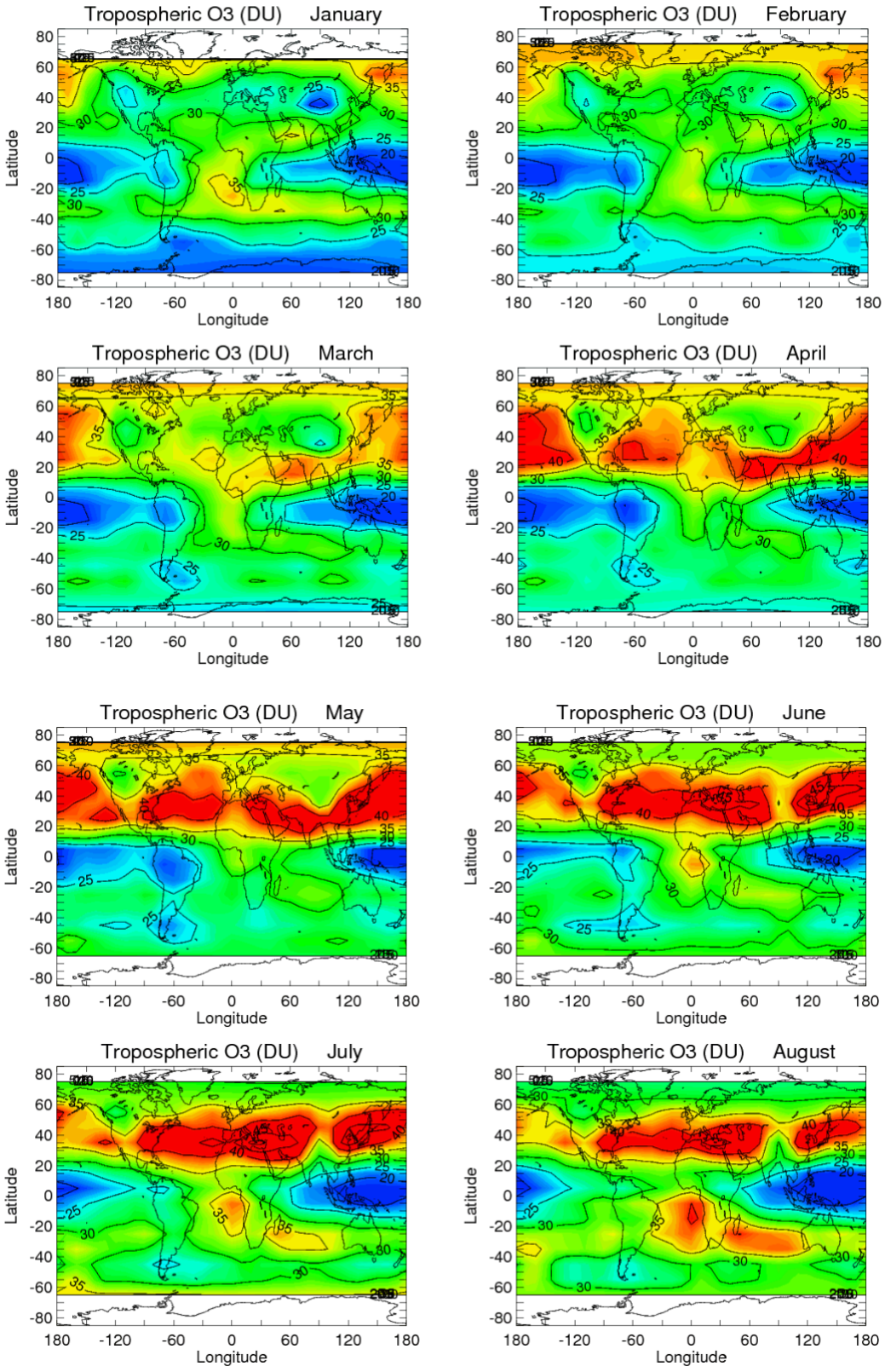

FIGURE 4.3: Tropospheric column ozone climatology (in Dobson Unit) for Jan. - Aug. from OMI/MLS residual ozone measurements. The color scale follows the contour lines (blue to red represent smallest to largest values, respectively; numbers on plot). (Taken from Ziemke et al. [2011])

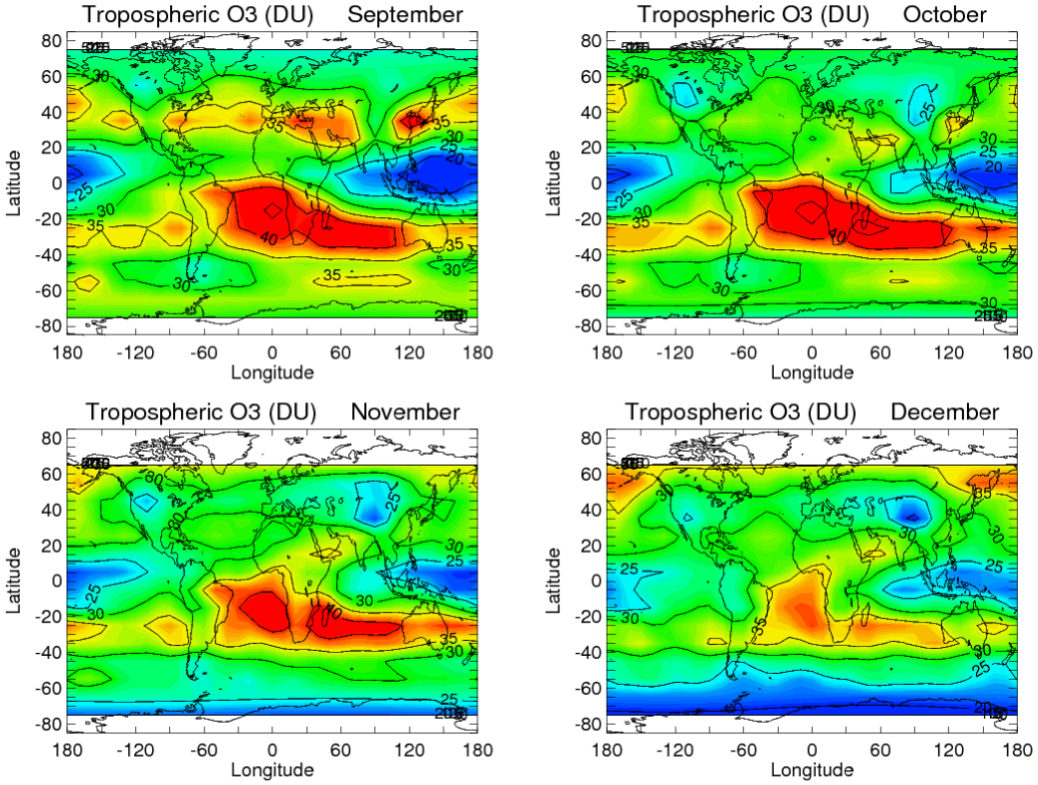

FIGURE 4.3: Continued figure, for Sept. - Dec.

4.2.2 Stratospheric ozone distribution

The stratospheric ozone distribution is driven by three processes: photochemical production and destruction, detailed in Sect. 4.1.2, and large-scale transport. The large-scale circulation starts from the tropics, where ozone-rich air ascends in the stratosphere and then follows a poleward and downward route. This process is called the Brewer-Dobson circulation and is graphically shown in fig. 4.4.

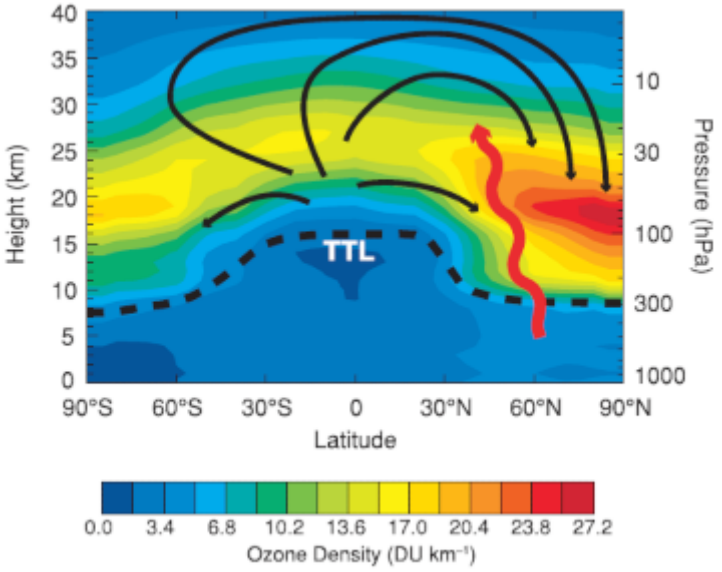

FIGURE 4.4: Meridional cross section of ozone concentration (in DU per km) during northern hemisphere winter (January to March). The dashed line denotes the approximate location of the tropopause, and TTL stands for tropical tropopause layer. The black arrows indicate the Brewer–Dobson circulation in northern hemisphere winter, and the wiggly red arrow represents planetary waves that propagate from the troposphere into the stratosphere. (Courtesy IPCC-TEAP [2005])

The Brewer-Dobson circulation is driven by planetary wave activity, which is stronger during the winter. Furthermore, because of the stronger thermal contrast over the land-dominated NH (as opposed to the sea-dominated SH) the planetary waves are stronger in the NH [Muller, 2012]. Therefore, the Brewer-Dobson circulation will be stronger in the NH winter than in the SH winter.

The ozone depleting substances also travel in the stratosphere with the Brewer-Dobson circulation, and when the meteorological conditions are favorable, they can cause severe loss of ozone, as mentioned in Section 4.1.2. Figure 4.5 shows the stratospheric ozone distribution for each month. The tropical region is well marked by low ozone concentration (in blue). February and March are associated to a peak of the stratospheric ozone in the NH, especially towards the North Pole. On the contrary, towards the austral spring (August to November), there are high concentrations in the SH mid-latitudes, while in

the south pole the Antarctic ozone hole is forming and it disappears in January. Finally, it is worth noting stratospheric loss of ozone occurs some years also in the Arctic, but not to the extent of the SH polar region.

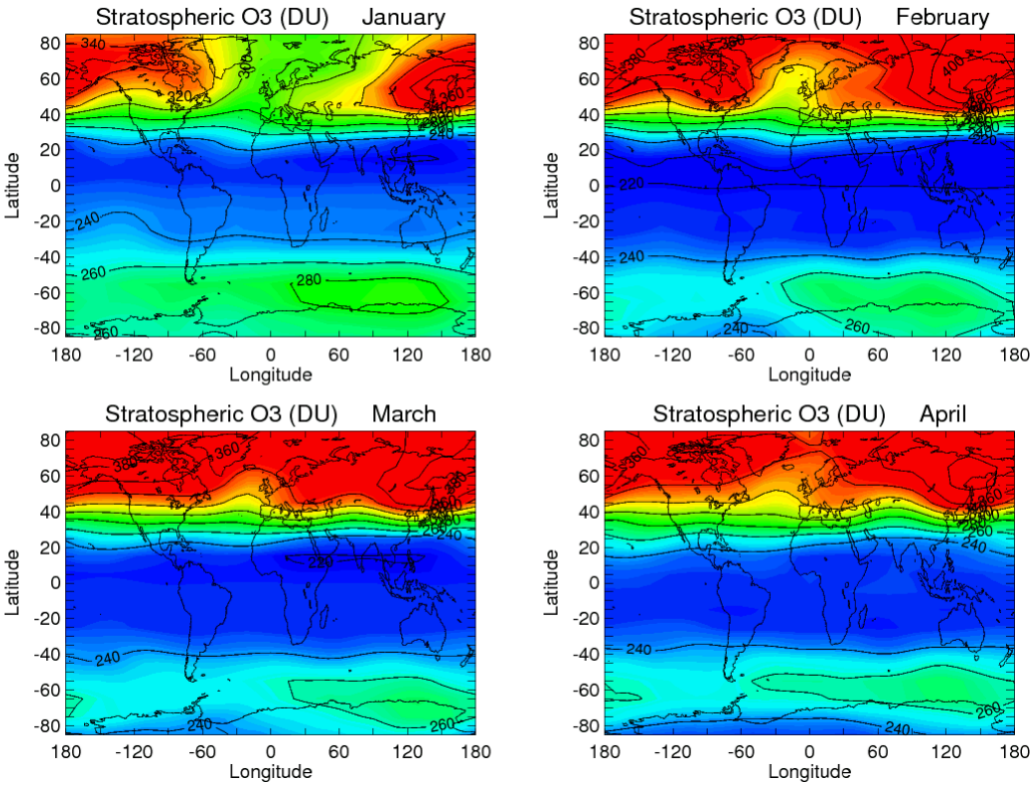

FIGURE 4.5: Stratospheric column ozone climatology (in Dobson Unit) for Jan - Apr from MLS ozone measurements. The color scale follows the contour lines (blue to red represent smallest to largest values, respectively; numbers on plot). (Taken from Ziemke et al. [2011])

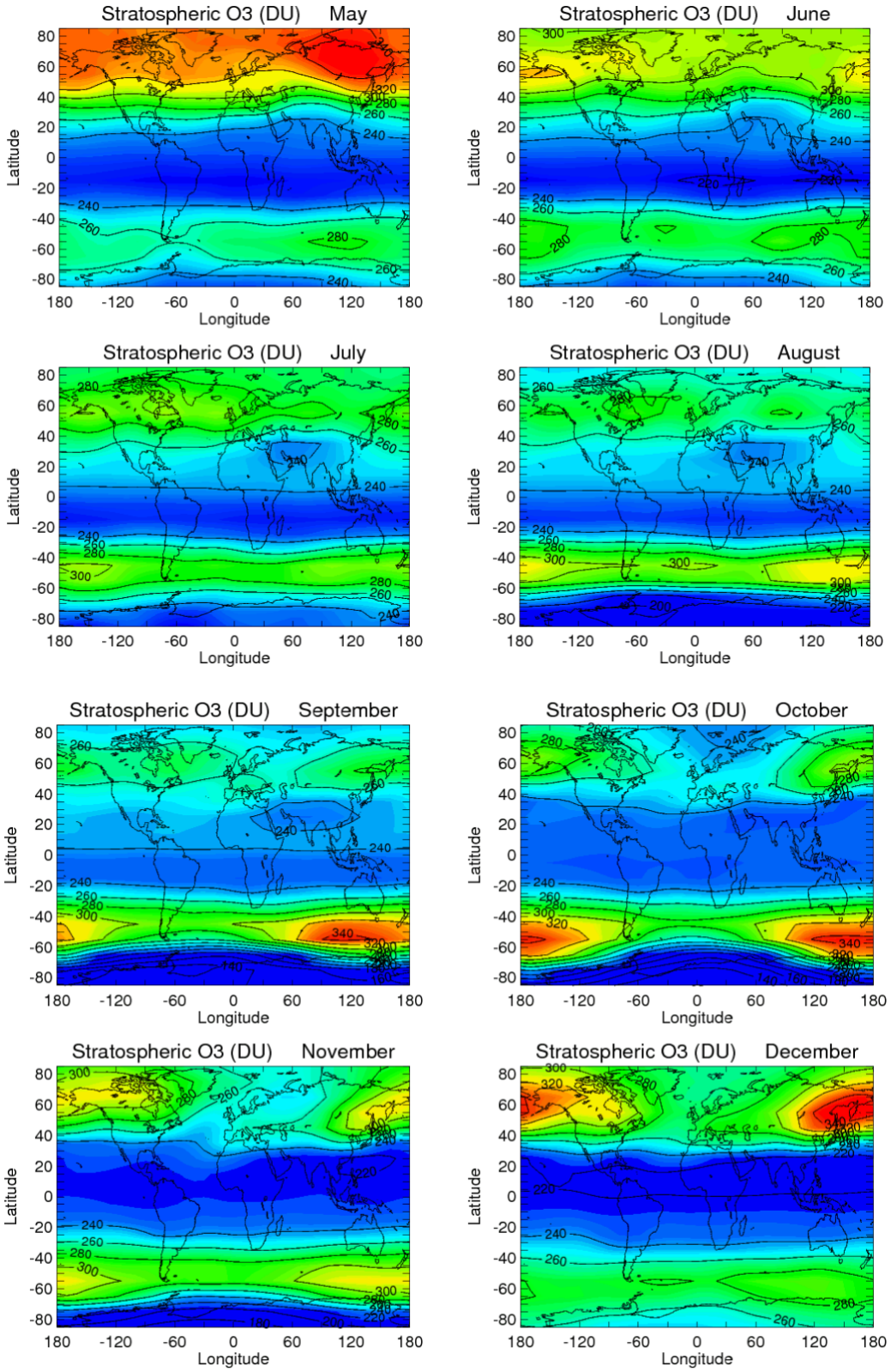

FIGURE 4.5: Continued figure, for May - Dec.

4.2.3 Stratosphere - Troposphere exchange

Stratosphere-troposphere exchange (STE) characterizes the transport of air through the tropopause in both directions. Although the stratosphere and the troposphere are coupled dynamically, chemically and radiatively, the two can be considered as two isolated layers on short-time scales, as the exchange of air between the two happen in scales of years. The STE generally follows the Brewer-Dobson circulation and the exchange happens when and where the tropopause intersects the isentropic surfaces that lie in the lower part of the stratosphere, as seen in fig. 4.6 [Mohanakumar, 2008]. The most prominent implication of the STE on the chemical composition of the atmosphere is on the distribution of ozone; particularly the decrease of stratospheric ozone and the increase of tropospheric ozone. The STE process slightly differ for the different latitudinal bands, therefore the exchange is distinguished in three main regions: the tropics, the subtropics and mid-latitudes, and the polar regions.

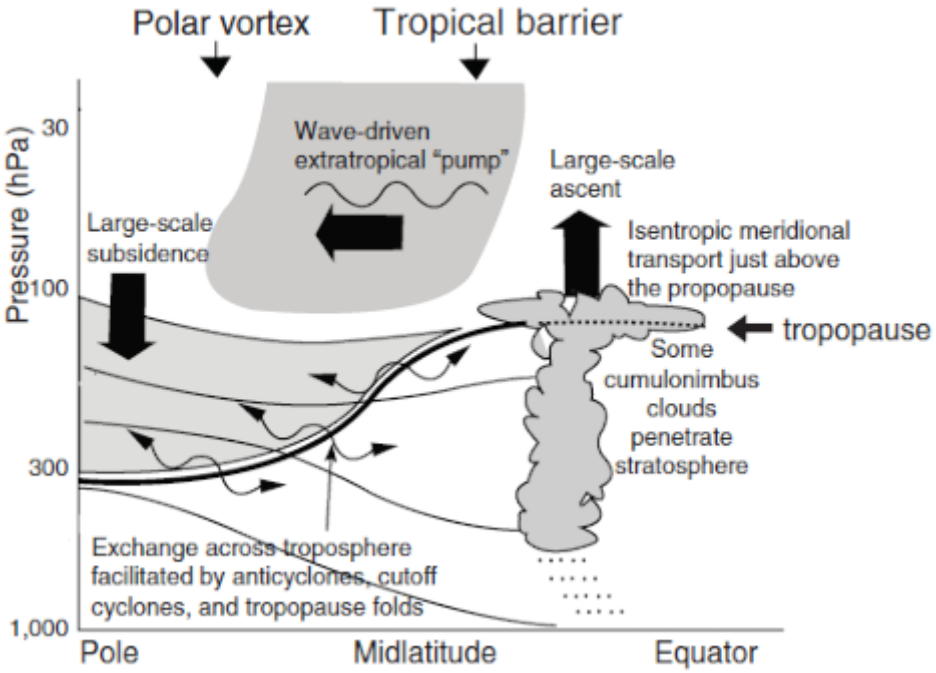

FIGURE 4.6: Schematic representation of stratosphere–troposphere exchange through tropopause. (Taken from Mohanakumar [2008])

In the tropical regions there are two main ways air can penetrate the stratosphere and vice versa [Mohanakumar, 2008]. Above the tropopause of the tropics, it is very common to find the tropical transition layer (TTL), characterized by a second, less strong, tropopause as its upper boundary. The water vapor-rich warm air of the tropics quickly ascends towards the first tropopause and gets trapped in the TTL. It then slowly penetrates to the stratosphere. This is the most common way of exchange. The second is due to convective clouds. Again, the warm air full of water vapor forms clouds (cumulonimbus),

whose upper parts penetrate to the stratosphere, as seen in fig. 4.6. In the tropics the STE happens in both ways, but mostly upwards.

In the subtropics and mid-latitudes again there are two main processes for STE: through tropopause folds and cut-off low pressure systems. The tropopause folding occurs when warm tropospheric air, poor in O_3, is ascending, while stratospheric O_3-rich air is subsiding. Because of the warmer tropospheric air, the isentropic surfaces tend to bend upwards, causing the folding. Tropopause folds usually occur in winter and spring and are found near jet streams. It is considered that these folding processes contribute about 15% to the global tropospheric ozone. The second process, the cut-off lows, are wind-flow regimes induced by the jet streams. The jet streams, while traveling, get distorted along the meridionals and the parts which are cut off − hence the name − isolate the cold air, that are keeping their polar characteristics [Mohanakumar, 2008]. They usually occur during summer. During the exchanges in these regions, the air is flowing both ways.

Finally, the STE in the polar regions is associated with the polar vortex. The polar vortex usually starts building up around the local autumn, getting stronger during local winter and finally breaking in spring. During the breaking, polar air is transported mostly towards the troposphere.

A thorough investigation in STE is presented in Lee et al. [2002] and Santee et al. [2011]. We refer the readers to these studies for more information.

4.3 Chemistry - Climate interactions

Chemistry and climate of the atmosphere are interconnected in various ways. Chemistry controls climate, but at the same time an imposed change on climate due to chemistry, will bring further changes in the chemistry itself. A well know example is ozone. As said before, the stratospheric ozone has been decreasing significantly in the 1980-2000 time frame, mainly due to depletion by chlorine radicals, generated from CFCs. This means that there is less ozone in the stratosphere to absorb the UV solar radiation, which in turn can penetrate further down to the troposphere. As presented in the first section of this chapter, the solar UV radiation favors the production of tropospheric ozone when reaching the lower layers of the atmosphere, which has been increasing, and consequently contributes to the total greenhouse effect in the lower atmosphere.

The process described above is a simplistic representation of the link between chemistry and climate. In reality the processes are much more complex and involve many more atmospheric constituents and dynamical processes. Figure 4.7 schematizes the connection

between atmospheric constituents and their impact on climate. It was produced by IPCC to explain how a possible control on the emissions of these species, involved in the tropospheric chemistry system and causing air pollution, would affect the climate. It is essential to point out, following fig. 4.7, that a change in one atmospheric constituent, will cause changes in many others and the result is not always straightforward. For example, reducing the emissions of VOCs can cause either cooling or warming, depending on where they are found and under which conditions.

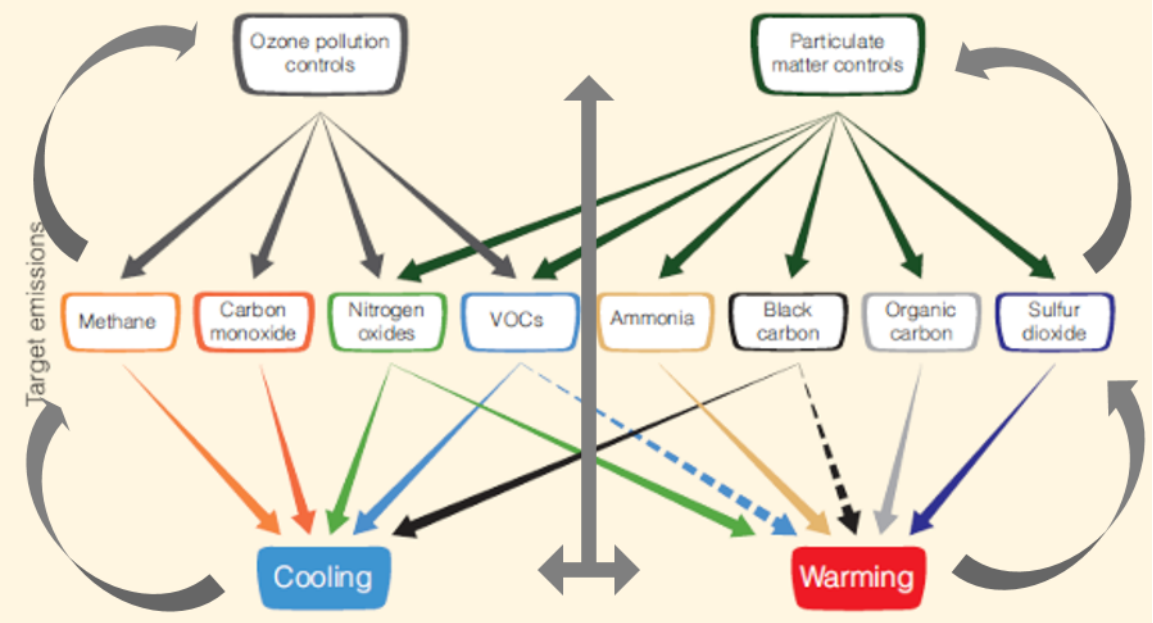

FIGURE 4.7: Schematic diagram of the impact of pollution controls on specific emissions and on climate. Solid lines indicate known impact; dashed lines indicate uncertain impact. The dark grey lines indicate the climate feedback. (Adapted from IPCC [2013])

Coupled chemistry-climate models have been at the center of scientific attention during the past years, to help representing and understanding the interactions between chemistry and climate, but also to forecast the results of possible changes. In the studies where chemistry-climate models are involved, the chemical part is represented by the species abundance, while the climate part is represented by the change imposed on the radiative budget, using the radiative forcing as a metric. Many studies have focused on ozone, e.g. MacIntosh et al. [2015]; Shindell et al. [2015]; Stevenson et al. [2013]; Young et al. [2013]. Different results were obtained, as models use different methods and assumptions. It is now common in chemistry-climate studies to use an ensemble of models, producing one average result and a model standard deviation around the average, to quantify the uncertainty.

4.4 Ozone radiative forcing

Ozone, as mentioned previously in this chapter, plays an important role both in the atmospheric chemistry and climate. The chemistry of ozone has been extensively studied throughout the decades, and the monitoring of its abundance and distribution that started after the discovery of the Antarctic ozone hole, has provided a wealth of crucial information for the understanding of the atmospheric system in general. However, the impact of ozone on climate was not directly observable, until the concept of radiative forcing was introduced. With the RF it was possible to quantify the ozone climate impact and behavior.

As introduced before in Section 3.5, the RF is calculated as the difference in the net radiative budget between the present and the pre-industrial era (the latter is also the reference era for monitoring how controlling emissions achieve ozone recovery). However, the pre-industrial ozone levels are not well known, as the available observations are limited and scattered. Therefore when using chemistry-climate models to estimate the RF of ozone, there is a large uncertainty. Apart from that, as different models use different methods and approximations, the present day ozone representation also differs between models, even though models are being assessed against observations almost constantly.

In an effort to gather all the information available for ozone and its impact on climate, the IPCC issues an assessment report about every four years, in which it presents all the recently acquired knowledge on climate and climate change. With the vast number of different groups working on the subject, it is now possible to assess the contribution of different atmospheric constituents to the total RF, as discussed in fig. 3.16. The next two subsections describe in detail the tropospheric and stratospheric ozone RF separately.

4.4.1 Tropospheric ozone radiative forcing

Tropospheric ozone is listed as the third most important GHG in terms of RF, after the well-mixed GHGs [IPCC, 2013]; however it is distinguished from the other GHGs due to its high spatial and temporal variability, caused by its short lifetime. Ozone calculations of the RF were until recently model-based only, resulting in discrepancies in the final estimation. This can be understood by looking at Table 4.1, where tropospheric ozone RF from various studies is shown in columns 2 to 4. In these studies a variety of chemistry-climate models is used, and as it can be seen, the values vary from $0.33\,\mathrm{Wm}^{-2}$ [Shindell et al., 2013] to $0.45\,\mathrm{Wm}^{-2}$ [Søvde et al., 2011], while the confidence intervals (given only in some studies) are always large, due to the inter-model spread (when multiple models

TABLE 4.1: Contributions of tropospheric and stratospheric ozone changes to radiative forcing (Wm^{-2}) from year 1750 to 2011. (Adapted from IPCC [2013])

	Troposphere			Stratosphere		
	LW	SW	Total	LW	SW	Total
AR4 Forster et al. (2007)			0.35 (0.25-0.65)			-0.05 (-0.15-0.05)
Shindell et al. (2013)			0.33 (0.31-0.35)			-0.08 (-0.10-0.06)
WMO (Forster et al., 2011)						-0.03 (-0.23-0.17)
Sovde et al. (2011)			0.45			-0.12
Skeie et al. (2011)			0.39			-0.12
ACCMIP	0.33 (0.24-0.42)	0.08 (0.06-0.10)	0.41 (0.21-0.61)	-0.13 (-0.26-0)	0.11 (0.03-0.19)	-0.02 (-0.09-0.05)
AR5			0.40 (0.20-0.60)			-0.05 (-0.15-0.05)

are used). The final value reported by the IPCC is an average of these studies, after adjustments, e.g. all studies do not cover the exact same time period. This value is set to $0.40\,Wm^{-2}$, which agrees with Skeie et al. [2011] and the Atmospheric Chemistry and Climate Model Project (ACCMIP), and is larger than the previous assessment report [Forster et al., 2007].

Tropospheric ozone thus contributes a positive forcing, as its increase causes a warming of the troposphere. This is shown in fig. 4.8, which presents the time evolution of the RF for tropospheric (blue) and stratospheric (green) ozone from 1750 to 2010. It is clearly shown that after 1950 there is a rapid increase in tropospheric ozone RF.

In an effort to make the RF calculations more precise, modern observations are used to assess the performance of the chemistry models. Such is the case in the study of Bowman et al. [2013], where satellite retrievals from the TES instrument were used to constrain the RF from the ACCMIP models. Interestingly, this reduced the inter-model uncertainty by 30%.

4.4.2 Stratospheric ozone radiative forcing

The situation of the stratospheric ozone RF is quite different. Stratospheric ozone has been decreasing due to depletion from anthropogenic emissions. As the RF is estimated by the net change in flux, it can be distinguished in shortwave and longwave. For the case of stratospheric ozone, a decrease produces a positive RF in the shortwave (the

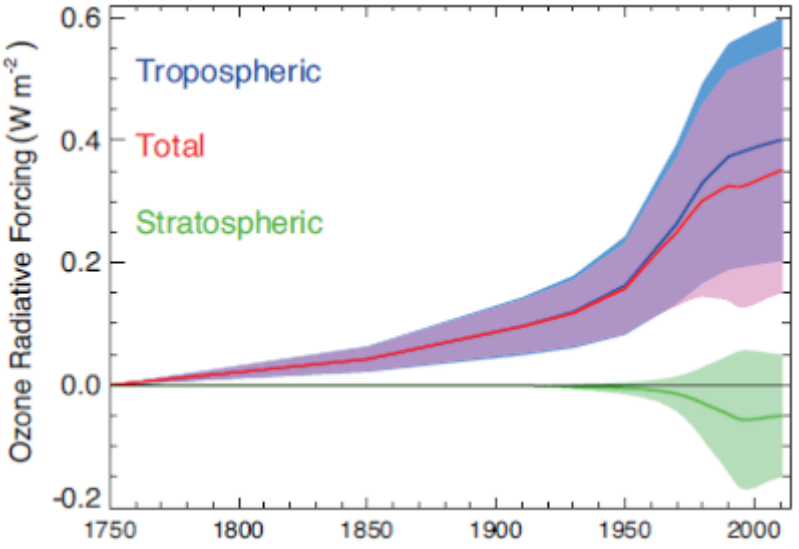

FIGURE 4.8: Time evolution of the radiative forcing from tropospheric and stratospheric ozone from year 1750 to 2010. Tropospheric ozone data are from Stevenson et al. [2013] scaled to give 0.40 Wm^{-2} in 2010. The stratospheric ozone RF follow the functional shape of the Effective Equivalent Stratospheric Chlorine assuming a 3-year age of air scaled to give -0.05 Wm^{-2} in 2010. (Taken from IPCC [2013])

incoming solar flux in the troposphere increases) and a negative RF in the longwave (less absorption, less heating of the stratosphere). The overall RF which accounts for the compensation effect is around -0.05 Wm^{-2}. The situation has not changed since the IPCC assessment report in 2007. It should also be noted that although different models were used, they give consistent estimates with RF values between +0.03 Wm^{-2} [Forster et al., 2011] to -0.12 Wm^{-2}, with high confidence intervals.

The time evolution of the stratospheric ozone RF is shown also in fig. 4.8, where the decrease due to the ozone depletion from the 1970's is clearly shown. With the regulations on CFCs after 2000, the RF shows a stabilization the past few years.

Chapter 5

Ozone infrared sounding from satellites

When it comes to observing the composition of the atmosphere, and in particular ozone, there are two main methods which can provide useful information: i) *in-situ* observations, and ii) remote observations.

5.1 *In situ* and remote observations

The *in situ* observations of ozone include the ozonesondes and the aircraft observations. Ozonesondes are historically one of the first methods to measure the ozone vertical distribution; they provide a high vertical resolution of 100 meters. It is common to couple ozonesondes along with weather balloons, and the measurements finally provide data of ozone, humidity, atmospheric pressure and temperature. The Northern Hemisphere is very well covered by ozonesondes; their data are archived and made available by the Network for the Detection of Atmospheric Composition Change (NDACC) (`http://www.ndsc.ncep.noaa.gov/`) [Leblanc et al., 2004] and the World Ozone and Ultraviolet Data Center (WOUDC) (`https://woudc.org/`). The Southern Hemisphere has less measurement sites and the historical data is not so extended; the data are handled and archived at the Southern Hemisphere Additional Ozone Sondes (SHADOZ) network [Thompson et al., 2004].

Aircraft observations are performed either by scientific aircraft missions or commercial airplanes, which carry all necessary instrumentation to measure the atmospheric composition. The scientific missions are quite expensive, therefore the conventional airplanes are the ones that are mostly used. The advantage of the aircraft measurements is that

they are performed at the "cruising" altitudes, that is 10 ± 2 km, and provide very useful information not only for the upper troposphere, but also for the cases of stratospheric-tropospheric exchange. Along with the atmospheric composition, they also provide measurements for atmospheric temperature and pressure, wind speed and many others. The disadvantage of the aircraft observations is the spatial coverage, which is limited around the trajectory of the airplane. Observations from commercial aircraft flights, such as from Lufthansa and Air France flights, are available through the In-service Aircraft for a Global Observing System (IAGOS) for the recent years [Petzold et al., 2015].

The remote observations include ground-based and spaceborne observations. The advantage of the ground-based observations is that they can provide very precise measurements, sometimes with fine vertical resolution. Many of these instruments can also provide, simultaneously, measurements of many other geophysical properties of the atmosphere, along with the ozone abundance.

The ground-based instruments for ozone measurements are distinguished in two main categories: active and passive remote sensors. The active remote sensors are mainly Lidar (Light Detection and Ranging). They make use of an emitted laser beam and measure the backscattered radiation, in distinct wavenumbers. The Lidar provide detailed ozone profiles, and are widely used for monitoring atmospheric ozone, temperature, aerosols, water vapor and stratospheric clouds (e.g., Wandinger et al. [2016]).

The passive remote sensors include a variety of instruments, operating in the UV, Visible, IR or microwave part of the spectrum. The most wide-spread of these instruments are those that provide total ozone columns, which are: the Dobson spectrophotometer (e.g., Evans [2006], operating under the Dobson network, `http://www.o3soft.eu/dobsonweb/network.html`), the Brewer spectrophotometer (e.g., Bais [1997], operating under the EUBREW network, `http://www.eubrewnet.org/cost1207/`) and the UV-Vis spectrometers (such as MAX-DOAS (e.g. Hönninger et al. [2004]) and SAOZ (e.g. Pommereau and Goutail [1988], `http://www.ndaccdemo.org/instruments/uv-visible-spectrometer`).

The passive sensors that provide O_3 profiles are the Microwave radiometer and the FTIR spectrometer. The Microwave radiometer makes use of the change in pressure broadening as a function of altitude (`http://www.ndaccdemo.org/instruments/microwave-radiometer`). The FTIR spectrometer records mid-IR solar transmission spectra, and a retrieval method is used to obtain the vertical profile information (e.g., Vigouroux et al. [2015], `http://www.ndaccdemo.org/instruments/ftir-spectrometer`).

All of the methods presented above can provide quality measurements, however their spatial coverage is limited around the instrument and cannot be representative of the

greater area. Coordinated networks, such as those identified above help to increase representativeness. In order to circumvent the problem of spatial coverage, the satellite remote sensors provide are used.

5.2 Satellite observations

Contrary to the ground-based measurements, spaceborne observations, i.e. from satellites, have the ability to provide global coverage. Atmospheric remote sensing from space makes use of the electromagnetic radiation at different wavelengths, from microwave to ultraviolet. Satellites are distinguished in two categories, regarding their orbit: those that fly on Low Earth Orbit (LEO), which is between 160 to 2000 km from the Earth's surface, and those on Geostationary Earth Orbit (GEO), where the satellite is placed at around 36000 km from the Earth's equator, traveling with the same period as the Earth's rotation, such as to always observe the same Earth disc. The GEO satellites are currently mainly employed for weather services and communications. On the other hand, the LEO satellites are used in most Earth observation missions, where they frequently take advantage of sun-synchronous orbits at around 800 km height. Remote sensing LEO satellites varies with the viewing geometry of the sensor (fig. 5.1: nadir, limb and occultation). Limb and occultation techniques are used mainly for profiling and stratospheric observations. Nadir is the most common technique; the sounder measures the signal from a field of view that is downward, i.e. the upwelling radiation. Nadir sounding is also widely used for ozone monitoring, as it provides in some cases better sensitivity to the troposphere than other techniques, while presenting a good spatial resolution and a high sampling frequency.

Historically, the first ozone measurements were focused on the monitoring of the stratosphere and were performed by the Total Ozone Mapping Spectrometer (TOMS) nadir sounder, around 1978 and afterwards, in the UV and visible range [Heath et al., 1975]. Since then there have been many advances in science and technology for the UV-Vis nadir sounders, which led to the Global Ozone Monitoring Experiment (GOME) launched in 1996 [Burrows et al., 1999], the Scanning Imaging Absorption Spectrometer for Atmospheric Cartography (SCIAMACHY) launched in 2002 [Gottwald et al., 2006], the Ozone Monitoring Instrument (OMI) launched in 2004 [Levelt et al., 2006] - which continued the TOMS record, and GOME-2 launched in 2007, to continue the GOME mission [Loyola et al., 2011]. The thermal IR range was used more recently to probe O_3; it offers the advantage over UV-Vis sounding of greater sensitivity in the troposphere. The first thermal IR sounder to provide measurements of tropospheric and total ozone was the Interferometric Monitor for Greenhouse Gases (IMG) in 1996, for only a short period [Turquety

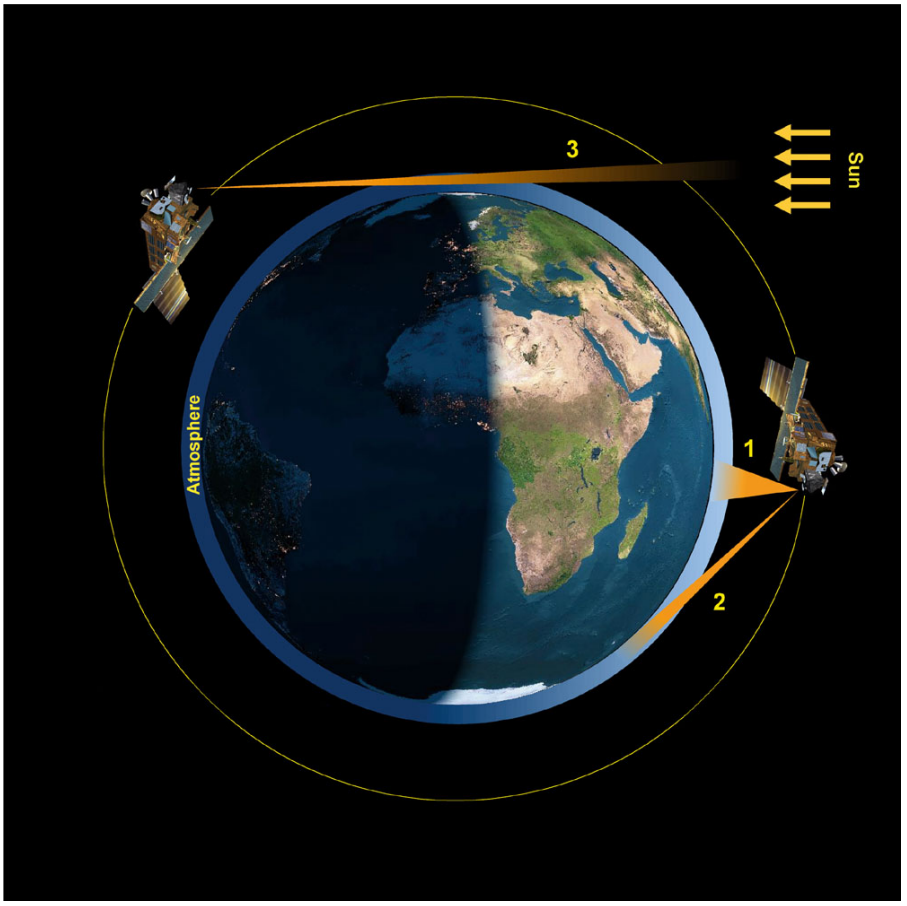

FIGURE 5.1: Observation modes for scientific measurements: 1 = Nadir, 2 = Limb, 3 = Occultation. (Courtesy ESA)

et al., 2002]. At the moment, there are several instruments in the thermal IR that provide detailed ozone measurements with global coverage. The Atmospheric Infrared Sounder (AIRS) [Aumann et al., 2003], the Cross-track Infrared Sounder (CrIS) [Bloom, 2001] and the Infrared Atmospheric Sounding Interferometer (IASI) [Clerbaux et al., 2009]. IASI is the main instrument for this work and it is presented in detail in Sect. 5.3; the Tropospheric Sounder Interferometer (TES) instrument will be also presented briefly, as it is used only for comparison purposes.

5.3 IASI on−board Metop

The Metop platform is a series of polar orbiting meteorological satellites, operated by the EUropean Organization for the exploitation of METeorological SATellites (EUMETSAT). Metop−A, −B and −C were launched in October 2006, September 2012, and November 2018, respectively. The platforms operate in a co-planar orbit.

5.3.1 Metop payload

The Metop satellites carry on-board around eight instruments, for Earth observation, along with a series of instrumentation for communications and support services, as shown in fig. 5.2. The instruments provide detailed observations of the atmosphere, oceans and land around the globe.

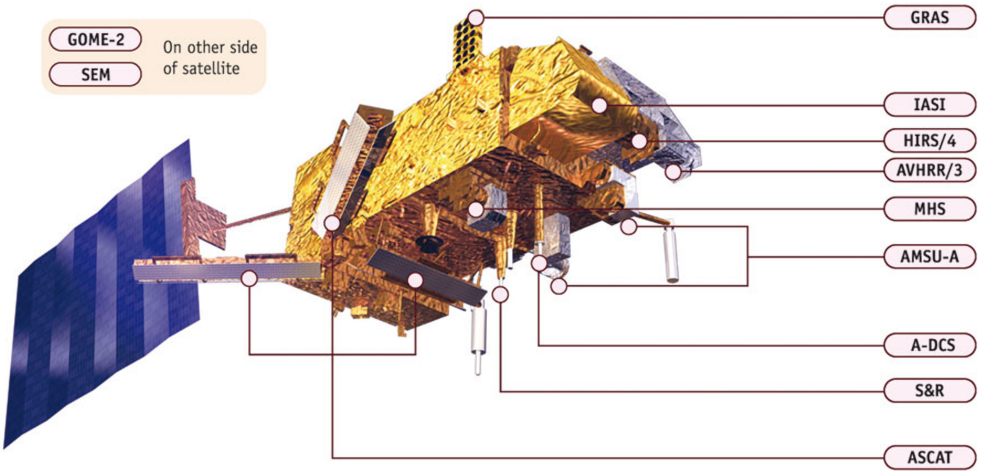

FIGURE 5.2: Schematic view of Metop and its payload accommodation. (Courtesy EUMETSAT)

The satellites have an inclination, measured relatively to the equatorial plane of Earth, of around 98.8° and fly at an altitude of approximately 817 km. Their orbit is elliptic, polar and sun-synchronous, with a period of around 101 minutes, which leads to around 14 orbits per day. Each satellite crosses the Equator two times per orbit, at 21:30 local time for the ascending node (Metop−A, from SH to NH) and at 9:30 local time for the descending node (Metop−A, from NH to SH). Since Metop−B is 180° in phase with Metop−A, which results to a 40-50 min difference, the crossing times and nodes will be the other way around. An example of the two satellites respective positions is given in fig. 5.3.

5.3.2 The IASI instrument

The Infrared Atmospheric Sounding Interferometer (IASI) was developed by the Centre National d'Études Spatiales (CNES) in collaboration with EUMETSAT. IASI is a top-of-the-art instrument designed to provide data of high radiometric quality to improve numerical weather predictions [Hilton et al., 2012]. In addition to the weather-related

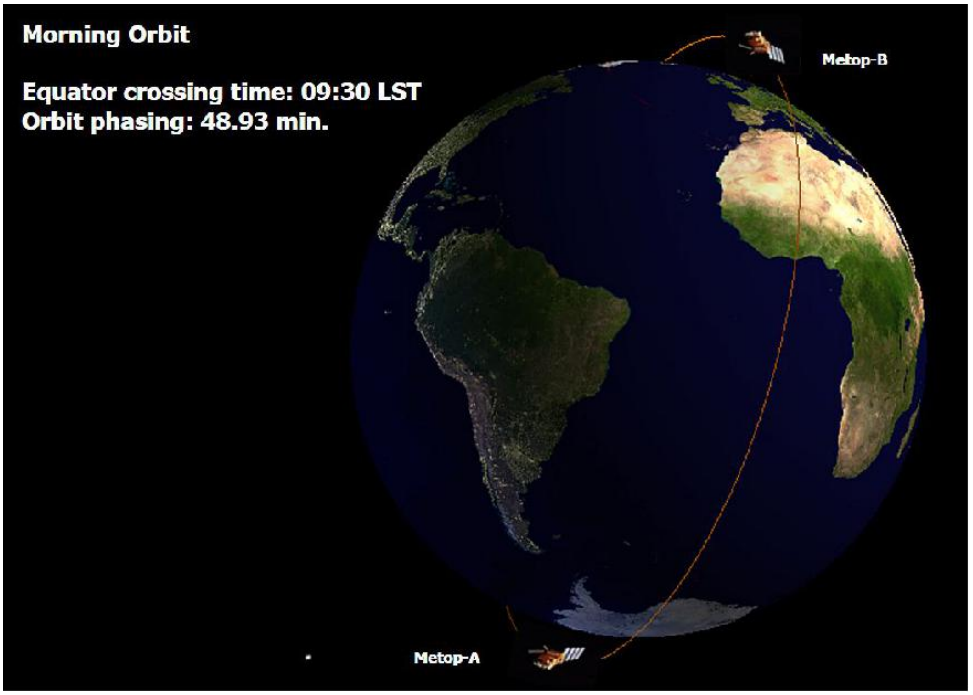

FIGURE 5.3: Metop-A and -B in orbit. (Courtesy EUMETSAT)

information, IASI also provides high-quality measurements for atmospheric composition monitoring. The instrument has already proved its capabilities by mesuring not only global distributions and time series of some strong absorbers, such as CO, CO_2, CH_4, O_3 and H_2O, but also short-lived species such as SO_2, NH_3 and others (e.g. Clarisse et al. [2011]; Clerbaux et al. [2009]; Coheur et al. [2009]; Crevoisier et al. [2009]; Karagulian et al. [2010]; Razavi et al. [2011] and references therein).

The IASI instrument observes and measures the spectrum of thermal infrared (TIR) radiation emitted by the Earth and the atmosphere twice per day, over a swath around 2200 km wide. Its spectral range covers the regions from 2760 cm^{-1} (3.62 µm) to 645 cm^{-1} (15.5 µm), in three separate spectral bands. IASI uses nadir geometry, complemented by off-nadir measurements up to 48.3° on both sides of the satellite track, as shown in fig. 5.4. The scanning is accomplished in 30 measurement positions, 15 on each side of the track, one every 216 ms (sampling interval). Each full scan cycle has a period of 8 s. The instantaneous field of view (IFOV) is composed of 2 ×2 elliptical pixels, each pixel having a 12 km diameter footprint on the ground at nadir. After each scan cycle, calibration is performed (cold-space and black-body view). The instrument is stable and accurate; its radiometric noise is between 0.25 and 0.3 K around 1000 cm^{-1} at a reference temperature of 280 K.

IASI has a spectral sampling of 0.25 cm^{-1}. In terms of spectral resolution, apodization is performed to provide users with a wavenumber-independent instrument spectral response

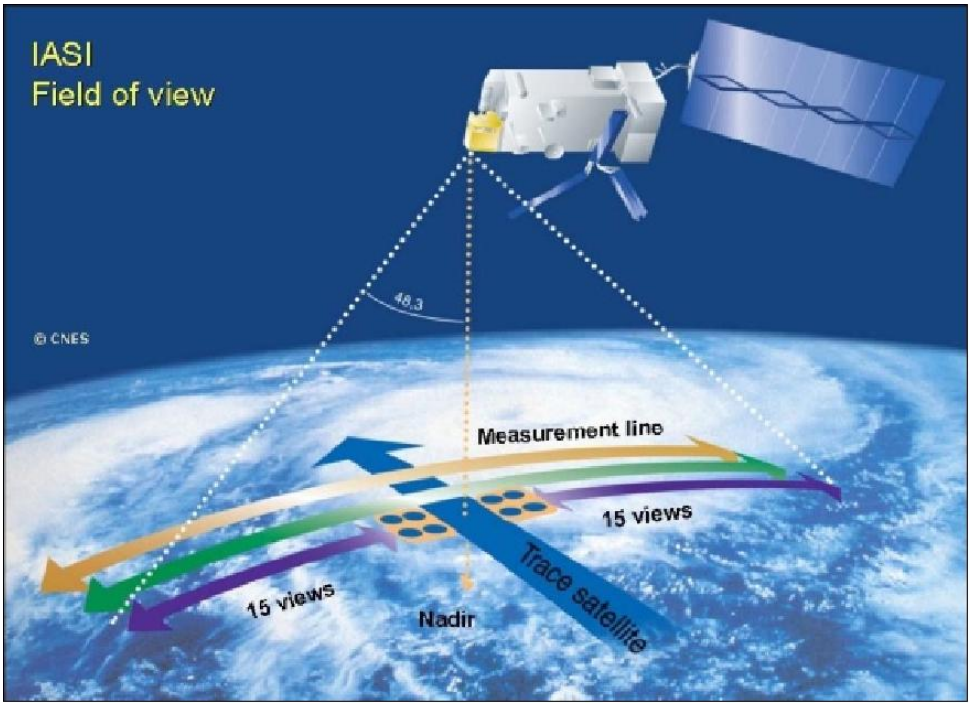

FIGURE 5.4: Observations principle of IASI. (Courtesy CNES)

function. The apodization degrades slightly the spectral resolution to $0.5\,\mathrm{cm}^{-1}$ over the entire spectral range.

As IASI is a Michelson interferometer, it does not measure a spectrum directly, but an interferogram. However, it holds an on-board processing system that performs the following functions, as soon as a measurement takes place: spike elimination, non-linearity corrections, filtering and resampling, Fourier Transform, phase correction, scan mirror reflectivity correction, radiometric calibration, and optimal bit encoding. This procedure helps to compress the volume of data and accelerate the instrument source data rate from 45 Mbits/s to only 1.5 Mbits/s. The Level 0 data are then created. The on-board processing is shown as in infographic in fig. 5.5, on the left side.

The right side of fig. 5.5 represents the ground processing of the IASI measurements. During the ground processing the spectra are calibrated spectrally, the measurements are geolocated, resampled and apodized. Level 1C data are used to retrieve Level 2 ozone profiles and columns. Level 2 ground processing is the phase of deriving geophysical parameters from the radiance measurements. The following complete the operational data processing chain at EUMETSAT, along with each processed spectrum: temperature and humidity profiles, surface temperature, surface emissivity, cloud coverage (in per cent of FOV), cloud top temperature, cloud top pressure, cloud phase, but also total and partial columns (and profiles) of traces gases, and quality flags. The Level 1C and the aforementioned Level 2 are disseminated to meteorological agencies and other institutions, where further processing or scientific studies are then conducted. Note that this work

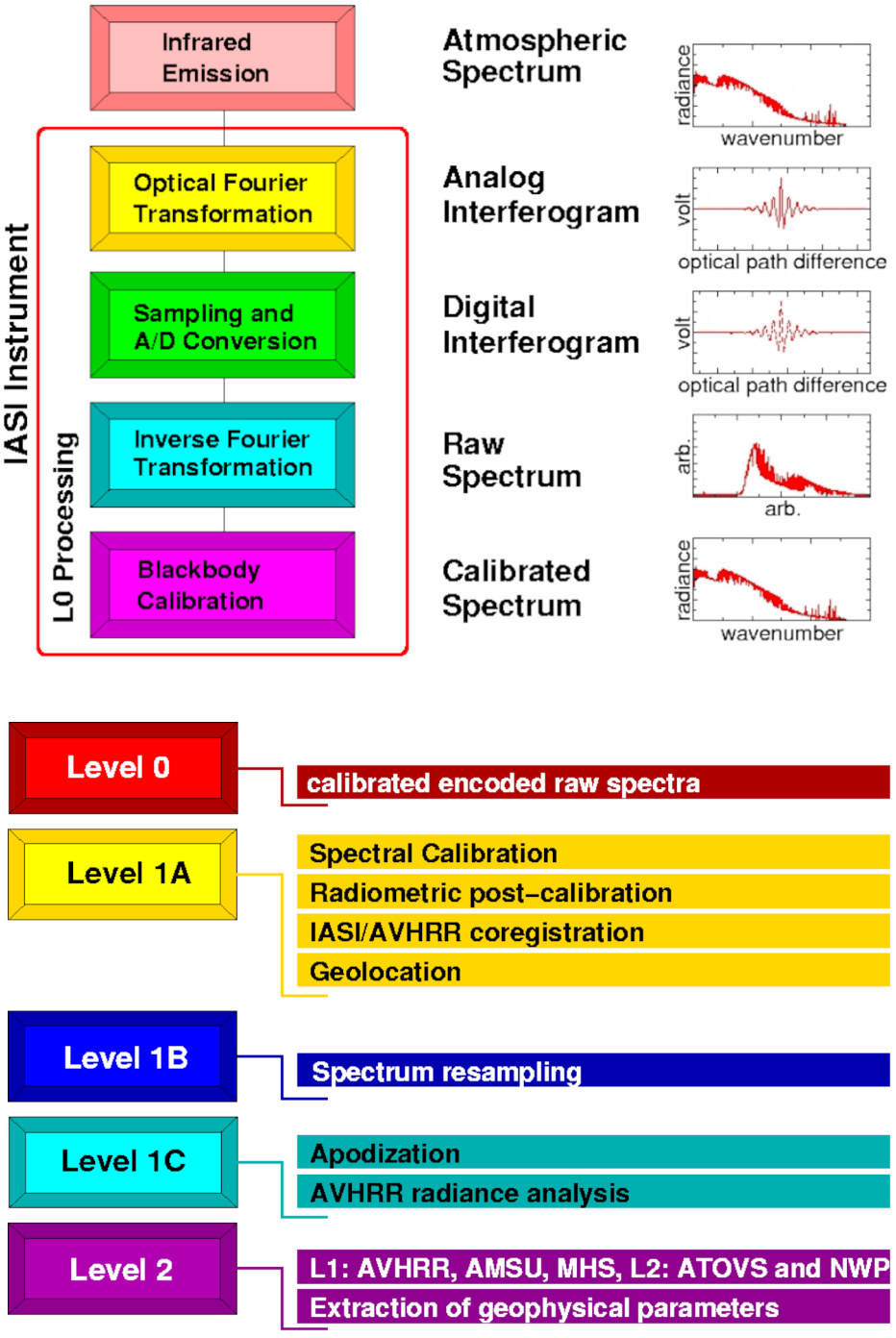

FIGURE 5.5: The IASI digital processing system concept. (Top) On-board processing chain and (bottom) ground processing chain. (Courtesy EUMETSAT)

does not use the operational L2 ozone product from EUMETSAT, but an independent product retrieved at ULB (see Ch. 6).

5.4 TES on−board Aura

This instrument will not be covered in the same detail as IASI, as it will only be used for comparison in the frame of this work. Its technical characteristics will be presented in order for the reader to understand the differences with IASI further on.

The Aura satellite is one of the satellites that take part in the "A−Train" satellite constellation, all of which fly in close proximity. The close proximity formation was decided in order to get the maximum possible information from consequtive overpasses over the same place. Aura flies about 15 minutes behind Aqua satellite. The satellite was launched in July 2004.

5.4.1 Aura characteristics

The Aura satellite carries on-board four instruments, all of which work in synergistic mode; the Microwave Limb Sounder (MLS), the Ozone Monitoring Instrument (OMI), the High Resolution Dynamics Limb Sounder (HIRDLS) and the Tropospheric Emission Spectrometer (TES). The satellite and its instruments are shown in fig. 5.6.

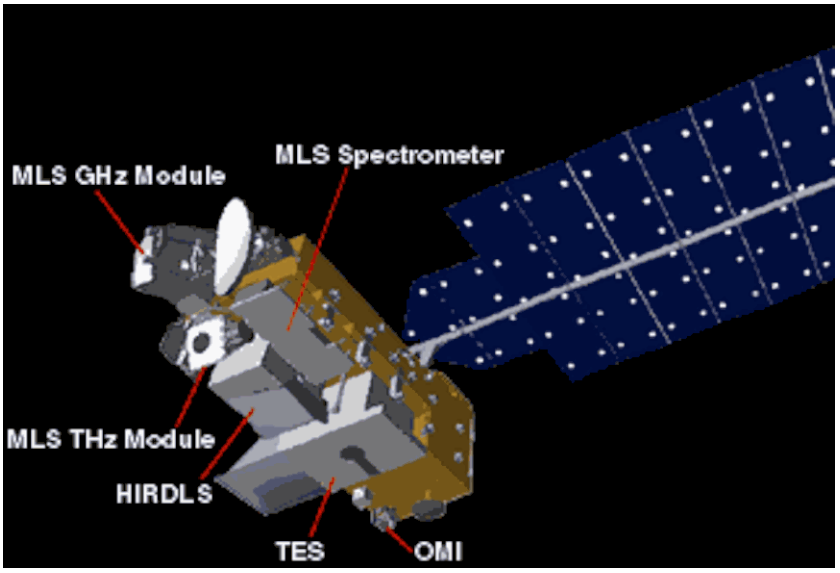

FIGURE 5.6: The Aura satellite and its instruments. (Courtesy NASA)

Aura is flying in a near polar, sun-synchronous orbit with a period of approximately 100 minutes and an inclination of 98.2°. Its orbit is located at around 705 km above Earth. It has a repeat cycle (passing over the exact same places) of 16 days, and performs 233 revolutions per cycle. The ascending node takes place always during daylight and crosses

the equator at 13:45 ±15 minutes local time. The Aura satellite was designed for a six-year lifetime; it is still operating, however some of its instruments ceased function, such as TES, which operation stopped on 13 Feb. 2018.

5.4.2 The TES instrument

The Tropospheric Emission Spectrometer (TES) is an infrared Fourier−transform spectrometer, that allows global mapping of several species in the atmosphere. However its primary objective is the detailed measurements of tropospheric ozone and of the physical−chemical factors that control its distribution [Beer et al., 2001]. TES operates in the thermal IR, covering the spectral range from 3050 to 650 cm^{-1} (3.3−15.4 µm), at a spectral resolution of 0.1 cm^{-1} or 0.025 cm^{-1} [Beer, 2006]. The spectral resolution changes with the viewing mode of the instrument; it will be explained further below. The instrument has a signal-to-noise ratio of 600:1, and separates the spectral range in four bands. Each band is separated further in 250 cm^{-1} sub-bands, using interchangeable filters. This allows the instrument to observe simultaneously 16 altitudes in the troposphere and lower stratosphere.

TES has two operating modes. The *Global surveys* (GS) and the *Special observations* (SO). For the GSs the observation procedure is the following: a view of cold space followed by a view of the internal 340 K black body (for calibration), followed by two 0.1 cm^{-1} resolution nadir scans and three 0.025 cm^{-1} resolution limb scans. The nadir and limb views are shown in fig. 5.7. The limb mode of the instrument was used in the early years of its operation; it was stopped in order to extend the lifetime of the instrument. Each sequence of observations needs 82 s and is repeated continuously for 16 orbits. After the 16-orbit cycle, two orbits of calibration are performed. For the SO, such as validation campaigns, volcano monitoring and others, there are 9 orbits available after each GS. If no SO are needed, the instruments rests, to extend its life and avoid destroying critical mechanical components [Beer, 2006]. The SOs include three modes: stare, transect and step-and-stare. Further information are available in https://tes.jpl.nasa.gov/instrument/specialobservations/.

When the instrument operates in the nadir view, its pixel footprint covers an area of approximately 5.3 km ×8.3 km, while during the limb view, the pixel size changes to 37 km ×23 km, and a vertical resolution of 2.3 km. This work uses only the TES nadir measurements.

A summary of the different characteristics of IASI and TES is given in Table 5.1.

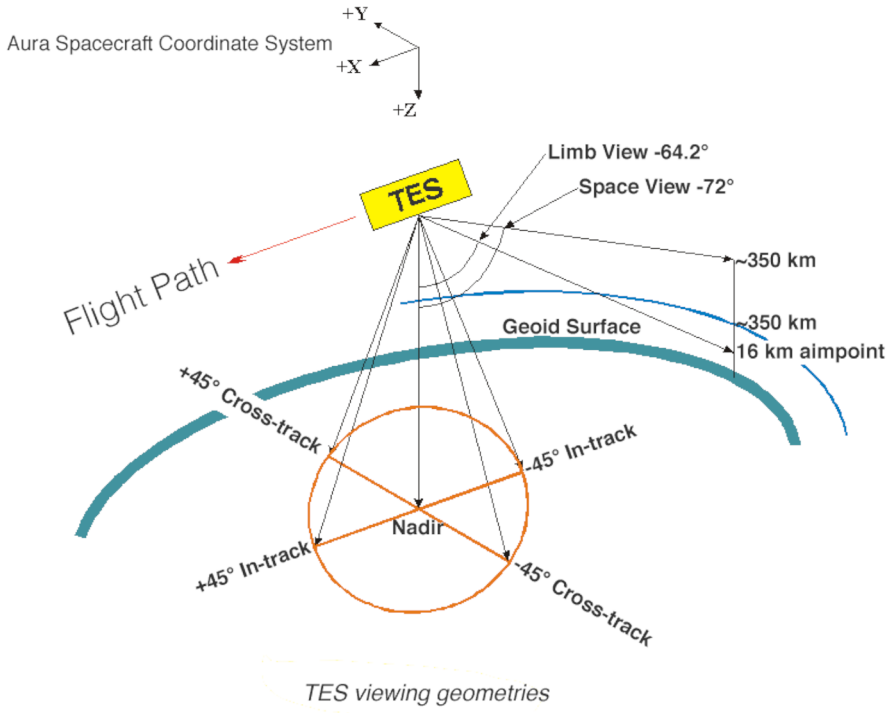

FIGURE 5.7: TES observation geometry. (Courtesy NASA/JPL)

TABLE 5.1: Summary of IASI and TES characteristics

	IASI	TES
Type	IR Michelson Interferometer	IR Fourier Transform Spectrometer
Resolution	$4 \times 12\,\mathrm{km}^2$	$0.5 \times 5\,\mathrm{km}^2$
Sampling interval	216 ms	4 s
Field of View	$48 \times 48\,\mathrm{km}^2$	$5.3 \times 8.5\,\mathrm{km}^2$
Global coverage	twice/day (14 orbits)	>1 day (15 orbits)
Orbit period	101 min	100 min
Inclination	98.8°	98.21°
Altitude	817 km	705 km
Equator crossing time	9:30 / 21:30	$13{:}45 \pm 15$ min
Spectral range	645 - 2760 cm^{-1}	650 - 3050 cm^{-1}
Spectral sampling	0.25 cm^{-1}	0.1 cm^{-1}
NEΔT [a]	0.2 - 5 K @ 280 K	<1 - 2 K @340 K [b]
Data rate	1.5 Mbit/s	4.5 Mbit/s

[a] Depending on spectral region.
[b] with multiple sub-ranges of 200-300 cm^{-1}

Chapter 6

Ozone retrievals from IASI

As it was presented in Chapter 5, as soon as a measurement is taken by IASI, Fourier-transformation and calibration, as well as other operations, are applied to the measurement, before it is transmitted to a ground station. In Chapter 3 we also presented the transfer of radiation through the atmosphere, its absorption and re-emission from atmospheric constituents and the surface of the Earth. In thermal IR radiation, the instrument detects the radiation emitted from the surface of the Earth, after passing through the atmosphere.

The equation that describes the radiative transfer in the IR region is eq. 3.42. If the surface temperature, and the atmospheric thermodynamic properties and composition are known, and making use of Planck's law (eq. 3.9), it is possible to determine the radiance at the top of the atmosphere by applying eq. 3.46 on each layer. This is called the forward problem.

In satellite remote sensing however, the inverse problem is the one to be solved. The instrument (IASI in our case), measures the radiance at the top of the atmosphere. The inverse problem relies in retrieving from the measured radiance, the surface temperature, air temperature, concentration of atmospheric species and others. Given the fact that the concentration profiles of the different species are related non-linearly with the spectral radiances, the retrieval is complex and requires certain statistical and numerical assumptions to be made.

In this work, the Fast Optimal Retrieval on Layers for IASI (FORLI) is used. FORLI is a radiative transfer and retrieval software developed at the Université Libre de Bruxelles (ULB) in collaboration with the Laboratoire Atmosphères, Milieux, Observations Spatiales (LATMOS), to serve the atmospheric composition objectives of the IASI mission.

FORLI is currently running at ULB in near-real time, providing total columns and vertical profiles of O_3, CO and HNO_3. The retrieval algorithm is based on the maximum *a posteriori* solution as described in Rodgers [2000], also known as the Optimal Estimation Method (OEM). A detailed description of FORLI for all species, methods, input parameters and approximations can be found in Hurtmans et al. [2012]. Here, only the method and product concerning O_3 will be discussed.

6.1 FORLI software for retrievals

FORLI is a near-real-time algorithm [Hurtmans et al., 2012], which means that it provides the desired Level 2 products in near-real time to the actual observations. In order to achieve this, FORLI uses look-up tables and analytical derivatives, which will be explained below.

6.1.1 Look-up Tables

To speed up the radiative transfer calculation, FORLI is assisted by Look-Up-Tables (LUTs). The LUTs include pre-calculated absorption cross-sections, calculated line-by-line, at various temperatures and pressures. The LUTs for O_3 and H_2O were computed using the HIgh resolution TRANsmission (HITRAN) spectroscopic database, the version of 2012 [Rothman et al., 2013], and cover the spectral range of $960-1105\,cm^{-1}$, at $0.0025\,cm^{-1}$ spectral sampling. Apart from the single spectral lines and absorption cross-sections, attention is also given to the "absorption continua" of H_2O, CO_2, O_2 and N_2, for which the semi-empirical representation of Clough et al. [2005] is used.

We should note here that this version of LUTs is different from the one introduced in Hurtmans et al. [2012], which used the HITRAN 2004 database, as they include 15 extra transitions for O_3 in the very weak hot band $\nu_1 + 2\nu_2 + \nu_3 - 2\nu_2 - \nu_3$(see Flaud et al. [1990]) [Boynard et al., 2016].

6.1.2 Input parameters

Surface temperature and pressure on the ground, but also air temperature and pressure at different altitudes, are critical for the calculation of radiative transfer. The temperature profile used in FORLI is provided by the dedicated Product Processing Facility (PPF) at EUMETSAT, including the inversion of the IASI spectra and the other instruments

on board Metop (e.g., AVHRR/3, AMSU-A, MHS). The retrieved products, i.e. the temperature and humidity profiles, are given on a pressure grid [Hurtmans et al., 2012]. Both profiles are disseminated by the operational processor through EUMETCast, in near-real time [Schlüssel et al., 2005]. Furthermore, ground temperature is also that of the operational processor, but they are adjusted further in FORLI to improve the spectral fits in the spectral region of interest (1025-1075 cm^{-1} for O_3). A constant vertical profile for CO_2 is also accounted for, since it is the most significant species interfering in the selected retrieval range.

Cloud coverage has also to be dealt with, as it affects the radiance significantly. Through various techniques, cloud characterization is derived from the IASI measurements, and tested against other sources, such as the NWP forecasts [August et al., 2012]. FORLI processes only scenes with a cloud coverage below 13%, while the corresponding impact is accounted as an error.

Another critical input parameter, in order to describe the surface, is the surface emissivity, $\epsilon_{\tilde{\nu}}$, wavenumber dependent (see Sect. 3.4.3). Currently FORLI uses a climatology introduced by Zhou et al. [2011], which is based on IASI data, complemented by the MODIS climatology of Wan [2008].

Finally, the topography, which is included in the forward model of FORLI, is based on the GTOPO30 global digital elevation model, available online.

6.2 The Optimal Estimation Method

The general radiative transfer equation (eq. 3.44) can be solved with respect to the measurement y, expressed as the vector of measured radiances [Rodgers, 2000]:

$$y = F(x, b) + \eta, \tag{6.1}$$

where y, the measured vector of radiances at the TOA, is used to retrieve x; F is the forward radiative transfer function; x is the state vector of atmospheric parameters one wishes to retrieve, e.g. the trace gas concentration in different altitudes; b includes all the fixed parameters that characterize the measurement, e.g. temperature, pressure, instrumental parameters, which are taken as known and will not be retrieved; and η represents the error of the forward model and the measurement, detector noise or random error.

6.2.1 General formulation

Given that IASI measures radiances, y, eq. 6.1 must be solved with respect to x. To determine x, FORLI uses the Optimal Estimation Method (OEM) [Rodgers, 2000]. The OEM is based on the concept of finding the optimal solution of a state vector $\hat{x}$, which will be an estimation of the true state. To perform the estimation, the method starts from some relevant *a priori* information (a specific prior knowledge of the atmospheric state), which consists of a mean state x_α and an allocated variance-covariance matrix, S_α. This *a priori* state, x_α, is then combined with the measured radiances, y, all weighted by the covariance matrix of x_α, $S_\alpha(n \times n)$. In the covariance matrix, n states the number of different layers that characterize the *a priori* state. For FORLI-O_3 the number of distinct layers, $n = 41$, with a 1 km-thick layers from the ground to 39 km and a layer from 40 km to the top of the atmosphere (TOA). The covariance matrix is generated by the set of data used to construct x_α, is independent of the measurements and is such as to represent the natural variability of the gas under study. The covariance matrix is defined as:

$$S_\alpha(i,j) = E[(x_i - x_{\alpha,i})^T (x_j - x_{\alpha,j})], \tag{6.2}$$

where E is the expected or average value operator.

The other parameters of FORLI for the O_3 retrievals are summarized in Table 6.1. The spectral range used for the retrieval is mostly dominated by O_3, with a few water vapor and methanol lines, which have little impact, as the high spectral resolution allows the distinction between the different species and furthermore, they are accounted for in the LUTs. For FORLI-O_3, the mean profile and the *a priori* covariance matrix S_α have been constructed from the McPeters/Labow/Logan climatology of ozone profiles [McPeters et al., 2007], which combines long-term satellite limb measurements and measurements from ozonesondes. Figure 6.1 shows the *a priori* profile and its variance (the diagonal elements of the S_α matrix), as used in FORLI. This profile is fixed and used for all observations around the globe. As it can be seen, the profile increases just below 10 km, and reaches its maximum in the middle stratosphere. S_α, associated with x_α, represents the variability around the *a priori* profile that is allowed during the inversion. The variability is calculated as the square root of the diagonal of the O_3 *a priori* covariance matrix and is highest in the upper troposphere - lower stratosphere (UTLS) region (60%). Finally, S_η is the approximate average noise in the retrieval spectral range, with an approximate value of 2×10^{-8} W cm^{-2} sr^{-1} cm, close to the IASI instrumental noise, implying only a supposed small impact of the forward model errors in this spectral range.

TABLE 6.1: Input parameters for O_3 *a priori* state in FORLI.

	FORLI-O_3
LUTs spectral range	$960-1105\,\mathrm{cm}^{-1}$
Retrieval spectral range	$1025-1075\,\mathrm{cm}^{-1}$
Spectral sampling	$0.25\,\mathrm{cm}^{-1}$
x_α, S_α	McPeters/Labow/Logan
S_η	$2 \times 10^{-8}\,\mathrm{W\,cm^{-2}\,cm\,sr^{-1}}$
n	41 distinct layers per 1 km

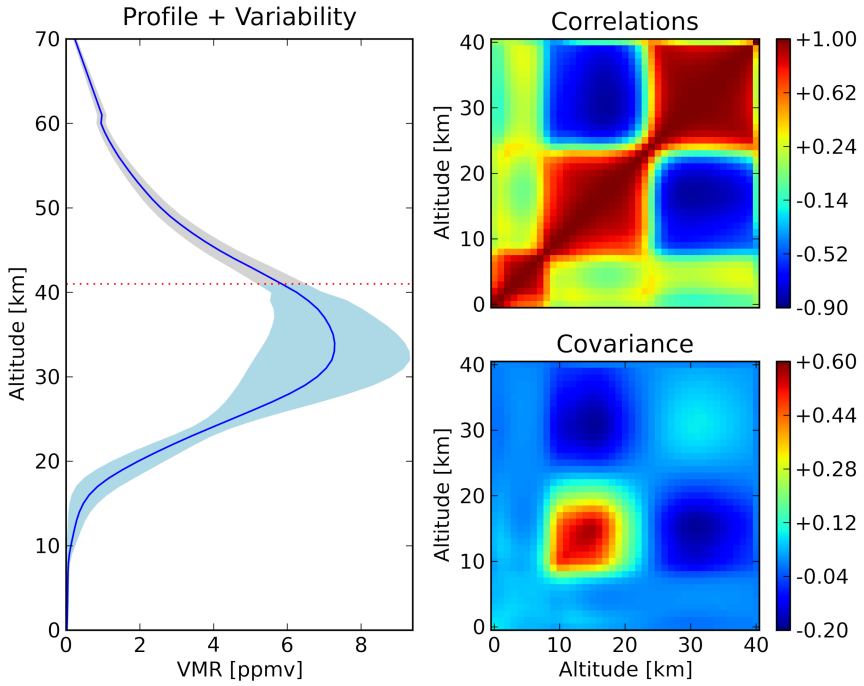

FIGURE 6.1: Left: Global O_3 *a priori* profile (blue line) and its variability (shaded blue). Right: Correlation (top) and global O_3 *a priori* covariance matrix (bottom). (Taken from Hurtmans et al. [2012])

6.2.2 Linearization

Generally, for a linear problem the forward model is able to put the solution in the form $y = F(x) + \eta = Kx + \eta$, if the *a priori* is Gaussian. In the OEM, the retrieved state solution is given by:

$$\hat{x} = x_\alpha + (K^T {S_\eta}^{-1} K + {S_\alpha}^{-1})^{-1} K^T {S_\eta}^{-1} (y - K x_\alpha), \tag{6.3}$$

where $\hat{x}$ is the best estimation of x, and is a linear function of x_α and y; K is the Jacobian of the forward model function, has the form of a matrix and represents the sensitivity of the measurement to the model parameters, e.g. the O_3 concentration in each layer.

Since the O_3 retrieval, in our situation, is moderately non-linear, it can be treated as linear, in order to find the best estimation of $\hat{x}$ and its error. This is accomplished by repeating eq. 6.3 iteratively, using a Gauss-Newton method, until convergence is achieved, as follows:

$$x_{i+1} = x_\alpha + ({K_i}^T {S_\eta}^{-1} K_i + {S_\alpha}^{-1})^{-1} {K_i}^T {S_\eta}^{-1} [y - F(x_i) + K(x_j - x_\alpha)]. \tag{6.4}$$

In simple words, the Gauss-Newton method linearizes the non-linear problem, at each iteration, based on the previous iteration. The convergence is achieved, when the difference of $x_{i+1} - x_i$ meets a minimum value (imposed by the user). After convergence, the fitted covariance matrix, $\hat{S}$, can be determined in the same manner as $\hat{x}$ and it represents the total statistical error after the retrieval.

6.2.3 Averaging kernels and degrees of freedom

In problems where the solution is the best estimate of a state, such as the inverse method described previously, the result should also be characterized by the minimum associated error. In this case, eq. 6.3 can be written as:

$$\hat{x} - x_\alpha = (K^T {S_\eta}^{-1} K + {S_\alpha}^{-1})^{-1} K^T {S_\eta}^{-1} (y - K x_\alpha) = G(y - k x_\alpha), \tag{6.5}$$

where G is the gain matrix, or contribution function matrix, defined by:

$$G = (K^T {S_\eta}^{-1} K + {S_\alpha}^{-1})^{-1} K^T {S_\eta}^{-1} \tag{6.6}$$

Introducing the averaging kernel (AVK) matrix:

$$A = GK, \tag{6.7}$$

eq. 6.3 can be rewritten as:

$$\hat{x} = Ax + (I - A)x_\alpha + G\eta, \tag{6.8}$$

where I is the identity matrix. The AVK represents the sensitivity of the retrieved state to the true state. It expresses the fraction that the retrieved value at a given altitude comes from the data, rather than the *a priori*, with additional error terms accounting for

the *a priori* contribution and the spectral noise. The AVK is an $n \times n$ matrix; its highest value (peak) identifies the altitude of maximum sensitivity.

The degrees of freedom for signal (DOFS) is the number of independent pieces of information in a retrieval, related to the signal of interest. It is described as:

$$DOFS = E[(x - x_\alpha)^T S_\alpha^{-1}(x - x_\alpha)], \tag{6.9}$$

and is well defined once the various components of the state vector have been chosen. It is the number of independent quantities in a particular retrieval from an observed spectrum. According to Rodgers [2000], the total DOFS is the trace of the AVKs matrix.

6.3 The FORLI−O_3 product

Through the years of the IASI operation and the FORLI processing chain, there have been many studies towards the validation of the FORLI−O_3 product. Starting with Boynard et al. [2009] and the first measurements of IASI against UV satellites and ground-based observations, along with ozonesonde data. More recently, and as IASI measurements were widely used, there have been a series of papers for the FORLI−O_3 validation, either in terms of columnar amounts (total/tropospheric) or vertical profiles, e.g. Antón et al. [2011]; Dufour et al. [2012]; Gazeaux et al. [2013]; Oetjen et al. [2014]; Pommier et al. [2012]; Safieddine et al. [2014]; Scannell et al. [2012]. In general, these studies have reported that the FORLI-O_3 product is positively biased against UV instruments of 3 to 6% for the total column on a global scale, and specifically around 10−15% for the 10−25 km altitudes. The DOFS vary over the globe from 2 to 4, depending on the latitude [Hurtmans et al., 2012]. The lowest sensitivity is found over polar regions, especially during night, which constrain the DOFS to around 2 (mostly stratospheric signal), while the largest is found over the Tropics. In general the altitude regions that provide information are distinguished as follows: troposphere (< 300 hPa), upper troposphere-lower stratosphere (UTLS, 300-150 hPa), lower to middle stratosphere (150-25 hPa) and middle to upper stratosphere (> 25 hPa). At this point it is worth mentioning that these studies refer to the FORLI-O_3 product before 2016. More information will be given below.

6.3.1 Errors in FORLI−O_3

The error associated with the ozone product of FORLI is estimated statistically, with contributions from the limited vertical sensitivity, measurement noise, uncertainty in

fitted or fixed parameters [Hurtmans et al., 2012]. Boynard et al. [2009] showed that uncertainties on the temperature profile can contribute up to 10% on the total error. Furthermore, the total error on the retrieved O_3 profile depends on the latitude and season, amongst others. In terms of partial columns, the error can vary between 10 and 30% in the troposphere and upper troposphere - lower stratosphere (UTLS) and only about 5% in the stratosphere. Finally, large relative errors are found in the tropics, related to lower O_3 amounts and large relative humidity, and high latitudes, due to the low radiances, hence low signal-to-noise ratios. [Wespes et al., 2016].

6.3.2 Biases in FORLI−O_3

In 2016, Boynard et al. [2016] performed an overall validation of O_3 for both IASI−A (2008−2014) and −B (2013−2014) instruments, retrieved with FORLI (v20140922), against data from the Global Ozone Monitoring Experiment−2 (GOME-2), Brewer−Dobson and UV−visible SAOZ (Système d'Analyse par Observation Zénithale) instruments and ozonesondes. For the total columns, between IASI and GOME−2, the authors have shown that FORLI-O_3 presents a positive bias of 5.5 to 7.1% depending on latitude and season. The highest bias is in the SH Polar region, and can reach up to 30% during the austral summer and fall. When compared to the Brewer−Dobson network, FORLI-O_3 was found biased around 5 ± 1 % in the NH and 6 ± 1 % in the SH, with differences over 20% in the Antarctic. The picture is similar when compared to the SAOZ data.

Regarding the O_3 vertical profile, which was compared against ozonesondes around the globe, the authors reported that FORLI-O_3 generally underestimates O_3 in the troposphere, up to 15% in the mid−latitudes, and overestimates it in the stratosphere, with up to 35% in the tropics. The largest biases are found in the UTLS altitudes, especially around the tropics.

The above validation results concern mostly IASI−A, with the longest observation record. IASI−B provides slightly lower values, with a global difference between the two instruments at around ± 2% for the total columns. The larger differences between IASI−A and −B are found again in the Antarctic region, but they remain below 10%. In general, the differences between IASI−A and −B on the vertical profiles vary between 5 and 20% and are larger in the tropopause region, especially in the Antarctic. We should remind here that the two instruments do not measure at the exact same time and location (40-50 min crossing time difference, see Ch. 5), and therefore small relative differences are expected from the diurnal variation of the ozone concentration and the surface temperature.

6.3.3 Updated FORLI−O_3 product

As already mentioned in Sections 1 and 2 of this chapter, the operational version of FORLI for ozone has been updated, since the one described in Hurtmans et al. [2012]. The above validation and comparison results all refer to retrievals which were performed while the data were processed with version FORLI-O3 v20140922. Since 2016 and after reprocessing the ozone records for both IASI instruments, the available data are based on the latest version described in the beginning of this chapter (FORLI-O3 v20151001).

A first validation of the latest version of the product was performed by Boynard et al. [2016], who reported much smaller biases than those given above. The two versions of FORLI−O_3 present a relative difference of 3−6%, which brings the latest version (FORLI-O3 v20151001) closer to the total O_3 columns of the UV instruments. In a more recent study, Boynard et al. [2018] compared the FORLI-O_3 v20151001 for both IASI−A and −B against GOME−2, Dobson, Brewer and SAOZ measurements, and reported an excellent agreement for the total O_3 columns, with global mean differences varying between 0.1 and 2%, depending on the instruments. The comparison against smoothed ozonesonde partial O_3 columns revealed a maximum standard deviation of 20 to 40% in the 300-150 hPa (UTLS) altitudes due to ozone variability and *a priori* uncertainty. In terms of O_3 profiles, the FORLI-O_3 product overestimates the O_3 abundance in the stratosphere, up to 20% for the 150-25 hPa altitude range, and underestimates the O_3 abundance in the troposphere, within 10% for the mid-latitudes and around 18% for the tropics. The worst agreement with the ozonesondes and the UV-VIS total O_3 columns is found again in the southern polar latitudes.

6.4 The TES O_3 product

The TES ozone product is presented briefly. The information will be useful for comparison purposes, later in this work. The ozone product from TES is obtained by similar calculations as for IASI−FORLI.

6.4.1 Retrieval algorithm and forward model

The retrieval algorithm and the forward model used for TES is a line-by-line radiative transfer model (LBL−RTM), which has been extensively described in Bowman et al. [2006] and Clough et al. [2006]. The retrieval is reported on a fixed pressure grid of 66 levels, covering from the ground up to 1 hPa. The temperature and water vapor profiles

used in the process, are obtained in the first step of the retrieval. Cloud fraction and other scene characteristics are also obtained during the retrieval [Kulawik et al., 2006].

The forward model, described in Clough et al. [2006], makes use of the Optimal Estimation Method [Rodgers, 2000]. The O_3 *a priori* profile and covariance matrix are taken from climatology based on results from the Model for OZone And Related chemical Tracers version 3 (MOZART 3) [Osterman et al., 2008] and calculated specifically by the Aura instrument science teams. This type of climatology is reported on spatial bins of 10° wide in latitude and 30° wide in longitude. The retrieval range covers the spectrum from 985 to 1080 cm^{-1}, with a resolution of 0.1 cm^{-1}-apodized [Worden et al., 2011]. The spectral line parameters are obtained from the HITRAN 2004 database and the following updates for the same version [Worden et al., 2011]. In general, the complete ozone profile retrieved has 3 to 4 DOFS, and around $1-2$ for the tropospheric part [Osterman et al., 2008].

6.4.2 Errors and biases

The TES O_3 product has been extensively validated against ozonesondes, ground-based and space-born instruments, throughout the years. Regarding the tropospheric profile, the retrieval error is around 20% and includes radiance errors and cross-state errors due to simultaneous retrieval of temperature and water vapor, but is dominated by the smoothing error [Bowman et al., 2006; Worden et al., 2011]. The reported biases include around 5% bias due to known biases in the HITRAN 2004 spectroscopic database [Worden et al., 2011] and the line parameters, and around 15% positive bias compared to ozonesondes for the tropospheric column [Nassar et al., 2008].

Chapter 7

Ozone longwave radiative effect - Method development

In Chapter 3, we explained the radiation transfer in the atmosphere and introduced the concept of radiative forcing. In Chapter 4, we specified the radiative forcing with respect to ozone. We also came across the problems posed on representing accurately ozone regarding climate, and the resulting discrepancies in chemistry-climate models.

In an effort to make the estimation of the climate effect of ozone independent of the climate models assumptions and errors, and all the difficulties they pose, Worden et al. [2011] introduced the concept of the instantaneous radiative kernel and longwave radiative effect to derive the climate effect of ozone directly from satellite measurements in the IR spectral band. The work of Worden et al. [2011] was the starting point in this thesis for developing the *Direct Integration Method* to estimate the longwave radiative effect of ozone from IASI measurements, which is explained below.

7.1 IASI instantaneous radiative kernels

As already explained, the radiative budget of the atmosphere and its changes through time are crucial indicators for climate studies. For the outgoing longwave radiation (OLR) measured by satellites, with respect to the top of the atmosphere, the flux is given by

eq. 3.7 and 3.8, and can be written in the form:

$$F_{\mathrm{TOA}} = \int_{\tilde{\nu}_1}^{\tilde{\nu}_2} \int_{0}^{2\pi} \int_{0}^{\pi/2} L_{\mathrm{TOA}}(\tilde{\nu}, \theta, \phi) \cos\theta \sin\theta d\theta d\phi d\tilde{\nu} = 2\pi \int_{\tilde{\nu}_1}^{\tilde{\nu}_2} \int_{0}^{\pi/2} L_{\mathrm{TOA}}(\tilde{\nu}, \theta) \cos\theta \sin\theta d\theta d\tilde{\nu} \tag{7.1}$$

where $L_{\mathrm{TOA}}(\tilde{\nu}, \theta, \phi)$ is the upwelling TOA radiance at zenith angle θ, azimuth angle ϕ, and wavenumber $\tilde{\nu}$. The first integral of eq. 7.1 refers to the spectral band used in the retrieval algorithm, which spans from $\tilde{\nu}_1 = 985\,\mathrm{cm}^{-1}$ to $\tilde{\nu}_2 = 1080\,\mathrm{cm}^{-1}$. Furthermore, as it was already introduced by Suttles et al. [1988] and Loeb et al. [2003], in the IR it is safe to use azimuthal symmetry to describe radiation transfer, and therefore the integral over ϕ can be reduced to 2π. Equation 7.1 can be transformed to represent the change of the flux at the top of the atmosphere, with respect to a change in the amount of an atmospheric parameter, as:

$$\frac{\partial F_{\mathrm{TOA}}}{\partial q(z_l)} = 2\pi \int_{\tilde{\nu}_1}^{\tilde{\nu}_2} \int_{0}^{\pi/2} \frac{\partial L_{\mathrm{TOA}}(\tilde{\nu}, \theta)}{\partial q(z_l)} \cos\theta \sin\theta d\theta d\tilde{\nu} \tag{7.2}$$

with $q(z_l)$ being an atmospheric parameter at mean altitude z of 1 km-thick layer l, while the fraction $\partial L_{\mathrm{TOA}}(\tilde{\nu}, \theta)/\partial q(z_l)$ is the Jacobians calculated from the forward model of the retrieval algorithm, first introduced in Chapter 6.

Equation 7.2 is the definition of the instantaneous radiative kernel (IRK) in $\mathrm{W\,m^{-2}\,ppb^{-1}}$, and quantifies the sensitivity of the TOA flux, F_{TOA}, to a change in the vertical distribution of an atmospheric parameter. In this study, the atmospheric parameter is the ozone mixing ratio. Furthermore, we should point out at this moment to avoid confusion later on, that all zenith angles are converted to equivalent TOA nadir viewing angles for IASI (calculated by FORLI; taking into account the Earth's curvature, the mean altitude of IASI from the Earth's surface, and the refractive indices of the different layers) and will be used as such hereafter, keeping the same notation, θ.

7.1.1 IASI–FORLI radiance Jacobians

As introduced in Ch. 6, the Jacobians are matrices that represent the sensitivity of the IASI TOA radiance measurements to the model parameters, and specifically to the ozone vertical distribution. To each measured radiance corresponds an $m \times l$ Jacobian matrix,

where m is the number of measured spectral elements and l is the number of the retrieval layers.

The Jacobians are calculated analytically during the retrieval of ozone (see Ch. 6, Sect. 6.2.2). They are expressed in units of $\mathrm{W\,cm^{-2}\,sr^{-1}\,cm\,ppb^{-1}}$ and correspond to layer averaged values, each assigned to the mean altitude or pressure of the layer. In the layers where strong absorption occurs, the Jacobians will have a negative sign, following the convention that an increase in the abundance of the absorbing gas results in a reduced TOA radiance.

Figure 7.1 shows an example of the IASI–FORLI Jacobians for ozone with respect to VMR(ppb). The Jacobians peak in the mid- and upper troposphere, around 600 to 250 hPa. This is common to thermal IR instruments, as other studies have shown that such instruments have their highest sensitivity to the ozone profile in the mid–troposphere [Bowman et al., 2002; Boynard et al., 2009; Coheur et al., 2005; Worden et al., 2011]. Note also the loss of sensitivity in the very first layer (1000 hPa) due to cold, winter conditions in the are of observation (January, NH). The units of the retrieved ozone may vary, e.g. volume mixing ratio (VMR), logarithm of VMR or Dobson units (DU). The Jacobians can be obtained or converted with respect to the preferred units, which however will affect the altitude of the maximum sensitivity. For example, if the Jacobians of fig. 7.1 are expressed in terms of ln(VMR), the sensitivity shifts upwards.

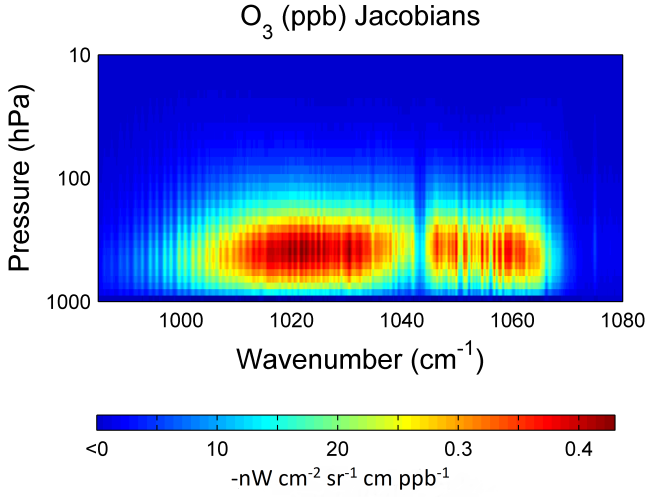

FIGURE 7.1: Example of O_3 Jacobians for a single observation on the 9.6 µm spectral band, with respect to ozone in ppb, for an observation taken by IASI on 15 January 2001, at (51.13 ° N, 42.3 ° W) and 04:57 UTC and for 47.48 ° viewing angle.

Regarding the spectral band, the maximum absorption is divided in two branches, with the first one peaking around $1025\,\mathrm{cm^{-1}}$ and the other one around $1055\,\mathrm{cm^{-1}}$. Interfering lines of water vapor and methanol in the retrieval spectral band have little or no impact

on the IASI sensitivity to ozone, as the high spectral sampling of IASI and FORLI allows the spectral distinction between the different species.

7.1.2 Angular integration of moments

The integral over angle θ in eq. 7.1 is very difficult to be solved arithmetically, and therefore a different approach is required. Abramowitz and Stegun [1972] are defining the Gaussian Quadrature (GQ), and Li [2000] has shown that this approximation is efficient for the directional integration of IR radiances. In the GQ, the angular integral is replaced by a sum over a finite number of angles. More specifically, for a function $g(\theta)$, the integral over $g(\theta)\cos(\theta)\sin(\theta)$ can be written as:

$$\int_0^{\pi/2} g(\theta)\cos\theta\sin\theta d\theta = \int_0^1 g(\cos^{-1}x)xdx = \int_0^1 x^k f(x)dx \approx \sum_{i=1}^{n} w_i f(x_i) \tag{7.3}$$

where $x = \cos\theta$ and $dx = -\sin\theta d\theta$. The GQ parameters $x_i = \cos\theta_i$, θ_i and weights w_i are provided in Table 7.1 for the first order of moment ($k = 1$) and for 5 nodes ($n = 5$). For more details on the GQ approximation, readers are referred to Abramowitz and Stegun [1972] and Li [2000].

TABLE 7.1: Zenith angle, cosine of zenith angle, equivalent TOA nadir angle for IASI and corresponding weight for the 5-node GQ.

Zenith angle (°) θ_i	$x_i = \cos\theta_i$	TOA Nadir angle (°)	Weight, w_i
84.3452	0.098535	61.2563	0.015748
72.2698	0.304536	57.0576	0.073909
55.8040	0.562025	46.7816	0.146387
36.6798	0.801987	31.7557	0.167175
16.2213	0.960190	14.2483	0.096782

7.1.3 Anisotropy approximation

The anisotropy is defined as the ratio of the equivalent Lambertian flux to the actual flux and is given by [Suttles et al., 1988]:

$$R(\tilde{\nu},\theta) = \frac{\pi L_{\mathrm{TOA}}(\tilde{\nu},\theta)}{F_{\mathrm{TOA}}(\tilde{\nu})} = \frac{L_{\mathrm{TOA}}(\tilde{\nu},\theta)}{2\int_0^{\pi/2} L_{\mathrm{TOA}}(\tilde{\nu},\theta)\cos\theta\sin\theta d\theta} \approx \frac{L_{\mathrm{TOA}}(\tilde{\nu},\theta)}{2\left[\sum_{i=1}^{5} w_i L_{\mathrm{TOA}}(\tilde{\nu},\theta_i)\right]} \tag{7.4}$$

where L_{TOA} is the radiance observed with a viewing angle θ and F_{TOA} is the angular integrated flux over a hemisphere, both depending on wavenumber, $\tilde{\nu}$. In the last step, the five−node GQ is applied, hence the sum is running from 1 to 5. Equation 7.4 suggests that the total flux can be evaluated, if the anisotropy and the radiance in only one direction are known. In order to calculate the anisotropy after the retrieval, the knowledge of all relevant surface and atmospheric parameters is required, which are: the observed radiance, the retrieved ozone profile, the retrieved surface temperature, the corresponding water vapour profile and the corresponding atmospheric temperature profile. The last two are obtained through EUMETCast and used for the initial retrieval. These parameters are then used to simulate spectra over the different GQ angles (Table 7.1).

The anisotropy is strongly dependent on cloud coverage, time of the day (day or night), surface type, surface temperature, temperature lapse rate and water vapor columnar content [Loeb et al., 2003; Suttles et al., 1988]. It has been used in many climate related studies, e.g. Clerbaux et al. [2002]; Worden et al. [2011], and has been applied to exploit measurements from broadband radiometers mainly, such as the Earth Radiation Budget Experiment (ERBE) and the Clouds and Earth's Radiant Energy System (CERES) (e.g. Li [1996]; Loeb et al. [2003]; Stubenrauch et al. [1994]). The concept of the anisotropy approximation for angular integration was also used recently by Worden et al. [2011] to calculate the O_3 IRKs from Aura-TES.

Trials have shown (not shown here) that for small viewing angles, the anisotropy is always larger than 1 throughout the whole spectral range, gradually decreasing to 1 as the viewing angle approaches 41°, and drops below 1 when the angle becomes larger than 41°. Regarding the number of nodes used for the approach, using the one-node GQ, which results to the diffusivity angle [Li, 2000], leads to a small positive bias of around 2% compared to the five-node approximation, whereas using more than five nodes does not improve the results significantly in terms of accuracy.

Once the anisotropy has been calculated (five-node GQ), the flux can be determined by using eq. 7.4 as $F_{\tilde{\nu}} = \pi L_{\tilde{\nu}}(\theta)/R(\tilde{\nu},\theta)$ and the IRK (eq. 7.2) as:

$$\frac{\partial F_{\mathrm{TOA}}}{\partial q(z_l)} = \frac{\partial}{\partial q(z_l)} \int_{\tilde{\nu}_1}^{\tilde{\nu}_2} \frac{\pi L_{\mathrm{TOA}}(\tilde{\nu},\theta)}{R(\tilde{\nu},\theta)} d\tilde{\nu} \approx \int_{\tilde{\nu}_1}^{\tilde{\nu}_2} \frac{\partial L_{\mathrm{TOA}}(\tilde{\nu},\theta)}{\partial q(z_l)} \frac{\pi d\tilde{\nu}}{R(\tilde{\nu},\theta)}, \tag{7.5}$$

where in the last step anisotropy was assumed constant with respect to $q(z_l)$. This approximation suggests that while the ozone dependence is taken into account in the Jacobian, it does not play an important role for the anisotropy. However, we show later

in this chapter that this approximation can lead to significant errors in the computation of the TOA fluxes.

7.1.4 Direct integration of Jacobians

The direct integration method is an approach that applies directly the GQ to the definition of the IRK (7.2). In the anisotropy method the GQ is applied on the radiances L_{TOA}, whereas in the direct integration approach it is applied on the Jacobians $\partial L_{\mathrm{TOA}}(\tilde{\nu},\theta)/\partial q(z_l)$. The calculation of the IRKs is now transformed to:

$$\frac{\partial F_{\mathrm{TOA}}}{\partial q(z_l)} = 2\pi \sum_{i=1}^{5} w_i \int_{\tilde{\nu}_1}^{\tilde{\nu}_2} \frac{\partial L_{\mathrm{TOA}}(\tilde{\nu},\theta_i)}{\partial q(z_l)} d\tilde{\nu}, \tag{7.6}$$

where the spectral range runs from $\tilde{\nu}_1 = 985\,\mathrm{cm}^{-1}$ to $\tilde{\nu}_2 = 1080\,\mathrm{cm}^{-1}$. The principle of the GQ is the same as for the anisotropy approximation, using five nodes, with the difference that the $f(x_i)$ function in eq. 7.3 does not refer anymore to the radiances, but to the Jacobians.

Using the same angles as for the anisotropy, given in Table 7.1, we compute with the forward model of FORLI the spectra and Jacobians of eq. 7.6 for each IASI measurement, based on the ozone vertical profile and other parameters obtained at the last iteration of the retrieval process. Each set of Jacobians is then weighted by the proper factor w_i, and integrated over the spectral band, with resulting units of $\mathrm{W\,m^{-2}\,ppb^{-1}}$. The IRK is thereby calculated for each layer and stored, to obtain the full profile.

Here, we should note that, as we assume azimuthal symmetry for the IR radiation, the IASI viewing angles are considered equivalent, e.g. $|\pm 48|$, in order to apply the GQ and the integration method.

7.1.5 IRK comparison

While the two methods explained above seem similar, there are some fundamental differences in their assumptions. Indeed, if we apply the chain rule on the second term of eq. 7.5, assuming now that the anisotropy R is not constant, rather that is a function of

the ozone abundance, we then have:

$$\frac{\partial F_{\mathrm{TOA}}}{\partial q(z_l)} = \int_{\tilde{\nu}_1}^{\tilde{\nu}_2} \frac{\partial L_{\mathrm{TOA}}(\tilde{\nu},\theta)}{\partial q(z_l)} \frac{\pi d\tilde{\nu}}{R(\tilde{\nu},\theta)} - \int_{\tilde{\nu}_1}^{\tilde{\nu}_2} F_{\mathrm{TOA}}(\tilde{\nu}) \frac{\partial}{\partial q(z_l)} \ln(R(\tilde{\nu},\theta,q(z_l)))d\tilde{\nu}. \tag{7.7}$$

The first term on the right−hand side of eq. 7.7 is the IRK in the anisotropy approximation. The second term therefore quantifies the difference between the direct integration method and the anisotropy method. The calculation of this extra term is more computational expensive than the direct integration method, as it requires separate simulations over the different angles, while the resulting matrices bind crucial computational memory. The magnitude of the extra term can be assessed by comparing the IRKs of both methods, as shown in fig. 7.2.

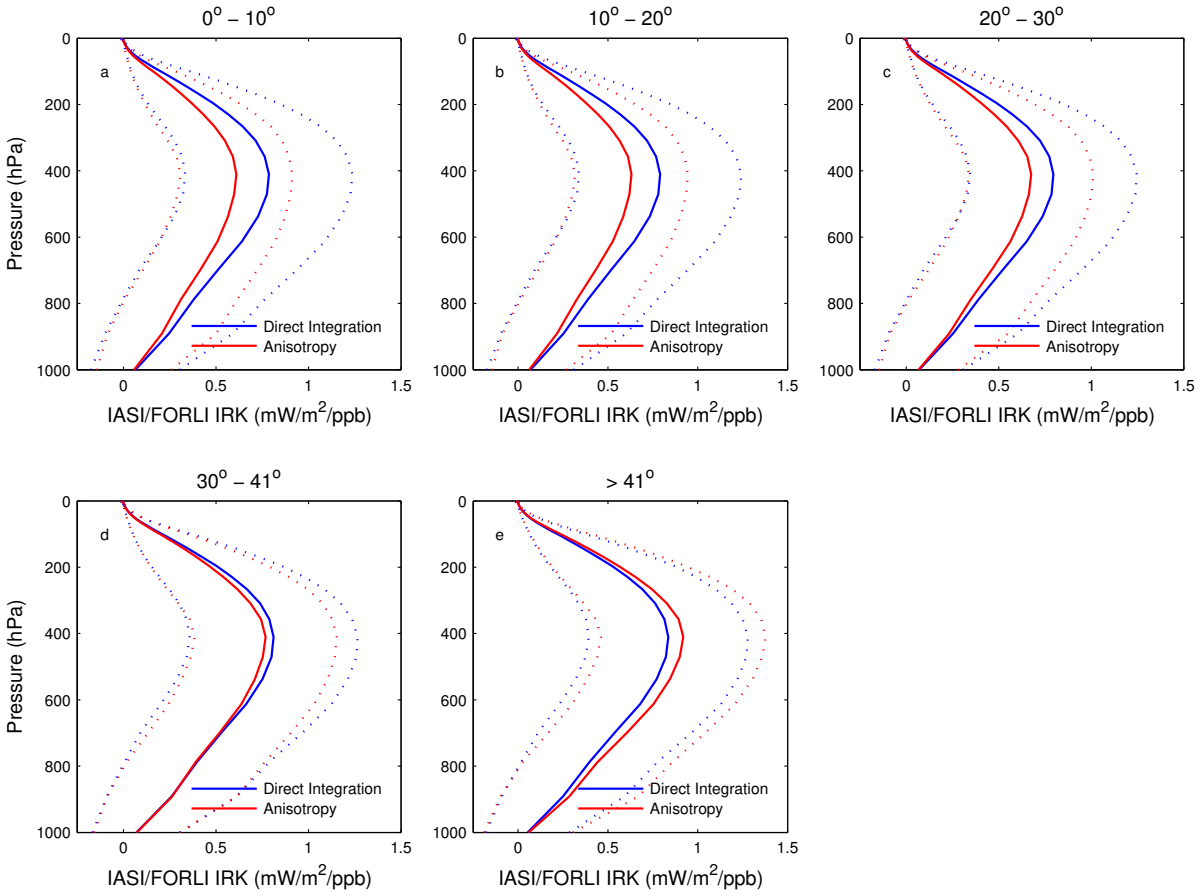

FIGURE 7.2: Global average clear−sky ozone IRK profiles as computed via the anisotropy approximation (red line) and the direct integration (blue line) on 15 April 2011. The dashed lines indicate $\pm 1\sigma$ standard deviations with the same color index. σ refers to the variability around the average IRK due to the different profiles. The averages were calculated in bins of 10 ° of nadir viewing angle, from 0 to 30 ° (a-c), 30 to 41 ° (d) and for angles larger than 41 ° to maximum 48.3 ° (e) for IASI.

Figure 7.2 shows the average IRKs of a single day, 15 April 2011, as computed by both the direct integration method (blue lines) and the anisotropy approximation (red lines). The average is performed on the global distribution of ozone profiles, considering bins of 10 ° from nadir. The last bin goes up to 48.3 °, the maximum angle of the IASI viewing swath. Following Worden et al. [2011], IRKs are plotted under the convention that the reduction of TOA flux corresponds to positive forcing; therefore we present the results as positive quantities. The IRKs peak for both methods around the mid−troposphere, which is consistent with the findings of previous studies [Lacis et al., 1990; Worden et al., 2011]. The maximum sensitivity for the direct integration method is $0.80 \pm 0.02\,\mathrm{mW\,m^{-2}\,ppb^{-1}}$ on average for all bins, and it is found at 8 km altitude or around 420 hPa. An important result of fig. 7.2 is that the anisotropy approximation underestimates the IRKs by about 22% at the maximum sensitivity for the bins of 0 to 10 ° (fig. 7.2a) compared to the direct integration results. The difference decreases as the viewing angle increases (fig. 7.2b and c) and is minimum when the angle approaches 41 ° (fig. 7.2d). Interestingly, the angle of 41 ° is the result of the one-node GQ for the anisotropy approximation [Worden et al., 2011]. For viewing angles larger than 41 ° (fig. 7.2e), the anisotropy approximation overestimates the IRKs compared to the direct integration by 10% at the altitude of the maximum sensitivity. The fact that the second term on the right-hand side of eq. 7.7 depends on the observation angle through the logarithm of R, explains the change from underestimation to overestimation as the viewing angle increases from 0 to 48 °. Here it should be mentioned that IASI has most of its measurements between 0 and 41 °, which means that on the global scale the anisotropy method would result to a significant underestimation of the IRKs. In integrated layer amounts the anisotropy method results in an underestimation of the IRKs of about 20% in the troposphere and 25% in total for viewing angles of 0 to 10 °, and an overestimation of about 10 and 12% for the troposphere and total, respectively, for angles larger than 41 °.

7.2 Longwave radiative effect

As explained above, an IRK (eq. 7.2) is the TOA flux sensitivity with respect to a change in the vertical distribution of ozone; it characterizes a single observation. According to that, for an observation at location and time i, we can apply the IRK to an associated difference in ozone abundance, e.g. the difference between a model (sim) and an observation (ref), as:

$$\Delta_{\mathrm{LWRE}(i,l)} = \frac{\partial F^{i}_{\mathrm{TOA}}}{\partial q_i(z_l)} \left[q_i^{\mathrm{sim}}(z_l) - q_i^{\mathrm{ref}}(z_l) \right] \tag{7.8}$$

where Δ_{LWRE} (in $\mathrm{W\,m^{-2}}$) is the difference of the TOA LWRE due to a difference in the ozone profile at a mean altitude z of a 1 km-thick layer l. Such a difference can be used to evaluate the impact of a biased chemistry-climate model parameter on the estimation of the overall radiative budget.

From eq. 7.8, assuming a reference of zero, we can use the retrieved ozone profile, accompanied by its own IRK, to compute the absolute LWRE for ozone as:

$$\mathrm{LWRE}_{i,l} \approx \frac{\partial F^{i}_{\mathrm{TOA}}}{\partial q_i(z_l)} q_i(z_l), \tag{7.9}$$

which represents the reduction in the OLR due to ozone absorption with respect to each atmospheric state at mean altitude z of layer l. From eq. 7.9 we can calculate the LWRE with respect to the ozone profile in each vertical layer, but we can also calculate LWRE separately for total columns and tropospheric or other subcolumns by simply summing over the appropriate vertical layer.

7.2.1 LWRE comparison

Earlier in this chapter, when the IRKs where introduced, along with the anisotropy approximation and the direct integration for their calculation, we also presented the differences the two methods exhibit on the IRKs (in fig. 7.2) and how the anisotropy approximation can lead to under- or overestimation of the results. We will do the same for the LWRE, as the biases are transferred through the equations. The LWRE is a columnar amount, and cannot be presented in the form of a profile; it is treated in the same manner as the ozone columns.

Figure 7.3 shows the zonal average vertical distribution of the LWRE for a single day of IASI measurements (15 April 2011) separated between local morning and evening overpasses. The ozone vertical profiles were retrieved with FORLI–O_3 using the parameters as specified in Ch. 6. The top row represents the results with the LWRE computed with the direct integration method (eq. 7.6), whereas the second row gives the LWRE calculated with the anisotropy approximation (eq. 7.5). All IASI viewing angles are included. The two methods show similar broad patterns with expectedly large LWRE values in the stratosphere, larger in the inter-tropical belt and lower in the polar regions due to higher and lower surface temperatures, respectively. The dependence of the LWRE on ozone, temperature and water vapor, is discussed later in Ch. 8.

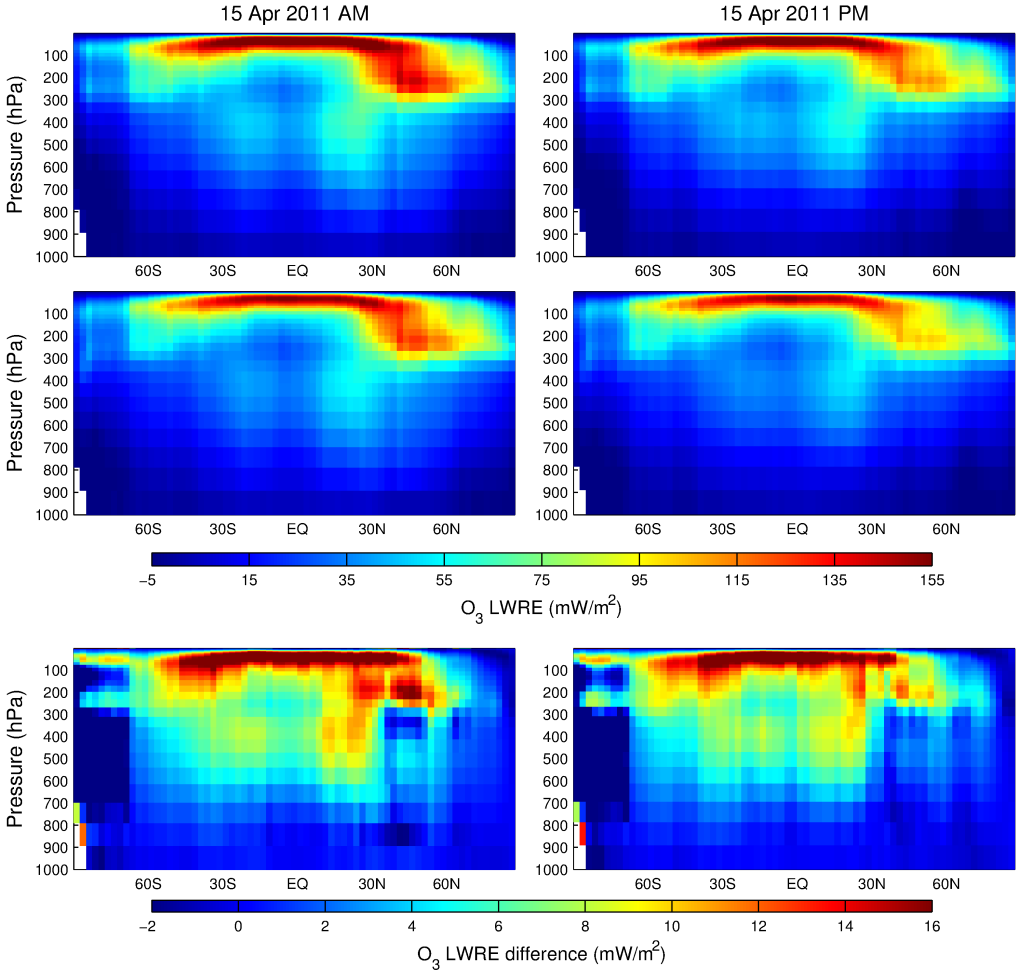

FIGURE 7.3: Single-day clear-sky zonal average ozone LWRE, in a 2.5° latitude bin, for local morning (left) and evening (right) IASI overpasses, on 15 April 2011. The top- and middle-row panels provide the LWRE calculated using the direct integration method and the anisotropy approximation, respectively. The bottom row shows the difference between the two methods.

The bottom row of fig. 7.3 shows the difference between the LWRE from the direct integration method and the anisotropy approximation. We can see significant differences over the entire distribution, with absolute differences following the distribution of the LWRE, with a maximum of $16\,\mathrm{mW\,m^{-2}}$ in the stratosphere. In the mid-troposphere the differences are about $6{-}7\,\mathrm{mW\,m^{-2}}$ in the inter-tropical region, decreasing to almost zero at the higher latitudes, where the LWRE itself is almost vanishing. Overall, we see an underestimation of the LWRE at all altitudes for the anisotropy methods, which is consistent with the IRK comparison (fig. 7.2) and the fact that the majority of the IASI measurements are made at angles between 0 and 41 ° (leading to the negative bias of the anisotropy approximation in the IRKs).

The difference in the LWRE between the two methods can also be seen, when comparing the total or tropospheric O_3 LWRE values spatially, as shown in figs. 7.4 and 7.5,

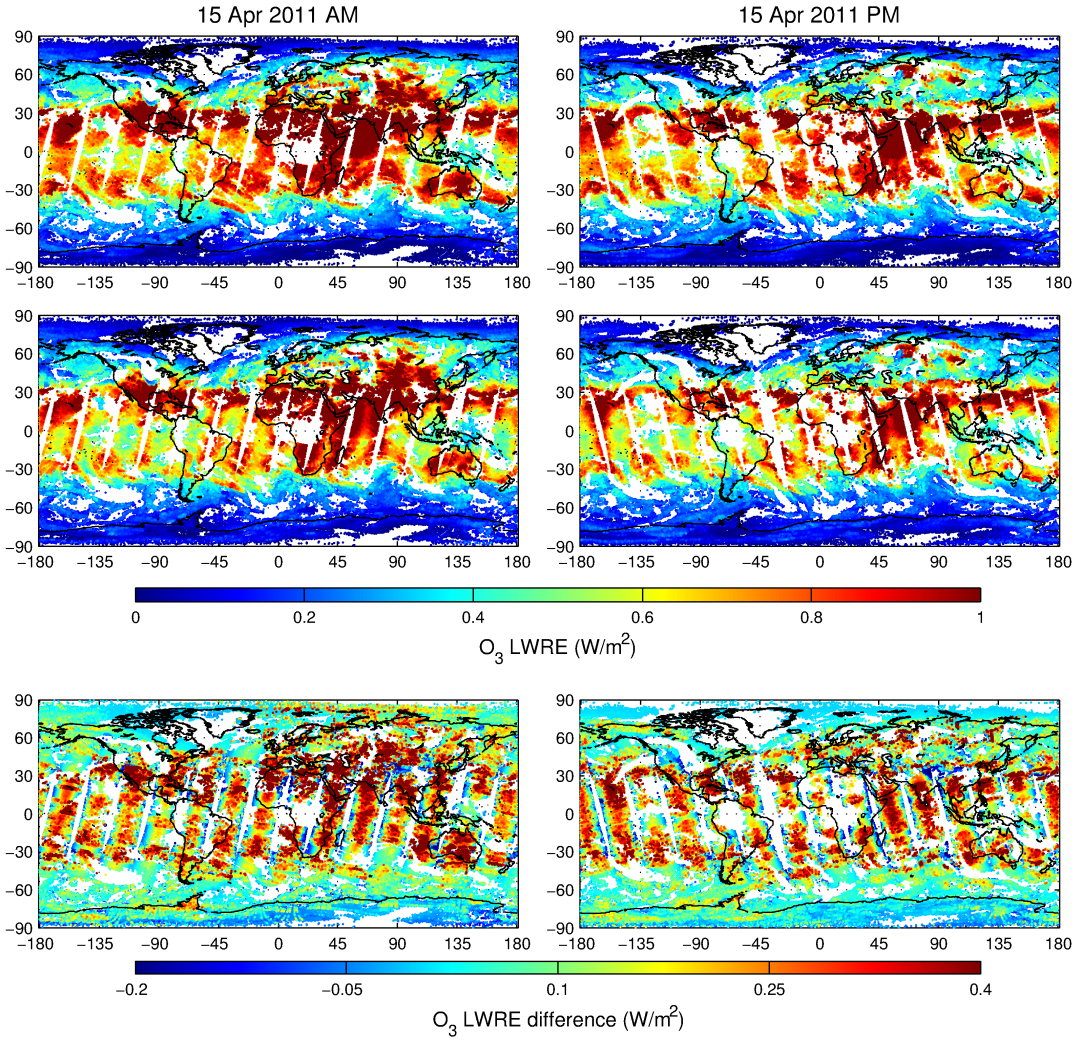

FIGURE 7.4: Global distribution of the total O_3 LWRE for morning (left) and evening (right) overpasses, taken by IASI on 15 April 2011. (top) Calculation using the direct integration method, (middle) calculation using the anisotropy approximation and (bottom) the difference between the two methods.

respectively. As for the zonal averages, in fig. 7.3, the general patterns are similar between the two methods, with the highest values of the LWRE in the inter-tropical belt and over several continental regions of the NH, logically related to the higher surface temperatures. This effect is more pronounced on the tropospheric LWRE (fig. 7.5) than on the total (fig. 7.4). Despite this qualitative agreement between the two methods, the angle-dependent bias of the anisotropy approximation is obvious in the bottom panels of figs. 7.4 and 7.5: the anisotropy approximation is biased low over most of the IASI swath (red to light-blue colors in the bottom panels) and biased high (blue colors only) at the edges of the swath. The bottom panels of figs. 7.4 and 7.5 correspond to the second term of the right-hand side of eq. 7.7, integrated over all (total) and tropospheric layers, respectively. The negative bias of the anisotropy approximation for the LWRE is larger near nadir and reaches almost $1\,\mathrm{W\,m^{-2}}$ (25%) on the total LWRE and around $0.4\,\mathrm{W\,m^{-2}}$

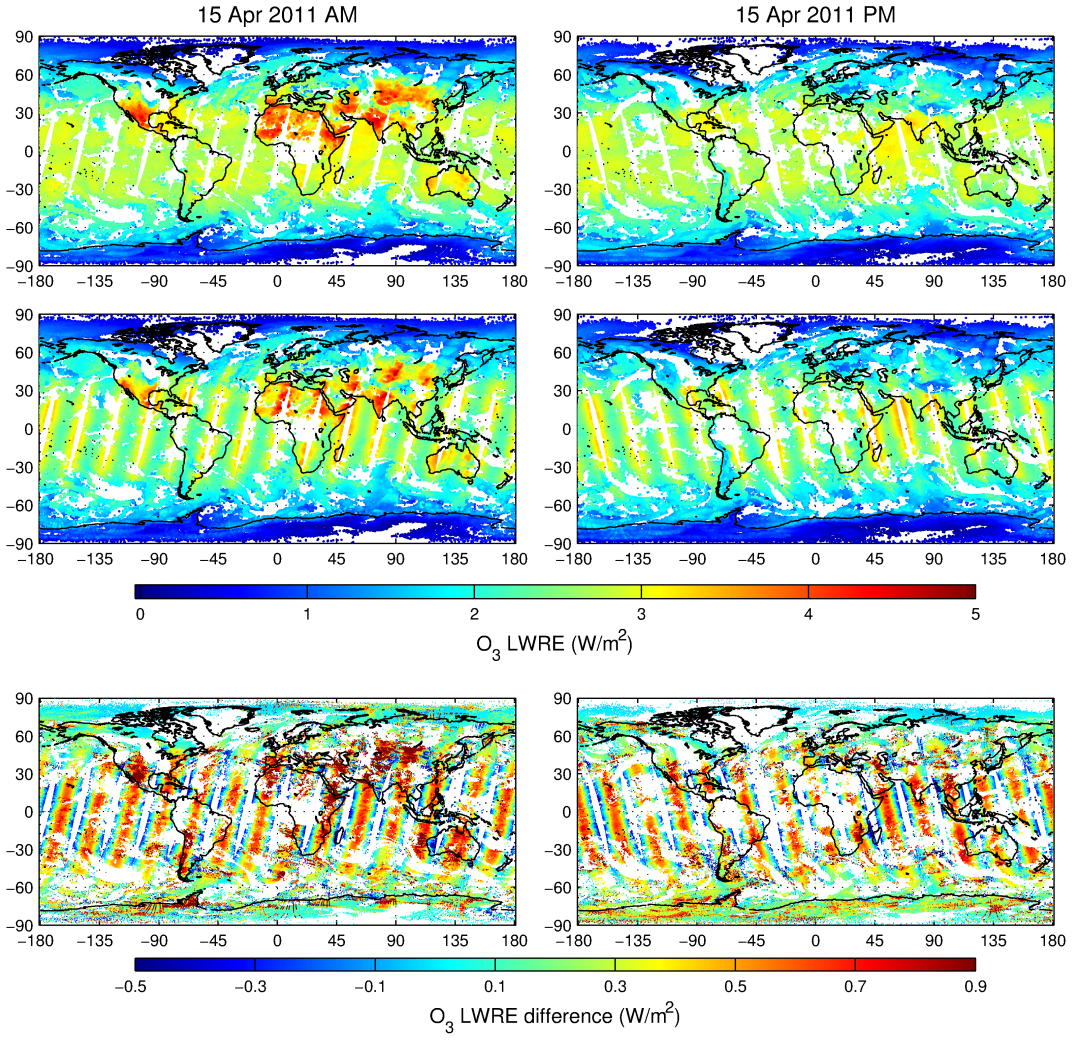

FIGURE 7.5: Same as fig. 7.4 but for the tropospheric O_3 LWRE. The calculation of the tropospheric LWRE relies on the definition of the tropopause by the World Meteorological Organization [1957].

(25%) on the tropospheric LWRE. The positive bias is slightly smaller for both total and tropospheric LWRE - 0.5 and 0.2 $\mathrm{W\,m^{-2}}$, respectively (around 20% in both cases) - due to the fact that both methods tend to agree at a viewing angle of 41 °. Note that the angle dependence is not observed at the polar regions, due to the compensation of positive and negative biases for overlapping orbits and the very low values of the LWRE.

7.2.2 LWRE error characterization

According to eq. 7.9, the error for the LWRE accounts for two contributions: that of the forward model, which originates from the IRK formulation, and that of the retrieval, for the O_3 profile, based on eq. 7.9. Contrary to the error proposed in Doniki et al. [2015], which was an acceptable approximation, we now propose a more rigorous calculation.

We consider eq. 7.9 in terms of matrices, which yields (for a single observation):

$$\mathrm{LWRE} = \mathrm{IRK}\,\beth(q), \tag{7.10}$$

where the LWRE and IRK are row vectors of dimension $1 \times N$, with N equal to the number of retrieval layers (e.g., $N = 41$), and $\beth(x)$ (daleth of x) represents the diagonal $N \times N$ matrix of the x property profile (here, ozone profile). Following the propagation of error, the error of the LWRE will then be:

$$S_{\mathrm{LWRE}} = S(\mathrm{IRK}\,\beth(q)) \tag{7.11}$$

$$= [\beth(\mathrm{IRK})^T S_q \beth(\mathrm{IRK})] + [\beth(q)^T S_{\mathrm{IRK}} \beth(q)], \tag{7.12}$$

where S_q is the error covariance matrix of the retrieved ozone profile ($N \times N$), and S_{LWRE}, S_{IRK}, are the error covariance matrices of the retrieved LWRE and IRK, respectively, with dimensions of $N \times N$ as well.

The first term (in brackets) of the right hand side of eq. 7.11 can be easily calculated, as the included parameters are all obtained during the O_3 retrieval to derive the LWRE. The second term of eq. 7.11 on the other hand, poses difficulties to evaluate, as S_{IRK} is unknown. The calculation of S_{IRK} requires the calculation of the exact differential of the IRK, as:

$$d\mathrm{IRK} = \frac{\partial^2 F_{\mathrm{TOA}}}{\partial q \partial q} dq + \frac{\partial^2 F_{\mathrm{TOA}}}{\partial q \partial b} db, \tag{7.13}$$

where:

- $\partial^2 F / \partial q \partial q$ is a Hessian tensor ($\mathcal{H}$), which is not computed (see Rodgers [2000]),
- b are all relevant spectral parameters of the retrieval,
- $\partial^2 F / \partial q \partial b$ cannot be calculated, given the numerous parameters that should be considered in the calculation (see Rodgers [2000]),

which yields, for the second term of the right hand side of eq. 7.11:

$$\daleth(q)^T S_{\mathrm{IRK}} \daleth(q) = \daleth(q)^T \mathcal{H}^T S_q \mathcal{H} \daleth(q). \tag{7.14}$$

However, it is possible to estimate an upper limit for the Hessian tensor of eq. 7.14 in only two dimensions, which is derived by the radiance estimation during the retrieval:

$$L \simeq L_a + \frac{\partial L}{\partial q}(q - q_a) + \frac{1}{2}\frac{\partial^2 L}{\partial q \partial q}(q - q_a)(q - q_a) + ..., \tag{7.15}$$

where L_a and q_a are the *a priori* radiance and ozone profile, respectively. Note that eq. 7.15 is not rigorous in the handling of vectors, matrices, tensors etc., as it is simplified and for indicative purpose.

As the retrieval is based on the linear approximation, then (in scalar form):

$$L - L_a + \frac{\partial L}{\partial q}(q - q_a) \simeq \frac{1}{2}\frac{\partial^2 L}{\partial q \partial q}(q - q_a)(q - q_a) + ..., \tag{7.16}$$

and the left hand side of eq. 7.16 (which is an estimation) must always be less or equal to the maximum room-mean-square (RMS) error of the noise in the retrieval, η, as it was defined in Table 6.1, therefore:

$$E[L - L_a + \frac{\partial L}{\partial q}(q - q_a)] \lesssim \eta \Rightarrow \tag{7.17}$$

$$E[\frac{1}{2}\frac{\partial^2 L}{\partial q \partial q}(q - q_a)(q - q_a)] \lesssim \eta \Rightarrow \tag{7.18}$$

$$E[\frac{1}{2}\int_{\tilde{\nu}} \frac{\partial^2 L}{\partial q \partial q}(q - q_a)(q - q_a)] \lesssim \int_{\tilde{\nu}}\int_{\tilde{\nu'}}\int_{\theta}\int_{\theta'} S_\eta d\tilde{\nu} d\tilde{\nu'} d\theta d\theta' \Rightarrow \tag{7.19}$$

$$E[\frac{1}{2}(q - q_a)\mathcal{H}|_{\tilde{\nu}}(q - q_a) \lesssim \int_{\tilde{\nu}}\int_{\tilde{\nu'}}\int_{\theta}\int_{\theta'} S_\eta d\tilde{\nu} d\tilde{\nu'} d\theta d\theta' \tag{7.20}$$

which in "matricial" form is:

$$\frac{1}{2}\daleth(q)^T \mathcal{H}^T S_q \mathcal{H} \daleth(q) \lesssim \int_{\tilde{\nu}}\int_{\tilde{\nu'}}\int_{\theta}\int_{\theta'} S_\eta d\tilde{\nu} d\tilde{\nu'} d\theta d\theta'. \tag{7.21}$$

where S_η is a diagonal matrix with the RMS^2 value in each position. Finally, the right hand side of eq. 7.21 is:

$$\int_{\tilde{\nu}}\int_{\tilde{\nu'}}\int_{\theta}\int_{\theta'} S_\eta d\tilde{\nu} d\tilde{\nu'} d\theta d\theta' = \frac{1}{2}(2\pi)^2 \int_{\tilde{\nu}}\int_{\tilde{\nu'}} \mathbb{1}^T S_\eta \mathbb{1} (\Delta\tilde{\nu})^2 \tag{7.22}$$

$$= (\pi\Delta\tilde{\nu})^2 \mathbb{1}^T S_\eta \mathbb{1}, \tag{7.23}$$

where $\Delta\tilde{\nu}$ is the spectral sampling interval in FORLI and equals to $0.25\,\mathrm{cm}^{-1}$, $\mathbb{1}$ is an $M \times N$ all-ones matrix, M is the number of samples in the spectrum interval, and N is the number of retrieval layers.

Going back to eq. 7.11, the error of the LWRE is:

$$S_{\mathrm{LWRE}}(i,j) \lesssim \langle [\gamma(\mathrm{IRK})^T S_q \gamma(\mathrm{IRK})] + 2(\pi\Delta\tilde{\nu})^2 \mathbb{1}^T S_\eta \mathbb{1} \rangle (i,j),\ \forall\, i,j = 1...N, \tag{7.24}$$

and results to the error covariance matrix of the LWRE. Figure 7.6 - left shows an example of the average LWRE error for a single day, while the middle and right figures correspond to single observations. The largest LWRE error is found in the region of greatest sensitivity of the instrument, in the middle and upper troposphere (top-middle panel), as explained in Ch. 6, but is also around the tropopause altitude. The largest error on the O_3 profile is observed near the ground (bottom-middle panel), where the instrument has limited sensitivity. The LWRE error correlations (top-right panel) agree with those of the retrieved ozone profile (bottom-right panel), showing a clear dependency of the LWRE on the retrieved O_3. Here we should note that the LWRE is also affected by the surface temperature (through the measured and integrated radiance, explained further in Ch. 8), the errors of which are not stored after the retrieval, in order to build similar matrices and compare. The observed discontinuities at around 7 km and 23 km, in both error covariance and correlation matrices of the LWRE and O_3, are associated with the *a priori* information in the retrievals, as they are also observable in the *a priori* O_3 covariance and correlation matrices (see fig. 6.1, [Hurtmans et al., 2012]). Finally, the inverse correlations (negative sign) observed at 39-40 km (right panels), are owed to the fact that in FORLI the last layer of the retrieval includes all the layers from 40 km to the top of the atmosphere, hence the increased LWRE error at the top of the error profile (left panel).

The above method results in a relative error of about 4.8% in the total LWRE, while for the tropospheric the relative error is about 9.4%. The largest contribution is owed to the terms in brackets in the right hand side of eq. 7.24 (e.g., for fig. 7.6, it is $0.13\,\mathrm{W\,m^{-2}}$

for the total LWRE and $0.06\,\mathrm{W\,m^{-2}}$ for the tropospheric), which is about 2-3 orders of magnitude greater than the second term of the right hand side of eq. 7.24 (which is around $0.003\,\mathrm{W\,m^{-2}}$). We should keep in mind that this is an upper limit of the error, as explained previously in this chapter.

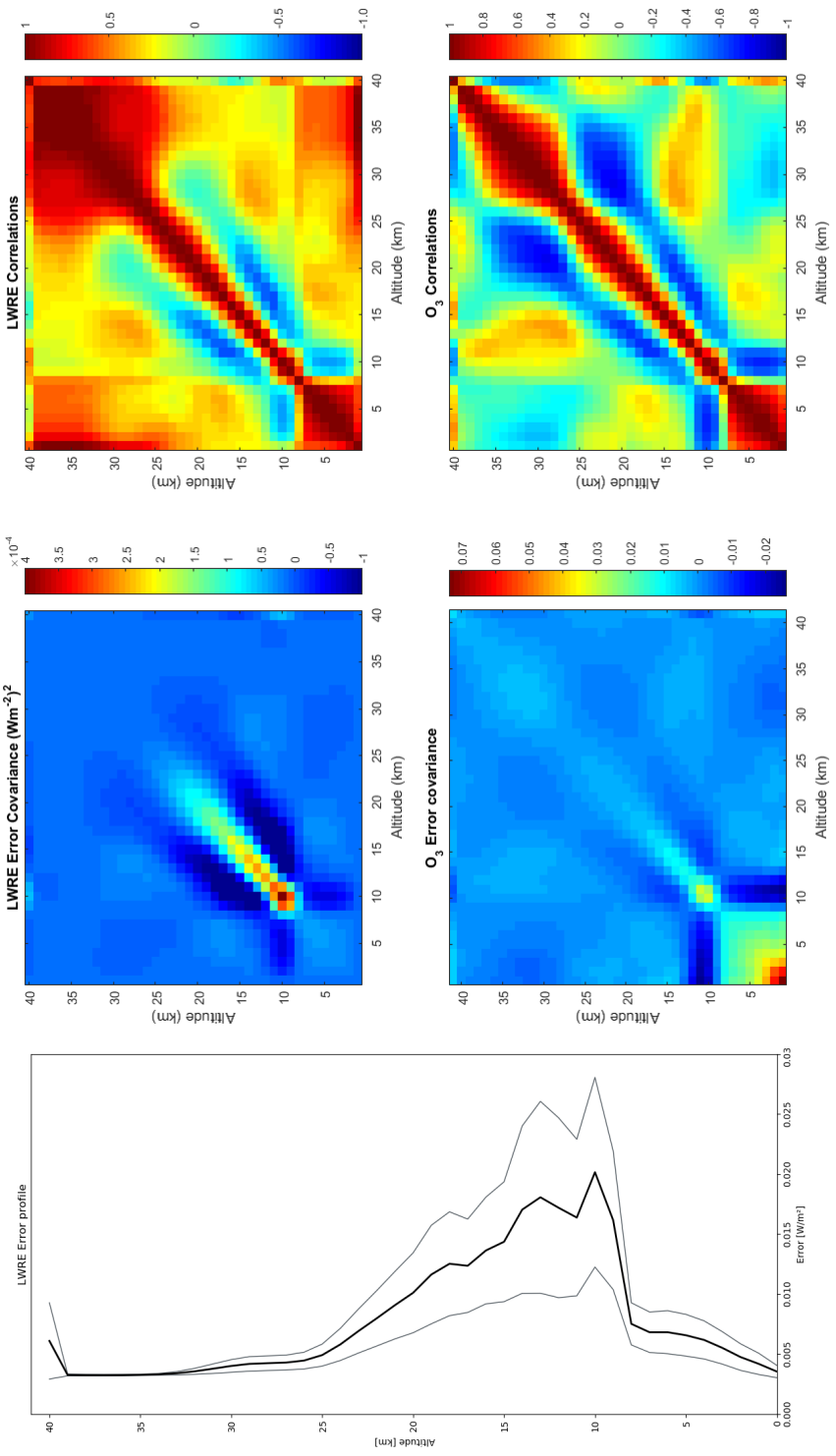

FIGURE 7.6: (Left) Example of a global average LWRE error profile for a single day. The black line denotes the average LWRE, while the grey lines denote the $\pm 1\,\sigma$ deviation from the mean. (Top) (middle) Example of the LWRE error covariance matrix and (right) the associated correlation matrix. (Bottom) (middle) The associated O_3 error covariance matrix and (right) its correlation matrix. The last four figures refer to a single observation in the 40-45° N and 20-30° E area, on 10 Jul. 2016.

Chapter 8

Ozone longwave radiative effect - Spatial and temporal analysis

In Chapter 7, we have described a method of Jacobians direct integration to calculate the IRKs and LWREs of O_3 from IASI observations. The direct integration method was compared to the anisotropy method, and we have shown that the two methods result in differences of up to 25% in the IRKs and the LWRE. The anisotropy method accounts for the angular integration of radiances with respect to the top of the atmosphere, while the direct integration performs the angular integration with respect to each vertical layer. We concluded that the direct integration method leads to more robust results, than the anisotropy one. In this chapter we investigate further the results of the direct integration method in terms of vertical and horizontal variability of the IRKs and the LWRE, and expand the study over the 9-year IASI record, from October 2007 to the first days of January 2017.

8.1 IRK vertical distribution

As already shown in the previous chapter, the IASI-FORLI IRKs peak in mid-troposphere (Sect. 7.1), indicating the altitude of maximum sensitivity of the IASI flux at the top of the atmosphere (calculated from the IASI radiances) to ozone, which is consistent with the findings for other thermal IR instruments, such as TES [Worden et al., 2011].

Figure 8.1 shows the zonal average IRKs of a single day (15 April 2011) for clear skies, as observed by IASI and calculated by FORLI, using the direct integration method. The sensitivity is highly variable. It shows an average distribution of $0.33 \pm 0.40\,\mathrm{W\,m^{-2}\,ppb^{-1}}$ (mean $\pm\, 1\,\sigma$) within 60° N and 60° S, with the maximum values at low latitudes, between

600 and 300 hPa. The sensitivity drops rapidly towards the Polar regions, due to low surface temperatures, that decrease the IASI signal-to-noise ratio and, hence, the sensitivity of the measurement to the target species, i.e. ozone in our case. The two maxima (dark red hot-spots) appearing in the tropical belt, which are consistent with the findings of Worden et al. [2011], are due to the presence of high temperatures and low ozone abundance in that region; it is better shown in the horizontal distribution further down in the text. The evening overpass view (fig. 8.1 right) shows a smaller sensitivity of the IRK, with an average value of $0.31 \pm 0.37\,\mathrm{W\,m^{-2}\,ppb^{-1}}$ (mean $\pm\, 1\,\sigma$), due to lower surface temperatures on average.

We should also point out the difference between the two views and the two hemispheres. The NH, dominated by land, shows greater changes between AM and PM, while the sensitivity in the SH shows little differences, due to the slow response of the ocean to temperature changes.

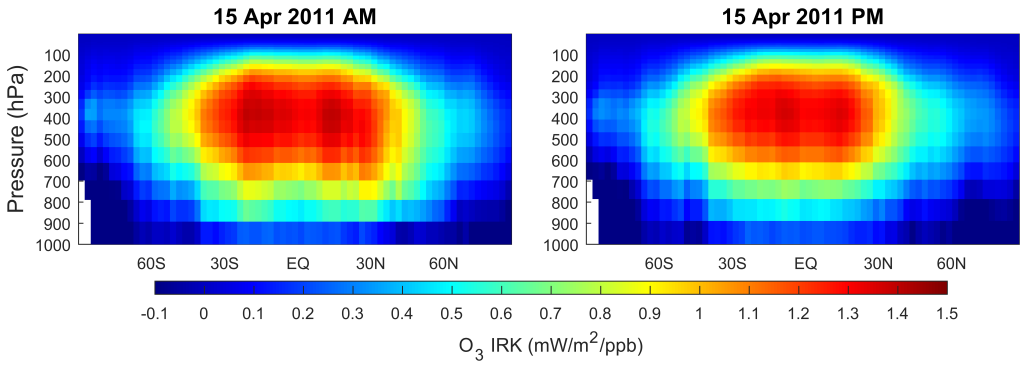

FIGURE 8.1: Zonal average IASI-FORLI IRKs for clear sky, all scenes, in 2.5° latitude bins, on 15 April 2011, for AM and PM view (left and right panels, respectively).

8.2 O_3 LWRE vertical and spatial distributions

The vertical and horizontal distributions of the LWRE were first presented in Chapter 7, to evaluate the impact of the two methods of the IRK calculation on the derived LWRE. A more in depth study will now be carried out, based on the results of the direct integration only.

8.2.1 Vertical distribution

The LWRE is proportional to the ozone abundance by definition (eq. 7.9), therefore it is expected to show higher values in altitude regions characterized by high ozone. As

already seen in fig. 7.3, the LWRE shows its highest values in the stratosphere, in the inter−tropical belt and gradually decreases towards the polar regions. The decrease from the Tropics towards the Poles is in contrast with the stratospheric ozone distribution at this time of the year (Sect. 4.2.2). However, it is expected to result from the decreasing surface temperature with latitude, knowing its role on the sensitivity of IASI radiance and flux, on the ozone changes (Sect.6.3).

Figure 8.2 shows the zonal average LWRE on 15 April 2011 for the AM and PM overpass views, along with the LWRE difference between the two views. The high LWRE found over the NH mid-latitudes are consistent with high cooling rates in the stratospheric mid-latitudes for this mid-spring periods (see Clough and Iacono [1995]). It is also possible to see high LWRE values in the NH mid-latitude mid- and upper-troposphere, which are explained by the combined effect of enhanced ozone, due to late effects of Brewer-Dobson circulation in spring (for 2011), and warm land, in contrast with the cooler and less polluted SH, which is dominated by ocean (also observable in the O_3 vertical distribution in fig. 8.3). Morning-evening differences in these regions are up to $25\,\mathrm{mW\,m^{-2}}$ near 250 hPa and $15\,\mathrm{mW\,m^{-2}}$ in the mid-troposphere. These differences are mostly related to changes in surface temperature, which was about 7 K between morning and evening at mid-latitudes, than to changes in the ozone content, which was about 4.2 DU for the total O_3 column between the two overpasses (or around 40 ppb locally). The contributions of ozone and surface temperature to the LWRE will be studied further in the text (Sect. 8.4).

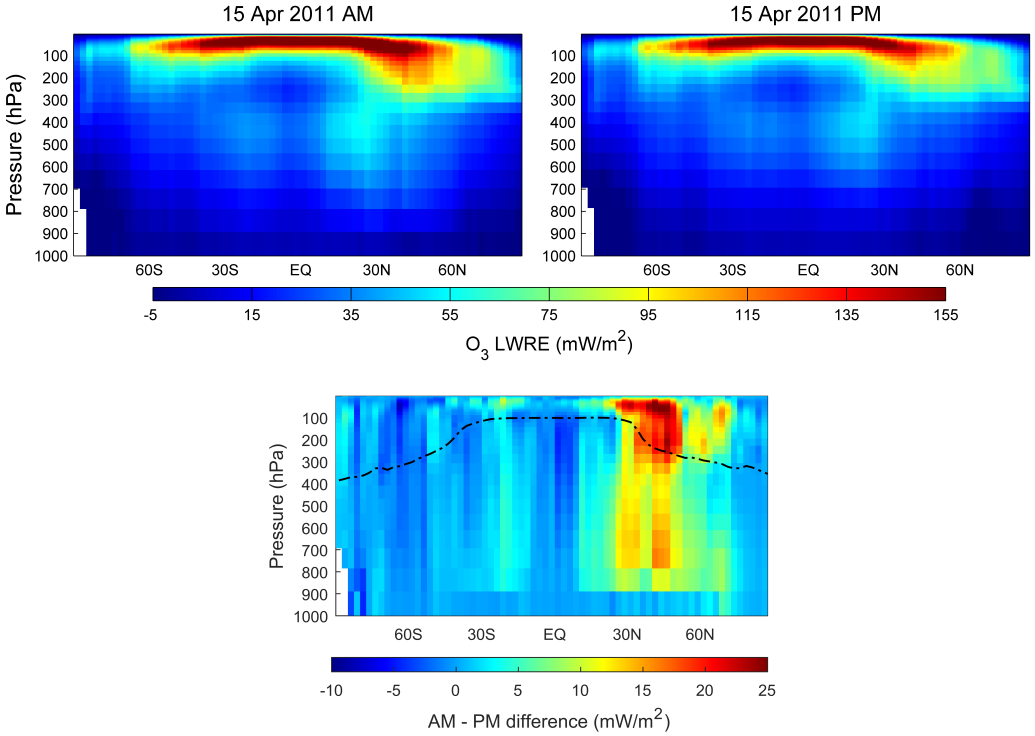

FIGURE 8.2: Zonal average IASI-FORLI LWRE for clear sky, all scenes, in 2.5° latitude bins, on 15 April 2011 (top) and the respective day-night difference (bottom). Black dashed line represents the tropopause.

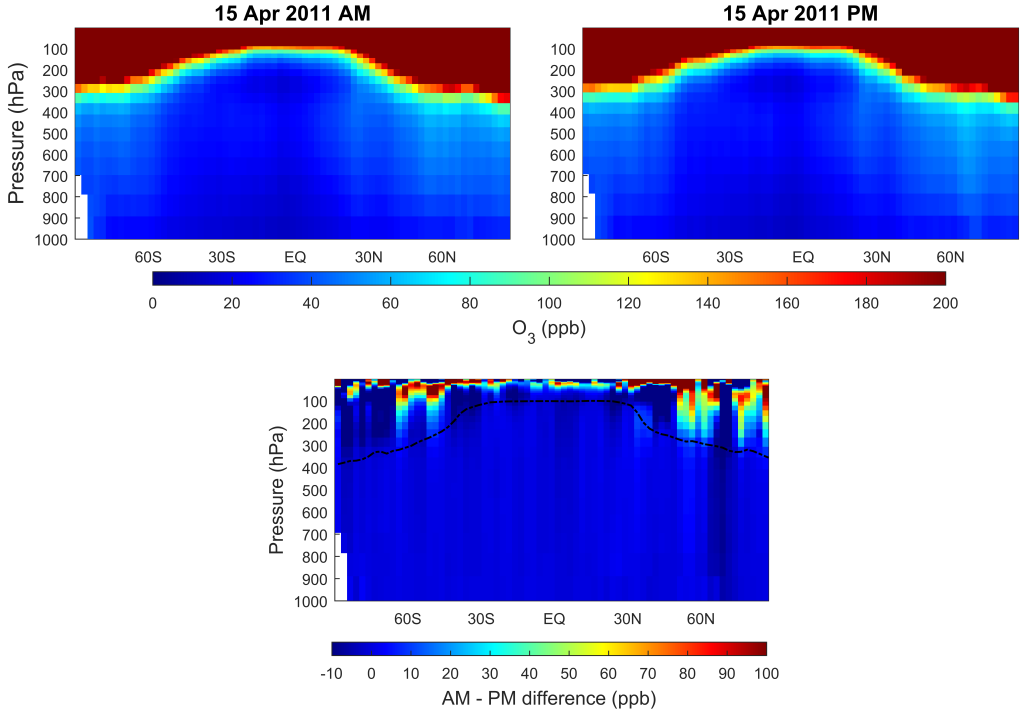

FIGURE 8.3: Zonal average IASI-FORLI O_3 (ppb) for clear sky, all scenes, in 2.5° latitude bins, on 15 April 2011 (top) and the respective day-night difference (bottom). Black dashed line represents the tropopause.

8.2.2 Spatial distribution

In Chapter 4, we have pointed out that the ozone distribution is highly uneven spatially and through the different seasons. In general, the total ozone amount is larger in the mid-latitude belts, during spring and summer of each hemisphere. Tropospheric ozone follows the same pattern, except it also exhibits medium to large amounts in the Tropics around November, mainly in the southern Tropics, due to large fire activity (see fig. 4.3). One would expect that the LWRE would follow the same spatial pattern.

Figure 8.4 shows the global spatial distribution of the total O_3 LWRE on 15 April 2011 for the morning and evening views, as well as the difference between the two. The LWRE shows its largest values within the tropics, reaching almost $5\,\mathrm{W\,m^{-2}}$, with an average value of $2.7\,\mathrm{W\,m^{-2}}$ and a relative spread of higher values also in the mid-latitudes. The polar regions on the other hand show minimum values. This is in contrast with the ozone spatial distribution (fig. 8.5), where for the same day, total O_3 columns exhibit their maximum values at high latitudes of the Northern Hemisphere. It is, however, following the spatial distribution of the surface temperature (fig. 8.6), and highlights again the significant contribution of the surface temperature to the LWRE.

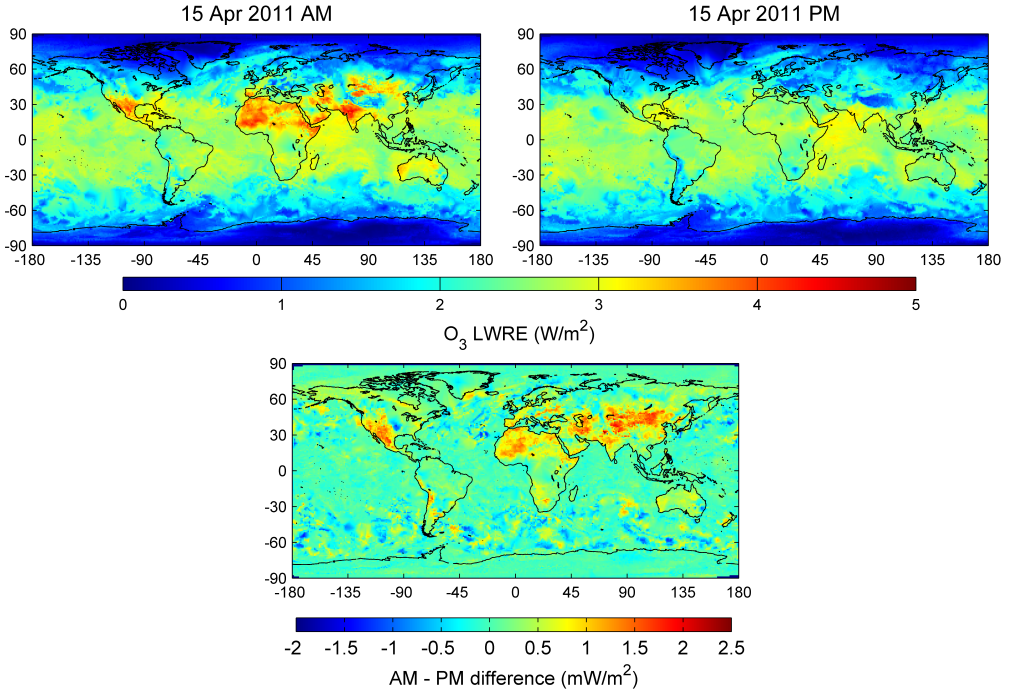

FIGURE 8.4: Global distribution of the total O_3 LWRE, clear sky, in $1°\times1°$ grid, on 15 April 2011 (top) and the respective AM-PM difference (bottom).

The impact of the surface temperature on the LWRE is also well seen by the presence of daytime hot-spots in fig. 8.4 (red regions in top-left panel), above regions of desert or rocky terrain. The bottom panel of fig. 8.4 which displays the LWRE differences between

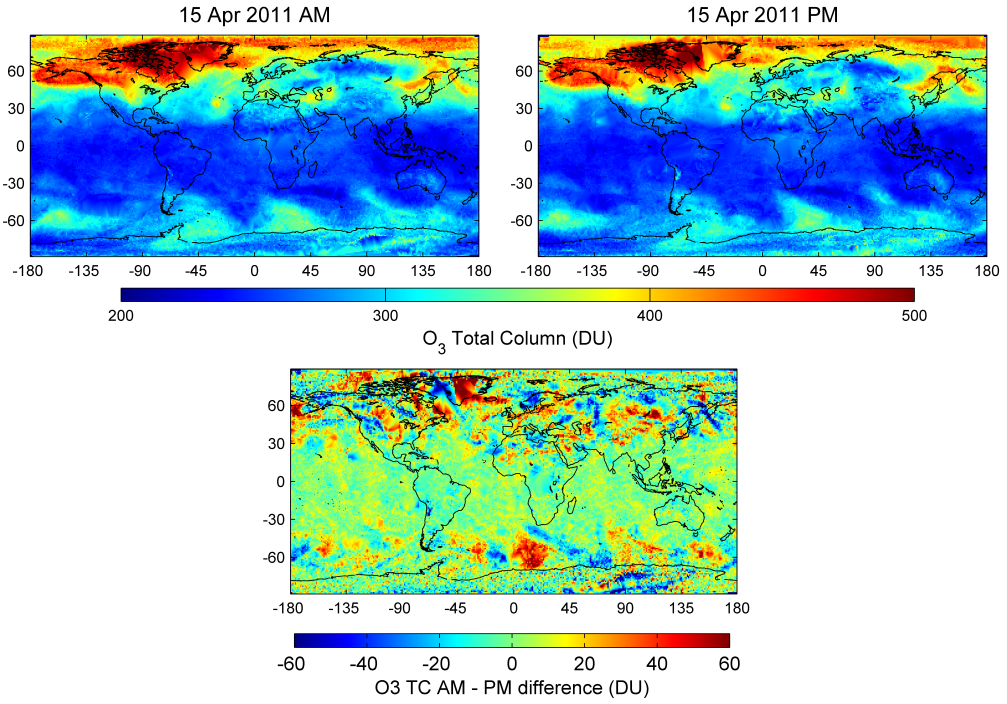

FIGURE 8.5: Global distribution of the total O_3 column, clear sky, in $1° \times 1°$ grid, on 15 April 2011 (top) and the respective AM-PM difference (bottom).

the day and night distributions of LWRE of the same day, shows that the hot-spot regions can reach up to 2.5 mW m^{-2}. Daily changes in O_3 values - less than 20 DU in the hot-spot regions (fig. 8.5, bottom panel) - do not explain such AM-PM differences in the LWRE , but it can be well explained by the changes of the surface temperature, shown in fig. 8.6 bottom panel, where the same hot-spots (regions in red) can be found. The rest of the map shows LWRE differences generally lower than 1 mW m^{-2}, reflecting a stable state within the 12 h difference of the two views, and agreeing with the situation of the total O_3 and surface temperature differences (fig. 8.5 and 8.6, respectively).

Figure 8.7 shows the tropospheric O_3 column of LWRE, for the same day as fig. 8.4. High values of LWRE are clearly marked in the inter-tropical belt, which also contains the hot-spots seen previously. As for the total O_3 LWRE, these are caused by the surface temperature, and they appear during the day overpass, but disappear during the night. The LWRE difference pattern, shown at the bottom of fig. 8.7, matches to some extent the surface temperature difference at the bottom of fig. 8.6.

It is of particular interest to focus over Indonesia and the western Pacific in fig. 8.7. This region, within the Tropics, is governed by high temperatures (around 300 K) almost all year round, but nonetheless there is a pool of low tropospheric LWRE which is maintained throughout the day. The region has low ozone as it is common within the Tropics (see Ch. 4), and as it can be seen in fig. 8.8, tropospheric ozone can reach as low as 15 DU. This region is also known for the high water vapour warm pool it forms [Zhou et al.,

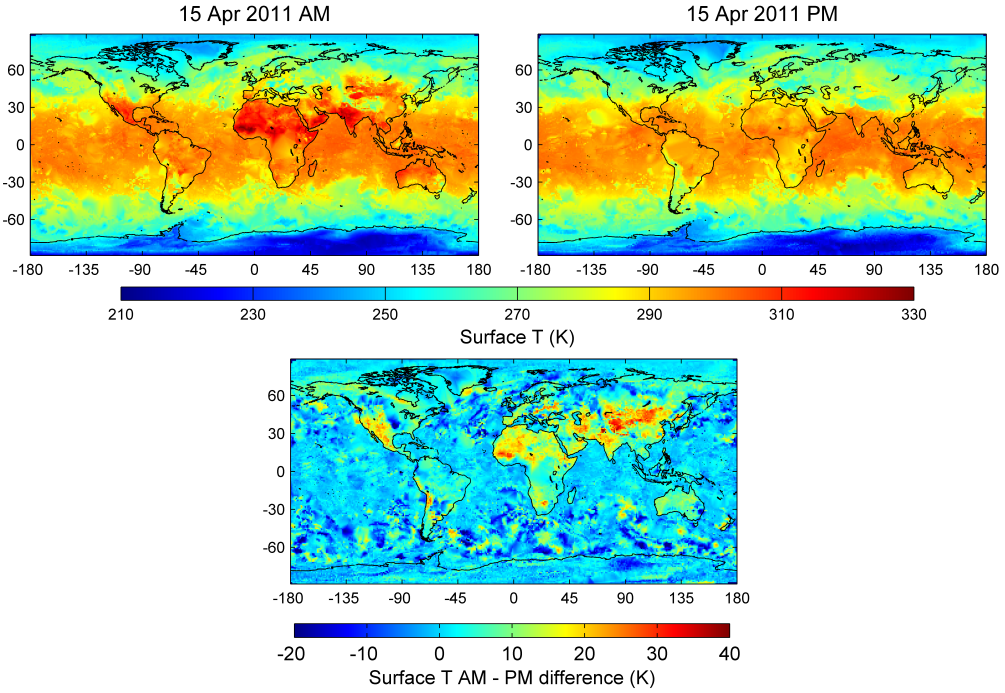

FIGURE 8.6: Global distribution of the surface temperature, clear sky, in 1°×1° grid, on 15 April 2011 (top) and the respective AM-PM difference (bottom).

2018]. The same distribution can be seen in fig. 6 in Worden et al. [2011], where they presented the average LWRE of tropospheric O_3 for August 2006.

Similar observations can be derived from the 5-year mean annual and mean seasonal distributions provided in Appendix C (see figures C.1 to C.3 and C.7 to C.13). While there is obviously a substantial impact of both the ozone amount and the surface temperature on the LWRE around the 9.6 µm band, it is not easy to disentangle their respective contributions. In Sec. 8.4, we investigate the contributions more in-depth. Furthermore, there has been evidence of the relative humidity significantly affecting the LWRE. In their work, Kuai et al. [2017] have found strong anti-correlations between the ozone LWRE and relative humidity in the Tropics, mainly in the troposphere, but also in the stratosphere. In cases where relative humidity was high (reaching 80% and above), the authors found significantly low LWRE, while in dry conditions (relative humidity around 40% and below), the LWRE was increased. The study concludes that in the presence of high water vapor content (winter or summer), the outgoing longwave radiation is strongly attenuated, reducing the absorption from ozone, and therefore leading to a decreased LWRE. Specifically for the Tropics, the low ozone LWRE is associated with high relative humidity, owed to the upwelling motion in the Hadley cell, which results to deep convection in the ITCZ.

A 5-year average and seasonal global distribution of LWRE, ozone and surface temperature is shown in Appendix C.

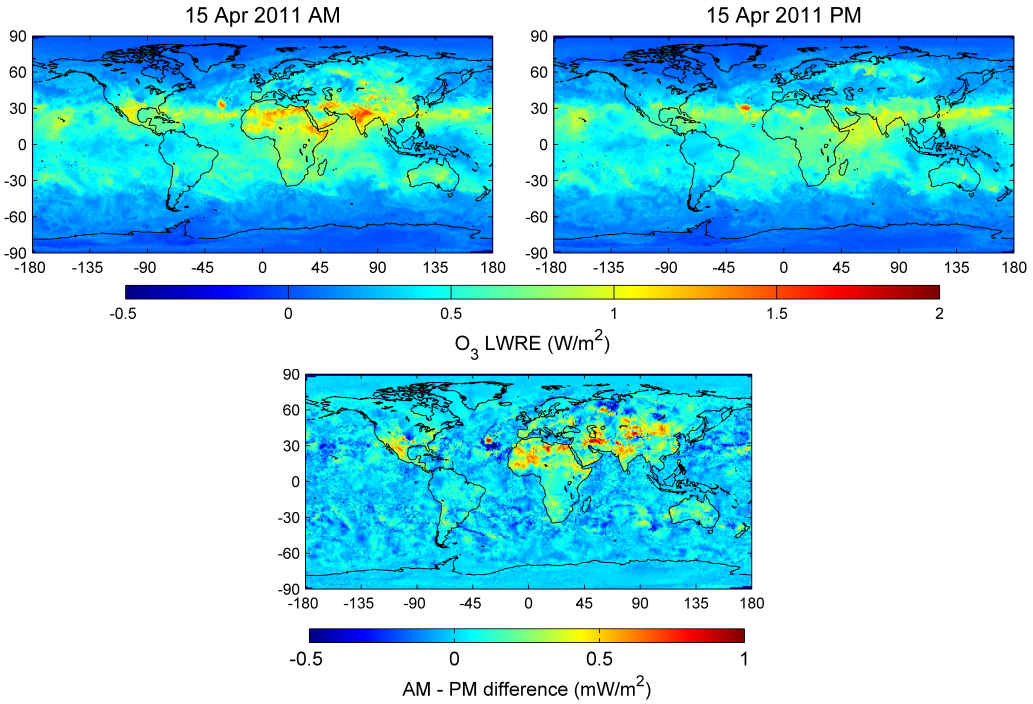

FIGURE 8.7: Global distribution of the tropospheric O_3 LWRE, clear sky, in 1°×1° grid, on 15 April 2011 (top) and the respective AM-PM difference (bottom).

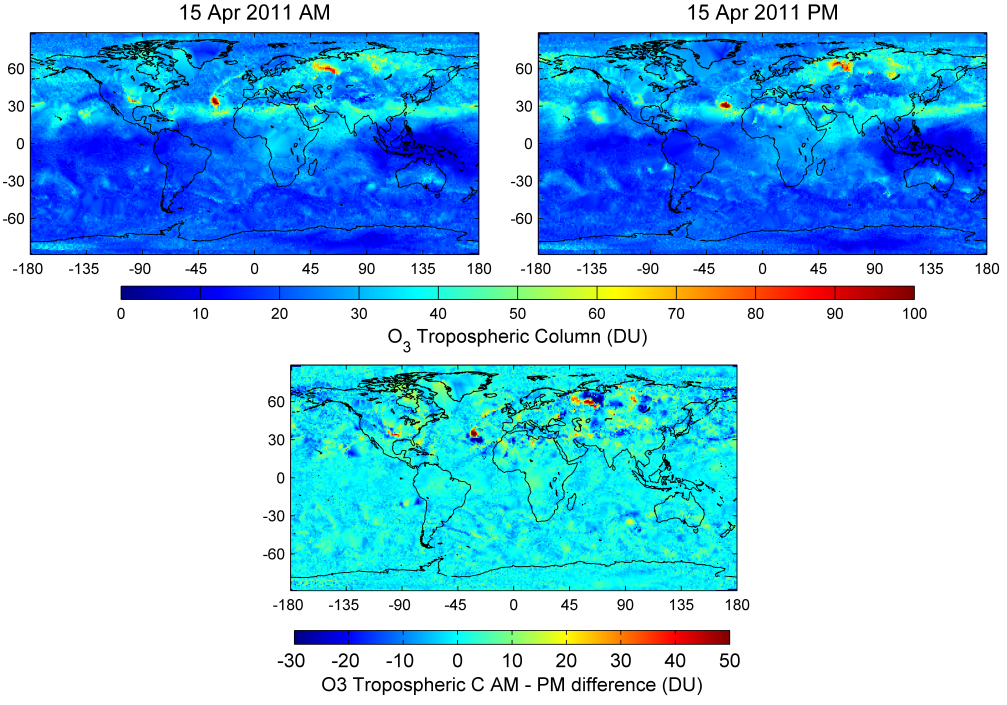

FIGURE 8.8: Global distribution of the tropospheric O_3 column, clear sky, in 1°×1° grid, on 15 April 2011 (top) and the respective AM-PM difference (bottom).

8.3 IASI-A vs IASI-B O_3 LWRE and product updates

For the purpose of this thesis, only the data of IASI-A were used. IASI-A has a longer observation record, starting at the end of 2007, compared to IASI-B, which was launched in the second half of 2012. However, both IASI-A and -B observations are processed with FORLI, and the results are similar. There have been extensive comparisons between the measurements of the two instruments, that show high consistency. Camy-Peyret et al. [2013] and Jouglet et al. [2014] have in particular shown in their respective works that IASI-A and IASI-B show excellent consistency both spectrally and radiometrically for the Level 1c data, with only few exceptions.

Regarding the O_3 from IASI and FORLI, Boynard et al. [2018] made a thorough investigation inter-comparing the ozone profiles and columns retrieved from the two instruments, as well as comparing these with other ozone measurements from ground-based and satellite instruments. The inter-comparison concluded that the FORLI-O_3 between IASI-A and IASI-B are in a very good agreement, with the difference for the total column lying within 0.4%, while for the tropospheric column around ± 2%. Local differences may be higher, up to 10%, mainly in the Polar regions, due to overlapping orbits that result to multiple views per day over the same region.

For the LWRE, there has not been such a study yet. Comparisons of latitudinal averages and time series of the LWRE from IASI-A and -B are provided in Appendix B. The comparisons clearly show the good agreement for the LWRE between the two instruments, for the time record available. More specifically, for the total LWRE the two instruments agree within 0.58% for the global average, with the Polar regions exhibiting the largest biases (around 0.32% for the NH and 0.63% for the SH, identical to the total O_3 column biases between IASI-A and -B [Boynard et al., 2018]), while for the tropospheric LWRE the bias is 1.87% for the global average, mainly influenced by the SH Polar region (around 1.74%).

8.3.1 Updates in Level 1 and Level 2 IASI measurements

As already mentioned, the ozone radiative forcing, and therefore the LWRE, is strongly dependent not only on the local ozone abundance, but also on the surface temperature, the atmospheric temperature and the humidity profile. A number of updates, corrections and calibrations have been performed since Metop-A was launched, which lead to changes in the Level 1c and Level 2 products. The effects of these changes at L1c

reflect on the retrieved L2 products and are registered under the User Notification Service (UNS) of EUMETSAT (https://uns.eumetsat.int/ and https://www.eumetsat.int/website/home/Data/ServiceStatus/ProductHistory/index.html). As the meteorological L2 products are used as input in FORLI, the LWRE data record analyzed here also suffers from inconsistencies. Table 8.1 provides a list of these effects and will be used for reference further in the text.

TABLE 8.1: IASI level 1 and level 2 changes over time.

	Date	Level	Product affected	Comments
1	21 Jan 2009	L2	Tsurf, LWRE	Update from version 4.3 to 4.3.2
2	14 Sept 2010	L2	Tsurf, LWRE	Update to version 5.0.6, with improved temperature profiles, but available for fewer observations
3	02 Dec 2010	L2	Tsurf, LWRE	Update to version 5.1
4	20 Oct 2011	L2	Tsurf, LWRE	Update to version 5.2.1, improved cloud coverage information
5	28 Feb 2012	L2	Tsurf, LWRE	Update to version 5.3
6	30 Sept 2014	L2	Tsurf, LWRE, O_3	Update version to 6.0.5, major update in the processing algorithm
7	13 Apr - Sept 2015	L1c	LWRE, O_3	Error in IASI-A pixel registration [Boynard et al., 2018]
8	Jul - Oct 2015	L1c	Tsurf, LWRE, O_3	Error in cloud coverage information
9	24 Sept 2015	L2	Tsurf, LWRE	Update to version 6.1 and the surface temperature algorithm
10	Nov & Dec 2015		Tsurf, LWRE, O_3	Instrument external calibration, poor spatial coverage

8.4 LWRE versus O_3 content and surface temperature

As seen in its vertical and horizontal distributions (Sec. 8.2), the O_3 LWRE exhibits effects that are owed to O_3 and surface temperature. It is also impacted by the temperature profile and the relative humidity, which however are not retrieved by FORLI, as their calculation is time and resources consuming. Therefore, the contribution from these two parameters to the LWRE is not considered in this study. The relation of the LWRE to O_3 and surface temperature is here evaluated in terms of correlation and regression slopes, separately for the total column, the troposphere and the stratosphere, in daily averages of five zonal bands (NH Pole, NH midlatitudes, Tropics, SH midlatitudes, SH Pole), in addition to the global scale. Note that the data affected by updates in the L2 products of EUMETSAT (Table 8.1, especially in lines 7, 8 and 10), strongly affect the homogeneity in the LWRE, O_3 and/or surface temperature time series (see Sect. 8.5.1 and 8.5.2), and therefore have been excluded from the following analysis.

8.4.1 Relation of LWRE to O_3 and surface temperature

Tropospheric LWRE

Fig. 8.9 shows the relation between tropospheric LWRE and O_3 (left panels) and surface temperature (right panels). The slopes of the fitted linear regression (expressed as the % change in the LWRE relative to the global average per DU or K), and the linear correlation/determination coefficients associated to the correlation patterns are provided in Table 8.2. One can observe that O_3 and surface temperature are competing drivers of the tropospheric LWRE, as the LWRE response to these two explanatory parameters are comparable for all bands and the global averages (e.g., $\mathrm{dLWRE/dO_3} = 2.25$ and $\mathrm{dLWRE/dTs} = 2.53$ globally). Regarding the correlation coefficients of the LWRE vs O_3 and surface temperature (here referred to as $R_{\mathrm{LWRE\text{-}O3}}$ and $R_{\mathrm{LWRE\text{-}Ts}}$), we find that LWRE-Ts correlation is generally larger than LWRE-O_3 correlation (e.g., $R_{\mathrm{LWRE\text{-}Ts}} = 0.95$ and $R_{\mathrm{LWRE\text{-}O3}} = 0.39$ for the global average), which indicates a strongest degree of linearity of the LWRE with the surface temperature than with O_3.

The greatest impact of O_3 and surface temperature to the LWRE is found in the NH midlatitudes and the Tropics ($\mathrm{dLWRE/dO_3}$ of 5.01 and 3.17, dLWRE/dTs of 3.78 and 3.05, respectively), regions that exhibit the largest surface temperatures. On the contrary, the Polar regions exhibit the lowest slopes for both O_3 and surface temperature, reflecting

the constrain in the IASI sensitivity to O_3 measurements, especially for altitudes near the ground.

The zonal values of $dLWRE/dO_3$ are consistent with the latitudinal distribution of the IRKs (fig. 8.1), with respect also to eq. 7.9. On the same note, considering the zonal distribution of the IRKs, one would expect a larger slope in the Tropics due to largest surface temperatures, however the observed slope (lower than that for the NH midlatitudes) could be due to the impact of the relative humidity and its strong presence in the tropical troposphere (large water vapor content results to strong absorption of the outgoing longwave radiation, which in turn leads to weaker ozone absorption and LWRE, see Sect. 8.2.2).

Regarding the correlations, the linearity is not straightforward, but it could be assessed when considering the formulation of the LWRE (eq. 7.9), which is derived by the IRKs, which in turn are a product of the radiance Jacobians with respect to O_3. The derivative of the radiative transfer equation (eq. 3.46) with respect to O_3 results to an exponential dependence of the Jacobians with the surface temperature through the Planck function (eq. 3.9), and to a linear relation with the O_3 absorption cross section $k_{\tilde{\nu}}$ (a function of air temperature and pressure, with its maximum in the middle and upper troposphere in the 9.6 µm band).

The colors in fig. 8.9 represent the days of the year of the data (the month-label denotes the 1st day of each month), to enhance the effect of the seasonality on the correlation patterns. Regarding the tropospheric LWRE against surface temperature, the data are mixed, except for the Southern Hemisphere. In more detail, in the SH midlatitudes, the data appear to be "split" in two sets. This is an artifact caused by an update on the EUMETSAT products (line 4 in Table 8.1), that affect the surface temperature and the LWRE. Regardless the artifact effect, the data of local autumn/winter are located mostly above the slope, while those of the local spring/summer, below the slope. In this case, correlations could become larger than the existing 0.81. On the other hand, in the SH Pole, the data of the local summer/autumn lie below the slope, neatly spread in a line, while those of the local winter/spring lie above the slope, causing the largest dispersion, due to limited sensitivity of the instrument in case of low surface temperatures. Regarding the tropospheric LWRE against tropospheric O_3, the data could be separated in local winter/spring and summer/autumn, to strengthen the correlations.

Stratospheric LWRE

The relation of the O_3 LWRE to O_3 and surface temperature is shown in fig. 8.10 with the respective linear regression, correlation and determination coefficients in Table 8.2.

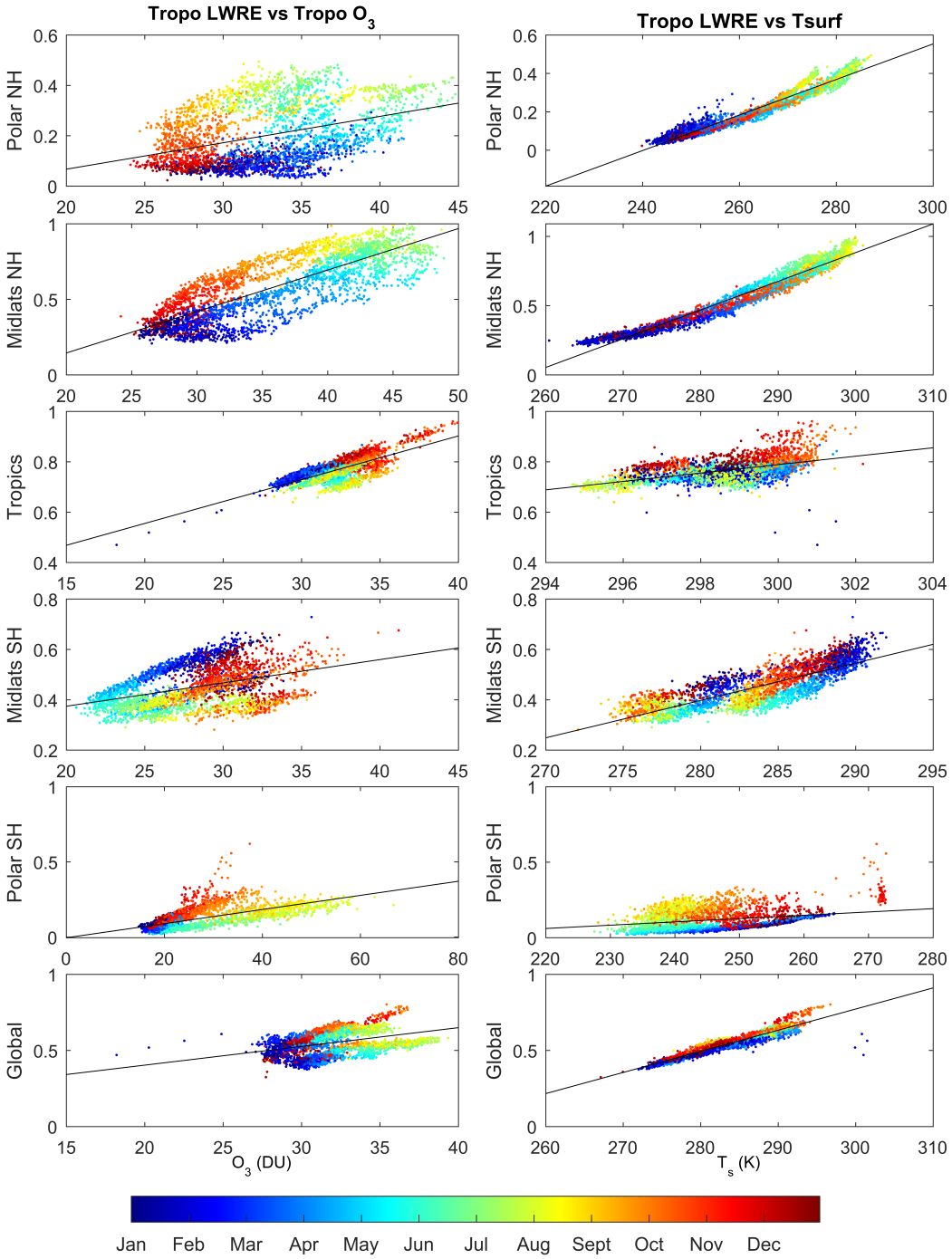

FIGURE 8.9: Scatter plot of daily averages between LWRE and O_3 (left) or surface temperature (right) in the troposphere, distinguished in five latitudinal bands and globally. The vertical axes represent the LWRE (in Wm^{-2}). The color scale represents the days of the year. The black lines represent the linear regression.

In general, both the slopes and the correlations with respect to either O_3 or surface temperature are lower than those in the troposphere.

Regarding the change with O_3, $dLWRE/dO_3$ is in agreement with the IRK vertical distribution (fig. 8.1), where the sensitivity in the stratosphere is lower compared to the troposphere. With respect to the surface temperature, dLWRE/dTs is obviously lower than in

TABLE 8.2: Linear regression slopes (% change of LWRE / DU or K), correlation (R) and determination coefficients (R^2) between LWRE and O_3, and surface temperature (Tsurf), for tropospheric, stratospheric and total amounts.

	LWRE vs. O_3			LWRE vs. T_{surf}		
Regions	Slope	R	R^2	Slope	R	R^2
			Tropospheric			
NH Pole	1.92	0.39	0.143	1.69	0.97	0.946
NH Mid-latitudes	5.01	0.81	0.660	3.78	0.98	0.951
Tropics	3.17	0.73	0.531	3.05	0.53	0.280
SH Mid-latitudes	1.69	0.39	0.154	2.71	0.81	0.663
SH Pole	0.86	0.64	0.412	0.40	0.26	0.067
Global	2.25	0.39	0.149	2.53	0.95	0.899
			Stratospheric			
NH Pole	-0.25	-0.67	0.444	1.44	0.91	0.829
NH Mid-latitudes	-0.28	-0.52	0.267	1.54	0.97	0.942
Tropics	0.22	0.54	0.288	1.00	0.50	0.248
SH Mid-latitudes	0.06	0.13	0.018	1.15	0.54	0.291
SH Pole	0.13	0.32	0.105	0.07	0.04	0.001
Global	-0.35	-0.45	0.202	1.83	0.97	0.939
			Total			
NH Pole	-0.23	-0.64	0.410	1.50	0.95	0.905
NH Mid-latitudes	-0.28	-0.39	0.56	2.08	0.99	0.994
Tropics	0.16	0.43	0.182	1.49	0.73	0.539
SH Mid-latitudes	-0.05	-0.13	0.018	1.53	0.82	0.680
SH Pole	0.08	0.22	0.048	0.15	0.10	0.010
Global	-0.38	-0.44	0.191	2.00	0.98	0.954

the troposphere, as its influence is attenuated upwards (eq. 3.46). In fact, dLWRE/dTs is lower by a factor of 2-3, especially for the regions with high surface temperatures (e.g., NH midlatitudes, Tropics), which showed the largest response of the LWRE to surface temperature in the troposphere.

Contrary to the troposphere, we observe negative slopes and anti-correlations between the LWRE and O_3 in the NH, which have their basis on the seasonal patterns of the two parameters (color scale). Stratospheric ozone maxima in the NH appear during late winter and spring, as ozone is driven mainly by the Brewer-Dobson circulation; especially for the NH Pole, this is the period when ozone-rich air is trapped in the Arctic Polar Vortex. However, during the same period, the surface temperature in these bands is significantly low following the winter, which results to reduced flux being emitted from Earth, and therefore reduced absorption (and consequently low LWRE). On the other hand, during late summer, when the surface temperature is larger and the emitted radiation from the Earth's surface is greater, the absorption from ozone is enhanced, resulting to larger LWRE values, as seen here, although stratospheric ozone itself has already declined. The effect of the seasonality is better explained in Sect. 8.5.

Finally, we should note that the SH Pole is governed by the lack of sensitivity due to low surface temperatures, as mentioned previously. The average surface temperature of this band can reach as low as 230 K during local winter, while it does not go higher than 272 K during local summer. Furthermore, a large number of the observations in this region is discarded because of the low sensitivity, influencing its spatial representation. Indicative of the difficulties are the low slopes and correlations the stratospheric LWRE exhibits with the surface temperature (0.07 and 0.04, respectively), which explain about 0.1% of the data.

Total LWRE

Figure 8.11 shows the relation of the LWRE to ozone (left) and to surface temperature (right), for the total amounts, while the respective linear regression slopes, correlation and determination coefficients are included in Table 8.2. Moreover, the linear regression of the stratospheric amounts is also shown in red. The slopes of the total LWRE with ozone and surface temperature follow in general the patterns of the stratospheric LWRE, mainly in the Polar regions, where the stratospheric contribution is larger, as well as in the seasonality patterns, indicated by the color scale. This is to be expected, as the tropospheric LWRE corresponds to roughly between 16 and 35% (from the Poles towards the Tropics) of the total LWRE, as it is with the tropospheric and the total O_3. The deviation between the regression lines regarding the total LWRE versus the stratospheric LWRE in the midlatitudes and the Tropics is attributed to the greater influence from the troposphere.

We should also stand on the relation between the total LWRE and total ozone in the SH midlatitudes, where the regression (black line) does not comply with either the stratospheric regression (red line) or the tropospheric one (fig. 8.9). In fact, it implies anti-correlation between the two parameters, contrary to the previous correlations. This result should be considered with caution, given the low tropospheric and stratospheric LWRE correlations (and slopes) with O_3, but also given the unrealistic "split" mentioned in the stratospheric SH midlatitudes correlations.

In summary, we can conclude to the following results:

- There is a strong relation between the LWRE and the surface temperature, particularly in the troposphere, where the emission from the surface has a stronger influence.
- The above is more prominent in the NH midlatitudes and the Tropics, which exhibit high surface temperatures, compared to the ocean governed SH, and the smaller changes in the ocean surface temperature.

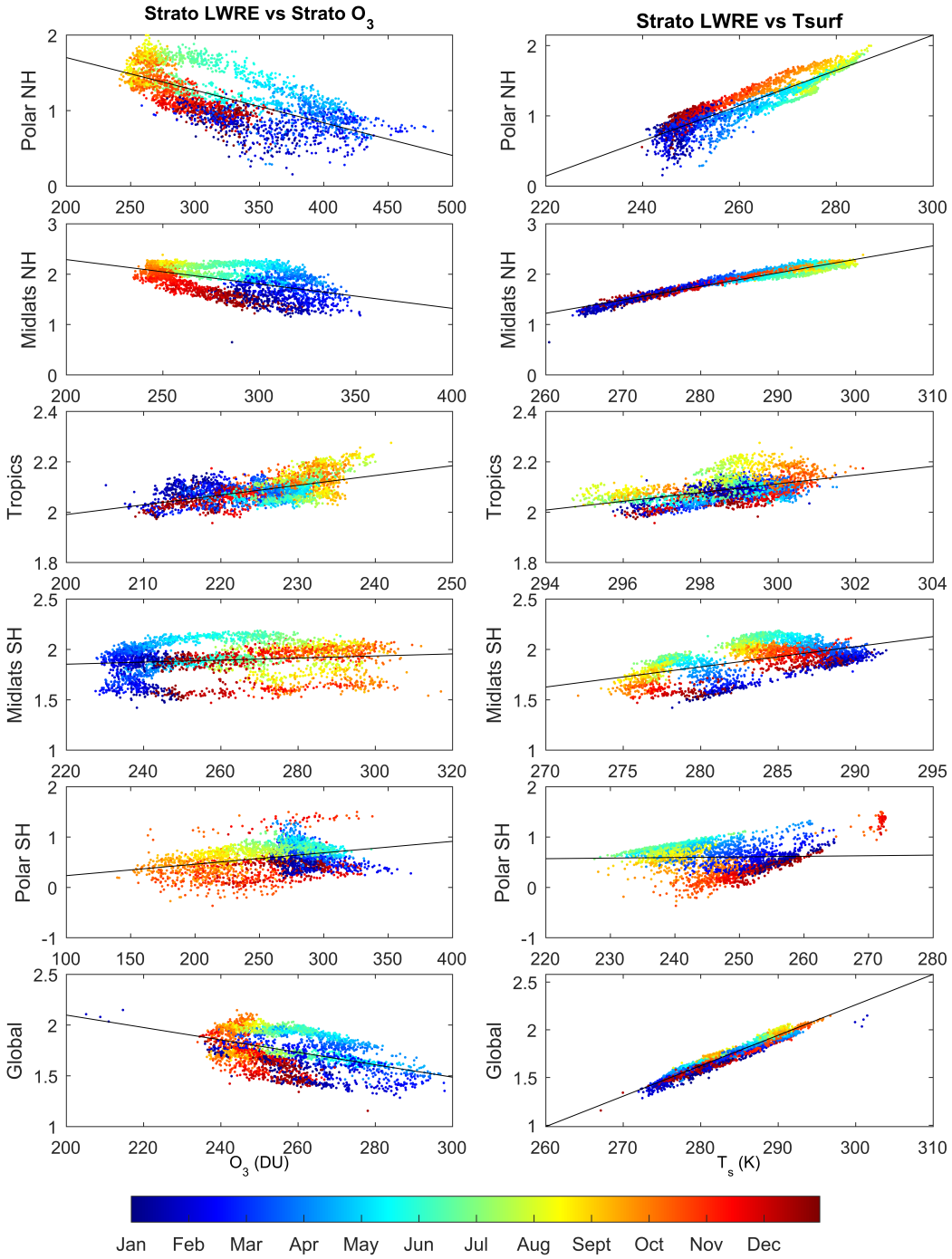

FIGURE 8.10: Scatter plot of daily averages between LWRE and O_3 (left) or surface temperature (right) in the stratosphere, distinguished in five latitudinal bands and globally. The vertical axes represent the LWRE (in Wm^{-2}). The color scale represents the days of the year. The black lines represent the linear regression.

- The Tropics show large spread of values, and the linear correlation is not sufficient to describe the relation. However, there is strong presence of water vapor, which masks both ozone and surface temperature effects.

- The SH Pole correlations pose inconsistencies, mainly because of the low sensitivity due to the very low temperatures, but also due to the lack of spatial sampling for

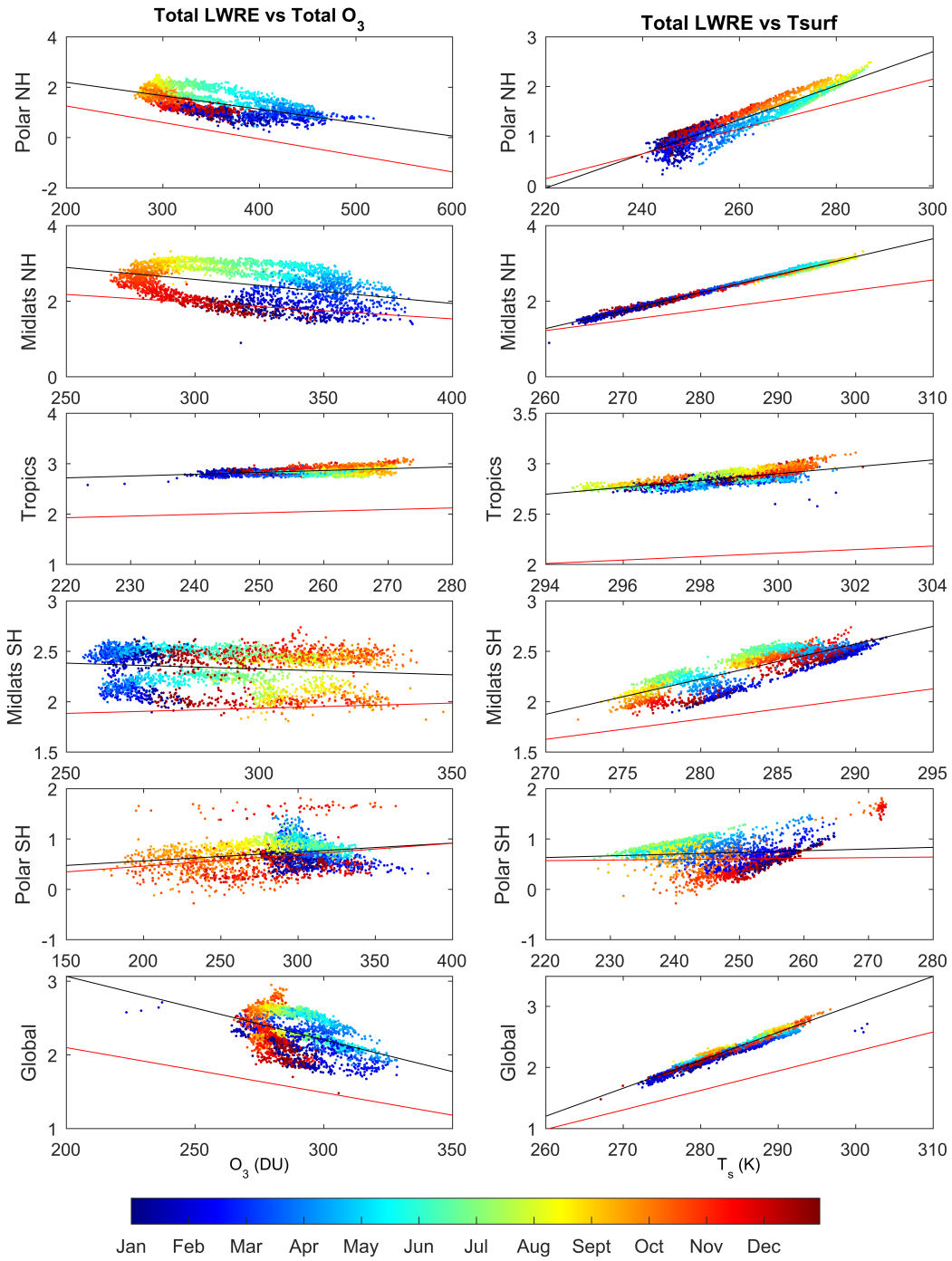

FIGURE 8.11: Scatter plot of daily averages between total LWRE and O_3 (left) or surface temperature (right), distinguished in five latitudinal bands and globally. The vertical axes represent the LWRE (in Wm^{-2}). The color scale represents the days of the year. The black lines represent the linear regression. The red lines represent the linear regression of the stratospheric amounts for comparison.

the same reasons.

8.4.2 Overview

As already discussed, it is difficult to disentangle the effects of ozone and surface temperature on the LWRE. The surface temperature influences the LWRE through the radiances, which are accounted for in the form of the Jacobians during the retrieval. Moreover, ozone is accounted for through the Jacobians, but also through eq. 7.9.

The above analysis points to the equation that defines the LWRE (eq. 7.9). The calculation of the surface temperature Jacobians ($\partial L/\partial T_{surf}$) or the Jacobians of the air temperature profile ($\partial L/\partial T_l$), with a formulation similar to the IRKs, would have made easier to isolate and study the temperature effect on the LWRE, in addition to the Jacobians of O_3 that are used in this study. Note however that the calculation of such derivatives is time and resources consuming. Finally, we have pointed out that water vapor is also an important driver, especially in regions where its presence is strong, such as the Tropics.

8.5 O_3 LWRE variations over time

In this section we present for the very first time the complete time series of O_3 LWRE, as it was derived from IASI and FORLI. Before doing so however, we explain a few points that are necessary to have in mind for the discussion.

As discussed in Sect. 3.5 and 4.3, in the study of climate and climate change there are many different contributions, from the chemical constituents of the atmosphere to the atmospheric dynamics, the surface scene and others. A change in one of the parameters results in a change in climate, which is translated to changes in the radiative budget (radiative forcing) of the overall system. It is however difficult to disentangle the different sources of climate forcings and their feedback, especially from observations, and furthermore, the radiative forcing is the result of a change, taking into account all other contributions as well. The O_3 LWRE represents an estimation of the real-time radiative budget that corresponds to ozone absorption, in the particular atmospheric state at any time and location. The study of the LWRE variations over time aims to describe the change of the radiative budget associated with ozone absorption through time and identify possible patterns throughout the year and inter-annually.

Regarding the data used, the record of IASI-A observations covers the period from 30/09/2007 to 10/01/2017. As already shown in Table 8.1, during this period, there

have been algorithm updates and instrumental maintenance processes that result to disruptions in the time series. To ensure continuity of the data record, we present the complete time series, however, the prolonged time periods of disruption are ultimately not taken into account for the analysis. The time series analysis is performed on latitudinal averages: NH Polar region, between 90° N and 60° N; NH mid-latitude region, between 60° N and 30° N; the Tropics, between 30° N and 30° S; SH mid-latitude region, between 30° S and 60° S; SH Polar region, between 60° S and 90° S; in addition to the global average, for the tropospheric, stratospheric and total amounts.

8.5.1 LWRE seasonality

In the previous section, the relation between the LWRE and O_3 or surface temperature shows a strong dependence on the seasons, which mainly reflects the role of the surface temperature on the radiances, hence, on the O_3 LWRE, especially in the troposphere, as well as on the sensitivity of the IASI measurements to O_3 changes.

Tropospheric LWRE

Figure 8.12 shows the daily variations of the tropospheric LWRE on the left, tropospheric O_3 in the middle and the respective variations of the surface temperature on the right. Lower to higher values run from the center (minimum) of the figure/circle towards the edges (maximum), while each year of data is indicated by a different color. The days start on 1 January of each year, marked at 3 o'clock, and running anti-clockwise.

In consistency with the correlation patterns described in the previous section, and provided in fig. 8.9, it is observed that, in general in the troposphere, the O_3 LWRE seasonality reproduces that of the surface temperature, while tropospheric O_3 is characterized by a shift in time in its minima and maxima, approximately one month earlier than those of the LWRE and surface temperature. More specifically, in a zonal basis, we observe that:

- In the NH polar and midlatitudes regions, the tropospheric O_3 LWRE and the surface temperature show their minima and maxima during the local winter and summer, respectively. On the contrary, the minima and maxima of the tropospheric O_3 seasonality develop earlier. The O_3 maxima in the polar NH are found in April, as a result of the large stratospheric contribution during that period, due to the medium vertical sensitivity of IASI in lower altitudes in these latitudes, to tropopause height variations or to stratospheric-tropospheric exchange processes [Wespes et al., 2016].

In the NH midlatitudes, the O_3 are observed in spring/summer, in agreement with the photochemical production of O_3 from anthropogenic precursor emissions.

- In the Tropics, the O_3 LWRE maxima appear in November and June, and the minima in August and February, consistent with the surface temperature seasonality, and 1-2 months later than the respective tropospheric O_3 pattern. This region appears to have two maxima and minima in a year, an effect caused by the merging of the whole tropical band in one.

- The O_3 LWRE in the SH midlatitudes exhibits maxima around January-February (local summer) and minima around July (local winter), as does the surface temperature, while tropospheric O_3 shows prolonged maxima during October-February, associated with biomass burning, and minima around June.

- An exception is observed in the SH Pole on the pattern of local summer and winter. The surface temperature maxima appear during January (local summer), while its minima span from May to October (local autumn, winter and spring). On the other hand, tropospheric O_3 maxima appear during July - August (local winter) - highly variable -, and the minima around February. The tropospheric LWRE maxima appear around September - October, influenced by ozone, while the minima appear in May, constrained by the low surface temperatures. However, as discussed in the previous section, the SH polar region poses difficulties in the observations due to the coverage of ice and the very low temperatures, causing problems in the measured spectra and therefore, in the retrieved parameters; tropospheric amounts are greatly affected in such cases, as the instrument sensitivity is very low, and the results should be considered with caution.

- Finally, the global tropospheric O_3 LWRE seasonality appears to be driven mainly by the NH, which exhibits the greatest variations, following the significant variations of ozone and surface temperature, due to land domination. In the NH Pole the LWRE reaches as low as $30\,\mathrm{mWm^{-2}}$ over the winter period, while it increases to around $500\,\mathrm{mWm^{-2}}$ during the summer. Likewise, the NH midlatitudes exhibit a variation between $200\,\mathrm{mWm^{-2}}$ and $1\,\mathrm{Wm^{-2}}$, during winter and summer respectively. The lowest variations of the tropospheric O_3 LWRE are found in the Tropics, ranging from 700 to $900\,\mathrm{mWm^{-2}}$.

Some discrepancies appear in the time series presented above. There are especially two periods, in 2010 and 2015, where the data suffer from abrupt increases and/or decreases, which appear as "jumps" creating gaps in between the different years, or spikes. In 2010, the discrepancies appear as extremely large values of O_3 (in all bands), LWRE

and surface temperature (mainly in the Tropics and the SH), around mid-September to early December, corresponding to retrieval algorithm updates, stated in lines 2 and 3 of Table 8.1. Likewise, in 2015 there is a prolonged period suffering from updates, corrections and calibrations, appearing mostly on the surface temperature and the LWRE. These span from mid-April to the end of 2015, and correspond to the changes stated in lines 7, 8, 9 and 10 in Table 8.1. Despite the discrepancies, the tropospheric O_3 LWRE exhibits a slight decrease over the years, with the exception of the Tropics, the SH Pole and the global average, which show an increasing LWRE. The respective evolutions are presented later, in Sect. 8.5.2.

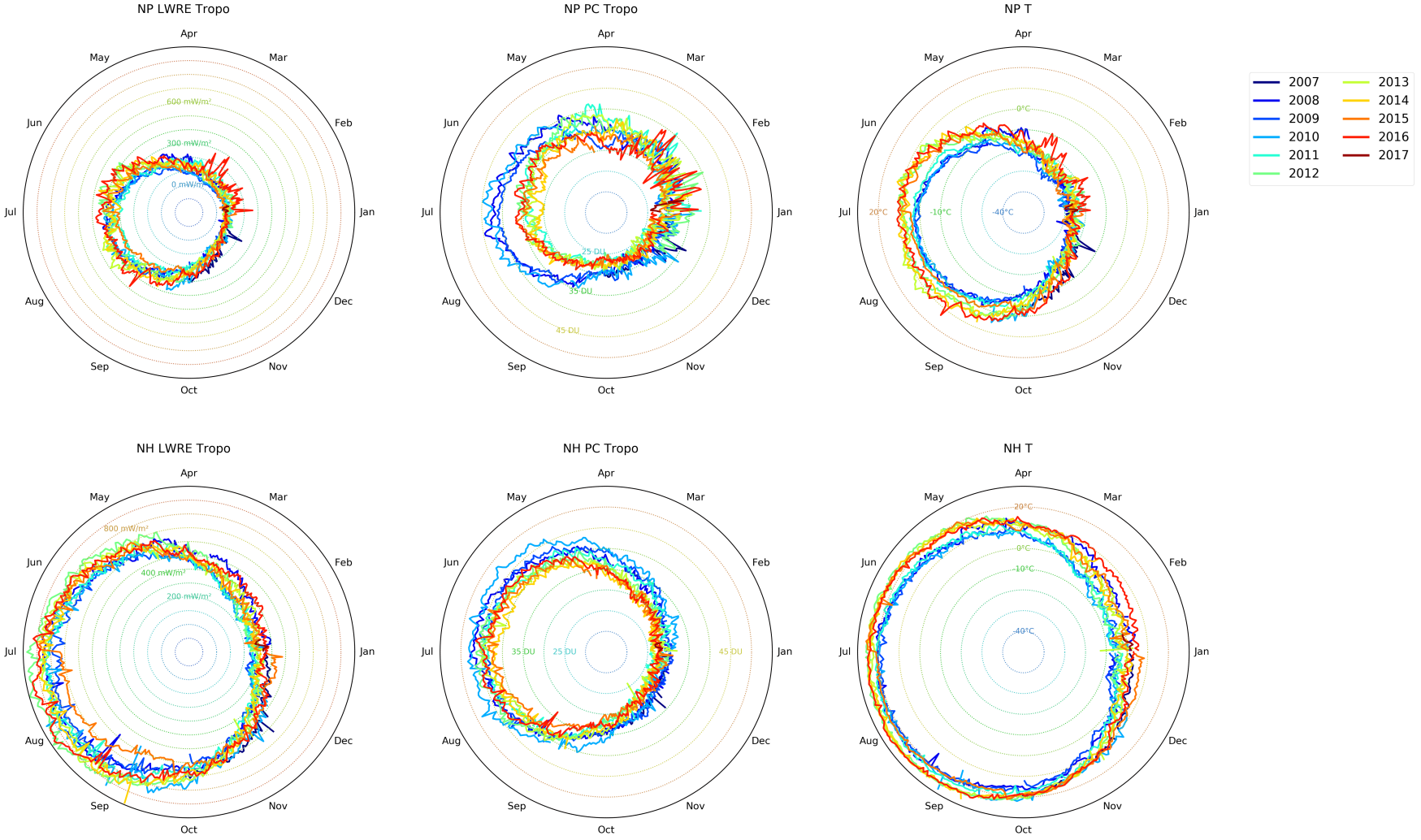

FIGURE 8.12: Time series of tropospheric O_3 LWRE ($mW\,m^{-2}$) (left), tropospheric O_3 column (DU) (middle) and surface temperature (K) (right), for NH Pole (NP - top) and NH midlatitudes (NH - bottom). Only day overpass. Data run from 30/09/2007 to 10/01/2017. Note the IASI instrument and software changes, especially in autumn 2010 (Table 8.1).

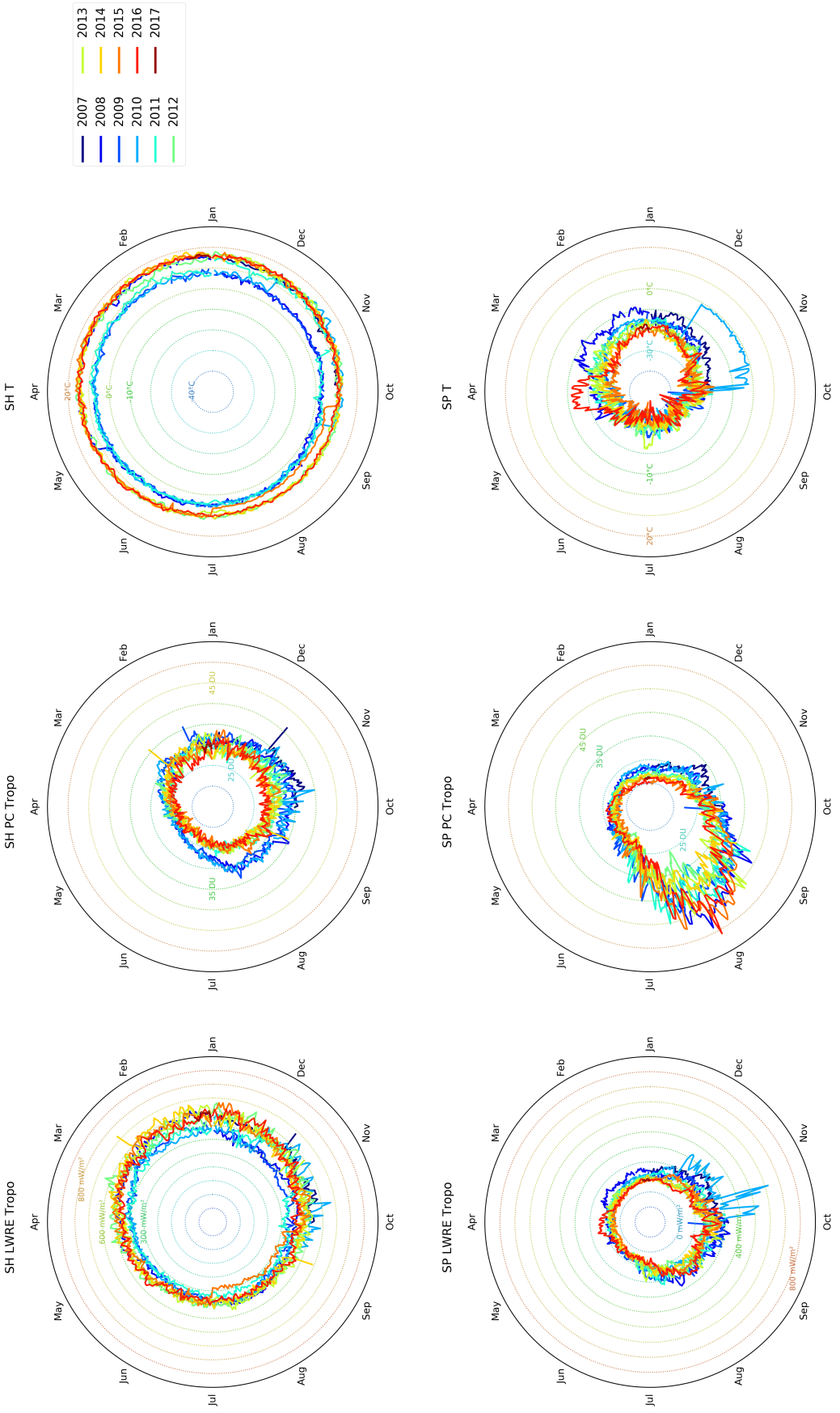

FIGURE 8.12: Continued figure. Same as before, but for SH midlatitudes (SH - top) and SH Pole (SP - bottom).

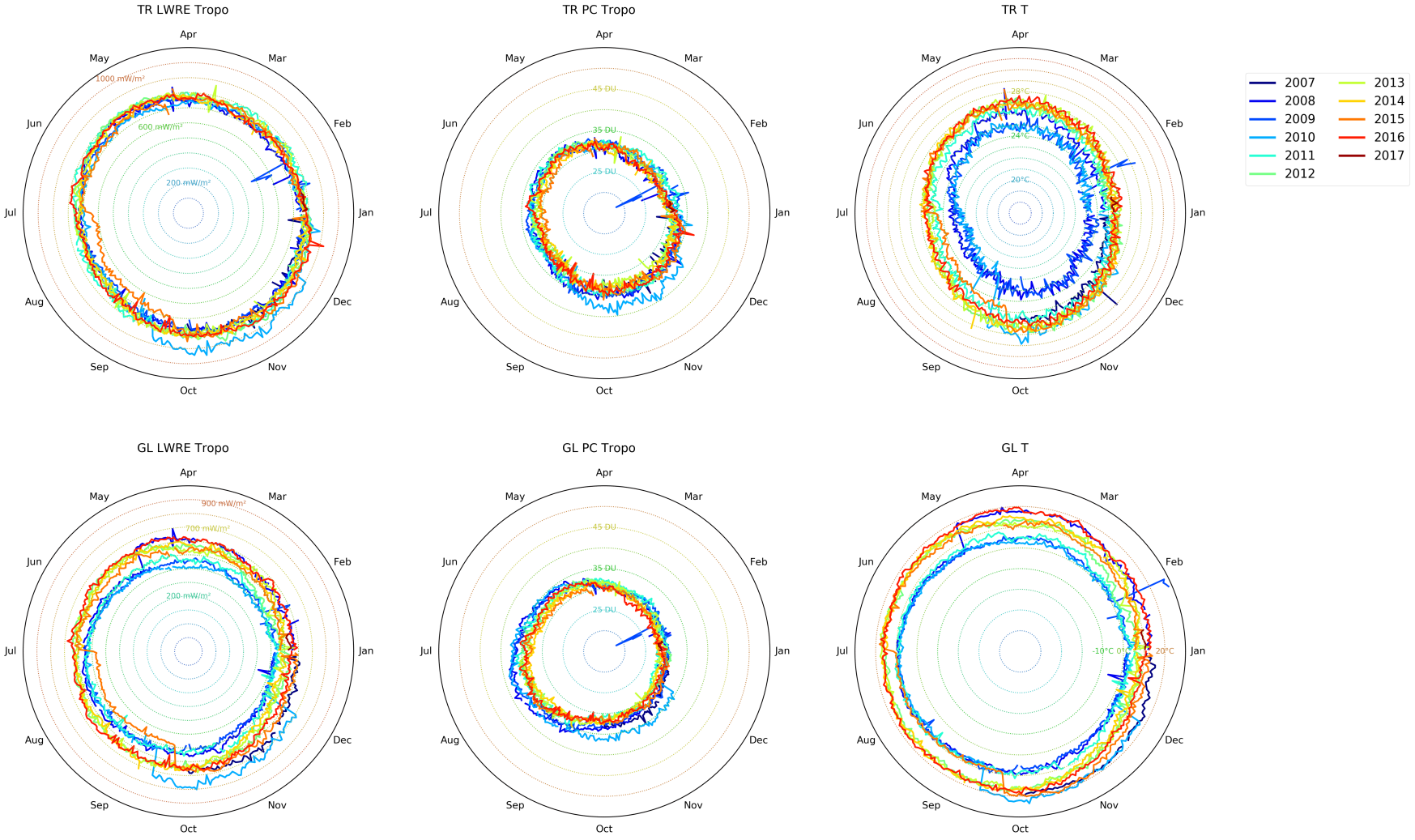

FIGURE 8.12: Continued figure. Same as before, but for Tropics (TR - top) and global average (GL - bottom).

Stratospheric LWRE

Figure 8.13 shows the daily variations of the stratospheric LWRE on the left, the respective stratospheric O_3 variations in the middle and those of the surface temperature on the right. Contrary to the seasonality of the tropospheric O_3 LWRE, in the stratosphere the LWRE shows better consistency with the stratospheric O_3 seasonality patterns, than with the surface temperature. In principle, ozone seasonal distribution in the stratosphere is driven by the Brewer-Dobson circulation. The ozone minima and maxima occur earlier than those in the troposphere, as the ozone-rich air ascends from the tropical troposphere, travels through the stratosphere from the Tropics pole-wards and then descends into the troposphere in the higher latitudes. As a result, in the NH O_3 maxima appear in late winter and spring and the minima in autumn; in the Tropics, stratospheric O_3 maxima occur between September and November, and the minima around February; in the SH midlatitudes, following the Brewer-Dobson circulation, the maxima appear in September-October and the minima around March; in the SH Pole, the stratospheric O_3 maxima appear during local winter (June-July) and the minima around October, marked by the ozone loss and the formation of the O_3-hole.

Regarding the stratospheric O_3 LWRE, in a zonal basis we observe that:

- In the NH polar and midlatitude regions, the LWRE seasonality patterns are similar to those in the troposphere, following the surface temperature seasonality. However, the LWRE maxima and minima occur slightly earlier (a month or less) than those of the surface temperature, driven by the O_3 maxima and minima. This is consistent with the strong correlations found between the stratospheric O_3 LWRE and the surface temperature in Sect. 8.4, although weaker than in the troposphere, but also with the anti-correlations observed with O_3, due to the different seasonality patterns.

- In the Tropics, the stratospheric LWRE seasonality is consistent with the stratospheric O_3 seasonality (minima and maxima occur approximately at the same time), though the annual and inter-annual variations are greatly affected by the respective variations of the surface temperature.

- Similar to the Tropics is the situation in the SH midlatitudes, where the stratospheric LWRE seasonality is in accordance with that of stratospheric O_3.

- In the SH Pole, the stratospheric LWRE is highly variable, especially between December and April, mainly due to the sensitivity difficulties already described. However, one can observed that during June - August the LWRE is driven by the

O_3 patterns, as the surface temperature is at its minimum, while the LWRE minima occur around October - November, within the Antarctic O_3 hole period (September - November). The stratospheric LWRE in this band is greatly constrained by the variations of ozone, especially during the ozone loss period, where the very low LWRE values imply limited absorption by ozone, resulting in the escape of outgoing longwave radiation, which further leads to cooling of the stratosphere and negative radiative effect.

- Finally, the global stratospheric O_3 LWRE seasonality is greatly influenced by the NH, which similar to the troposphere, exhibits the largest variations. The O_3 LWRE in the NH Pole varies from as low as $0.2\,\mathrm{Wm}^{-2}$ up to $2\,\mathrm{Wm}^{-2}$, while the NH midlatitudes show variations from 1.2 to $2.4\,\mathrm{Wm}^{-2}$. The weakest variations are found again in the Tropics, where the stratospheric O_3 LWRE varies between 1.9 and $2.25\,\mathrm{Wm}^{-2}$. Note also the different order of magnitude of the stratospheric LWRE, which is larger by a factor of 2-3 compared to the tropospheric LWRE.

Stratospheric O_3 LWRE and O_3 time series experience discrepancies similar to those observed in the troposphere previously, stated in lines 2, 3 (for 2010) and 7, 8, 9, 10 (for 2015) in Table 8.1. Nonetheless, the stratospheric O_3 LWRE exhibits a general decrease over the years, with the exception of the NH midlatitudes, and is discussed in Sect. 8.5.2.

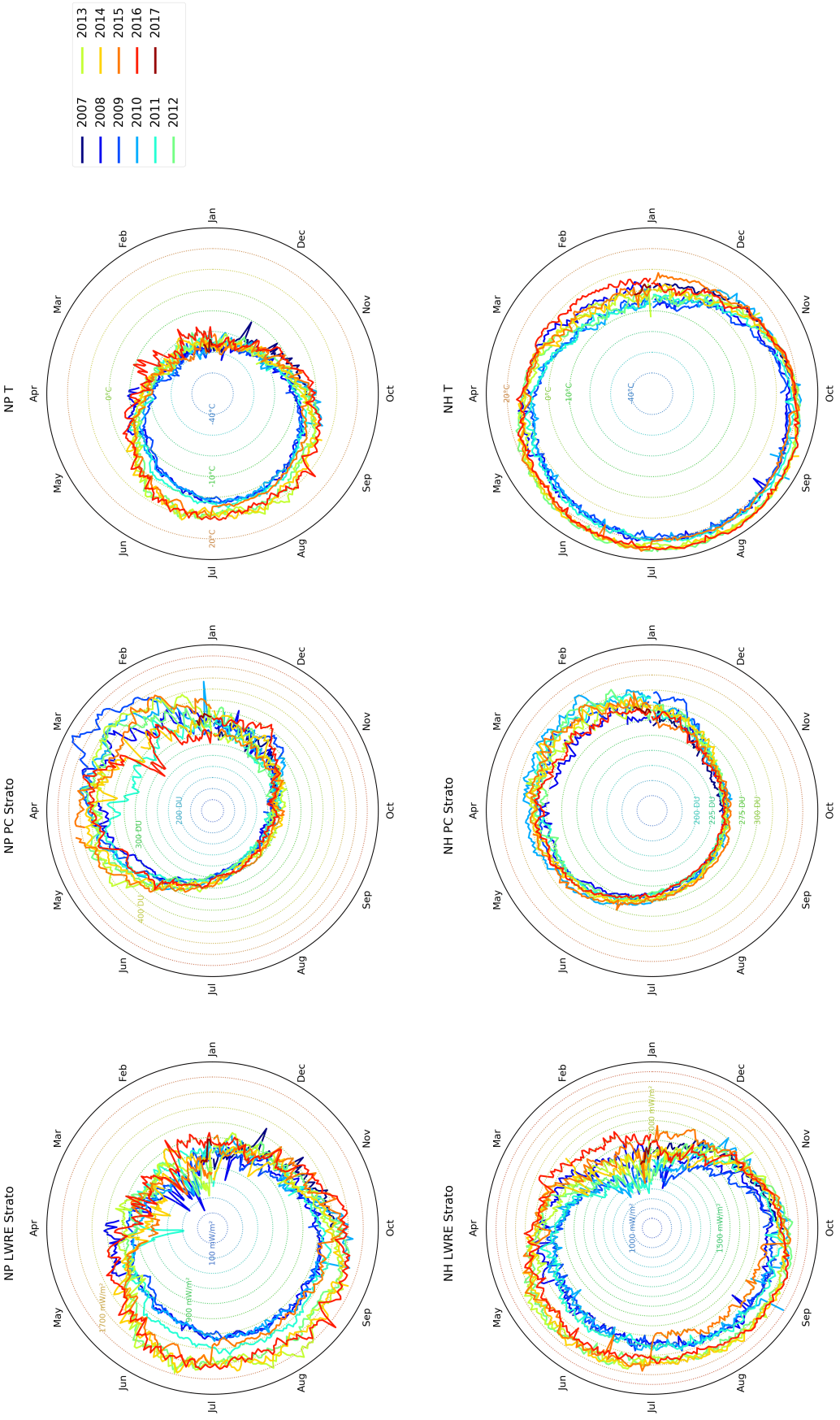

FIGURE 8.13: Time series of stratospheric O_3 LWRE (mW m^{-2}) (left), stratospheric O_3 column (DU) (middle) and surface temperature (K) (right), for NH Pole (NP - top) and NH midlatitudes (NH - bottom). Only day overpass. Data run from 30/09/2007 to 10/01/2017. Note the IASI instrument and software changes, especially in autumn 2010 (Table 8.1).

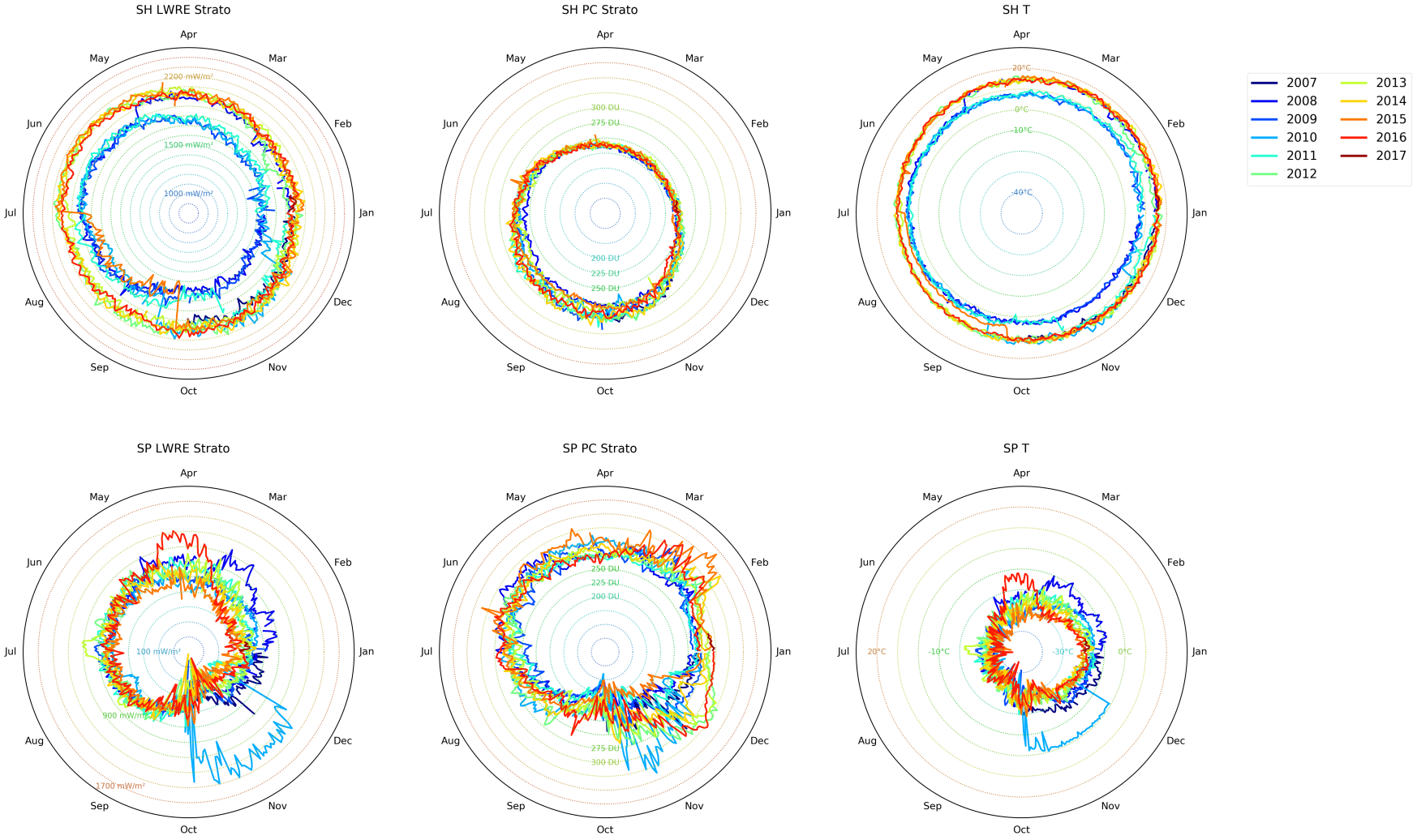

FIGURE 8.13: Continued figure. Same as before, but for SH midlatitudes (SH - top) and SH Pole (SP - bottom).

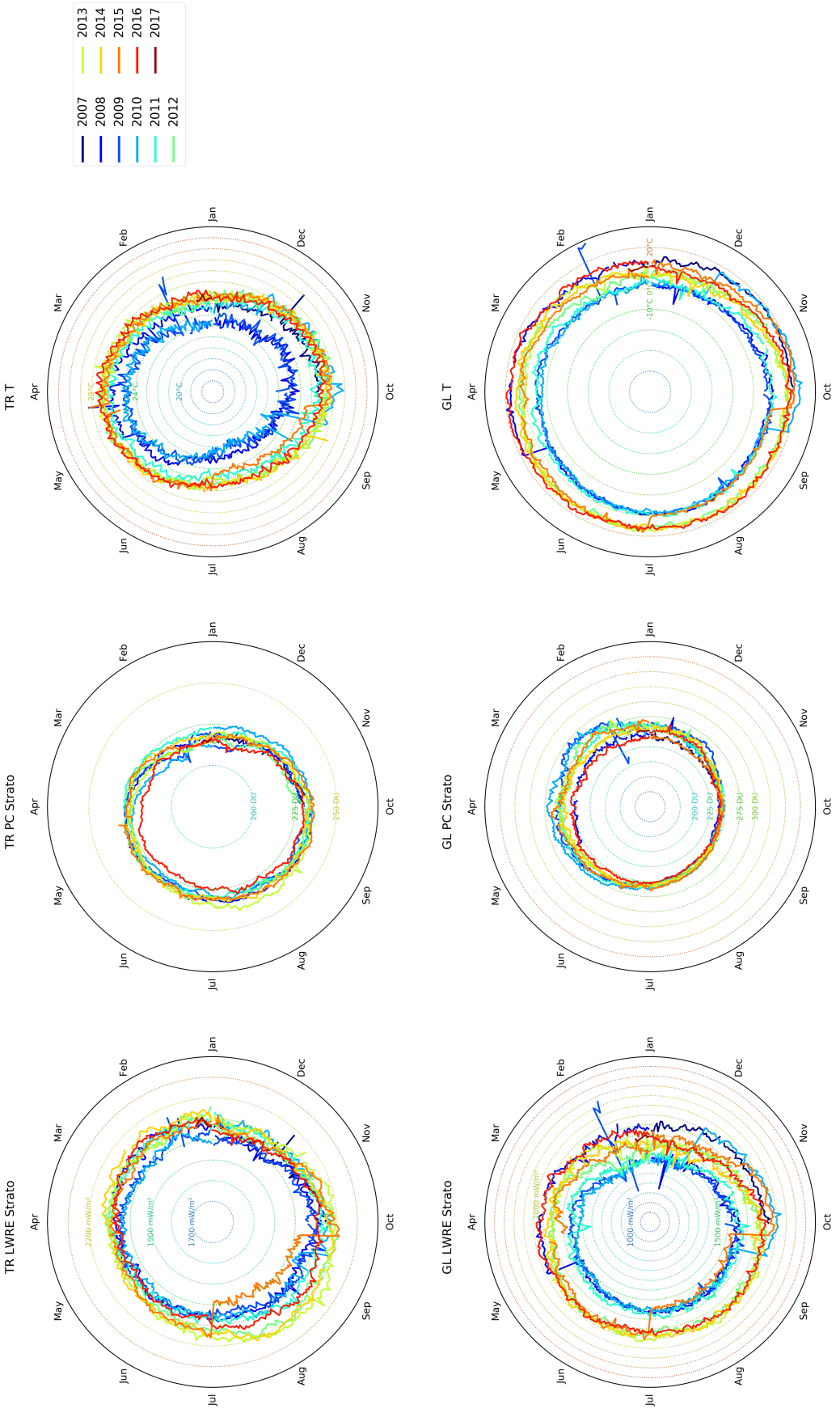

FIGURE 8.13: Continued figure. Same as before, but for Tropics (TR - top) and global average (GL - bottom).

Total LWRE

In order to have a sense of the overall variations, fig. 8.14 presents the time series of the total LWRE on the left, total ozone in the middle and surface temperature on the right. The time series of the total LWRE are in general following the patterns of the stratospheric LWRE, as well as the LWRE order of magnitude, due to the fact that stratospheric LWRE accounts for about 70-80% of the total LWRE, as it is for the stratospheric ozone.

However, in consistency with the results for the total O_3 LWRE in Sect. 8.4, the seasonality patterns of both NH and SH polar regions are greatly affected by the stratospheric LWRE seasonal patterns, where in general the stratospheric contribution is greater, while the NH and SH midlatitudes show greater contribution from the tropospheric LWRE. The greatest contribution of the troposphere in the O_3 LWRE is found in the Tropics and the global average. For example, in the tropical total O_3 LWRE, we clearly observe the effect of the tropospheric LWRE between April and June, while the time period between July and October is marked by the stratospheric LWRE patterns.

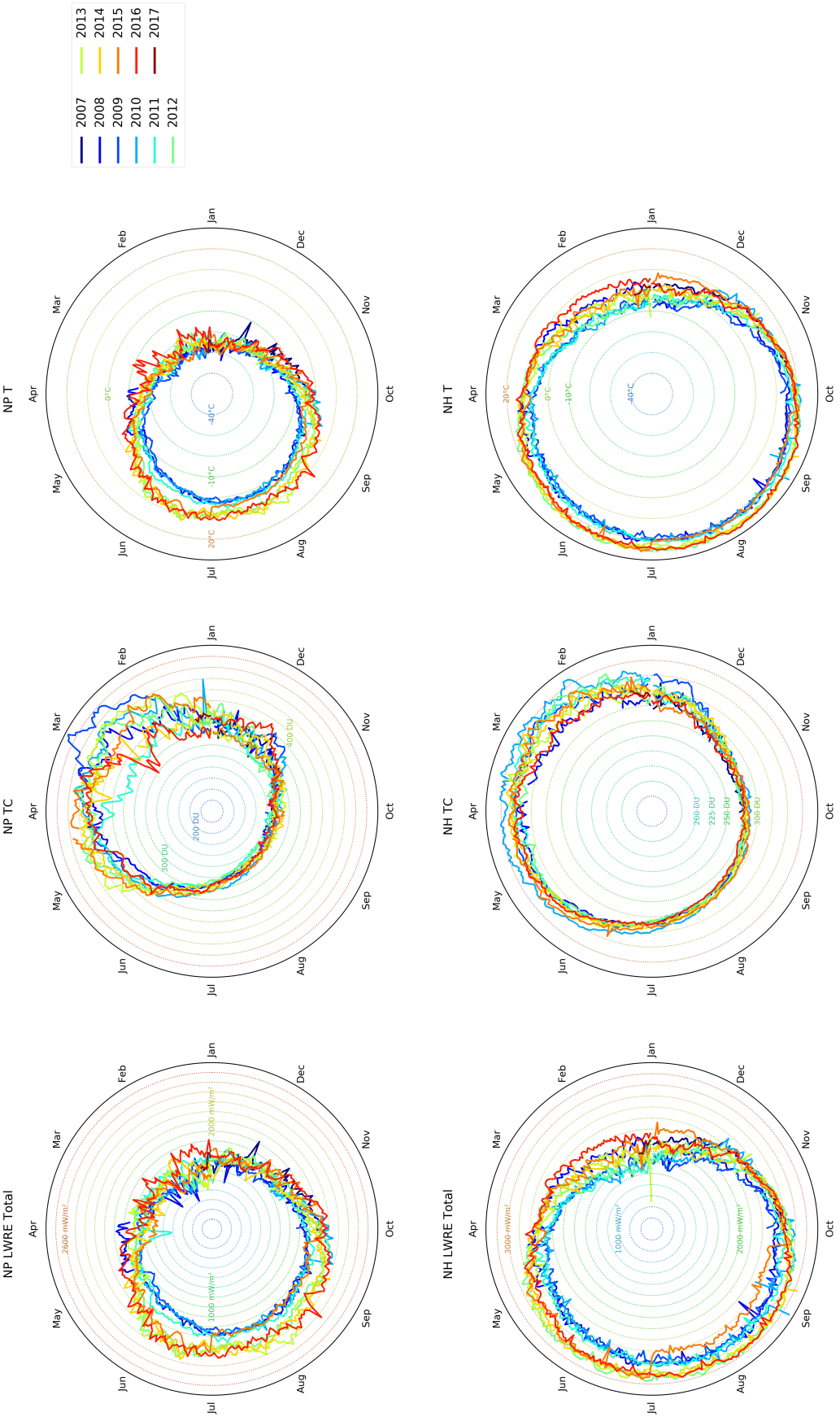

FIGURE 8.14: Time series of total O_3 LWRE ($mW\,m^{-2}$) (left), total O_3 column (DU) (middle) and surface temperature (K) (right), for NH Pole (NP - top) and NH midlatitudes (NH - bottom). Only day overpass. Data run from 30/09/2007 to 10/01/2017. Note the IASI instrument and software changes, especially in autumn 2010 (Table 8.1).

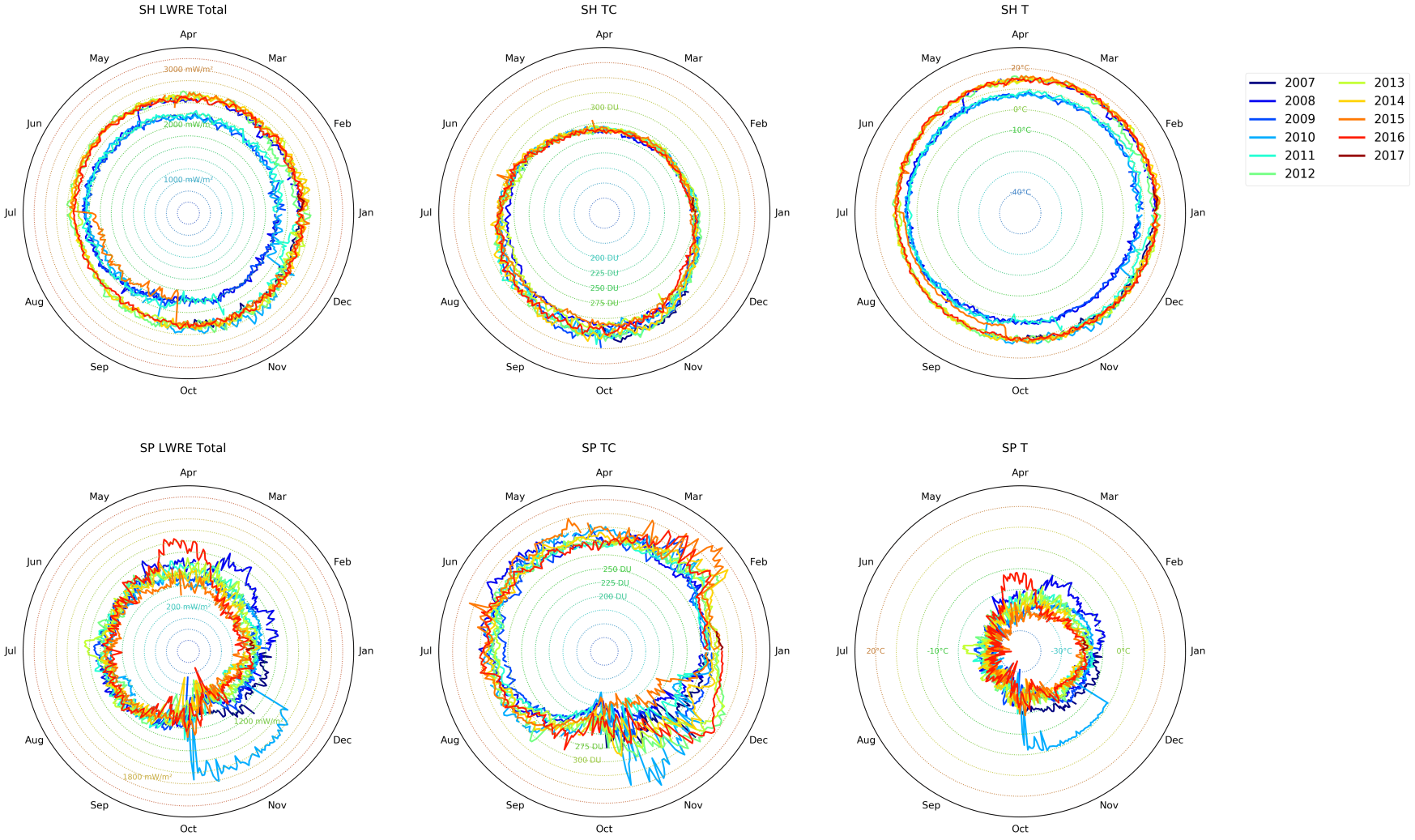

FIGURE 8.14: Continued figure. Same as before, but for SH midlatitudes (SH - top) and SH Pole (SP - bottom).

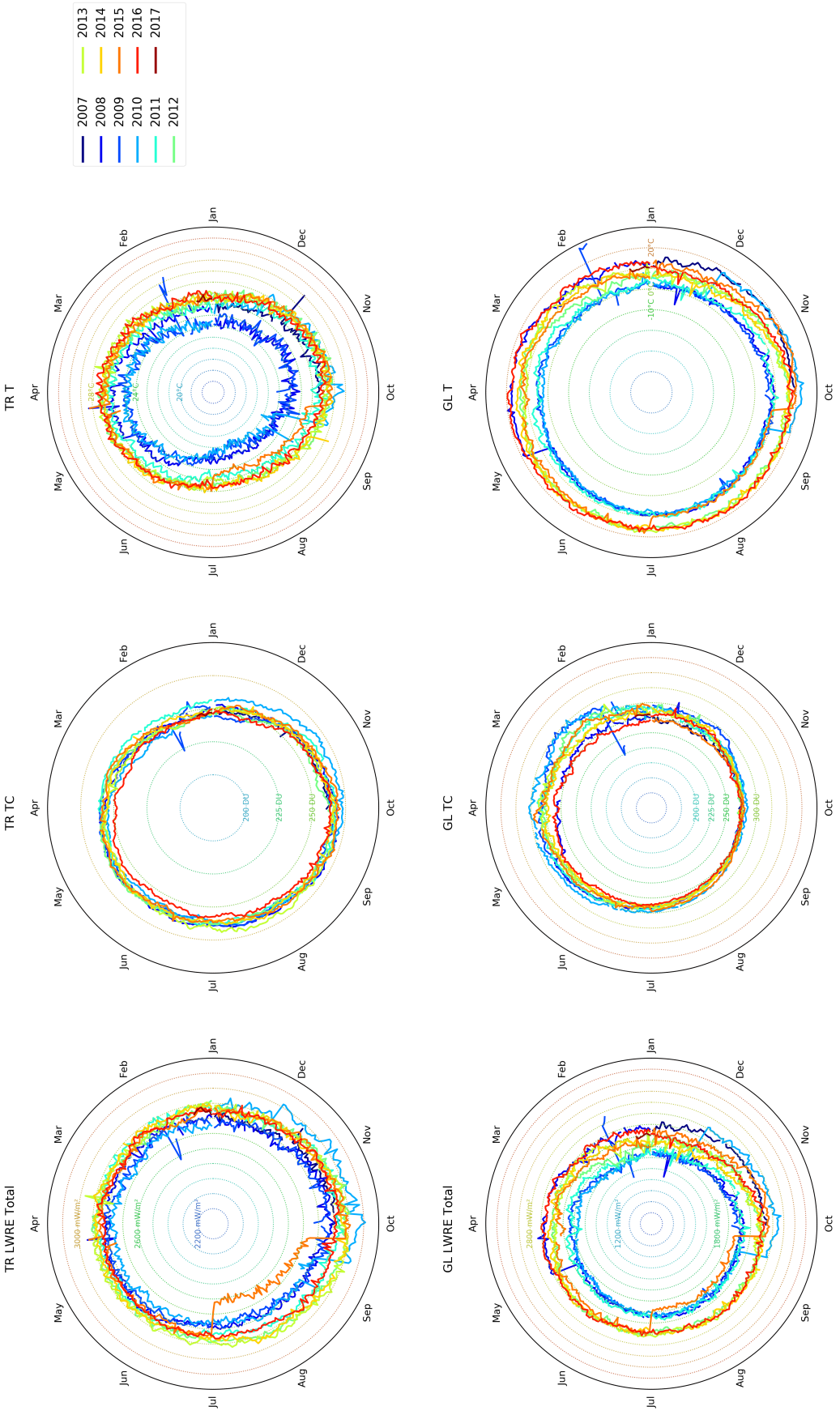

FIGURE 8.14: Continued figure. Same as before, but for Tropics (TR - top) and global average (GL - bottom).

8.5.2 LWRE temporal evolution

In addition to the time series, we have also calculated the evolution of the O_3 LWRE over the years. However, for the study of the trends we have limited the time period from 01/03/2012 to 10/01/2017, as before the starting day there are changes that influence the data (see Table 8.1). The trends are estimated by a single linear fit, to assess the sign and amplitude towards which the LWRE is changing with respect to climate and the radiative forcing.

The estimated trends for the zonal daily averages, as well as for the global average, are presented in fig. 8.15, 8.16, 8.17 and 8.18, for the surface temperature, as well as for the tropospheric, the stratospheric and the total LWRE and O_3, respectively. Our results suggest that the trend values in terms of zonal averages, and within the 95% confidence limit, are non- or almost non-significant, probably because of the short time period (5 years) used for the regression and of the large variations in the time series. The only latitudinal band that shows consistently significant trends is the Tropics, where the LWRE trends are more significant in the stratosphere than in the troposphere, possibly pointing to the effect of water vapor in the troposhere (see Sect. 8.2.2).

On the global scale, the average O_3 LWRE in the stratosphere shows a trend of -0.2 $\mathrm{mWm^{-2}y^{-1}}$, consistent with the decrease of stratospheric O_3 (-2.3 $\mathrm{DU\,y^{-1}}$). Though the observed trend is not significant, its low value is in agreement with the IPCC reports (IPCC [2013], Ch. 2 and 8), where the stratospheric ozone RF has not changed notably since the previous estimation (see Sect. 4.4.2).

In the troposphere, the global average LWRE shows a significant positive trend of around 5.4 $\mathrm{mWm^{-2}y^{-1}}$, despite the decrease of 0.16 $\mathrm{DU\,y^{-1}}$ of the tropospheric O_3, over the 5 years under study. The increase of the LWRE is in line with the increase of the global surface temperature (0.38 $\mathrm{K\,y^{-1}}$). Furthermore, the increasing O_3 LWRE is consistent with the increasing longwave RF of O_3 reported in IPCC, which was expected to further increase since the last assessment report [IPCC, 2013].

Finally, the total O_3 LWRE evolution in each latitudinal band, shown in fig. 8.18, is greatly affected by the sub-layer (tropospheric or stratospheric) that exhibits the largest slope in their trends. For example, in the NH midlatitudes, the LWRE exhibits a decrease consistent with that of the tropospheric LWRE, which is 8 times larger than the respective increase in the stratospheric LWRE. Reversely, in the Tropics, the total O_3 LWRE follows the stratospheric LWRE decrease, which in turn is larger than the tropospheric LWRE increase. The overall situation is assessed by the global average, where the total O_3

LWRE exhibits an increase similar to the tropospheric O_3 LWRE, as the change in the stratospheric LWRE is rather small, as discussed above.

The O_3 LWRE represents a metric of how ozone absorption impacts the radiative budget in a particular moment. Although the estimated trends are calculated on a short time period, and therefore do not stand as climatological results, the increasing tropospheric O_3 LWRE implies the heating of the troposphere, as it corresponds to greater absorption from ozone, and points towards the direction of climate change. The above highlights the importance of the atmospheric temperature profile on the LWRE, although it was not included in this study. Finally, the trends of the surface temperature are in the correct direction and order of magnitude with independent datasets (e.g., NASA GISS [1]) for the time period under study. Regarding ozone, its temporal evolution in the troposphere is under debate, as studies have shown strong inconsistencies between the tropospheric O_3 trends calculated from different satellite data sets (e.g., Gaudel et al. [2018]).

Similar results are also observed in the 5-year trend global distributions in Appendix C (see figures C.4 to C.6.

[1]GISS Surface Temperature Analysis, https://data.giss.nasa.gov/gistemp/maps/index_v3.html

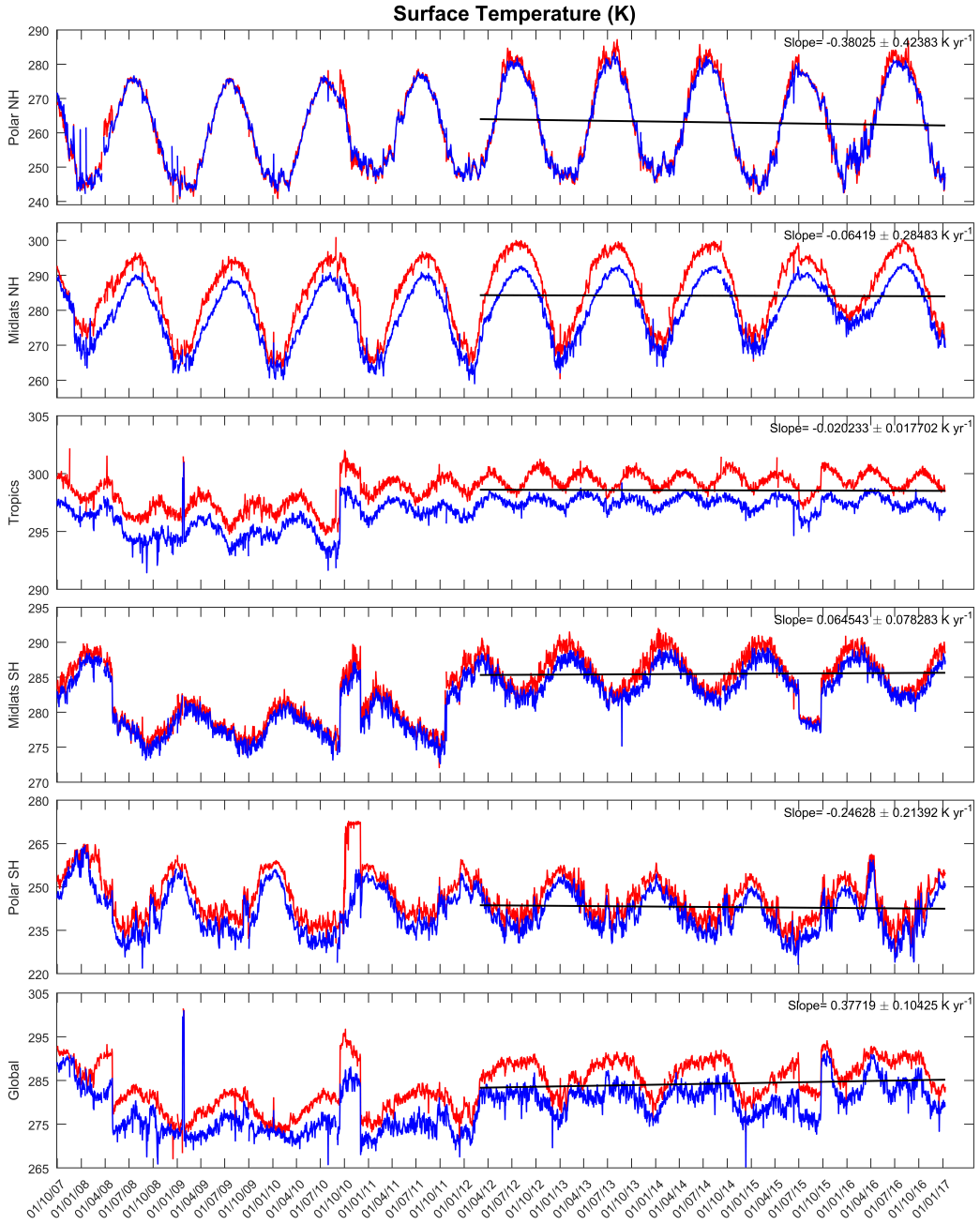

FIGURE 8.15: Daily time series of surface temperature (K), distinguished in five latitudinal bands and globally. Day and night overpasses are marked with red and blue color, respectively, while the black line denotes the trend. Data run from 30/09/2007 to 10/01/2017. Note the IASI instrument and software changes, especially in autumn 2010 (Table 8.1).

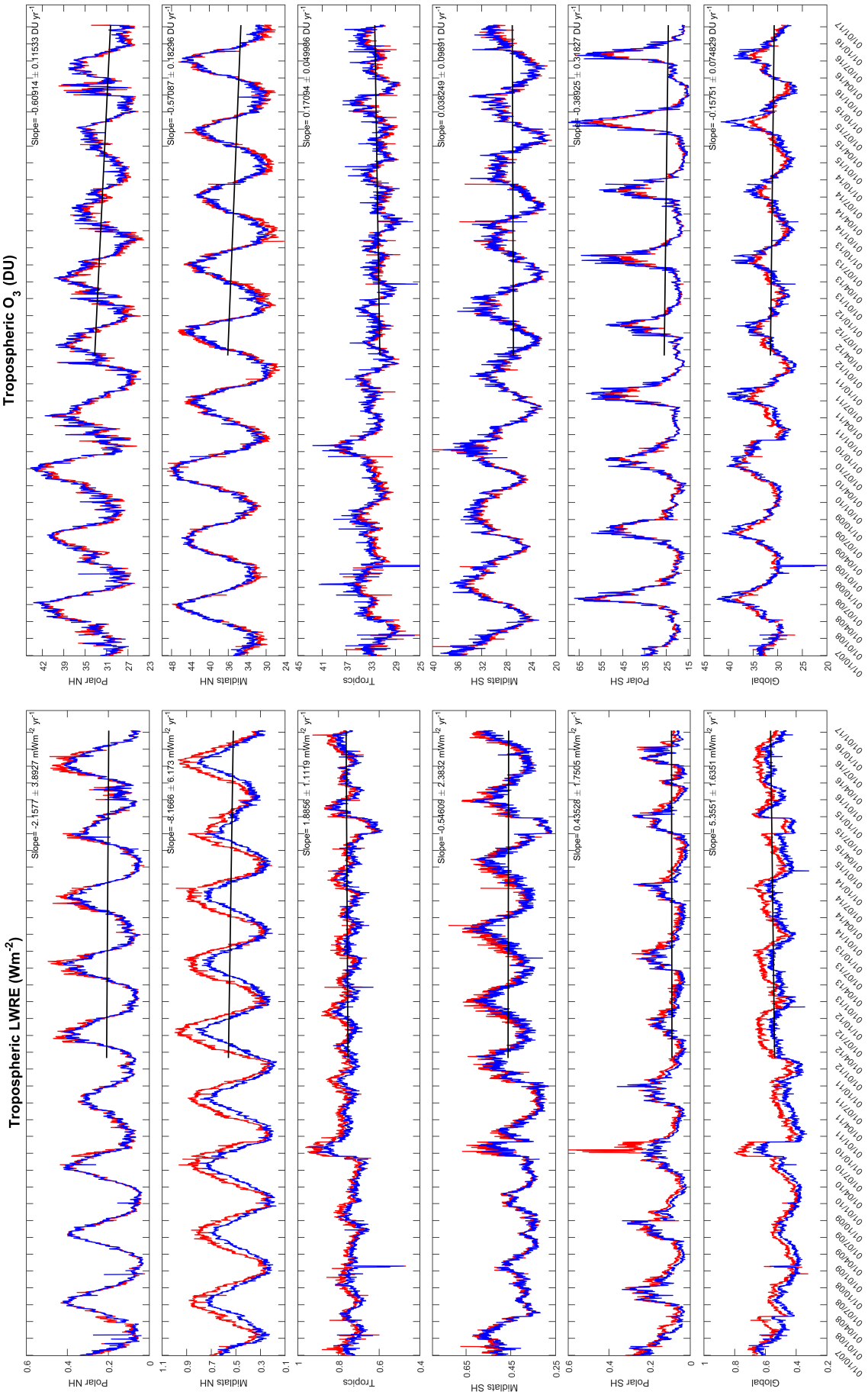

FIGURE 8.16: Daily time series of tropospheric O_3 LWRE (W m^{-2}) (left) and O_3 column (DU) (right), distinguished in five latitudinal bands and globally. Day and night overpasses are marked with red and blue color, respectively, while the black line denotes the trend. Data run from 30/09/2007 to 10/01/2017. Note the IASI instrument and software changes, especially in autumn 2010 (Table 8.1).

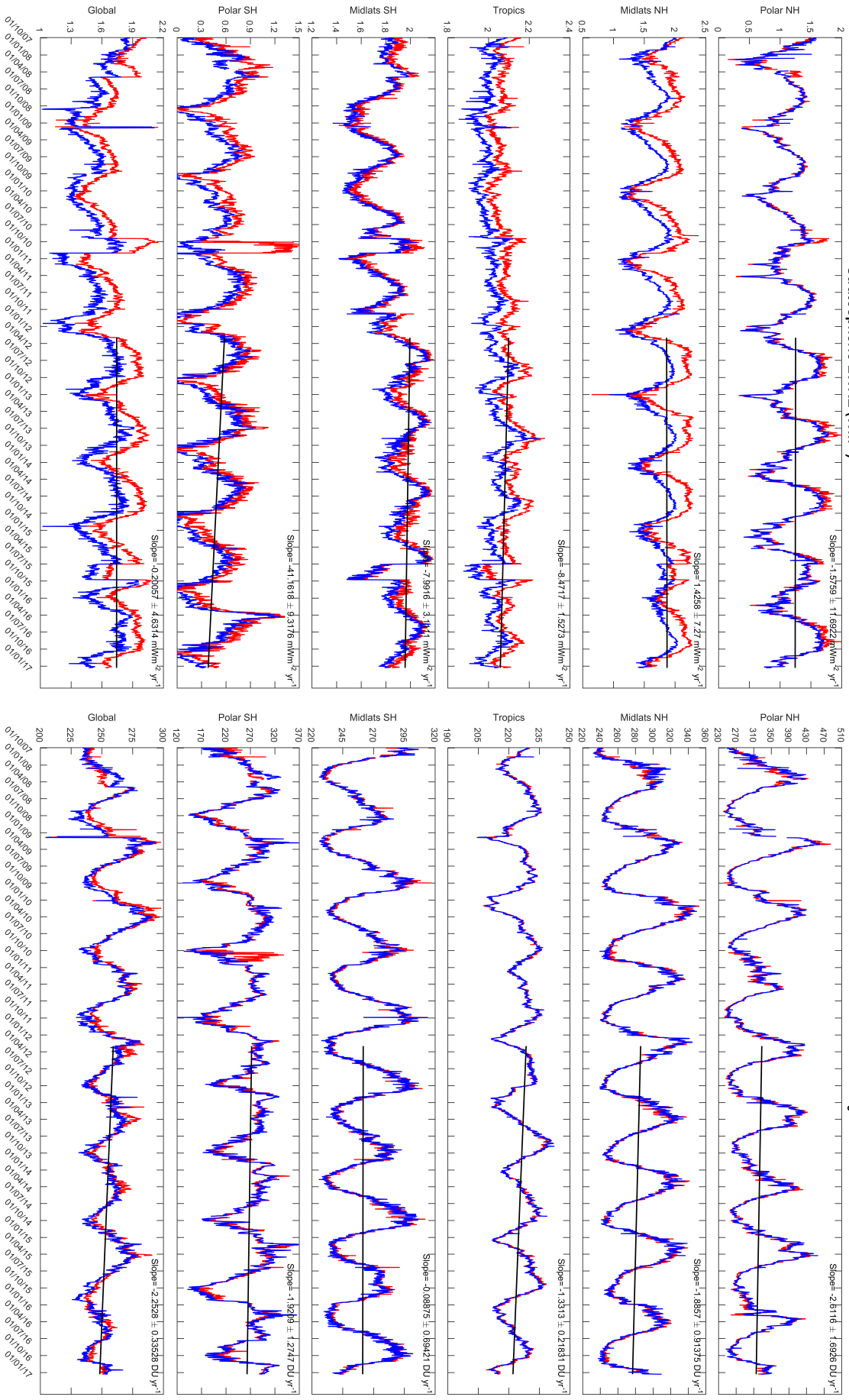

FIGURE 8.17: Daily time series of stratospheric O_3 LWRE (W m^{-2}) (left) and O_3 column (DU) (right), distinguished in five latitudinal bands and globally. Day and night overpasses are marked with red and blue color, respectively, while the black line denotes the trend. Data run from 30/09/2007 to 10/01/2017. Note the IASI instrument and software changes, especially in autumn 2010 (Table 8.1).

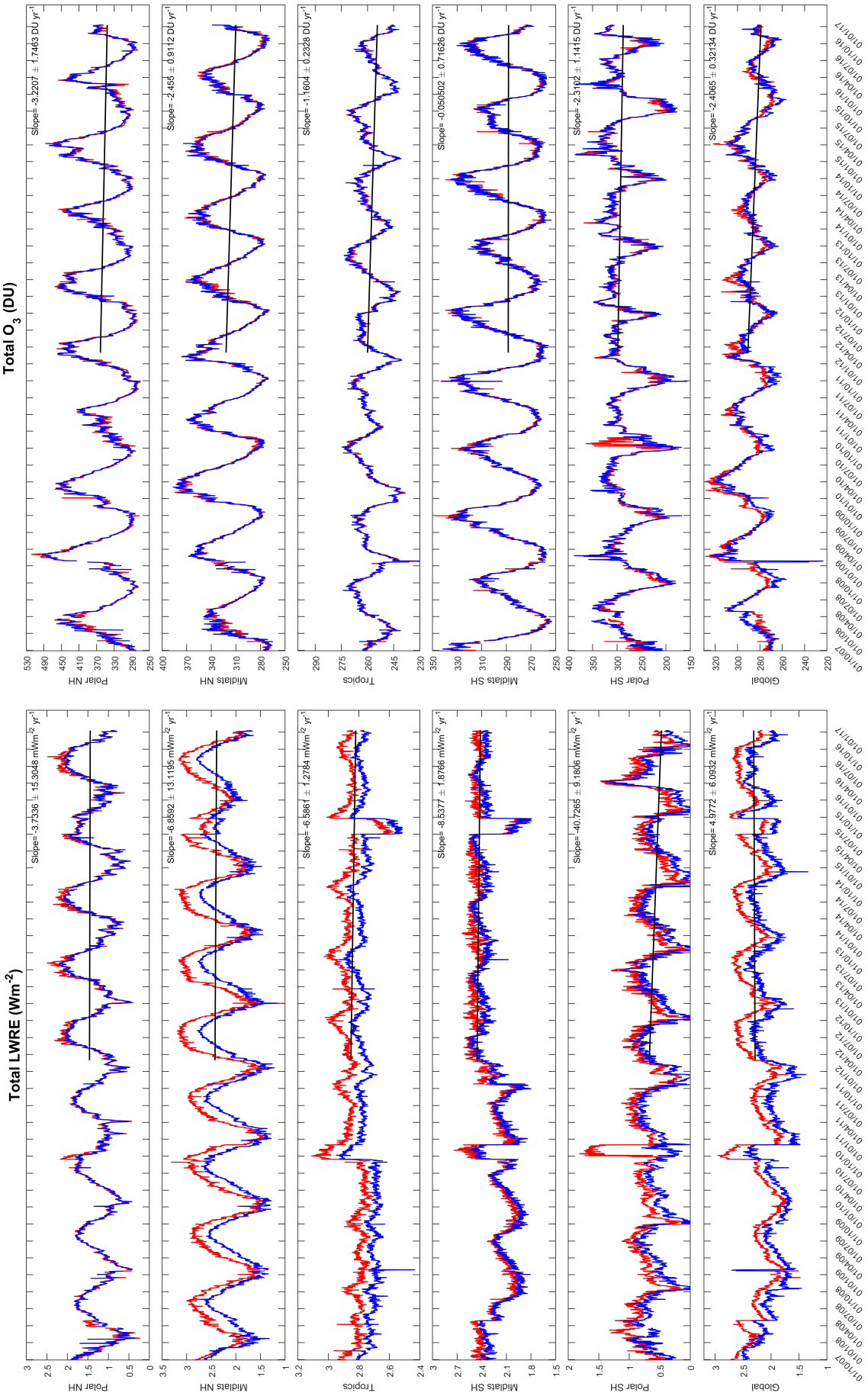

FIGURE 8.18: Daily time series of total O_3 LWRE ($W\,m^{-2}$) (left) and O_3 column (DU) (right), distinguished in five latitudinal bands and globally. Day and night overpasses are marked with red and blue color, respectively, while the black line denotes the trend. Data run from 30/09/2007 to 10/01/2017. Note the IASI instrument and software changes, especially in autumn 2010 (Table 8.1).

8.5.3 Focusing on individual cases

The study of climate and the assessment of the radiative forcing is based on how the atmospheric system adapts to a posed change. Specifically for ozone, such studies include all possible dynamics, which are accounted for through the climate models. The estimation of the O_3 LWRE from the IASI observations gives the ability to assess the radiative impact of cases that include both chemistry and dynamics as one and study the overall effect on climate.

Ozone loss in the Arctic and LWRE

Ozone loss (Sect. 4.1, 4.2) in the Antarctic is a well-known and studied phenomenon, the effects of which are clearly observable also in the LWRE, as discussed in Sect. 8.5.1. However, in the past decade there were cases of ozone loss in the Arctic as well, though not in the same extent as in the Antarctic. Similarly to the Antarctic, ozone loss in the Arctic occurred during the period of local winter, where the stratosphere of the region is governed by the Polar Vortex. During the Polar Vortex, atmospheric constituents are trapped within the area of the vortex, as the mixing of air from/to the vortex and the rest of the atmosphere is constrained. For ozone, due to the Brewer-Dobson circulation, this results to increased concentrations in the stratosphere. However, except ozone, ODSs are also trapped in the vortex (captured in the Polar Stratospheric clouds due to the very low atmospheric temperatures inside the vortex), and are then released, when the atmospheric temperature increases with the coming spring, reacting and finally depleting ozone. It is of interest to look at those individual cases in terms of LWRE.

In the stratospheric O_3 time series (fig. 8.13 and 8.17) we can identify three registered cases of unusual ozone loss in the Arctic: i) from 01/10/2010 until 01/04/2011, as studied in Balis et al. [2011] and Manney et al. [2011]; ii) from 01/12/2012 until 01/04/2013, as studied in Manney et al. [2015]; and iii) from 01/12/2015 until 01/04/2016, as studied in Manney and Lawrence [2016]. The first and last cases are more pronounced on the ozone time series compared to the one at the end of 2012.

Case I: Oct. 2010 - Mar. 2011 In fig. 8.17 and for the period of October 2010 - end of March 2011, stratospheric ozone exhibits a disruption in its time series (phase of increasing stratospheric ozone), which results to a decreased maximum in that year. The time period of the phenomenon is prolonged, covering five months. The surface temperature at that time is at its minimum, following its seasonal variations. At the same time, though the stratopsheric LWRE is towards its minimum following the seasonality discussed in Sect. 8.5.1, it experiences an abrupt decline from $1.2\,\mathrm{Wm}^{-2}$ to a $0.2\,\mathrm{Wm}^{-2}$ within the 5-month span, with the largest decline happening in the first month of the phenomenon and

around the beginning of January. The average stratospheric LWRE over this period is $0.93\,\mathrm{Wm}^{-2}$. The average stratospheric LWRE of October - March over all years, excluding those of the three cases under study, is $0.9\,\mathrm{Wm}^{-2}$. This corresponds to a slightly increased LWRE compared to other years. However, the surface temperature (fig. 8.17) over the same period is larger than its usual winter values, and therefore results to increased LWRE. We should note here, that over the aforementioned time period, the IASI time series are affected by an algorithm update (Table 8.1, line 3), hence the increased surface temperature might be an artifact.

Case II: Dec. 2012 - Mar. 2013 The situation is similar for the second case as well, where in fig. 8.17 the ozone loss is not much pronounced in the stratospheric ozone time series (a negative spike from 360 DU to 290 DU), however, the stratospheric LWRE shows a negative spike centered in the beginning of January 2013, where the LWRE decreases from $1\,\mathrm{Wm}^{-2}$ to $0.3\,\mathrm{Wm}^{-2}$. The average stratospheric LWRE over this time period is $0.88\,\mathrm{Wm}^{-2}$, while the respective average LWRE over December-March of all years is $0.8\,\mathrm{Wm}^{-2}$. Again, the surface temperature appears increased over the same period.

Case III: Dec. 2015 - Mar. 2016 Likewise, in the last case, ozone loss appears as an abrupt decrease in the time series (around January 2016), with the stratospheric column dropping from around 350 DU to just 270 DU. At the same time, the stratospheric LWRE drops from $1.2\,\mathrm{Wm}^{-2}$ to $0.57\,\mathrm{Wm}^{-2}$. However, the average stratospheric LWRE over this period is $0.95\,\mathrm{Wm}^{-2}$, with the all-year average stratospheric LWRE over these months at $0.8\,\mathrm{Wm}^{-2}$. In this case, the surface temperature exhibits unusual large values for winter in the NH Pole.

In summary, the stratospheric LWRE experiences abrupt drops, following the ozone loss in the Polar stratosphere, giving an estimation of the radiative impact in a short time span. However, in a more general view, because of the surface temperature being increased over the full time period of the phenomenon compared to the rest of the years for the same period, the stratospheric LWRE is finally increased compared to the other years, over the same time frame. Shortening the time frame of the study around the days the negative spikes appear, gives a better estimation of the radiative effect change due to ozone loss, but the effect is only temporal. In the long run, the dynamics governing the region result to the opposite effect on the stratospheric LWRE.

Stratospheric intrusions to the troposphere and LWRE

Earlier in this chapter, while studying the daily time series of the tropospheric LWRE, we referred to the stratospheric intrusions; ozone-rich air masses penetrating into the Troposphere. As mentioned previously, these intrusions occur mainly in the mid-latitude

and polar bands. However sometimes, they also appear closer to the Tropics, usually during sudden stratospheric warmings (e.g. Albers et al. [2016]).

If we look closely into the daily time series, it is possible to detect many cases of such intrusions. For example, in the NH midlatitudes, around the beginning of April 2011, we observe an abrupt increase in the tropospheric O_3 from 32 to 40 DU (fig. 8.16), which is accompanied by a respective decrease in the stratospheric O_3 (fig. 8.17). At the same time period we can observe a small increase in the LWRE (of 0.1 Wm^{-2}), accompanied by a small decrease in the stratospheric LWRE, of the same order of magnitude. Likewise, in the SH Pole, around January 2014, we observe a decrease of almost 40 DU in the stratospheric O_3, associated with a decrease of 0.2 Wm^{-2} in the LWRE. This decrease is accompanied by an increase of 5 DU and 0.07 Wm^{-2} in the tropospheric ozone and LWRE respectively. Generally, a stratospheric intrusion of ozone in the troposphere results to enhanced tropospheric LWRE, and decreased stratospheric LWRE.

Contrary to the time series, if we focus over a specific area, it is easier to construct the ozone and LWRE amounts in 3D, and therefore to identify stratospheric intrusions in the Troposphere. Such an example is shown in fig. 8.19, for the region of latitude 45° N to 0°, and longitude 90° W to 0°, occurring on 29 March 2015. The top panel of fig. 8.19 shows the isolated stratospheric partial column of ozone, while the bottom panel shows the LWRE corresponding to the aforementioned ozone column. In order for the effect to be visible, it was also mandatory to remove a portion of the stratospheric layer, as the phenomenon occured in the middle of the chosen area.

As seen in fig. 8.19, there is a discontinuity in the stratospheric O_3 column just above the Atlantic ocean (top panel). A stratospheric O_3 mass (cyan) seems to be moving downwards. Over the same spot, we also detect a LWRE mass (yellow) (bottom panel), partly detached from the rest of the layer, which represents the LWRE corresponding to the intruding O_3 mass.

The purpose of this figure is qualitative, and shows the capability to directly assess the LWRE of such geophysical anomalies. With further isolation and study of such a spot, it is possible to finally quantify the exact LWRE. This is a result that underlines the decisive contribution that IASI could have for the representation of stratospheric intrusions into Chemistry–Climate models.

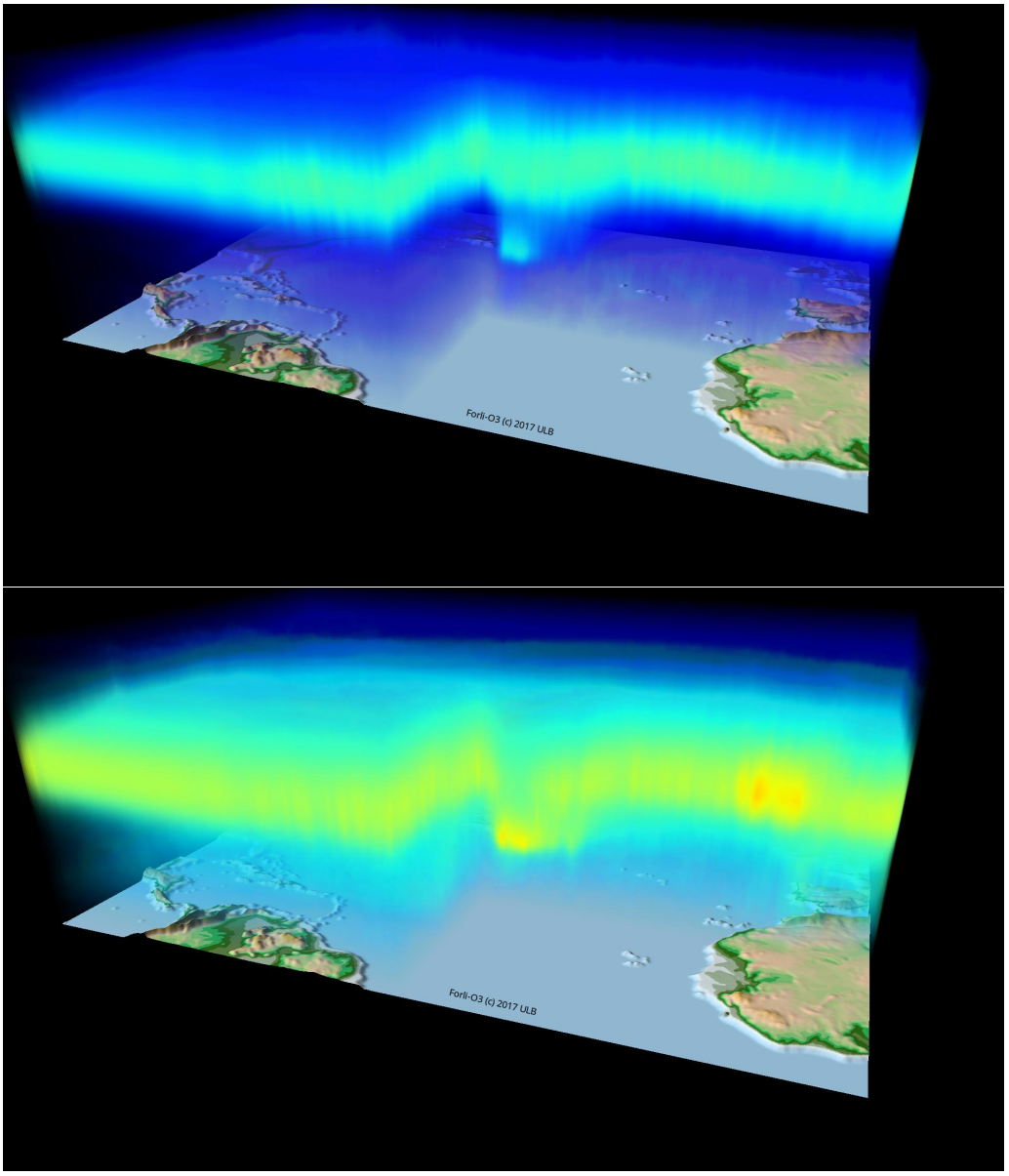

FIGURE 8.19: Stratospheric O_3 partial column (top) and corresponding LWRE (bottom), on 29 March 2015, over the area of lat: 45° N to 0° and long: 90° W to 0°.

8.5.4 Overview

Following the radiative forcing concept, the LWRE is an estimation of the radiative budget change due to ozone absorption, accounting for all other contributions from the atmosphere at a specific moment. As the product of integrated radiances with respect to ozone absorption, the LWRE seasonality is greatly influenced by ozone and the surface temperature. In the troposphere, the LWRE follows the seasonality of the surface temperature, being consistent with the strong correlations observed in Sect. 8.4. Exception to this pattern is the SH Pole, which is governed by low surface temperatures and the atmospheric dynamics in the area. In the stratosphere, in the NH the LWRE is influenced by the surface temperature, reflecting the land domination in this hemisphere, however

the ozone seasonality forces the LWRE minima and maxima to occur earlier as compared to the troposphere. For the Tropics and the SH midlatitudes, which are dominated by ocean, in the stratosphere, the effect of ozone is more prominent, driving the LWRE seasonality. Overall, in the annual cycles, the NH exhibits the greatest variations, in compliance with the large variations of both ozone and the surface temperature.

Regarding the estimated trends, though most of the observed changes are insignificant due to the short time series, the global average LWRE trends point to the direction of a warming troposphere (increasing LWRE) and a cooling stratosphere (decreasing LWRE), a result of the climate change, as stated in IPCC [2013].

Finally, when focusing over specific regions and time periods, it is possible to infer the radiative change in the outgoing longwave radiation of individual cases such as the Arctic ozone loss or stratospheric intrusions in the troposphere.

Chapter 9

LWRE: IASI vs TES vs Chemistry - Climate Models

Disclaimer: All results and figures presented in this chapter are the outcome of the project "Benchmarking climate model top-of-atmosphere radiance in the 9.6 μm ozone band compared to TES and IASI observations", funded by NASA ROSES 2013 Solicitation: NNH13ZDA001N. Publication of the findings is under preparation. Credits are given to: H. Worden (NCAR), K. Bowman (JPL), J.-F. Lamarque (NCAR), A. Conley (NCAR), D. Shindell (NASA-GISS, Columb. Uni.), O. Pechony (Columb. Uni.), C. Clerbaux (LATMOS-IPSL), P.-F. Coheur (ULB), W. Collins (Uni. Cal., Berkeley), A. Lacis (NASA-GISS), S. Massie (NCAR), G. Faluvegi (NASA-GISS), and S. Doniki (ULB).

The idea of the project "Benchmarking climate model top-of-atmosphere radiance in the 9.6 μm ozone band compared to TES and IASI observations" is to bring together the accuracy and information availability of IR remote sensing and Chemistry−Climate models (CCMs), in order to improve the simulations and forecasting of the latter. Furthermore, as TES has stopped operating since February 2018, it is an effort to extend the TES data record with IASI measurements.

The IASI and TES instruments produce IRKs and LWRE along with the ozone retrievals, based on the method presented in Chapter 7. These parameters can also be calculated from CCMs. Regarding ozone RF estimations, the CCMs produce different results, caused by different input parameters and algorithms. In an effort to bring models and satellites into agreement, we have worked on a first comparison, which will be presented below.

The IRKs and LWRE computed for IASI, use all the characteristics presented in the previous chapters. On the other hand, for TES, which is very similar to IASI, its own retrieval algorithm is used, but nonetheless the calculations of IRKs and LWRE follow

the exact same procedure. The CCMs taking part in this work are: CAM-RT [Lamarque et al., 2012], and GISS-RT [Schmidt et al., 2006]. The CAM-RT can be operated with two different radiative transfer models, its own and the RRTMG; the chemistry model is the same in both cases. The CCMs for this work use as input the profiles and their related parameters as obtained from the TES retrievals.

The data used for the comparison are of a single day, on 15 July 2011, where we found 81 collocated cases of clear−sky, ocean scenes. The collocation criteria are: $IASI = TES \pm 100\,\text{km}$ for latitude and longitude, and for time, $0 \leq TES\text{-}IASI \leq 6\,\text{h}$.

Although IASI and TES have never been compared to each other in detail, the work of Oetjen et al. [2014, 2016] shows that the two instruments are in agreement regarding the ozone retrievals. The differences rely mostly on the different retrieval algorithms. To that end, they have applied the TES retrieval algorithm on IASI observations, which resulted to differences less than 5 ppb, with IASI underestimating the results, due to its coarse vertical sensitivity compared to TES. Moreover, they have concluded that the differences are not dependent on season or any other factor, and therefore, the measurements of the two instruments can be merged, after accounting for the observed bias.

Keeping all of the above in mind, the average IRKs of IASI, TES and the CCMs are presented in fig. 9.1, along with their variability. IASI and TES agree well within the standard deviation margins (about $\pm 0.2\,\text{W/m}^2\text{/ppb}$), given the differences in instrumental characteristics and retrieval algorithms. Except the GISS-RT model, which agrees with IASI well below the standard deviation, the other two models produce IRKs significantly different.

Going one step further to the total O_3 LWRE and fig. 9.2, IASI indeed agrees well with TES, with IASI higher at around 10% and a correlation of 0.95. The GISS-RT model is also within the IASI variation around TES, but with a larger spread of values, bringing the differences at around 10% and a correlation of 0.97. The other two models, especially CAM-RT, are strongly biased positively to IASI and TES. The CAM-RT is overestimating the total LWRE compared to TES by almost 25%, however the correlation is at 0.97. The RRTMG is overestimating the total LWRE by almost 17% and a correlation of 0.92.

Although the CCMs use as input the TES profiles, which explains the large correlations, there is a major difference in the radiative transfer scheme that accounts for the largest part of the observed differences. The IASI and TES IRKs are computed based on eq. 7.6, while the models use the anisotropy approximation, based on eq. 7.5. As already shown in Ch. 7, the anisotropy approximation results in biases of 22% in the IRKs and 25% in the total LWRE. Moreover, the CAM-RT and RRTMG models use pre-calculated

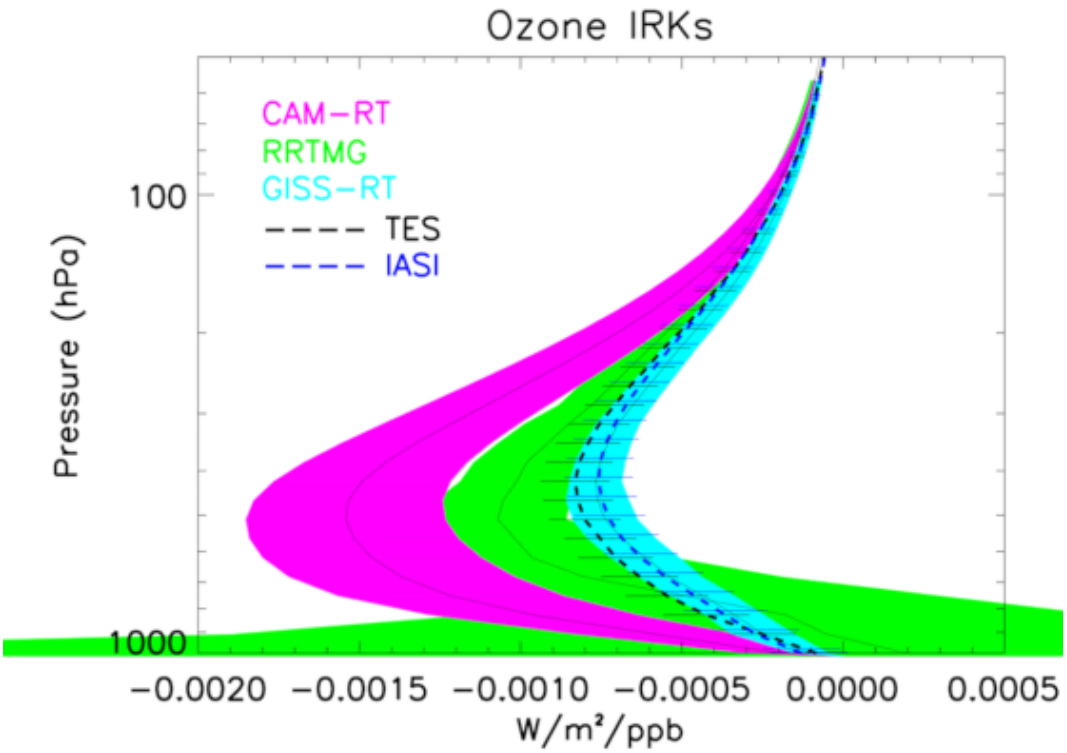

FIGURE 9.1: Average IRKs $\pm 1\,\sigma$of IASI (dashed blue), TES (dashed black), CAM-RT (magenta), RRTMG (green) and GISS-RT (cyan), for 81 collocated cases of clear-sky, ocean scenes on 15 July 2011.

anisotropies, based on the angular distribution models (ADMs) built from the Earth Radiation Budget Experiment (ERBE) and the Clouds and Earth's Radiant Energy System (CERES) (e.g. Li [1996]; Loeb et al. [2003]; Stubenrauch et al. [1994]), while the GISS-RT calculates the anisotropy each time, as proposed in Worden et al. [2011], which results to a more accurate representation than pre-calculated ADMs.

It is interesting to look at the two different RT models for the CAM-RT model, its own - under the same label -, and RRTMG. As shown in fig. 9.3-left, although the model is using the same atmospheric and surface conditions for each simulation, their different radiative transfer assumptions can lead to differences 40-50% in the tropospheric LWRE. On the right of fig. 9.3, a comparison between TES and GISS-RT IRKs is shown. The results of GISS-RT are close to TES in most latitudes, however there are large differences of 80 mW m^{-2} in the Northern Hemisphere.

We have also made the comparison of the tropospheric column, as shown in fig. 9.4, where we distinguish two cases: the raw tropospheric column (on the left) and that from 700 hPa to the tropopause (on the right), in order to remove from the comparison the lower part of the atmosphere, where the instruments have limited sensitivity. For all data sets the tropopause was calculated based on the WMO definition. IASI LWRE results

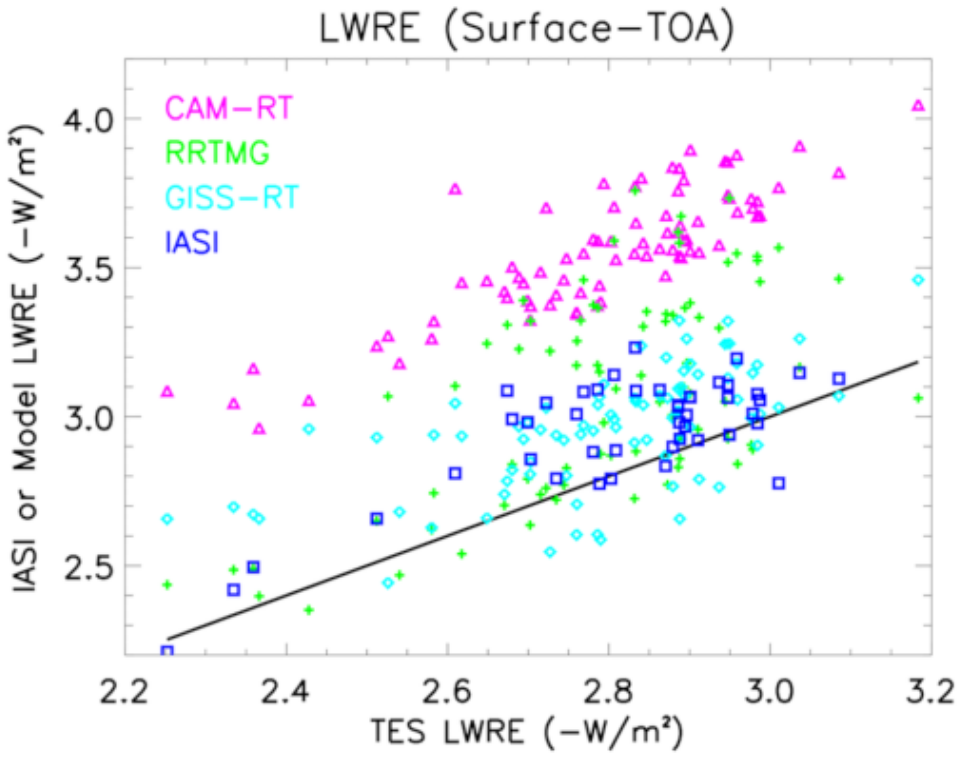

FIGURE 9.2: Correlation of the total O_3 LWRE for IASI (blue), CAM-RT (magenta), RRTMG (green) and GISS-RT (cyan), against TES, for 81 collocated cases of clear-sky, ocean scenes on 15 July 2011. The black line indicates $y = x$.

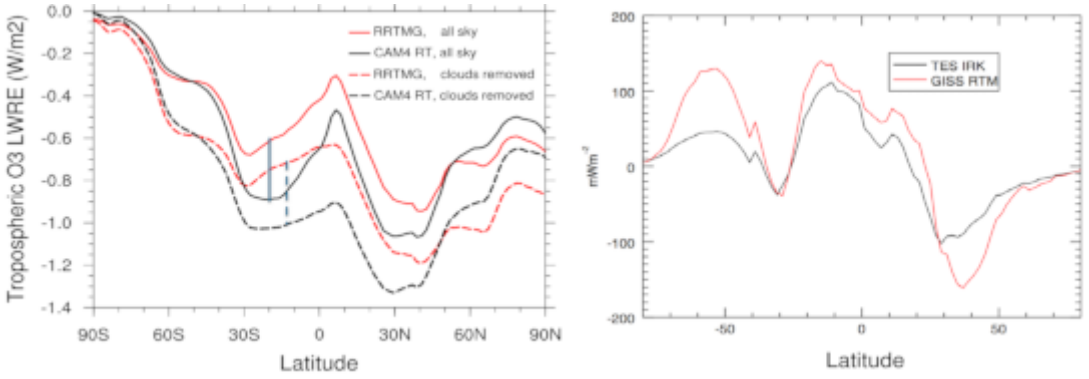

FIGURE 9.3: (Left) JJA zonal averages for tropospheric LWRE from two RT models applied to the same atmospheric and surface conditions. Differences are only due to the different assumptions for radiative transfer in CAM-RT vs. RRTMG. (Right) Latitudinal zonal averages of Δ LWRE computed for differences (modeled - observed) in tropospheric ozone distributions using the TES IRK compared to the GISS RTM IRKs.

are in agreement with TES, with a bias less than 10%, and become even closer, when the first couple of layers are not considered in the calculations, where the bias is around 7-8% and the correlation 0.97. The GISS-RT results produce a bias of 4% and a correlation of 0.97. The RRTMG seems to perform better in the troposphere, however it is known that its water vapour sensitivity near the ground is not well defined, causing spurious values (clearly shown at the bottom of fig. 9.1 in green), which results to additional bias in the

LWRE, leading to an overall bias of 15% and a correlation of 0.92. Finally, the CAM-RT still has a large bias of 25%, which does not change between the two tropospheric columns, and therefore its problems need a more thorough investigation. Its correlation with TES is at 0.93.

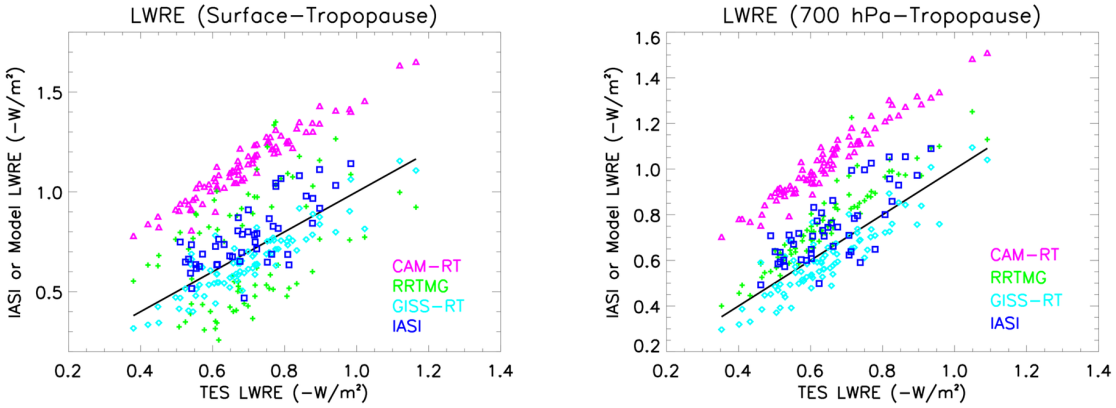

FIGURE 9.4: Correlation of the tropospheric O_3 LWRE (left) and tropospheric O_3 LWRE from 700 hPa to tropopause (right) for IASI (blue), CAM-RT (magenta), RRTMG (green) and GISS-RT (cyan), against TES, for 81 collocated cases of clear-sky, ocean scenes on 15 July 2011. The black line indicates $y = x$.

On a final note, we should point out the importance of water vapor in the O_3 LWRE estimation, as discussed previously in Ch. 8. The known weak sensitivity ofthe RRTMG to water vapor produces faulty results, especially in the lower troposphere. Water vapor is accounted for in IASI calculations through look-up tables (see Ch. 6) and in TES, through its line-by-line retrieval algorithm.

The CCMs used in this study are also used in the ACCMIP and IPCC studies. The ability of comparing IASI and TES IRKs and LWRE directly with the models, is a big step towards the accurate representation of ozone in models, its radiative impact and limiting the uncertainties in the RF calculations.

Chapter 10

Conclusions and Perspectives

The climate of Earth has changed dramatically in the past decades, mainly because the atmosphere has been altered through pollution and release of greenhouse gases. Natural effects have been enhanced by anthropogenic pollution, resulting to changes in the dynamical processes of the atmosphere. In order to quantify the extent of a change due to anthropogenic influence, the scientific community proposed the concept of the radiative forcing, the net change in the energy balance of the Earth due to some imposed perturbation [IPCC, 2013]. The change refers to the state between the pre-industrial era and the present day. The factors contributing to the radiative forcing are countless. Each factor has to be studied individually, before assessing its overall impact. However, most factors are inter-connected with others, multiplying the difficulties. The different factors influencing the radiative forcing have been ranked in terms of largest contribution, with ozone taking the third place.

The difficulty with ozone relies in the fact that the radiative forcing it causes, changes with the altitude; it is positive in the Troposphere and negative in the Stratosphere. It is also a secondary product in polluted areas, with a wide variety of precursors. The reactions controlling its production and destruction in the atmosphere are numerous. It is important to note, that ozone started being extensively studied and monitored only a few decades ago, which means little available information for earlier periods, and almost non-existent for the pre-industrial era.

The radiative forcing calculations come as a result of climate models. For more accurate representations, the climate models are coupled with chemistry models, to account for the complex chemical reactions in the atmosphere. Hence, a chemistry-climate model calculates the radiative impact on climate of ozone, and of other factors as well. However, the models are evaluated against actual measurements, ground-based, airborne and

satellite, only in terms of ozone amounts. Everything else is based on the models ans their algorithms and how well these perform. The different results of radiative forcing from different models have been presented in Table 4.1 of Ch. 4 and reflect the difficulties of this approach.

Here lies the need of calculating the radiative impact of different atmospheric constituents from independent measurements; to create references closer to the true state and assess the climate models. To this end, we developed and present an improved method to estimate the O_3 LWRE, tailored on IASI, as well as the first results covering a 9-year period.

10.1 General Conclusions

The direct integration method for calculating the O_3 LWRE, was built for IASI, but can be applied on any similar instrument, as shown for example for TES. The concept of the method is based on the same principles as the anisotropy method, which was also the starting point for this work. The wide range of the measurement angles of IASI proved that the anisotropy method is insufficient and that a more accurate approach is needed. The direct integration, though more computationally expensive, offers this accuracy and can be calculated along with the retrieval of O_3.

The way the LWRE is calculated, offers information for each retrieved layer. This gives the ability to study the impact vertically, but also to focus on the tropospheric, stratospheric or total amount, as done for the O_3 columns. Moreover, the unprecedented coverage achieved by IASI allows global or regional studies, in a daily, monthly, annual or even a 10-year period basis. In addition to this, the bi-daily coverage of IASI helps to assess the impact of day-to-night differences.

To that end, we have constructed the daily time series of the ozone LWRE, tropospheric, stratospheric and total, which where studied along the respective columns of O_3 and surface temperature. Based on the same time series, we have also estimated the respective correlations between the LWRE and ozone/surface temperature. The correlation study revealed a strong impact of ozone and surface temperature on the LWRE, especially in the troposphere. In regions of high water vapor abundance - mainly within the Tropics -, the LWRE in the ozone band is weak, and the correlations with ozone and surface temperature are insignificant. We have also observed anti-correlation of the LWRE with ozone in the stratosphere, as a result of the different seasonal variations.

Equation 7.9 assumes a linear relation between the LWRE and ozone. However, a linear correlation was frequently insufficient to describe the relation of the two parameters, and although correlation coefficients were in general significant, the determination coefficients were small, as a result of the large spread of measurements of LWRE and O_3. On the same question, we have pointed out that the ozone amount is accounted for in eq. 7.9 both as an individual parameter, but also included in the IRKs. Furthermore, the same results point towards the importance of the temperature profile in the study, although here it was not available at the time of this work.

The daily time series analysis revealed similar results. As expected from the LWRE formulation, the LWRE seasonal variations in the troposphere follow closely those of the surface temperature, while in the stratosphere the LWRE patterns coincide mostly with the ones of ozone. Furthermore, the calculated trends of the ozone LWRE point to the direction of the changes in the ozone radiative forcing, justifying the LWRE as a suitable metric for climate studies. Finally, through the LWRE time series, we were also able to estimate for a few individual cases the LWRE related with phenomena such as the O_3-holes in the Northern Hemisphere and stratospheric intrusions in the Troposphere. The ozone loss in the Arctic reveals a short-term decrease of the LWRE in the stratosphere, associated with the respective ozone decrease. In the long-term however, the surface temperatures of the region are generally higher during the phenomenon, resulting to a slight increase of the LWRE. For the stratospheric intrusions, the increased ozone in the troposphere is followed by an increase in the tropospheric LWRE, which are associated with the respective decreases of ozone and LWRE in the stratosphere.

In an effort to show the importance of the LWRE, and as a result of an international project, we have compared the results computed for IASI, with those for TES and the simulations of three major Chemistry-Climate Models, which are used widely by the scientific community for climate studies. IASI and TES show very good agreement in terms of LWRE, given the differences between the two instruments. On the contrary, the models present different results, although all three of them used as input the atmospheric states retrieved from TES. Only one of the three models was able to produce results close to the IASI and TES instruments. The study has concluded that the differences rely on the assumptions in the radiative transfer algorithm of each model.

10.2 Future Work

The method presented in this work is an inovative step to obtain the radiative impact of ozone on climate; the analysis provides the first information on the O_3 LWRE behavior

with respect to the O_3 and the surface temperature. The estimation of the different contributions of ozone and surface temperature on the LWRE is not straightforward. The results of this study open perspectives for further investigation on disentangling the effects of the surface temperature, ozone and relative humidity on the calculated O_3 LWRE. For example, the use of multilinear regressions accounting for each of these drivers of the LWRE, similarly to the work of Wespes et al. [2016], could provide more detailed insight in the behavior of the LWRE.

As a result of the significant impact of the surface temperature on the O_3 LWRE, the inclusion of the Jacobians as a function of the surface temperature and the temperature profile should be considered. With a formulation similar to the IRK, these parameters would help in quantifying the role of the surface temperature and temperature profile on the O_3 LWRE, especially in the troposphere where the greatest relation was observed.

This study referred only to clear-sky measurements. The inclusion of other algorithms that treat all-sky measurements should be considered, as clouds are an important driver of climate. All-sky results will provide an even better estimation of the radiative impact of ozone, as regions such as the Tropics exhibit extensive cloud coverage throughout the year.

An interesting aspect is the attribution of the ozone LWRE to the emissions of the ozone precursors. In a recent study, Bowman and Henze [2012] used the ozone LWRE, derived from the TES measurements, and a chemical transport model (GEOS-Chem), to calculate the sensitivity of the LWRE to the anthropogenic emissions of NO_x, CO and NMHC (non-methane hydrocarbons). They were able to identify 15 regions over China and the United States that accounted for 8% of the global average tropospheric ozone LWRE, establishing a direct link between air pollution and radiative forcing. However, this study followed the work of Worden et al. [2011] and the anisotropy approximation (see Ch. 7) for the LWRE, therefore the results are probably underestimated. By following the same principle as in Bowman and Henze [2012], and exploiting the IASI spatial coverage and the ozone LWRE, as presented in this work, the results would be more robust and allow better spatial resolution, benefiting the chemistry models and the coupled chemistry-climate models.

At present, only IASI can provide a consistent and extended LWRE record, from the beginning of the IASI mission until now, and in a near-real time basis. There are also data available from TES, but only for a few individual days. The contribution of new instruments will provide more solid databases for reference and instrumental inter-comparison, which will leverage our understanding of the radiative impact on climate. To that extent, the application of the method presented here to other atmospheric constituents should

also be considered, as for example water vapor, which was recently proven to have a major influence [Kuai et al., 2017].

Regarding the climate models and the results from a first comparison, the main issue to be addressed is the consistency of the respective radiative transfer algorithms. As seen in fig. 9.3, the application of two different radiative transfer schemes on the same chemistry-climate model results to relative differences of 40 to 50%. The consistency of the models in terms of radiative transfer is of utmost importance. Moreover, extensive comparisons of major climate models with satellite-derived LWRE is crucial, as the climate models are our only mean to project into the future and assess the climate state of Earth.

A variety of such LWRE independent measurements for different atmospheric constituents, such as water vapor or carbon monoxide, will constrain model biases and lead to more accurate RF estimations. As a result, future projections from climate models will become more precise, and help for better climate mitigation planning.

Appendix A

The Dobson unit

Let us assume that all the ozone contained in a vertical column of air, from the Earth's surface to the top of the atmosphere, were contained in a single layer of pure ozone at the surface of the Earth, at 273 K and 1.013 hPa (= 1 atm) pressure. If the thickness of that layer was measured in hundredths of a millimeter (0.01 mm = 0.001 cm), then this would be the ozone column abundance expressed in *Dobson units* (DU). It was named after G. Dobson, who designed and manufactured the first O_3 spectrometer, named also after him. The Dobson spectrometer is a ground−based instrument that measures O_3 concentrations using the solar UV radiation. It measures at four wavelengths, two that are known to absorb O_3 and two that do not.

One DU equals to 2.69×20^{16} molecules of O_3 per cm^2. An average value of an O_3 column corresponds to about 300 DU, which is just a 3 mm−thick layer at the surface. The ozone column burden is determined by:

$$\tilde{n}_{O_3} = \int_{\infty}^{0} n_{O_3}(z)dz, \tag{A.1}$$

where z is the altitude. To determine $\tilde{n}_{O_3}$ (in molecules cm^{-2}) in terms of DU, we need to calculate its thickness as a pure−O_3 layer at 273 K and 1.013 hPa (= 1 atm). Based on eq. A.1, $n\tilde{_{O_3}}$ molecules exist over a 1 cm^2 area.

Making use of the ideal-gas law:

$$PV = (\tilde{n}_{O_3}/N_A)RT, \tag{A.2}$$

where $\tilde{n}_{O_3}/N_A$ is the number of moles of O_3, with N_A the Avogadro constant equal to $6.02214129 \times 10^{23}\,\mathrm{mol}^{-1}$; R is the ideal gas constant equal to $8.3144621\,\mathrm{JK}^{-1}\mathrm{mol}^{-1}$; T the surface temperature of 273 K; P the pressure of 1.013 hPa and V the layer volume of $1\,\mathrm{cm}^2 \times 0.001\,\mathrm{cm}$. The height of the layer was chosen according to the definition of DU, at the beginning of the appendix. Solving eq. A.2 with respect to $\tilde{n}_{O_3}$:

$$\tilde{n}_{O_3} = \frac{(1.013 \times 10^5)(10^{-3} \times 10^{-6})(6.022 \times 10^{23})}{(8.314)(273)} \tag{A.3}$$

$$= 2.69 \times 10^{16}\,\mathrm{molecules\,cm}^{-2} \tag{A.4}$$

Appendix B

IASI-A vs IASI-B LWRE

The differences between IASI-A and IASI-B with respect to the FORLI-O_3 product, have been studied in detail by Boynard et al. [2018]. However, there has never been a comparison for the ozone LWRE, derived from FORLI. Below, we show the first results of such a comparison, in terms of daily averages for five latitudinal bands and globally.

Figure B.1 shows the time series of IASI-A and -B, only for the overlapping time periods (starting on 23 Apr. 2013), for the total LWRE of ozone. Along with the time series, the figure shows the residual $IASI_A - IASI_B$, for the common time record. The second and third columns of Table B.1 present the mean biases between the two instruments in terms of LWRE and with respect to IASI-A; the negative sign implies that IASI-B is slightly higher than IASI-A. In general, the LWRE of the two instruments show excellent agreement, with the bias of the global average roughly at 0.5%. In a few cases, the LWRE from IASI-A is larger, maximum around 20%; in the NH and SH Polar regions, and the NH mid-latitudes. However, if we look closer in the time period these differences occur, we understand that they belong in the cases, where external effects influence the data (see Table 8.1), as explained in subsection 8.3.1. Otherwise the differences do not exceed 0.63% in terms of total LWRE.

Figure B.2 is the same with fig. B.1, but for the tropospheric LWRE. Here, the situation is similar to the total LWRE, as we can identify that the differences are mainly in the NH and SH Polar regions, and the NH mid-latitudes, while the largest differences occur again during the time periods stated in Table 8.1. The biases vary well below 2%, 1.87% for the global average, which confirm the excellent agreement between the two instruments, with regard to the LWRE.

From this brief comparison, we conclude that in terms of daily averages, and consequently monthly and annual averages also, it is safe to use the LWRE of IASI-A, as it presents the longest time record.

TABLE B.1: Total LWRE bias between IASI-A and IASI-B

	Total LWRE		Tropospheric LWRE	
Region	Bias	Bias (%)	Bias	Bias (%)
NH Pole	0.003	0.32	0.013	1.32
NH Midlats	–	0.04	0.009	0.93
Tropics	–	0.03	0.008	0.78
SH Midlats	–	0.06	0.013	1.33
SH Pole	0.006	0.63	0.017	1.74
Global	0.006	0.58	0.019	1.87

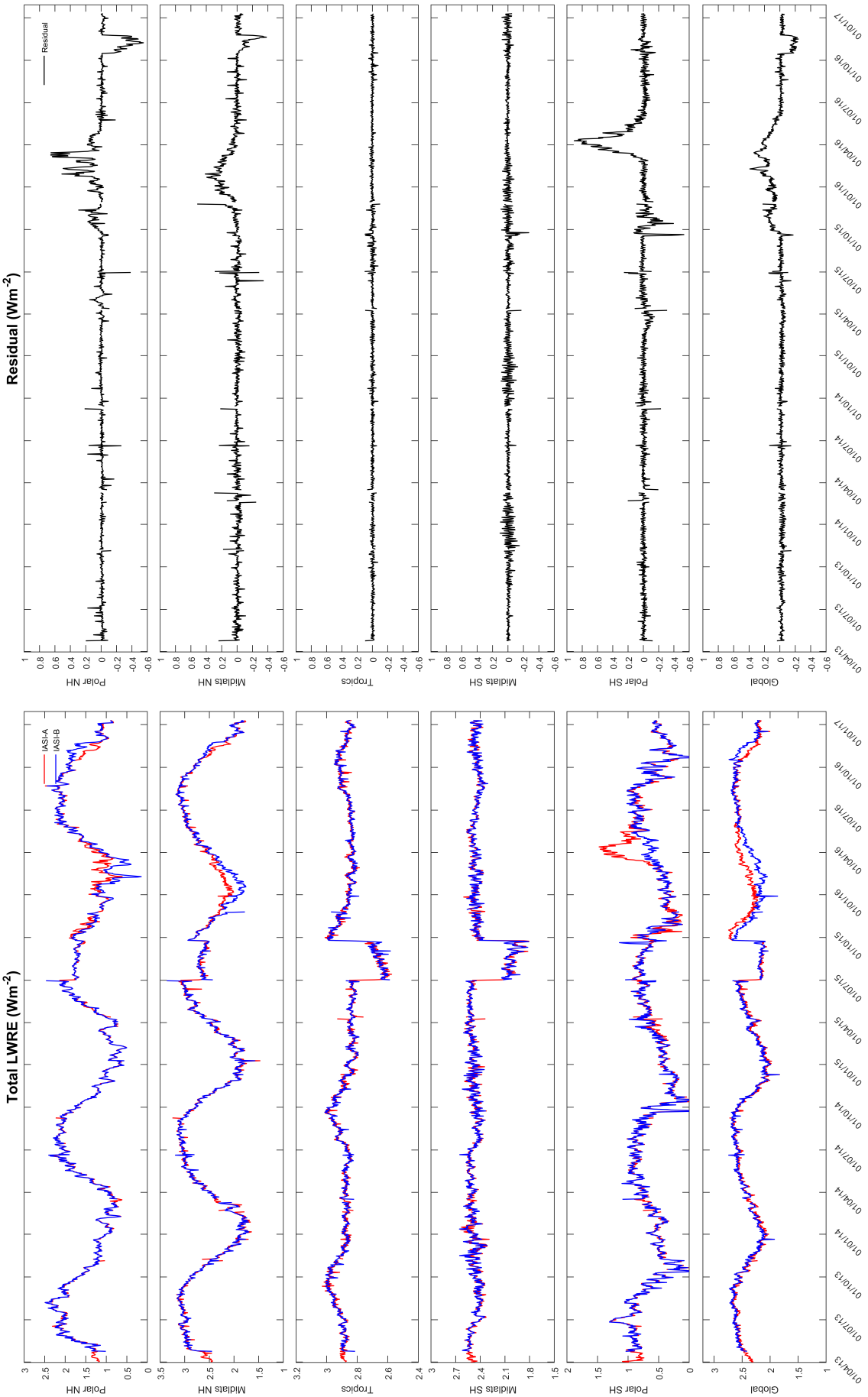

FIGURE B.1: Daily time series of total LWRE ($\mathrm{W\,m^{-2}}$) (left) and the IASI-A − IASI-B residual (right), distinguished in five latitudinal bands and globally. Large discrepancies are related to instrumental/software updates (see Table 8.1).

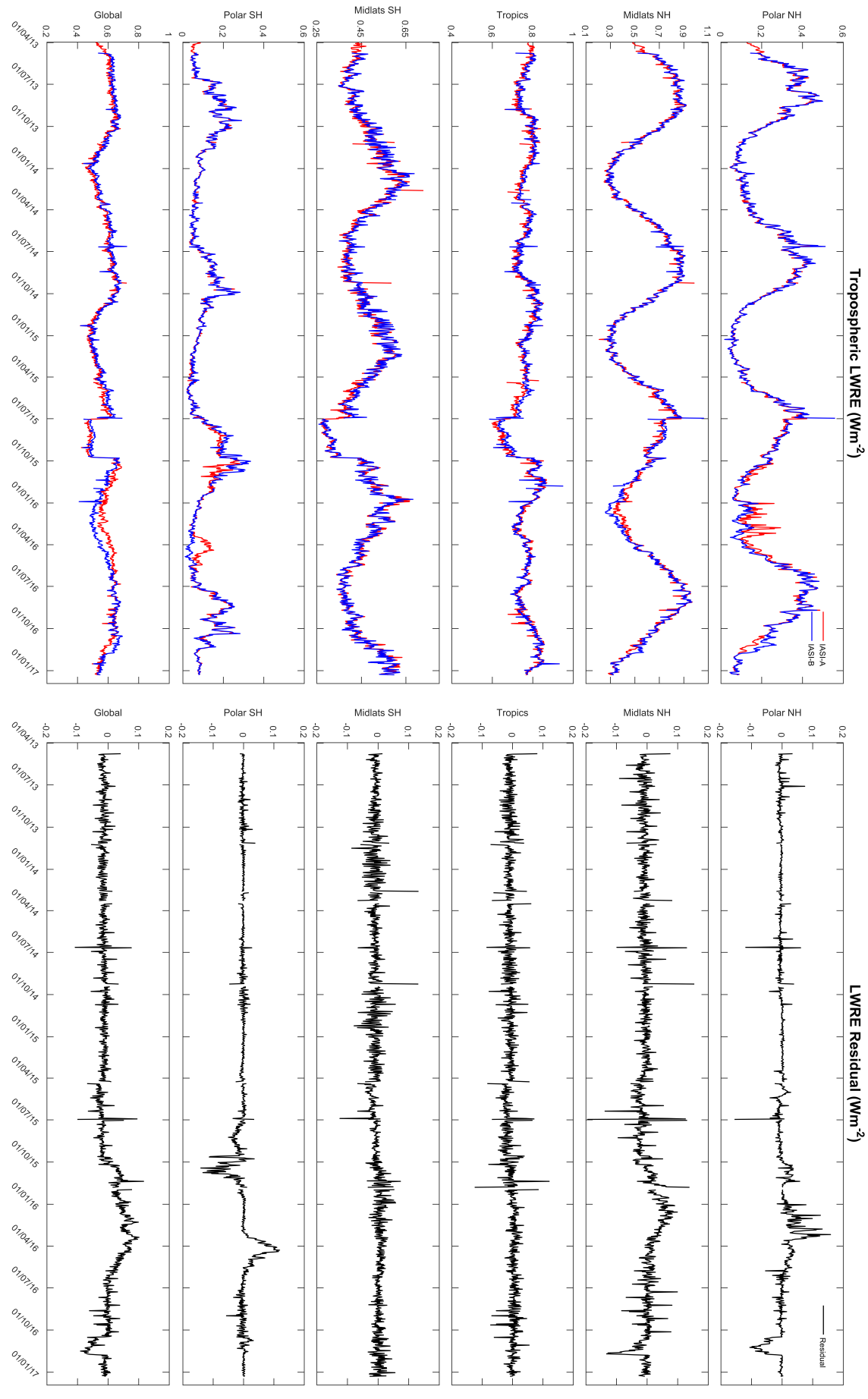

FIGURE B.2: Daily time series of tropospheric LWRE (W m^{-2}) (left) and the $IASI_A - IASI_B$ residual (right), distinguished in five latitudinal bands and globally. Large discrepancies are related to instrumental/software updates (see Table 8.1).

Appendix C

Global Distributions

In Ch. 8, we have shown the global distribution of a single day for the O_3 LWRE, for the total and tropospheric columns, as well as the global distribution of ozone and of the surface temperature for the same day. Furthermore, we have discussed the seasonality patterns of the LWRE compared to ozone and surface temperature, as well as the 5-year trends of these parameters. Here, we provide the 5-year global average distributions and trends of the LWRE and ozone, for the tropospheric, stratospheric and total columns, along with the surface temperature. Furthermore, we provide the seasonal global distributions of the same parameters. The data cover the period of 1 Mar. 2012 to 28 Feb. 2017, slightly extended than the data used in Ch. 8 in order to have five complete years.

5-year global average

Figures C.1 to C.3 show the 5-year global average distributions for the tropospheric, stratospheric and total LWRE and ozone, and the surface temperature. Figures are complementary to Sect. 8.2.2.

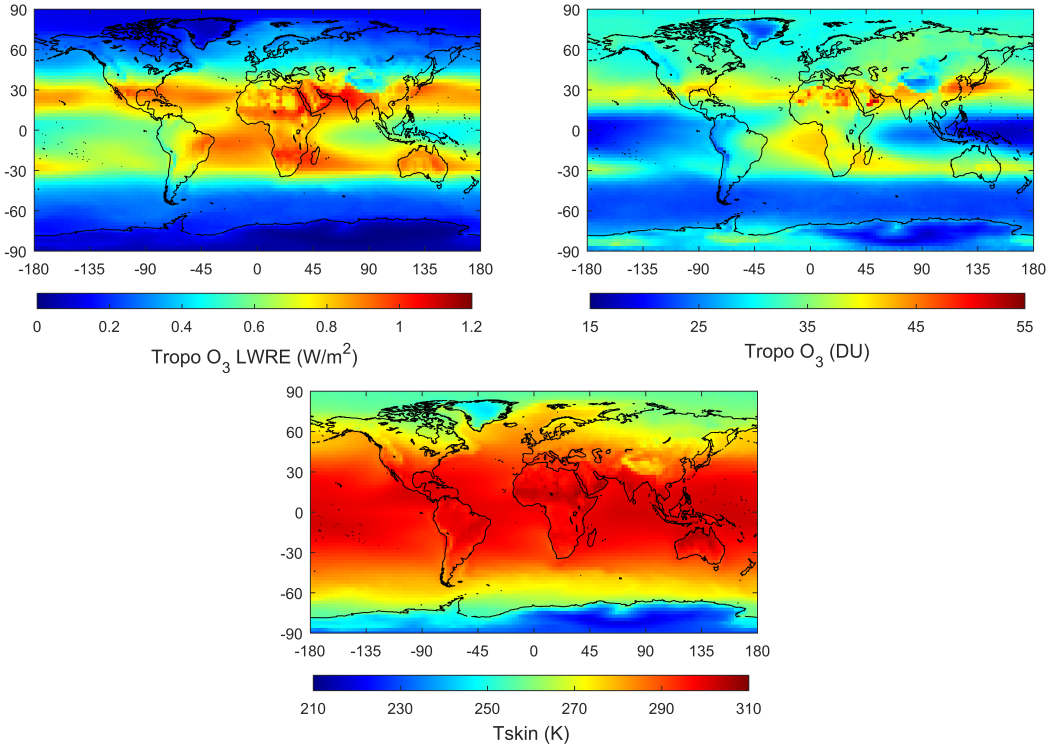

FIGURE C.1: 5-year global distribution of (top - left) tropospheric LWRE ($\mathrm{W\,m^{-2}}$), (top - right) tropospheric O_3 (DU) and (bottom) surface temperature (K). Data cover the period from 1/3/2012 to 28/2/2017.

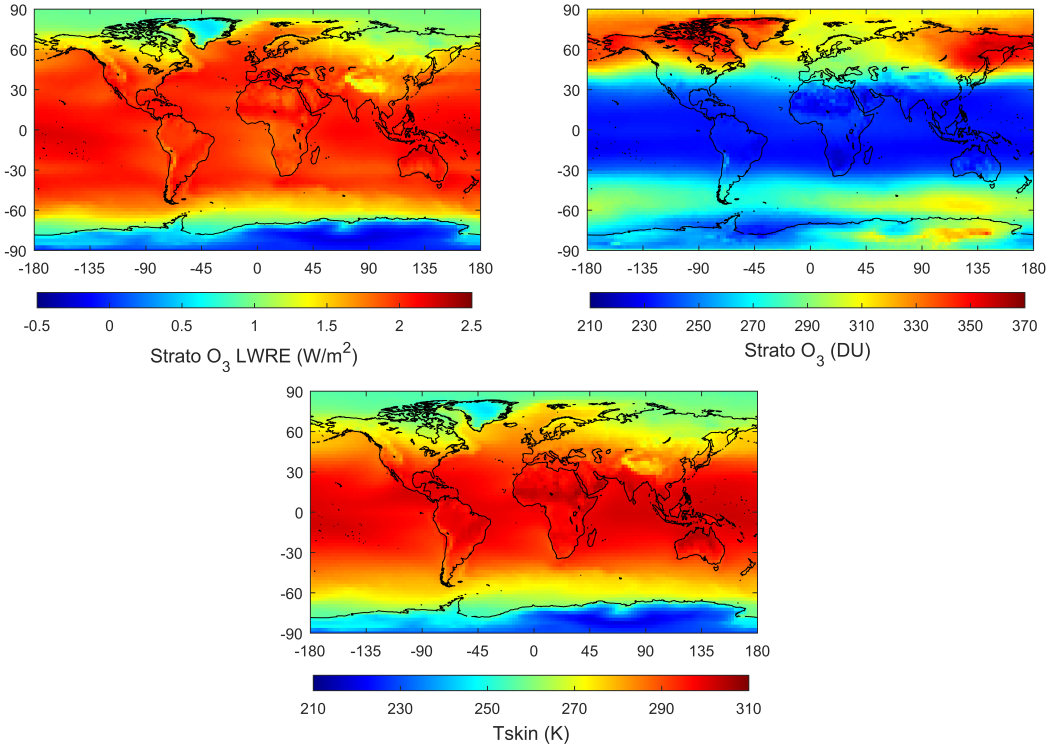

FIGURE C.2: 5-year global distribution of (top - left) stratospheric LWRE ($\mathrm{W\,m^{-2}}$), (top - right) stratospheric O_3 (DU) and (bottom) surface temperature (K). Data cover the period from 1/3/2012 to 28/2/2017.

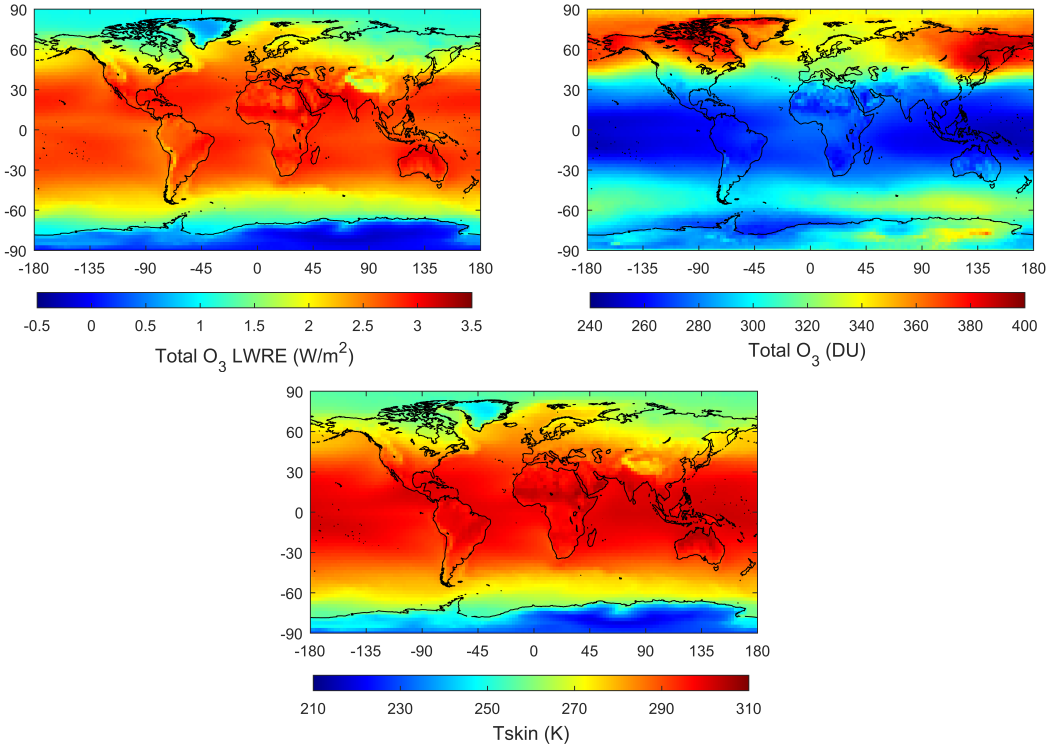

FIGURE C.3: 5-year global distribution of (top - left) total LWRE ($\mathrm{W\,m^{-2}}$), (top - right) total O_3 (DU) and (bottom) surface temperature (K). Data cover the period from 1/3/2012 to 28/2/2017.

5-year trend

Figures C.4 to C.6 show the 5-year trend global distribution of the tropospheric, stratospheric and total LWRE, ozone and surface temperature. Figures are complementary to Sect. 8.5.2.

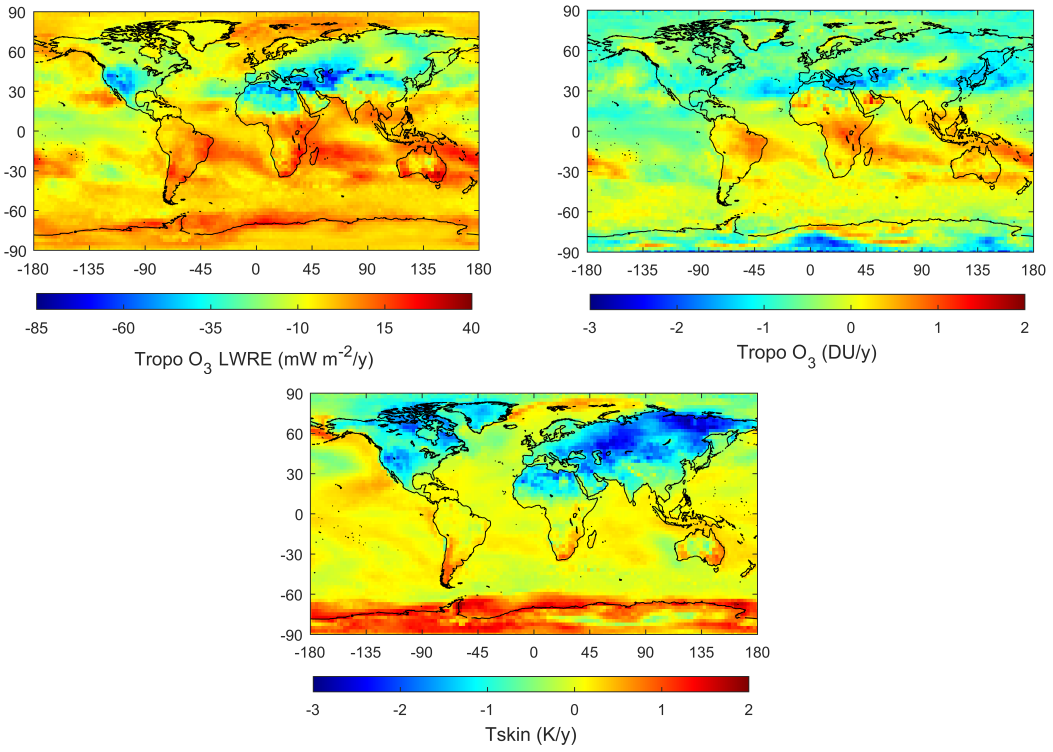

FIGURE C.4: Global distribution of the 5-year-trend of (top - left) tropospheric LWRE ($\mathrm{mW\,m^{-2}/y}$), (top - right) tropospheric O_3 (DU/y) and (bottom) surface temperature (K/y). Data cover the period from 1/3/2012 to 28/2/2017.

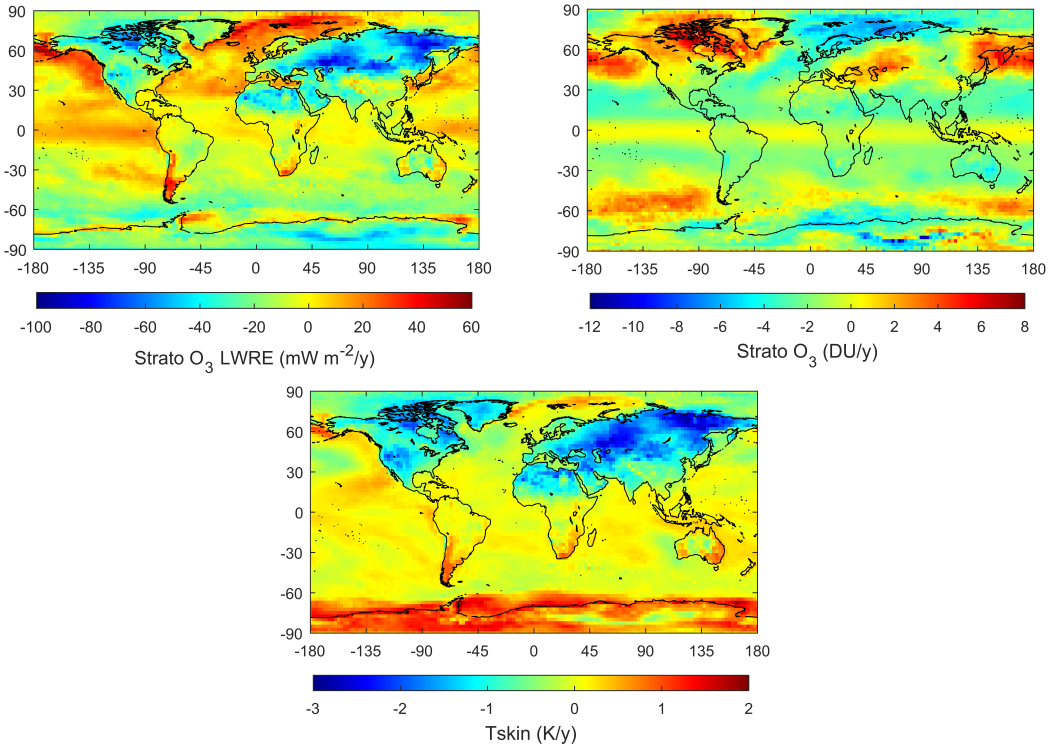

FIGURE C.5: Global distribution of the 5-year-trend of (top - left) stratospheric LWRE ($\mathrm{mW\,m^{-2}/y}$), (top - right) stratospheric O_3 (DU/y) and (bottom) surface temperature (K/y). Data cover the period from 1/3/2012 to 28/2/2017.

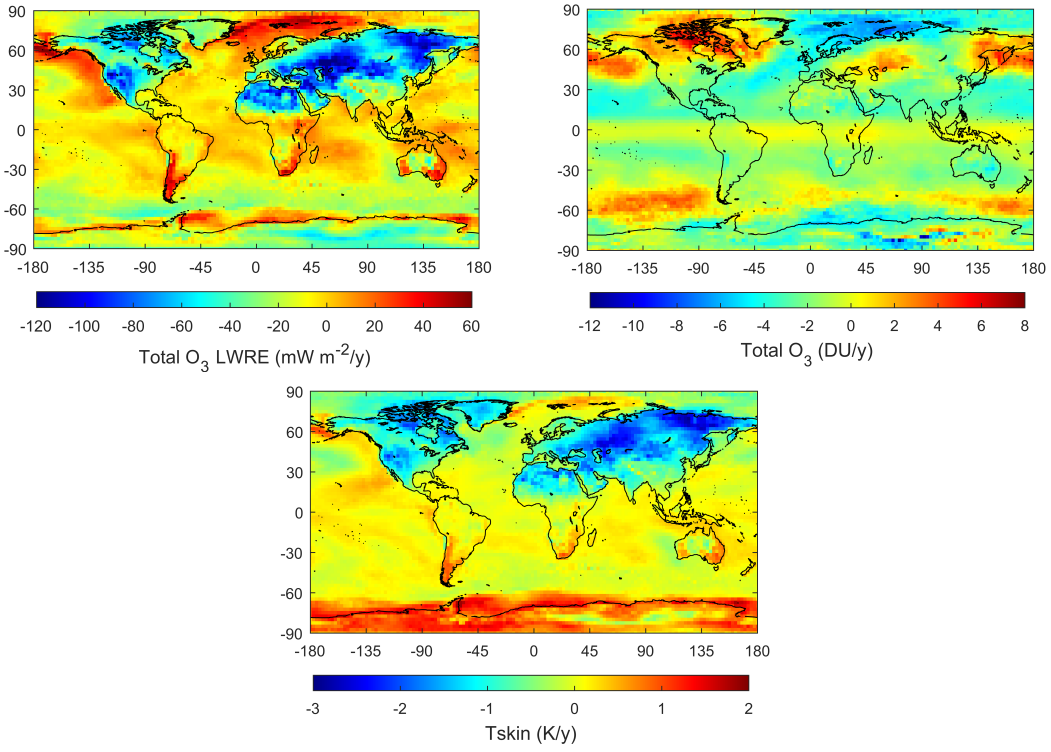

FIGURE C.6: Global distribution of the 5-year-trend of (top - left) total LWRE ($\mathrm{mW\,m^{-2}/y}$), (top - right) total O_3 (DU/y) and (bottom) surface temperature (K/y). Data cover the period from 1/3/2012 to 28/2/2017.

Seasonal distribution

The seasonal patterns of the O_3 LWRE were discussed in Sect. 8.5.1. Here, we provide the seasonal distributions, of a 5-year average (1/3/2012 to 28/2/1017), for the tropospheric, stratospheric and total columns of the LWRE and ozone, along with the surface temperature (figures C.7 to C.13).

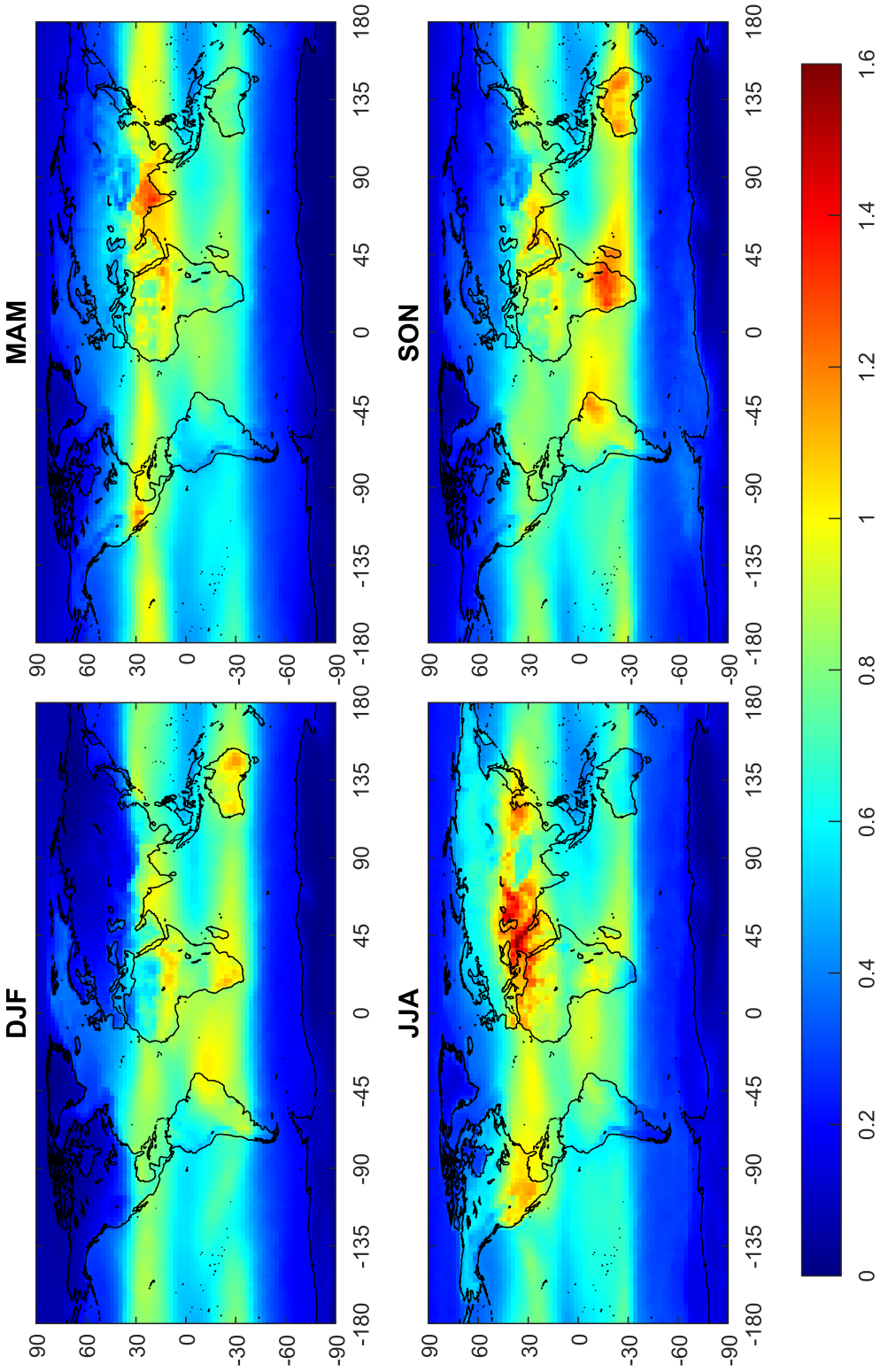

FIGURE C.7: Seasonal 5-year-average global distribution of tropospheric O_3 LWRE (W m^{-2}). Data cover the period from 1/3/2012 to 28/2/2017.

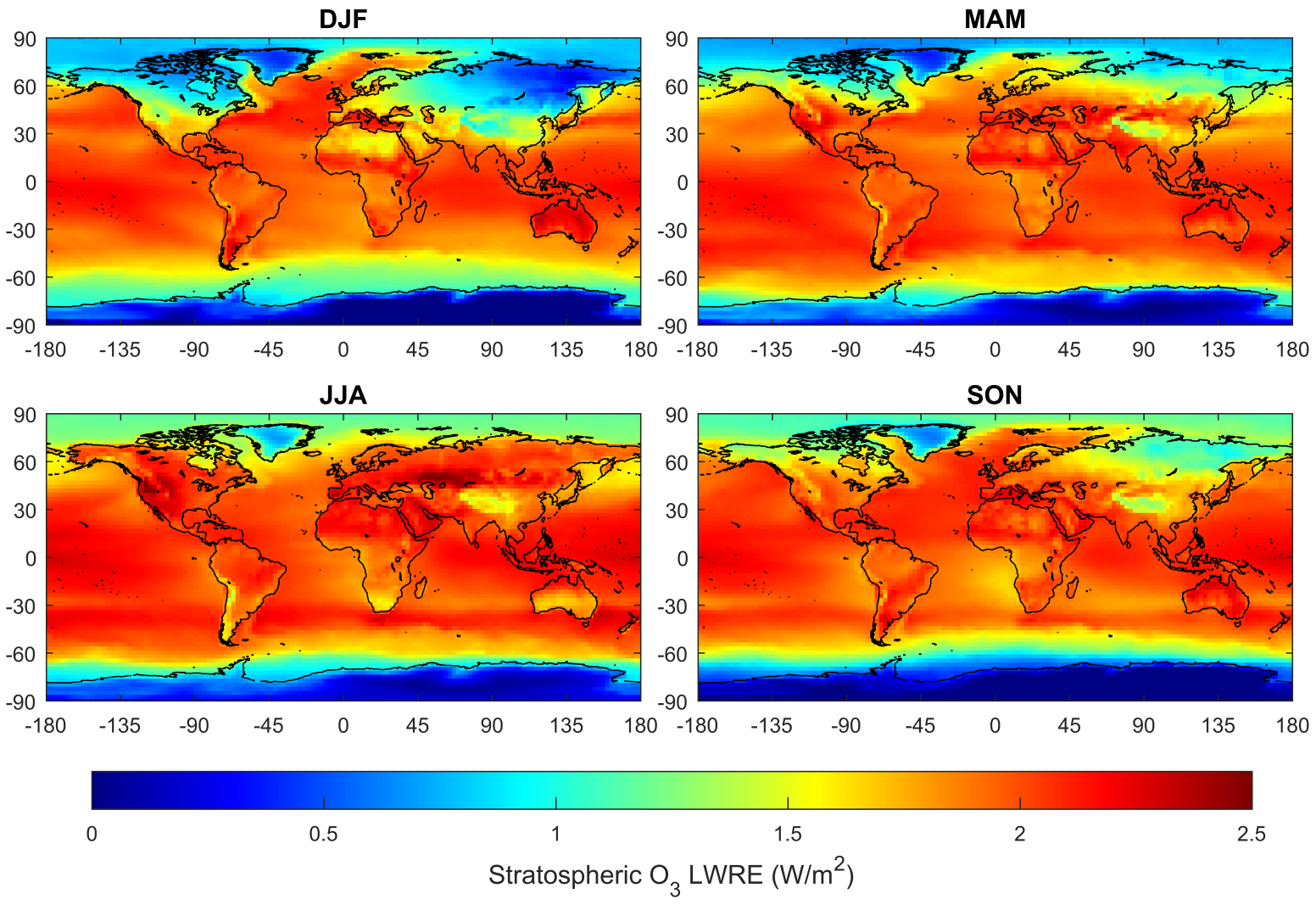

FIGURE C.8: Seasonal 5-year-average global distribution of stratospheric O_3 LWRE ($W\,m^{-2}$). Data cover the period from 1/3/2012 to 28/2/2017.

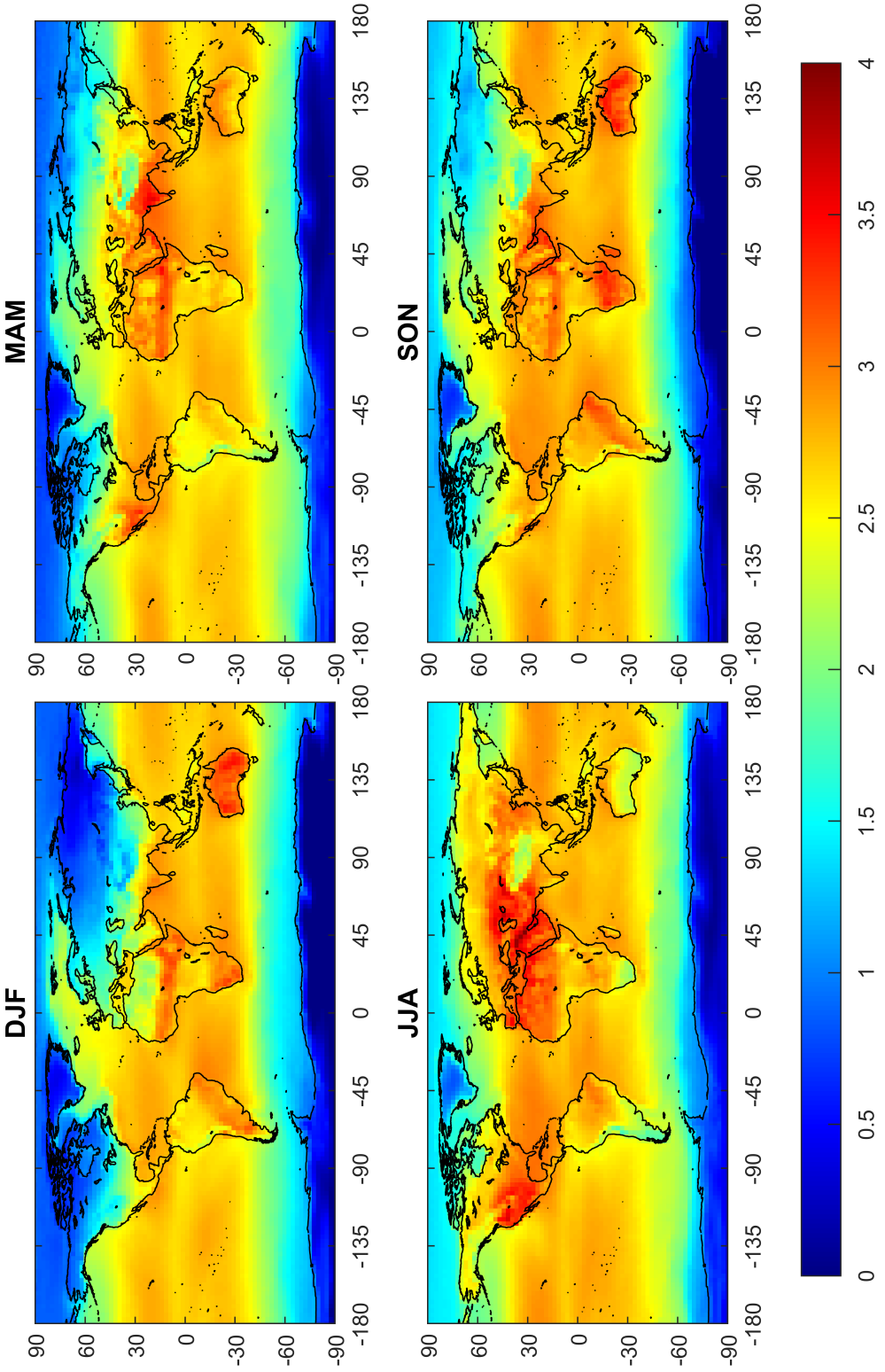

FIGURE C.9: Seasonal 5-year-average global distribution of total O_3 LWRE (W m^{-2}). Data cover the period from 1/3/2012 to 28/2/2017.

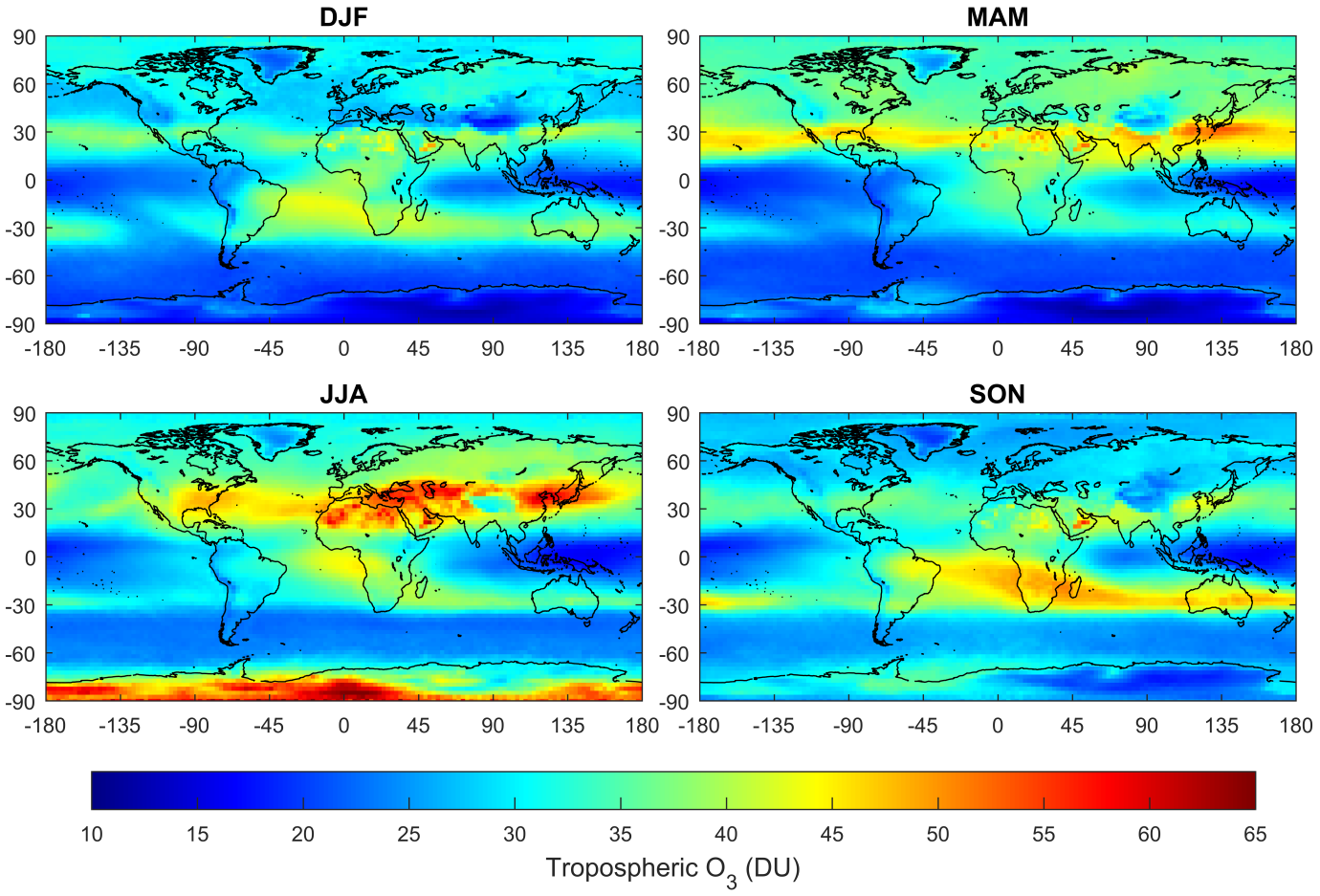

FIGURE C.10: Seasonal 5-year-average global distribution of tropospheric O_3 (DU). Data cover the period from 1/3/2012 to 28/2/2017.

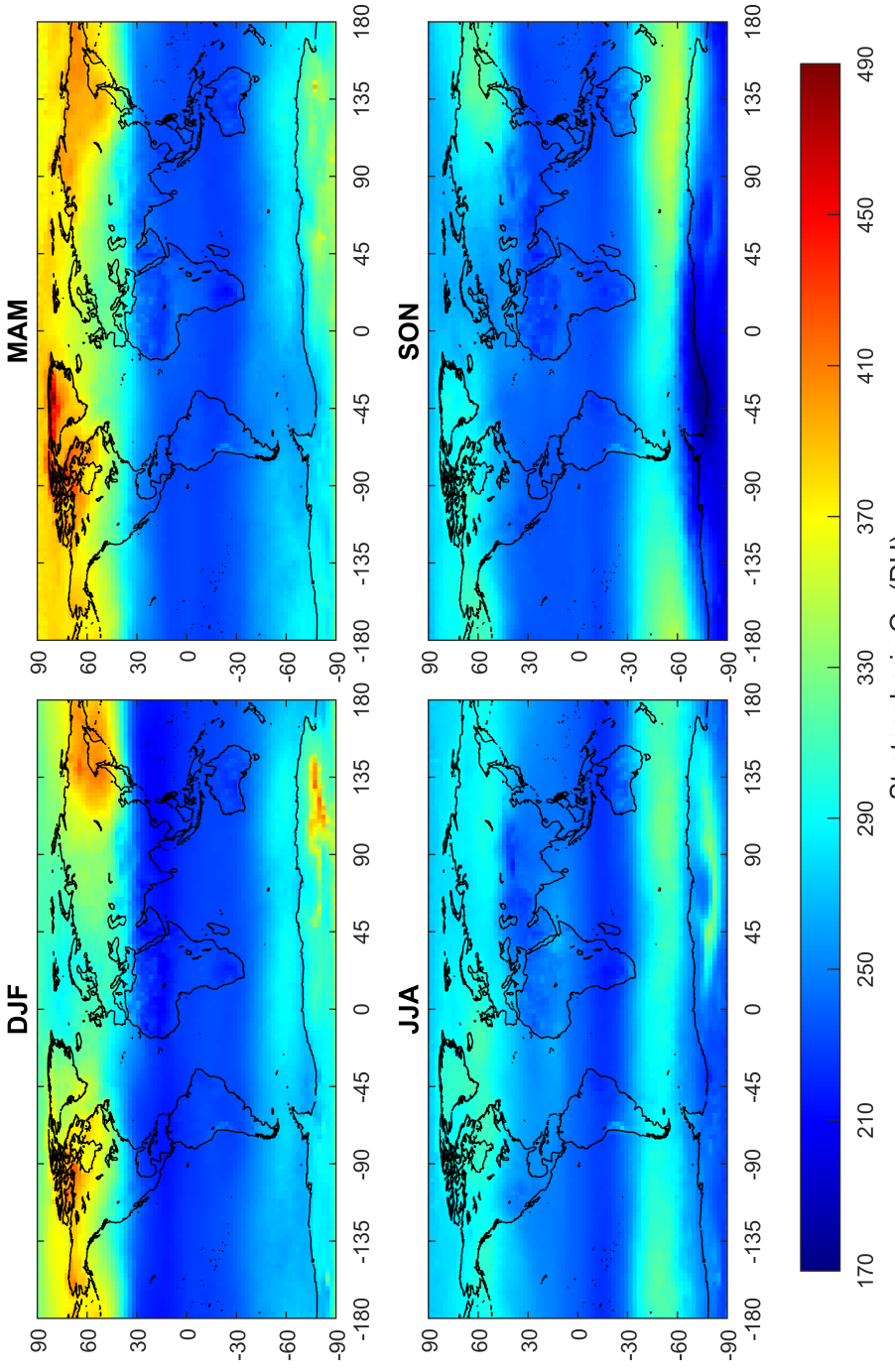

FIGURE C.11: Seasonal 5-year-average global distribution of stratospheric O_3 (DU). Data cover the period from 1/3/2012 to 28/2/2017.

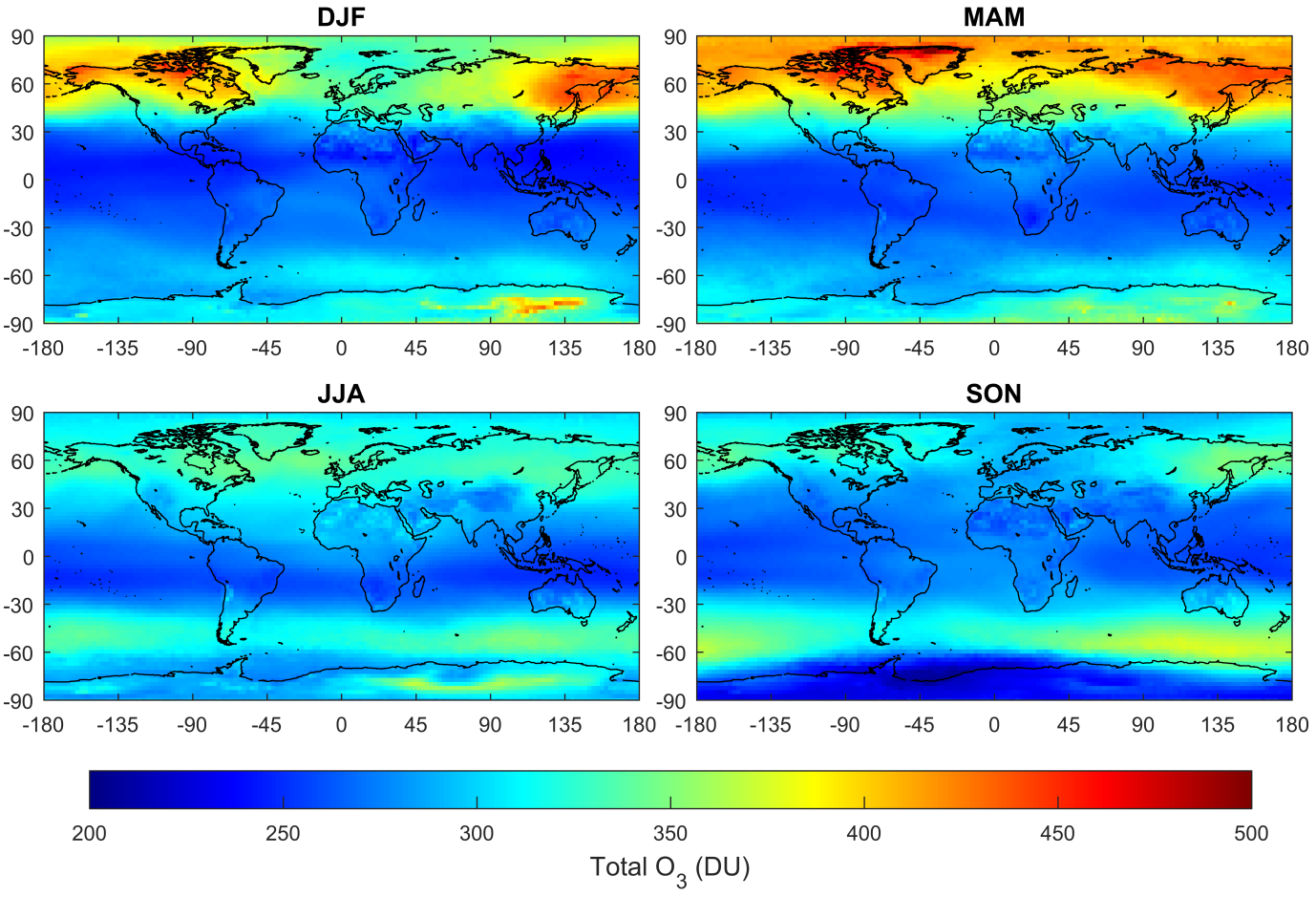

FIGURE C.12: Seasonal 5-year-average global distribution of total O_3 (DU). Data cover the period from 1/3/2012 to 28/2/2017.

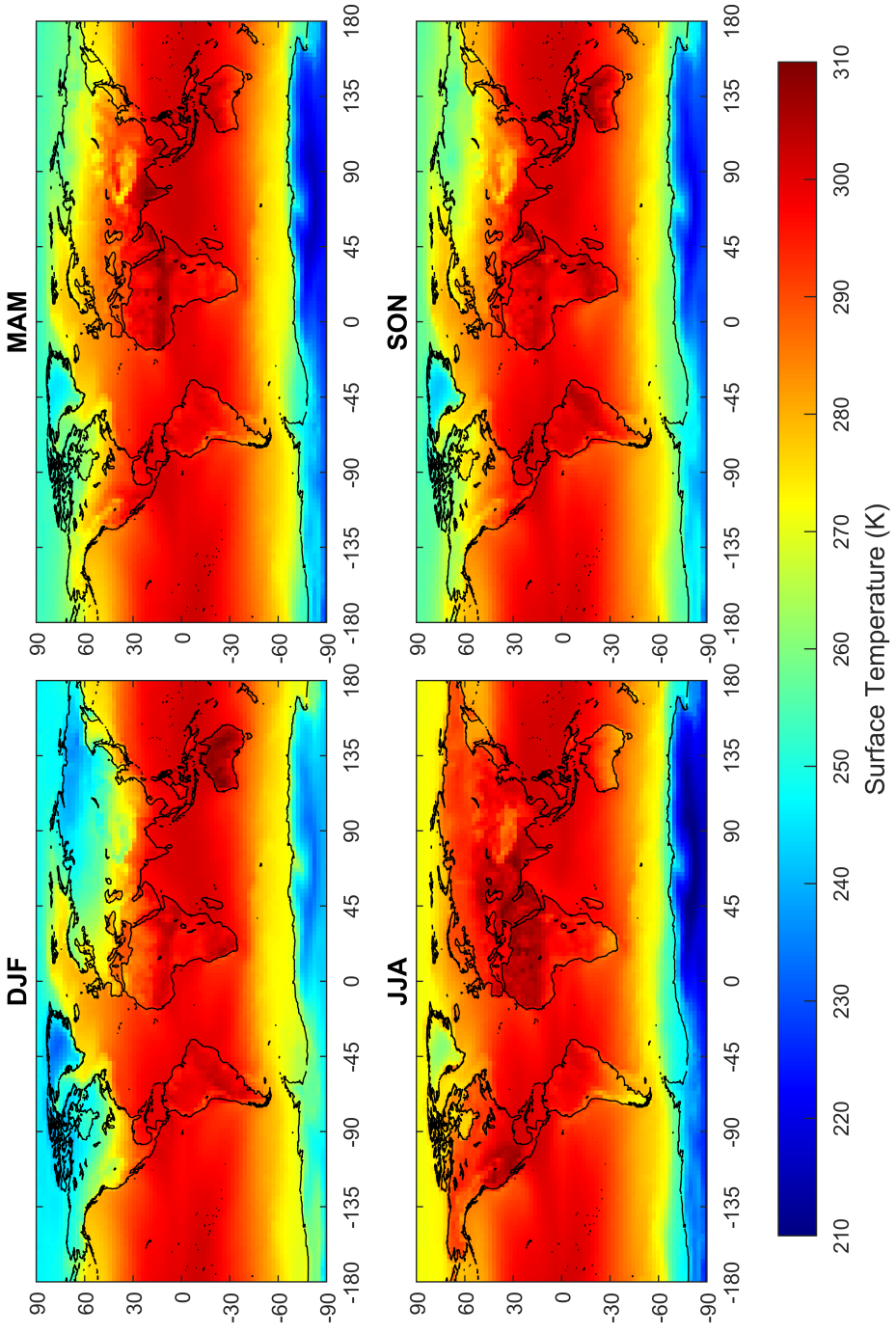

FIGURE C.13: Seasonal 5-year-average global distribution of surface temperature (K). Data cover the period from 1/3/2012 to 28/2/2017.

5-year assessment

Based on the definitions given in Sect. 3.5, the LWRE calculated in this study is closer to the definition of the effective radiative forcing (ERF), as it is defined with respect to the top of the atmosphere and allows rapid adjustments in the atmosphere and the surface (feedback). Similarly, the LWRE evaluates the TOA IR flux change due to ozone absorption, taking into account atmospheric and surface changes. Furthermore, according to IPCC [2013], for ozone, the RF and ERF estimations are similar, hence the use of only the RF. Based on the above, we extend Table 4.1 to include the estimations of this study, with the results of 5 years (1/3/2012 to 28/2/2017). Note that the results of this study include only clear-sky observations, which is likely to result in overestimation of the LWRE.

TABLE C.1: Contributions of tropospheric and stratospheric ozone changes to radiative forcing (Wm^{-2}) from year 1750 to 2011 [IPCC, 2013] and LWRE.

	Troposphere			Stratosphere		
	LW	SW	Total	LW	SW	Total
AR4 Forster et al. (2007)			0.35 (0.25-0.65)			-0.05 (-0.15-0.05)
Shindell et al. (2013)			0.33 (0.31-0.35)			-0.08 (-0.10-0.06)
WMO (Forster et al., 2011)						-0.03 (-0.23-0.17)
Sovde et al. (2011)			0.45 0.39			-0.12 -0.12
Skeie et al. (2011)			0.41 (0.21-0.61)			
ACCMIP	0.33 (0.24-0.42)	0.08 (0.06-0.10)	0.41 (0.21-0.61)	-0.13 (-0.26-0)	0.11 (0.03-0.19)	-0.02 (-0.09-0.05)
AR5			0.40 (0.20-0.60)			-0.05 (-0.15-0.05)
This study	**0.028 ± 0.008**			**-0.001 ± 0.023**		

Bibliography

M. Abramowitz and I. A. Stegun. *Handbook of Mathematical Functions With Formulas, Graphs, and Mathematical Tables*. National Bureau of Standards, Applied Mathematics Series - 55, 1972.

A. M. Aghedo, K. W. Bowman, H. M. Worden, S. S. Kulawik, D. T. Shindell, J. F. Lamarque, G. Faluvegi, M. Parrington, D. B. A. Jones, and S. Rast. The vertical distribution of ozone instantaneous radiative forcing from satellite and chemistry climate models. *J. Geophys. Res.*, 116(D1), 2011. ISSN 2156-2202. doi: 10.1029/2010JD014243.

C. D. Ahrens. *Meteorology Today, 9th Edition*. Brooks Cole, 9 edition, 2008. ISBN 9780495555735, 0495555738.

J. R. Albers, G. N. Kiladis, T. Birner, and J. Dias. Tropical upper-tropospheric Potential Vorticity intrusions during sudden stratospheric warmings. *J. Atmos. Sci.*, 73(6): 2361–2384, 2016. doi: 10.1175/JAS-D-15-0238.1.

M. Antón, D. Loyola, C. Clerbaux, M. López, J. Vilaplana, M. Bañón, J. Hadji-Lazaro, P. Valks, N. Hao, W. Zimmer, P. Coheur, D. Hurtmans, and L. Alados-Arboledas. Validation of the MetOp-A total ozone data from GOME-2 and IASI using reference ground-based measurements at the Iberian Peninsula. *Remote Sens. Environ.*, 115(6): 1380 – 1386, 2011. ISSN 0034-4257. doi: 10.1016/j.rse.2011.01.018.

U. S. Atmosphere. U.S. Standard Atmosphere, 1976. Technical report, NOAA, NASA and USAF, 1976. URL https://ntrs.nasa.gov/search.jsp?R=19770009539.

T. August, D. Klaes, P. Schlüssel, T. Hultberg, M. Crapeau, A. Arriaga, A. O'Carroll, D. Coppens, R. Munro, and X. Calbet. IASI on Metop-A: Operational Level 2 retrievals after five years in orbit. *J. Quant. Spectrosc. Radiat. Transfer*, 113(11):1340 – 1371, 2012. ISSN 0022-4073. doi: 10.1016/j.jqsrt.2012.02.028.

H. H. Aumann, M. T. Chahine, C. Gautier, M. D. Goldberg, E. Kalnay, L. M. McMillin, H. Revercomb, P. W. Rosenkranz, W. L. Smith, D. H. Staelin, L. L. Strow, and J. Susskind. AIRS/AMSU/HSB on the Aqua mission: design, science objectives, data

products, and processing systems. *IEEE Trans. Geosci. Remote Sens.*, 41(2):253–264, Feb 2003. ISSN 0196-2892. doi: 10.1109/TGRS.2002.808356.

A. F. Bais. Absolute spectral measurements of direct solar ultraviolet irradiance with a Brewer spectrophotometer. *Appl. Opt.*, 36(21):5199–5204, Jul 1997. doi: 10.1364/AO.36.005199.

D. Balis, I. S. A. Isaksen, C. Zerefos, I. Zyrichidou, K. Eleftheratos, K. Tourpali, R. Bojkov, B. Rognerud, F. Stordal, O. A. Søvde, and Y. Orsolini. Observed and modelled record ozone decline over the Arctic during winter/spring 2011. *Geophys. Res. Lett.*, 38(23), 2011. ISSN 1944-8007. doi: 10.1029/2011GL049259.

R. Beer. TES on the Aura mission: scientific objectives, measurements, and analysis overview. *IEEE Trans. Geosci. Remote Sens.*, 44(5):1102–1105, May 2006. ISSN 0196-2892. doi: 10.1109/TGRS.2005.863716.

R. Beer, T. A. Glavich, and D. M. Rider. Tropospheric emission spectrometer for the Earth Observing System's Aura satellite. *Appl. Opt.*, 40(15):2356–2367, May 2001. doi: 10.1364/AO.40.002356.

H. Bloom. The Cross-Track Infrared Sounder (CrIS): A sensor for operational meterological remote sensing. In *Opt. Rem. Sens.* Optical Society of America, 2001. doi: 10.1364/FTS.2001.JTuB1.

K. Bowman and D. K. Henze. Attribution of direct ozone radiative forcing to spatially resolved emissions. *Geophys. Res. Lett.*, 39(L22704), 2012. doi: 10.1029/2012GL053274.

K. Bowman, C. Rodgers, S. Kulawik, J. Worden, E. Sarkissian, G. Osterman, T. Steck, M. Lou, A. Eldering, M. Shephard, H. Worden, M. Lampel, S. Clough, P. Brown, C. Rinsland, M. Gunson, and R. Beer. Tropospheric emission spectrometer: retrieval method and error analysis. *IEEE Trans. Geosci. Remote Sens.*, 44(5):1297–1307, May 2006. ISSN 0196-2892. doi: 10.1109/TGRS.2006.871234.

K. W. Bowman, T. Steck, H. M. Worden, J. Worden, S. Clough, and C. Rodgers. Capturing time and vertical variability of tropospheric ozone: A study using TES nadir retrievals. *J. Geophys. Res.*, 107(D23):ACH 21–1–ACH 21–11, 2002. ISSN 2156-2202. doi: 10.1029/2002JD002150.

K. W. Bowman, D. T. Shindell, H. M. Worden, J. Lamarque, P. J. Young, D. S. Stevenson, Z. Qu, M. de la Torre, D. Bergmann, P. J. Cameron-Smith, W. J. Collins, R. Doherty, S. B. Dalsøren, G. Faluvegi, G. Folberth, L. W. Horowitz, B. M. Josse, Y. H. Lee, I. A. MacKenzie, G. Myhre, T. Nagashima, V. Naik, D. A. Plummer, S. T. Rumbold,

R. B. Skeie, S. A. Strode, K. Sudo, S. Szopa, A. Voulgarakis, G. Zeng, S. S. Kulawik, A. M. Aghedo, and J. R. Worden. Evaluation of ACCMIP outgoing longwave radiation from tropospheric ozone using TES satellite observations. *Atmos. Chem. Phys.*, 13(8): 4057–4072, 2013. doi: 10.5194/acp-13-4057-2013.

A. Boynard, C. Clerbaux, P.-F. Coheur, D. Hurtmans, S. Turquety, M. George, J. Hadji-Lazaro, C. Keim, and J. Meyer-Arnek. Measurements of total and tropospheric ozone from IASI comparison with correlative satellite, ground-based and ozonesonde observations. *Atmos. Chem. Phys.*, 9(16):6255–6271, 2009. doi: 10.5194/acp-9-6255-2009.

A. Boynard, D. Hurtmans, M. E. Koukouli, F. Goutail, J. Bureau, S. Safieddine, C. Lerot, J. Hadji-Lazaro, C. Wespes, J.-P. Pommereau, A. Pazmino, I. Zyrichidou, D. Balis, A. Barbe, S. N. Mikhailenko, D. Loyola, P. Valks, M. Van Roozendael, P.-F. Coheur, and C. Clerbaux. Seven years of IASI ozone retrievals from FORLI: validation with independent total column and vertical profile measurements. *Atmos. Meas. Tech.*, 9 (9):4327–4353, 2016. doi: 10.5194/amt-9-4327-2016.

A. Boynard, D. Hurtmans, K. Garane, F. Goutail, J. Hadji-Lazaro, M. E. Koukouli, C. Wespes, A. Keppens, J.-P. Pommereau, A. Pazmino, D. Balis, D. Loyola, P. Valks, P.-F. Coheur, and C. Clerbaux. Validation of the IASI FORLI/Eumetsat ozone products using satellite (GOME-2), ground-based (Brewer-Dobson, SAOZ) and ozonesonde measurements. *Atmos. Meas. Tech.*, 2018:1–35, 2018. doi: 10.5194/amt-2017-461.

J. P. Burrows, M. Weber, M. Buchwitz, V. Rozanov, A. Ladstätter-Weissenmayer, A. Richter, R. DeBeek, R. Hoogen, K. Bramstedt, K.-U. Eichmann, M. Eisinger, and D. Perner. The Global Ozone Monitoring Experiment (GOME): Mission concept and first scientific results. *J. Atmos. Sci.*, 56(2):151–175, 1999. doi: 10.1175/1520-0469(1999)056<0151:TGOMEG>2.0.CO;2.

C. Camy-Peyret, J. Bureau, D. Coppens, B. Théodore, and T. August. L1c comparison of IASI-A and IASI-B on MetOp satellites: monitoring of radiometric and spectral performances and possible use for climate studies. In *2013 EUMETSAT Meteorological Satellite Cionference 19th American Meteorological Society (AMS) Satellite Meteorology, Oceanography, and Climatology Conference, Sept. 2013, Vienne, Austria*, 2013. URL https://hal.archives-ouvertes.fr/hal-00993380.

L. Clarisse, Y. R'Honi, P.-F. Coheur, D. Hurtmans, and C. Clerbaux. Thermal infrared nadir observations of 24 atmospheric gases. *Geophys. Res. Lett.*, 38(10), 2011. ISSN 1944-8007. doi: 10.1029/2011GL047271.

L. Clarisse, D. Hurtmans, C. Clerbaux, J. Hadji-Lazaro, Y. Ngadi, and P.-F. Coheur. Retrieval of sulphur dioxide from the Infrared Atmospheric Sounding Interferometer (IASI). *Atmos. Meas. Tech.*, 5(3):581–594, 2012. doi: 10.5194/amt-5-581-2012.

C. Clerbaux, A. Boynard, L. Clarisse, M. George, J. Hadji-Lazaro, H. Herbin, D. Hurtmans, M. Pommier, A. Razavi, S. Turquety, C. Wespes, and P.-F. Coheur. Monitoring of atmospheric composition using the thermal infrared IASI/MetOp sounder. *Atmos. Chem. Phys.*, 9(16):6041–6054, 2009. doi: 10.5194/acp-9-6041-2009.

N. Clerbaux, S. Dewitte, L. Gonzalez, C. Bertrand, B. Nicula, and A. Ipe. Outgoing longwave flux estimation: improvement of angular modelling using spectral information. *Remote Sens. Environ.*, 85(3):389 – 395, 2002. ISSN 0034-4257. doi: 10.1016/S0034-4257(03)00015-4.

S. Clough, M. Shephard, E. Mlawer, J. Delamere, M. Iacono, K. Cady-Pereira, S. Boukabara, and P. Brown. Atmospheric radiative transfer modeling: a summary of the AER codes. *J. Quant. Spectrosc. Radiat. Transfer*, 91(2):233 – 244, 2005. ISSN 0022-4073. doi: 10.1016/j.jqsrt.2004.05.058.

S. Clough, M. Shephard, J. Worden, P. Brown, H. Worden, M. Luo, C. Rodgers, C. Rinsland, A. Goldman, L. Brown, S. Kulawik, A. Eldering, M. Lampel, G. Osterman, R. Beer, K. Bowman, K. Cady-Pereira, and E. Mlawer. Forward model and Jacobians for Tropospheric Emission Spectrometer retrievals. *IEEE Trans. Geosci. Remote Sens.*, 44(5):1308–1323, May 2006. ISSN 0196-2892. doi: 10.1109/TGRS.2005.860986.

S. A. Clough and M. J. Iacono. Line-by-line calculation of atmospheric fluxes and cooling rates: 2. Application to carbon dioxide, ozone, methane, nitrous oxide and the halocarbons. *J. Geophys. Res.*, 100(D8):16519–16535, 1995. ISSN 2156-2202. doi: 10.1029/95JD01386.

P.-F. Coheur, B. Barret, S. Turquety, D. Hurtmans, J. Hadji-Lazaro, and C. Clerbaux. Retrieval and characterization of ozone vertical profiles from a thermal infrared nadir sounder. *J. Geophys. Res.*, 110(D24), 2005. ISSN 2156-2202. doi: 10.1029/2005JD005845.

P.-F. Coheur, L. Clarisse, S. Turquety, D. Hurtmans, and C. Clerbaux. IASI measurements of reactive trace species in biomass burning plumes. *Atmos. Chem. Phys.*, 9(15): 5655–5667, 2009. doi: 10.5194/acp-9-5655-2009.

C. Crevoisier, D. Nobileau, A. M. Fiore, R. Armante, A. Chédin, and N. A. Scott. Tropospheric methane in the tropics – first year from IASI hyperspectral infrared observations. *Atmos. Chem. Phys.*, 9(17):6337–6350, 2009. doi: 10.5194/acp-9-6337-2009.

W. Demtröder. *Atoms, Molecules and Photons: An Introduction to Atomic-, Molecular- and Quantum Physics*. 1868-4513. Springer-Verlag Berlin Heidelberg, 2 edition, 2010. ISBN 978-3-642-10298-1. doi: 10.1007/978-3-642-10298-1.

S. Doniki, D. Hurtmans, L. Clarisse, C. Clerbaux, H. M. Worden, K. W. Bowman, and P.-F. Coheur. Instantaneous longwave radiative impact of ozone: an application on IASI/MetOp observations. *Atmos. Chem. Phys.*, 15(22):12971–12987, 2015. doi: 10.5194/acp-15-12971-2015.

G. Dufour, M. Eremenko, A. Griesfeller, B. Barret, E. LeFlochmoën, C. Clerbaux, J. Hadji-Lazaro, P.-F. Coheur, and D. Hurtmans. Validation of three different scientific ozone products retrieved from IASI spectra using ozonesondes. *Atmos. Meas. Tech.*, 5(3):611–630, 2012. doi: 10.5194/amt-5-611-2012.

R. D. Evans. Ozone Observations with a Dobson Spectrophotometer - Operations Handbook. NOAA/ESRL Global Monitoring Division, Sept. 2006. URL http://www.o3soft.eu/dobsonweb/messages/revisedNo6NewFigsA.pdf.

J. C. Farman, B. G. Gardiner, and J. D. Shanklin. Large losses of total ozone in Antarctica reveal seasonal ClOx/NOx interaction. *Nature*, 315(6016):207–210, May 1985. ISSN 1476-4687. doi: 10.1038/315207a0.

J.-M. Flaud, C. Camy-Peyret, and R. A. Toth. *Water Vapour line parameters from Microwave to Medium Infrared*, volume 19 of *Selected Constants*. Pergamon Press, CNRS, 1981.

J.-M. Flaud, C. Camy-Peyret, C. P. Rinsland, M. A. H. Smith, and V. M. Devi. *Atlas of Ozone Spectral Parameters from Microwave to Medium Infrared*. Academic Press, Inc., 1990.

P. Forster, V. Ramaswamy, P. Artaxo, T. Berntsen, R. Betts, D. Fahey, J. Haywood, D. L. J. Lean, G. Myhre, J. Nganga, R. Prinn, M. S. G. Raga, and R. V. Dorland. Changes in Atmospheric Constituents and in Radiative Forcing. In: Climate Change 2007: The Physical Science Basis. Contribution of Working Group I to the Fourth Assessment Report of the Intergovernmental Panel on Climate Change. 2007.

P. Forster, D. Thompson, M. Baldwin, M. Chipperfield, M. Dameris, J. Haigh, D. Karoly, P. Kushner, W. Randel, K. Rosenlof, D. Seidel, S. Solomon, G. Beig, P. Braesicke, N. Butchart, N. Gillett, K. Grise, D. Marsh, C. McLandress, T. Rao, S.-W. Son, G. Stenchikov, and S. Yoden. Stratospheric changes and climate, Chapter 4 in Scientific Assessment of Ozone Depletion: 2010, Global Ozone Research and Monitoring

Project – Report No. 52. Technical report, World Meteorological Organization, Geneva, Switzerland, 2011.

P. M. Forster and K. P. Shine. Radiative forcing and temperature trends from stratospheric ozone changes. *J. Geophys. Res.*, 102(D9):10841–10855, 1997. ISSN 2156-2202. doi: 10.1029/96JD03510.

A. Gaudel, O. Cooper, G. Ancellet, B. Barret, A. Boynard, J. Burrows, C. Clerbaux, P.-F. Coheur, J. Cuesta, E. Cuevas, S. Doniki, G. Dufour, F. Ebojie, G. Foret, O. Garcia, M. Granados Muños, J. Hannigan, F. Hase, G. Huang, B. Hassler, D. Hurtmans, D. Jaffe, N. Jones, and et al. Tropospheric Ozone Assessment Report: Present-day distribution and trends of tropospheric ozone relevant to climate and global atmospheric chemistry model evaluation. *Elem. Sci. Anth.*, 6(1):39, 2018. doi: 10.1525/elementa.291.

M. Gauss, G. Myhre, G. Pitari, M. J. Prather, I. S. A. Isaksen, T. K. Berntsen, G. P. Brasseur, F. J. Dentener, R. G. Derwent, D. A. Hauglustaine, L. W. Horowitz, D. J. Jacob, M. Johnson, K. S. Law, L. J. Mickley, J.-F. Müller, P.-H. Plantevin, J. A. Pyle, H. L. Rogers, D. S. Stevenson, J. K. Sundet, M. van Weele, and O. Wild. Radiative forcing in the 21st century due to ozone changes in the troposphere and the lower stratosphere. *J. Geophys. Res.*, 108(D9), 2003. ISSN 2156-2202. doi: 10.1029/2002JD002624.

J. Gazeaux, C. Clerbaux, M. George, J. Hadji-Lazaro, J. Kuttippurath, P.-F. Coheur, D. Hurtmans, T. Deshler, M. Kovilakam, P. Campbell, V. Guidard, F. Rabier, and J.-N. Thépaut. Intercomparison of polar ozone profiles by IASI/MetOp sounder with 2010 Concordiasi ozonesonde observations. *Atmos. Meas. Tech.*, 6(3):613–620, 2013. doi: 10.5194/amt-6-613-2013.

M. Gottwald, H. Bovensmann, G. Lichtenberg, S. Noel, A. von Bargen, S. Slijkhuis, A. Piters, R. Hoogeveen, C. von Savigny, M. Buchwitz, A. Kokhanovsky, A. Richter, A. Rozanov, T. Holzer-Popp, K. Bramstedt, J.-C. Lambert, J. Skupin, F. Wittrock, H. Schrijver, and J. Burrows. *SCIAMACHY, Monitoring the Changing Earth's Atmosphere*. DLR, Institut für Methodik der Fernerkundung, 2006. URL https://atmos.eoc.dlr.de/projects/scops/sciamachy_book/sciamachy_book_dlr.html.

D. Hauglustaine, L. Emmons, M. Newchurch, G. Brasseur, T. Takao, K. Matsubara, J. Johnson, B. Ridley, J. Stith, and J. Dye. On the Role of Lightning NOx in the Formation of Tropospheric Ozone Plumes: A Global Model Perspective. *J. Atmos. Chem.*, 38(3):277–294, Mar 2001. ISSN 1573-0662. doi: 10.1023/A:1006452309388.

D. F. Heath, A. J. Krueger, H. A. Roeder, and B. D. Henderson. The Solar Backscatter Ultraviolet and Total Ozone Mapping Spectrometer (SBUV/TOMS) for NIMBUS G. *Opt. Eng.*, 14(4):144323–144323–, 1975. doi: 10.1117/12.7971839.

F. Hilton, R. Armante, T. August, C. Barnet, A. Bouchard, C. Camy-Peyret, V. Capelle, L. Clarisse, C. Clerbaux, P.-F. Coheur, A. Collard, C. Crevoisier, G. Dufour, D. Edwards, F. Faijan, N. Fourrié, A. Gambacorta, M. Goldberg, V. Guidard, D. Hurtmans, S. Illingworth, N. Jacquinet-Husson, T. Kerzenmacher, D. Klaes, L. Lavanant, G. Masiello, M. Matricardi, A. McNally, S. Newman, E. Pavelin, S. Payan, E. Péquignot, S. Peyridieu, T. Phulpin, J. Remedios, P. Schlüssel, C. Serio, L. Strow, C. Stubenrauch, J. Taylor, D. Tobin, W. Wolf, and D. Zhou. Hyperspectral Earth Observation from IASI: Five Years of Accomplishments. *Bull. Amer. Meteor. Soc.*, 93(3):347–370, Sept. 2012. ISSN 0003-0007. doi: 10.1175/BAMS-D-11-00027.1.

G. Hönninger, C. von Friedeburg, and U. Platt. Multi axis differential optical absorption spectroscopy (MAX-DOAS). *Atmos. Chem. Phys.*, 4(1):231–254, 2004. doi: 10.5194/acp-4-231-2004.

D. Hurtmans, P.-F. Coheur, C. Wespes, L. Clarisse, O. Scharf, C. Clerbaux, J. Hadji-Lazaro, M. George, and S. Turquety. FORLI radiative transfer and retrieval code for IASI. *J. Quant. Spectrosc. Radiat. Transfer*, 113(11):1391 – 1408, 2012. ISSN 0022-4073. doi: 10.1016/j.jqsrt.2012.02.036. Three Leaders in Spectroscopy.

IPCC. *Climate Change 2013: The Physical Science Basis. Contribution of Working Group I to the Fifth Assessment Report of the Intergovernmental Panel on Climate Change*. Cambridge University Press, Cambridge, United Kingdom and New York, NY, USA, 2013.

IPCC-TEAP. *IPCC/TEAP Special Report on safeguarding the ozone layer and the global climate system: issues related to hydrofluorocarbons and perfluorocarbons*. 2005. URL https://www.ipcc.ch/report/safeguarding-the-ozone-layer-and-the-global-climate-system/.

D. J. Jacob. *Introduction to Atmpsheric Chemistry*. Princeton University Press, Princeton, New Jersey, Jan 1999.

M. Z. Jacobson. *Atmospheric pollution: history, science, and regulation*. Cambridge University Press, 1 edition, 2002. ISBN 0521811716, 9780521811712, 0521010446, 9780521010443.

J. Joiner, M. R. Schoeberl, A. P. Vasilkov, L. Oreopoulos, S. Platnick, N. J. Livesey, and P. F. Levelt. Accurate satellite-derived estimates of the tropospheric ozone impact

on the global radiation budget. *Atmos. Chem. Phys.*, 9(13):4447–4465, 2009. doi: 10.5194/acp-9-4447-2009.

D. Jouglet, J. Chinaud, C. Maraldi, E. Jacquette, V. Lonjou, D. Blumstein, O. Vandermarcq, and X. Lenot. Radiometric and spectral inter-comparison of IASI: IASI-A / IASI-B, IASI / AIRS, IASI / CrIS. In *CALCON 2014 Meeting, August 12, 2014, Salt Lake City, USA*, 2014.

F. Karagulian, L. Clarisse, C. Clerbaux, A. J. Prata, D. Hurtmans, and P. F. Coheur. Detection of volcanic SO2, ash, and H2SO4 using the Infrared Atmospheric Sounding Interferometer (IASI). *J. Geophys. Res. Atm.*, 115(D2), 2010. doi: 10.1029/2009JD012786.

L. Kuai, K. W. Bowman, H. M. Worden, R. L. Herman, and S. S. Kulawik. Hydrological controls on the tropospheric ozone greenhouse gas effect. *Elem. Sci. Anth.*, 5(10), 2017.

S. S. Kulawik, J. Worden, A. Eldering, K. Bowman, M. Gunson, G. B. Osterman, L. Zhang, S. A. Clough, M. W. Shephard, and R. Beer. Implementation of cloud retrievals for Tropospheric Emission Spectrometer (TES) atmospheric retrievals: Part 1. description and characterization of errors on trace gas retrievals. *J. Geophys. Res. Atm.*, 111(D24), 2006. ISSN 2156-2202. doi: 10.1029/2005JD006733. D24204.

A. A. Lacis, D. J. Wuebbles, and J. A. Logan. Radiative forcing of climate by changes in the vertical distribution of ozone. *J. Geophys. Res.*, 95(D7):9971–9981, 1990. ISSN 2156-2202. doi: 10.1029/JD095iD07p09971.

J.-F. Lamarque, T. C. Bond, V. Eyring, C. Granier, A. Heil, Z. Klimont, D. Lee, C. Liousse, A. Mieville, B. Owen, M. G. Schultz, D. Shindell, S. J. Smith, E. Stehfest, J. Van Aardenne, O. R. Cooper, M. Kainuma, N. Mahowald, J. R. McConnell, V. Naik, K. Riahi, and D. P. van Vuuren. Historical (1850–2000) gridded anthropogenic and biomass burning emissions of reactive gases and aerosols: methodology and application. *Atmos. Chem. Phys.*, 10(15):7017–7039, 2010. doi: 10.5194/acp-10-7017-2010.

J.-F. Lamarque, L. K. Emmons, P. G. Hess, D. E. Kinnison, S. Tilmes, F. Vitt, C. L. Heald, E. A. Holland, P. H. Lauritzen, J. Neu, J. J. Orlando, P. J. Rasch, and G. K. Tyndall. CAM-chem: description and evaluation of interactive atmospheric chemistry in the Community Earth System Model. *Geosci. Model Dev.*, 5(2):369–411, 2012. doi: 10.5194/gmd-5-369-2012.

T. Leblanc, S. McDermid, M. Müller, F. Immler, O. Schrems, K. Stebel, G. Hansen, W. Steinbrecht, H. Claude, A. Pazmino, S. Godin-Beekmann, G. Ancellet, J. L. Baray, H. Bencherif, Y. Meijer, D. Swart, L. Twigg, T. McGee, J. Thayer, J. Livingston,

P. Keckhut, A. Hauchcorne, J. E. Barnes, and P. von der Gathen. The NDSC ozone and temperature lidar algorithm intercomparison initiative (A2I): project overview. In *22nd International Laser Radar Conference (ILRC 2004) : 12 - 16 July 2004, Matera, Italy / European Space Agency*, volume 881, July 2004.

A. M. Lee, R.-L. Jones, I. Kilbane-Dawe, and J. A. Pyle. Diagnosing ozone loss in the extratropical lower stratosphere. *J. Geophys. Res.*, 107(D11), 2002. doi: 10.1029/2001JD000538.

P. F. Levelt, G. H. J. van den Oord, M. R. Dobber, A. Malkki, H. Visser, J. de Vries, P. Stammes, J. O. V. Lundell, and H. Saari. The Ozone Monitoring Instrument. *IEEE Trans. Geosci. Remote Sens.*, 44(5):1093–1101, May 2006. ISSN 0196-2892. doi: 10.1109/TGRS.2006.872333.

J. Li. Gaussian Quadrature and its Application to Infrared Radiation. *J. Atmos. Sci.*, 57(5):753–765, Mar. 2000. ISSN 0022-4928. doi: 10.1175/1520-0469(2000)057<0753:GQAIAT>2.0.CO;2.

Z. Li. On the angular correction of satellite radiation measurements: The performance of ERBE angular dependence model in the Arctic. *Theor. Appl. Climatol.*, 54(3-4):235–248, 1996. ISSN 0177-798X. doi: 10.1007/BF00865166.

K. N. Liou. *An Introduction to Atmospheric Radiation.* Academic Press, second edition, 2002.

N. G. Loeb, N. Manalo-Smith, S. Kato, W. F. Miller, S. K. Gupta, P. Minnis, and B. A. Wielicki. Angular Distribution Models for Top-of-Atmosphere Radiative Flux Estimation from the Clouds and the Earth's Radiant Energy System Instrument on the Tropical Rainfall Measuring Mission Satellite. Part I: Methodology. *J. Appl. Meteor.*, 42(2):240–265, Feb. 2003. ISSN 0894-8763. doi: 10.1175/1520-0450(2003)042<0240:ADMFTO>2.0.CO;2.

D. G. Loyola, M. E. Koukouli, P. Valks, D. S. Balis, N. Hao, M. Van Roozendael, R. J. D. Spurr, W. Zimmer, S. Kiemle, C. Lerot, and J.-C. Lambert. The GOME-2 total column ozone product: Retrieval algorithm and ground-based validation. *J. Geophys. Res. Atm.*, 116(D7), 2011. ISSN 2156-2202. doi: 10.1029/2010JD014675. D07302.

C. R. MacIntosh, K. P. Shine, and W. J. Collins. Radiative forcing and climate metrics for ozone precursor emissions: the impact of multi-model averaging. *Atmos. Chem. Phys.*, 15(7):3957–3969, 2015. doi: 10.5194/acp-15-3957-2015.

G. L. Manney and Z. D. Lawrence. The major stratospheric final warming in 2016: dispersal of vortex air and termination of Arctic chemical ozone loss. *Atmos. Chem. Phys.*, 16(23):15371–15396, 2016. doi: 10.5194/acp-16-15371-2016.

G. L. Manney, M. L. Santee, M. Rex, N. J. Livesey, M. C. Pitts, P. Veefkind, E. R. Nash, I. Wohltmann, R. Lehmann, L. Froidevaux, L. R. Poole, M. R. Schoeberl, D. P. Haffner, J. Davies, V. Dorokhov, H. Gernandt, B. Johnson, R. Kivi, E. Kyro, N. Larsen, P. F. Levelt, A. Makshtas, C. T. McElroy, H. Nakajima, M. C. Parrondo, D. W. Tarasick, P. von der Gathen, K. A. Walker, and N. S. Zinoviev. Unprecedented Arctic ozone loss in 2011. *Nature*, 478(7370):469–475, Oct. 2011. ISSN 0028-0836. doi: 10.1038/nature10556.

G. L. Manney, Z. D. Lawrence, M. L. Santee, N. J. Livesey, A. Lambert, and M. C. Pitts. Polar processing in a split vortex: Arctic ozone loss in early winter 2012/2013. *Atmos. Chem. Phys.*, 15(10):5381–5403, 2015. doi: 10.5194/acp-15-5381-2015.

R. D. McPeters, G. J. Labow, and J. A. Logan. Ozone climatological profiles for satellite retrieval algorithms. *J. Geophys. Res. Atm.*, 112(D5), 2007. ISSN 2156-2202. doi: 10.1029/2005JD006823. D05308.

K. Mohanakumar. *Stratosphere Troposphere Interactions*. Number 1. Springer Netherlands, 2008. ISBN 978-1-4020-8216-0. doi: 10.1007/978-1-4020-8217-7.

R. Muller. *Stratospheric Ozone Depletion and Climate Change*. The Royal Society of Chemistry, 2012. ISBN 978-1-84973-002-0. doi: 10.1039/9781849733182.

L. T. Murray. Lightning NOx and Impacts on Air Quality. *Current Pollution Reports*, 2 (2):115–133, Jun 2016. ISSN 2198-6592. doi: 10.1007/s40726-016-0031-7.

R. Nassar, J. A. Logan, H. M. Worden, I. A. Megretskaia, K. W. Bowman, G. B. Osterman, A. M. Thompson, D. W. Tarasick, S. Austin, H. Claude, M. K. Dubey, W. K. Hocking, B. J. Johnson, E. Joseph, J. Merrill, G. A. Morris, M. Newchurch, S. J. Oltmans, F. Posny, F. J. Schmidlin, H. Vömel, D. N. Whiteman, and J. C. Witte. Validation of Tropospheric Emission Spectrometer (TES) nadir ozone profiles using ozonesonde measurements. *J. Geophys. Res. Atm.*, 113(D15), 2008. ISSN 2156-2202. doi: 10.1029/2007JD008819.

H. Oetjen, V. H. Payne, S. S. Kulawik, A. Eldering, J. Worden, D. P. Edwards, G. L. Francis, H. M. Worden, C. Clerbaux, J. Hadji-Lazaro, and D. Hurtmans. Extending the satellite data record of tropospheric ozone profiles from Aura-TES to MetOp-IASI. *Atmos. Meas. Tech.*, 7(7):7013–7051, 2014. doi: 10.5194/amt-7-7013-2014.

H. Oetjen, V. H. Payne, J. L. Neu, S. S. Kulawik, D. P. Edwards, A. Eldering, H. M. Worden, and J. R. Worden. A joint data record of tropospheric ozone from Aura-TES and MetOp-IASI. *Atmos. Chem. Phys.*, 16(15):10229–10239, 2016. doi: 10.5194/acp-16-10229-2016.

G. B. Osterman, S. S. Kulawik, H. M. Worden, N. A. D. Richards, B. M. Fisher, A. Eldering, M. W. Shephard, L. Froidevaux, G. Labow, M. Luo, R. L. Herman, K. W. Bowman, and A. M. Thompson. Validation of Tropospheric Emission Spectrometer (TES) measurements of the total, stratospheric, and tropospheric column abundance of ozone. *J. Geophys. Res.*, 113(D15), 2008. ISSN 2156-2202. doi: 10.1029/2007JD008801.

G. W. Petty. *A First Course in Atmospheric Radiation*. Sundog Publishing, Madison, Wisconsin, 2nd edition, 2006. ISBN 978-0-9729033-1-8.

A. Petzold, V. Thouret, C. Gerbig, A. Zahn, C. A. M. Brenninkmeijer, M. Gallagher, M. Hermann, M. Pontaud, H. Ziereis, D. Boulanger, J. Marshall, P. Nédélec, H. G. J. Smit, U. Friess, J.-M. Flaud, A. Wahner, J.-P. Cammas, A. Volz-Thomas, and IAGOS Team. Global-scale atmosphere monitoring by in-service aircraft – current achievements and future prospects of the European Research Infrastructure IAGOS. *Tellus B: Chemical and Physical Meteorology*, 67(1):28452, 2015. doi: 10.3402/tellusb.v67.28452.

J. P. Pommereau and F. Goutail. Stratospheric O3 and NO2 observations at the Southern Polar circle in summer and fall 1988. *Geophys. Res. Lett.*, 15(895), 1988.

M. Pommier, C. Clerbaux, K. S. Law, G. Ancellet, P. Bernath, P.-F. Coheur, J. Hadji-Lazaro, D. Hurtmans, P. Nédélec, J.-D. Paris, F. Ravetta, T. B. Ryerson, H. Schlager, and A. J. Weinheimer. Analysis of IASI tropospheric O3 data over the Arctic during POLARCAT campaigns in 2008. *Atmos. Chem. Phys.*, 12(16):7371–7389, 2012. doi: 10.5194/acp-12-7371-2012.

V. Ramaswamy. *Radiative Forcing in Climate Change. In: Climate Change 2001: The Scientific Basis. Contribution of Working Group I to the Third Assessment Report of The Intergovernmental Panel on climate change*. Cambridge University Press, Cambridge, United Kingdom and New York, NY, USA, 2001.

A. Razavi, F. Karagulian, L. Clarisse, D. Hurtmans, P. F. Coheur, C. Clerbaux, J. F. Müller, and T. Stavrakou. Global distributions of methanol and formic acid retrieved for the first time from the IASI/MetOp thermal infrared sounder. *Atmos. Chem. Phys.*, 11(2):857–872, 2011. doi: 10.5194/acp-11-857-2011.

C. D. Rodgers. *Inverse Methods For Atmospheric Sounding: Theory and Practice*, volume 2 of *Series on Atmospheric, Oceanic and Planetary Physics*. World Scientific Publishing Co. Pte. Ltd., Singapore, 2000.

L. Rothman, I. Gordon, Y. Babikov, A. Barbe, D. C. Benner, P. Bernath, M. Birk, L. Bizzocchi, V. Boudon, L. Brown, A. Campargue, K. Chance, E. Cohen, L. Coudert, V. Devi, B. Drouin, A. Fayt, J.-M. Flaud, R. Gamache, J. Harrison, J.-M. Hartmann, C. Hill, J. Hodges, D. Jacquemart, A. Jolly, J. Lamouroux, R. L. Roy, G. Li, D. Long, O. Lyulin, C. Mackie, S. Massie, S. Mikhailenko, H. Müller, O. Naumenko, A. Nikitin, J. Orphal, V. Perevalov, A. Perrin, E. Polovtseva, C. Richard, M. Smith, E. Starikova, K. Sung, S. Tashkun, J. Tennyson, G. Toon, V. Tyuterev, and G. Wagner. The HITRAN 2012 molecular spectroscopic database. *J. Quant. Spectrosc. Radiat. Transfer*, 130(0):4 – 50, 2013. ISSN 0022-4073. doi: 10.1016/j.jqsrt.2013.07.002. HITRAN 2012 special issue.

M. B. Rubin. The History of Ozone. the Schönbein Period, 1839 - 1868. *Bull. Hist. Chem.*, 26(1), 2001.

S. Safieddine, A. Boynard, P.-F. Coheur, D. Hurtmans, G. Pfister, B. Quennehen, J. L. Thomas, J.-C. Raut, K. S. Law, Z. Klimont, J. Hadji-Lazaro, M. George, and C. Clerbaux. Summertime tropospheric ozone assessment over the Mediterranean region using the thermal infrared IASI/MetOp sounder and the WRF-Chem model. *Atmos. Chem. Phys.*, 14(18):10119–10131, 2014. doi: 10.5194/acp-14-10119-2014.

M. L. Santee, G. L. Manney, N. J. Livesey, L. Froidevaux, M. J. Schwartz, and W. G. Read. Trace gas evolution in the lowermost stratosphere from Aura Microwave Limb Sounder measurements. *J. Geophys. Res.*, 116(D18306), 2011. doi: 10.1029/2011JD015590.

C. Scannell, D. Hurtmans, A. Boynard, J. Hadji-Lazaro, M. George, A. Delcloo, O. Tuinder, P.-F. Coheur, and C. Clerbaux. Antarctic ozone hole as observed by IASI/MetOp for 2008-2010. *Atmos. Meas. Tech.*, 5(1):123–139, 2012. doi: 10.5194/amt-5-123-2012.

P. Schlüssel, T. H. Hultberg, P. L. Phillips, T. August, and X. Calbet. The operational IASI Level 2 processor. *Adv. Space Res.*, 36(5):982 – 988, 2005. ISSN 0273-1177. doi: 10.1016/j.asr.2005.03.008.

G. A. Schmidt, R. Ruedy, J. E. Hansen, I. Aleinov, N. Bell, M. Bauer, S. Bauer, B. Cairns, V. Canuto, Y. Cheng, A. Del Genio, G. Faluvegi, A. D. Friend, T. M. Hall, Y. Hu, M. Kelley, N. Y. Kiang, D. Koch, A. A. Lacis, J. Lerner, K. K. Lo, R. L. Miller, L. Nazarenko, V. Oinas, J. Perlwitz, J. Perlwitz, D. Rind, A. Romanou, G. L. Russell,

M. Sato, D. T. Shindell, P. H. Stone, S. Sun, N. Tausnev, D. Thresher, and M.-S. Yao. Present-Day Atmospheric Simulations Using GISS Model: Comparison to In Situ, Satellite, and Reanalysis Data. *J. Climate*, 19(2):153–192, 2006. doi: 10.1175/JCLI3612.1.

D. Shindell, G. Faluvegi, L. Nazarenko, K. Bowman, J.-F. Lamarque, A. Voulgarakis, G. A. Schmidt, O. Pechony, and R. Ruedy. Attribution of historical ozone forcing to anthropogenic emissions. *Nature Clim. Change*, 3(6):567–570, jun 2013. ISSN 1758-678X. doi: 10.1038/nclimate1835.

D. T. Shindell, G. Faluvegi, L. Rotstayn, and G. Milly. Spatial patterns of radiative forcing and surface temperature response. *J. Geophys. Res. Atm.*, 120(11):5385–5403, 2015. ISSN 2169-8996. doi: 10.1002/2014JD022752.

R. B. Skeie, T. K. Berntsen, G. Myhre, K. Tanaka, M. M. Kvalevåg, and C. R. Hoyle. Anthropogenic radiative forcing time series from pre-industrial times until 2010. *Atmos. Chem. Phys.*, 11(22):11827–11857, 2011. doi: 10.5194/acp-11-11827-2011.

O. A. Søvde, C. R. Hoyle, G. Myhre, and I. S. A. Isaksen. The HNO3 forming branch of the HO2 + NO reaction: pre-industrial-to-present trends in atmospheric species and radiative forcings. *Atmos. Chem. Phys.*, 11(17):8929–8943, 2011. doi: 10.5194/acp-11-8929-2011.

G. L. Stephens, D. O'Brien, P. J. Webster, P. Pilewski, S. Kato, and J.-l. Li. The albedo of Earth. *Reviews of Geophysics*, 53(1):141–163, 2015. doi: 10.1002/2014RG000449.

D. S. Stevenson, F. J. Dentener, M. G. Schultz, K. Ellingsen, T. P. C. van Noije, O. Wild, G. Zeng, M. Amann, C. S. Atherton, N. Bell, D. J. Bergmann, I. Bey, T. Butler, J. Cofala, W. J. Collins, R. G. Derwent, R. M. Doherty, J. Drevet, H. J. Eskes, A. M. Fiore, M. Gauss, D. A. Hauglustaine, L. W. Horowitz, I. S. A. Isaksen, M. C. Krol, J.-F. Lamarque, M. G. Lawrence, V. Montanaro, and J.-F. Müller. Multimodel ensemble simulations of present-day and near-future tropospheric ozone. *J. Geophys. Res.*, 111, 2006. doi: 10.1029/2005JD006338.

D. S. Stevenson, P. J. Young, V. Naik, J.-F. Lamarque, D. T. Shindell, A. Voulgarakis, R. B. Skeie, S. B. Dalsoren, G. Myhre, T. K. Berntsen, G. A. Folberth, S. T. Rumbold, W. J. Collins, I. A. MacKenzie, R. M. Doherty, G. Zeng, T. P. C. van Noije, A. Strunk, D. Bergmann, P. Cameron-Smith, D. A. Plummer, S. A. Strode, L. Horowitz, Y. H. Lee, S. Szopa, K. Sudo, T. Nagashima, B. Josse, I. Cionni, M. Righi, V. Eyring, A. Conley, K. W. Bowman, O. Wild, and A. Archibald. Tropospheric ozone changes, radiative forcing and attribution to emissions in the Atmospheric Chemistry and Climate Model

Intercomparison Project (ACCMIP). *Atmos. Chem. Phys.*, 13(6):3063–3085, 2013. doi: 10.5194/acp-13-3063-2013.

C. Stubenrauch, J.-P. Duvel, and R. Kandel. Determination of longwave anisotropic emission factors from combined broad- and narrow-band radiance measurements. *Adv. Space Res.*, 14(1):103 – 107, 1994. ISSN 0273-1177. doi: 10.1016/0273-1177(94)90356-5.

R. Stull. *Meteorology For Scientists And Engineers.* Brooks Cole, 2000. ISBN 9780534408022.

J. T. Suttles, R. N. Green, P. Minnis, G. L. Smith, W. F. Staylor, B. A. Wielicki, I. J. Walker, D. F. Young, V. R. Taylor, and L. L. Stowe. *Angular Radiation Model for Earth-Atmosphere System, Vol. II.* NASA Reference Publication 1184, 1988.

A. M. Thompson, J. C. Witte, S. J. Oltmans, and F. J. Schmidlin. SHADOZ-A Tropical Ozonesonde–Radiosonde Network for the Atmospheric Community. *Bull. Amer. Meteor. Soc.*, 85(10):1549–1564, 2004. doi: 10.1175/BAMS-85-10-1549.

S. Turquety, J. Hadji-Lazaro, and C. Clerbaux. First satellite ozone distributions retrieved from nadir high-resolution infrared spectra. *Geophys. Res. Lett.*, 29(24):51–1–51–4, 2002. ISSN 1944-8007. doi: 10.1029/2002GL016431. 2198.

C. Vigouroux, T. Blumenstock, M. Coffey, Q. Errera, O. García, N. B. Jones, J. W. Hannigan, F. Hase, B. Liley, E. Mahieu, J. Mellqvist, J. Notholt, M. Palm, G. Persson, M. Schneider, C. Servais, D. Smale, L. Thölix, and M. De Mazière. Trends of ozone total columns and vertical distribution from FTIR observations at eight NDACC stations around the globe. *Atmos. Chem. Phys.*, 15(6):2915–2933, 2015. doi: 10.5194/acp-15-2915-2015.

J. M. Wallace and P. V. Hobbs. *Atmospheric Science, An Introductory Survey*, volume 92 of *International Geophysics Series.* Academic Press, second edition, 2006.

Z. Wan. New refinements and validation of the MODIS Land-Surface Temperature/Emissivity products. *Remote Sens. Environ.*, 112(1):59 – 74, 2008. ISSN 0034-4257. doi: 10.1016/j.rse.2006.06.026.

U. Wandinger, V. Freudenthaler, H. Baars, A. Amodeo, R. Engelmann, I. Mattis, S. Groß, G. Pappalardo, A. Giunta, G. D'Amico, A. Chaikovsky, F. Osipenko, A. Slesar, D. Nicolae, L. Belegante, C. Talianu, I. Serikov, H. Linné, F. Jansen, A. Apituley, K. M. Wilson, M. de Graaf, T. Trickl, H. Giehl, M. Adam, A. Comerón, C. Muñoz Porcar, F. Rocadenbosch, M. Sicard, S. Tomás, D. Lange, D. Kumar, M. Pujadas, F. Molero, A. J. Fernández, L. Alados-Arboledas, J. A. Bravo-Aranda, F. Navas-Guzmán, J. L.

Guerrero-Rascado, M. J. Granados-Muñoz, J. Preißler, F. Wagner, M. Gausa, I. Grigorov, D. Stoyanov, M. Iarlori, V. Rizi, N. Spinelli, A. Boselli, X. Wang, T. Lo Feudo, M. R. Perrone, F. De Tomasi, and P. Burlizzi. EARLINET instrument intercomparison campaigns: overview on strategy and results. *Atmos. Meas. Tech.*, 9(3):1001–1023, 2016. doi: 10.5194/amt-9-1001-2016.

C. Wespes, D. Hurtmans, L. K. Emmons, S. Safieddine, C. Clerbaux, D. P. Edwards, and P.-F. Coheur. Ozone variability in the troposphere and the stratosphere from the first 6 years of IASI observations (2008–2013). *Atmos. Chem. Phys.*, 16(9):5721–5743, 2016. doi: 10.5194/acp-16-5721-2016.

H. M. Worden, K. W. Bowman, J. R. Worden, A. Eldering, and R. Beer. Satellite measurements of the clear-sky greenhouse effect from tropospheric ozone. *Nature Geosci.*, 1(5):305–308, May 2008. ISSN 1752-0894. doi: 10.1038/ngeo182.

H. M. Worden, K. W. Bowman, S. S. Kulawik, and A. M. Aghedo. Sensitivity of outgoing longwave radiative flux to the global vertical distribution of ozone characterized by instantaneous radiative kernels from Aura-TES. *J. Geophys. Res.*, 116(D14), 2011. ISSN 2156-2202. doi: 10.1029/2010JD015101.

World Meteorological Organization. Meteorology A Three-Dimensional Science: Second Session of the Commission for Aerology. *WMO Bulletin IV (4), WMO, Geneva*, pages 134–138, 1957.

P. J. Young, A. T. Archibald, K. W. Bowman, J.-F. Lamarque, V. Naik, D. S. Stevenson, S. Tilmes, A. Voulgarakis, O. Wild, D. Bergmann, P. Cameron-Smith, I. Cionni, W. J. Collins, S. B. Dalsøren, R. M. Doherty, V. Eyring, G. Faluvegi, L. W. Horowitz, B. Josse, Y. H. Lee, I. A. MacKenzie, T. Nagashima, D. A. Plummer, M. Righi, S. T. Rumbold, R. B. Skeie, D. T. Shindell, S. A. Strode, K. Sudo, S. Szopa, and G. Zeng. Pre-industrial to end 21st century projections of tropospheric ozone from the Atmospheric Chemistry and Climate Model Intercomparison Project (ACCMIP). *Atmos. Chem. Phys.*, 13(4):2063–2090, 2013. doi: 10.5194/acp-13-2063-2013.

D. K. Zhou, A. M. Larar, X. Liu, W. L. Smith, L. L. Strow, P. Yang, P. Schlussel, and X. Calbet. Global Land Surface Emissivity Retrieved From Satellite Ultraspectral IR Measurements. *IEEE Trans. Geosci. Remote Sens.*, 49(4):1277–1290, April 2011. ISSN 0196-2892. doi: 10.1109/TGRS.2010.2051036.

X. Zhou, J. Li, F. Xie, R. Ding, Y. Li, S. Zhao, J. Zhang, and Y. Li. The effects of the Indo-Pacific warm pool on the stratosphere. *Climate Dyn.*, 51(11):4043–4064, 2018. ISSN 1432-0894. doi: 10.1007/s00382-017-3584-2.

J. R. Ziemke, S. Chandra, G. J. Labow, P. K. Bhartia, L. Froidevaux, and J. C. Witte. A global climatology of tropospheric and stratospheric ozone derived from Aura OMI and MLS measurements. *Atmos. Chem. Phys.*, 11(17):9237–9251, 2011. doi: 10.5194/acp-11-9237-2011.